Tracing Enriched Mantle Components along the Gakkel Ridge, Arctic Ocean

---

A Thesis Presented to

the Faculty of the Department of Earth and Atmospheric Sciences

University of Houston

---

in Partial Fulfillment

of the Requirements for the Degree

Master of Science

By

Nam Hien Nguyen

December, 2013

Tracing Enriched Mantle Components along the Gakkel Ridge, Arctic Ocean

Nam Hien Nguyen

APPROVED:

Supervisor, Dr. Jonathan Snow

Dr. Alan Brandon

Dr. Yongjun Gao

Dr. Steven Bergman

Dean, College of Natural Sciences and Mathematics

ACKNOWLEDGEMENTS

Thank you, Dr. Snow, for all the help.

December, 2013

Tracing Enriched Mantle Components along the Gakkel Ridge, Arctic Ocean

---

An Abstract of a Thesis

Presented to

the Faculty of the Department of Earth and Atmospheric Sciences

University of Houston

---

in Partial Fulfillment

of the Requirements for the Degree

Master of Science

By

Nam Hien Nguyen

December, 2013

ABSTRACT

Mid-ocean ridge basalts (MORBs) along the Gakkel Ridge in the Arctic Eurasian basin have varying levels of trace element enrichment. The purpose of this research is to determine the extent to which the trace element enrichment of basalts along the Gakkel Ridge is influenced by magmatic differentiation processes or mantle heterogeneity. This was accomplished by calculating the effects of magmatic differentiation on basalt trace element ratios and by defining the compositions of mantle components in the mantle along Gakkel Ridge and interpreting their origins, scales, and distribution. Electron microprobe and laser-ablation inductively-coupled-plasma mass-spectrometer (LA-ICP-MS) instruments were used to analyze major element and trace element concentration data in glass chips of basalt samples dredged from the Gakkel Ridge. As a consequence of Gakkel Ridge's ultraslow spreading rate, fractional crystallization has only a minimal effect on trace element ratios of Gakkel Ridge MORBs. Trace elements plotted on ternary plots reveal four main aspects about the nature of the enriched component along Gakkel Ridge: 1) Sparsely Magmatic Zone (SMZ) and Eastern Volcanic Zone (EVZ) basalt trace element data plot along a two-component mixing line trending between a depleted MORB mantle (DMM) composition and an average Mid-Atlantic Ridge enriched-MORB (MAR E-MORB) composition. This mixing line is separate from the mixing line on which the Western Volcanic Zone (WVZ) trace element data plot, which trends between the DMM and the high-K_2O Central Lena Trough (CLT) source; 2) The level of enrichment in MORB samples of the SMZ and EVZ varies from being relatively similar across a span of 97 km in the EVZ at 31-47°E, to changing significantly between individual dredging stations in the SMZ at 13°E, 19°E, and in the EVZ at 55°E. This shows that the size and distribution of enriched reservoirs drastically vary; 3) Trace elements indicate that the main enriched source of the EVZ and SMZ basalts resemble MAR E-MORB source mantle and is not continental in origin; and 4) At least one additional enriched source exists along Gakkel Ridge, as evidenced by the chemical signature in the EVZ at 55°E, which shows at least three different mixing component compositions.

TABLE OF CONTENTS

LIST OF FIGURES

LIST OF TABLES

1) INTRODUCTION

1.1) Geochemical connection between mantle and MORB

Earth's mantle is defined as the region in the planet's interior located between the crust and the core. The mantle shares an important geochemical connection with the crust, because the crust was originally formed from melts derived from the mantle; thus, the geochemistry of crustal rocks reflects their genetic relationship with the rocks of the mantle (Hofmann, 1988). Indeed, it can be said that the crust is "genetically" related to the mantle.

To understand how the crust and the mantle are geochemically related, it is important to understand the processes by which crustal rocks are formed. At mid-ocean ridges, seafloor spreading separates the tectonic plates, leading to upwelling of asthenospheric mantle material beneath the ridge axes (Langmuir et al., 1992; Hofmann, 1997; Klein, 2003b). As mantle convection brings mantle rocks upward, the pressure exerted downwards by the overlying rocks upon mantle rocks decreases, resulting in decompression melting of the rising mantle rocks, thereby producing magma melts that flow upwards, erupt, and cool to form the oceanic crust, the upper layer of which is composed of mid-ocean ridge basalt (MORB) (Fig. 1; Langmuir et al., 1992; Klein, 2003b).

Peridotite is a rock type mainly composed of olivine, pyroxene, garnet, and spinel group minerals. Peridotite is the dominant rock-type of the upper mantle (Helffrich & Wood, 2001; Sobolev et al., 2005). The peridotite-dominated region extends down at least as deep in the mantle as 150 km (Helffrich & Wood, 2001). This region of the mantle is relevant to the study of MORB chemistry, because MORBs are derived from

shallow mantle depths, meaning that MORBs are derived primarily from peridotites. The mineral olivine, which composes more than 50% of earth's upper mantle, is the most abundant mineral in the peridotite portion of the mantle (Sobolev, 2005).

The depleted MORB mantle (DMM) is recognized as the most widespread magmatic source component in the upper mantle and the dominant source of magmatic melts in the generation of mid-ocean ridge magma (Zindler & Hart, 1986). Basalts derived from this source are characterized by a depletion in the more highly incompatible elements, such as light rare earth elements, relative to the primordial undifferentiated primitive mantle (PM) composition (Zindler & Hart, 1986). The depletion of incompatible elements in DMM is considered to be evidence that the DMM has experienced previous partial melting events, during which the more incompatible elements were extracted in greater proportion than the less incompatible elements (Zindler & Hart, 1986).

The degree of enrichment in MORBs can vary with distance along a single ridge. For instance, a notable example of such a ridge is the ultraslow spreading Gakkel Ridge in the Arctic Basin, where the MORBs show significantly different degrees of variation in isotopic and trace element enrichment (Michael et al., 2003; Goldstein et al., 2008; Shaw et al., 2010).

It has generally been assumed that two major factors can affect basalt compositions (e.g., Grove et al., 1992; Klein et al., 2003b): 1) magmatic differentiation processes experienced by magmas prior to erupting (e.g., Ohara, 1965; Kay et al., 1970) and/or 2) chemical and mineralogical compositional heterogeneity in the mantle source from which magmas were derived (e.g., Schilling, 1973).

This study examines how the chemistry of Gakkel Ridge MORB compositions were affected by differentiation processes and by mantle heterogeneity. A better understanding of Gakkel Ridge chemical diversity can lead to better understandings of slow spreading ridge evolution as well as the global MORB diversity.

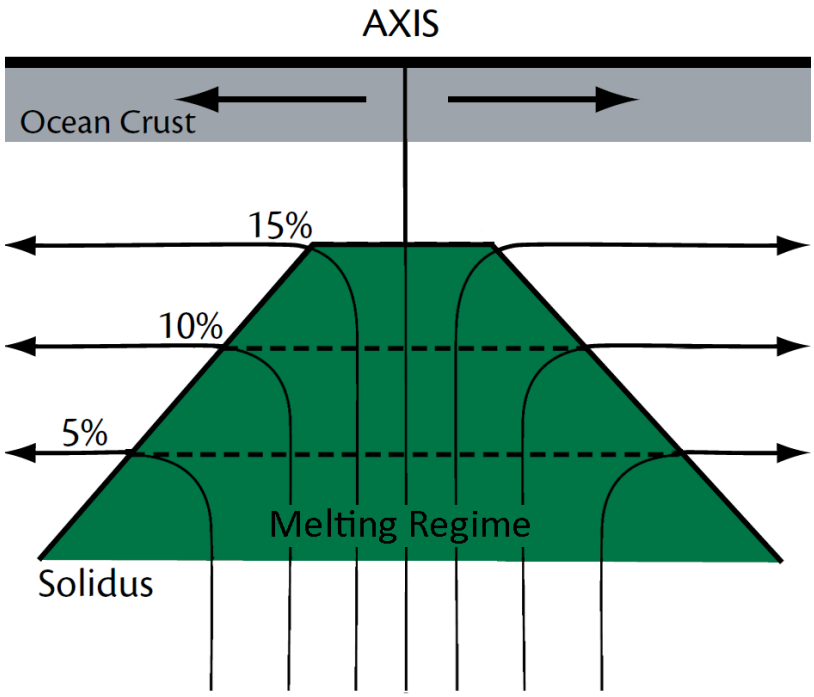

Figure 1a. Generalized MORB subaxial melting regime triangle, showing varying percentages of mantle melting and melt extraction correlating with the depth and direction of the melt flow (Modified from Langmuir & Forsyth, 2007).

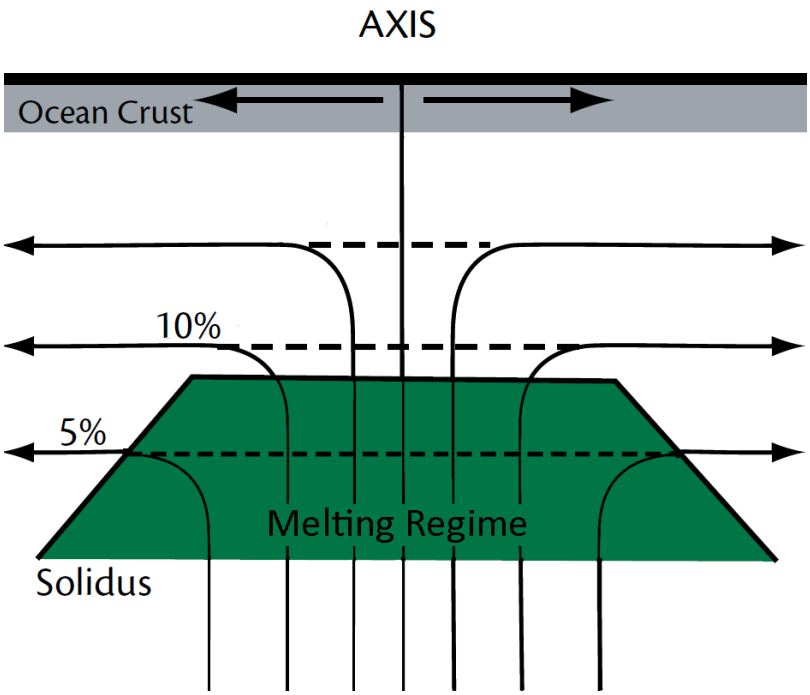

Figure 1b. MORB subaxial melting triangle at ultraslow spreading ridges (Modified from Langmuir & Forsyth, 2007)

1.2) Basalt enrichment

Basalt geochemistry studies generally categorize MORBs based on their relative levels of incompatible trace element enrichment or depletion. Under this classification system, MORBs vary in composition from normal mid-ocean ridge basalt (N-MORB) to trace element enriched mid-ocean ridge basalt (E-MORB). E-MORBs are characterized by elevated amounts of incompatible trace elements compared to N-MORB. Intermediate compositions are categorized as transitional mid-ocean ridge basalt (T-MORB) (Sun & McDonough, 1989).

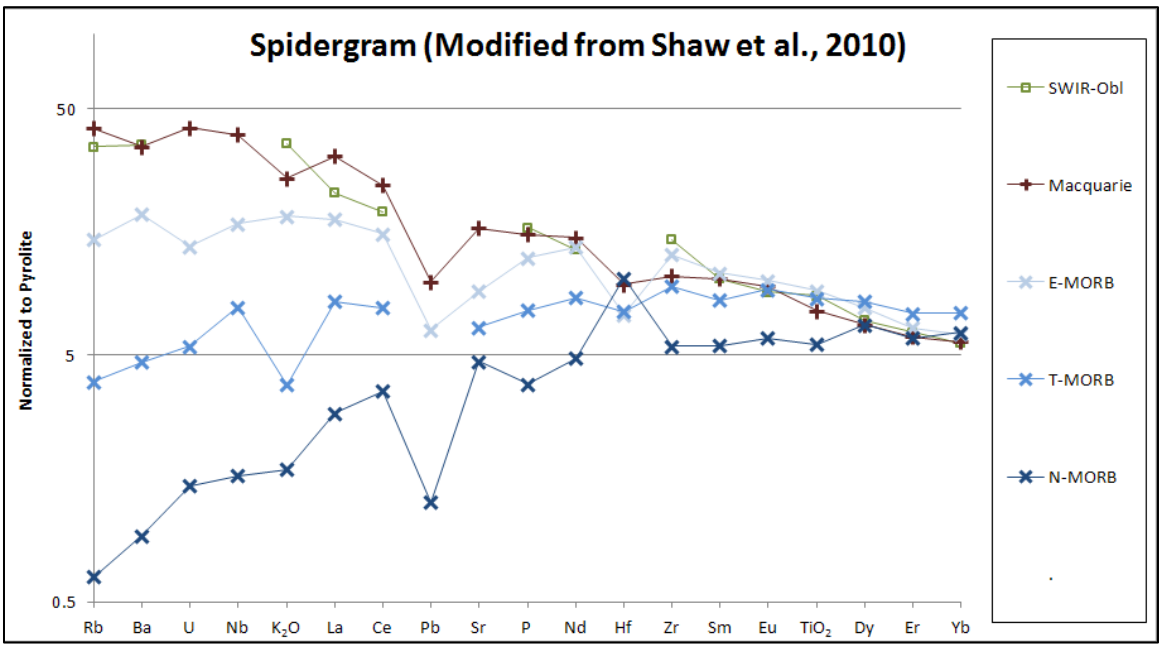

Figure 2. Spidergram showing average trace elements of Mid-Atlantic Ridge (MAR) N-MORB, T-MORB, and E-MORB (Klein, 2003b). Average Macquarie Island basalt (Kamenetsky et al., 2000) and Southwest Indian Ridge - oblique segment MORBs (Standish et al., 2008) are plotted as additional examples of different E-MORB compositions. Elements are normalized to pyrolite (McDonough & Sun, 1995).

The La/Sm ratio, which has long been used to measure enrichment in MORBs (e.g., Schilling, 1971), compares the highly incompatible rare earth element lanthanum (La) with the less incompatible rare earth element samarium (Sm). In order to distinguish between N-MORB, T-MORB, and E-MORB, the La/Sm ratio can be used to define the boundaries in the levels of enrichment between the different MORB types (Sun & McDonough, 1989). However, the ratios corresponding with each type of MORB are not precisely defined by any widely agreed upon convention, so they must be arbitrarily decided for this study. In this thesis, the La/Sm ratio that was used to define the MORB types are: N-MORB La/Sm <0.8; T-MORB La/Sm 0.8-1.8; E-MORB La/Sm >1.8.

Trace element concentrations of average MAR N-MORB and E-MORB, as well as a DMM composition, are shown in Table 1 for comparison with Gakkel Ridge concentration data. Among these compositions, DMM is the most depleted, MAR N-MORB is the next most depleted, and MAR E-MORB is the most enriched.

	Rb	Sr	Y	Zr	Nb	Cs	Ba	La	Ce	Pr	Nd	Sm	Eu	Gd
DMM	0.1	0.1	4.1	7.9	0.2	0.001	1.2	0.2	0.8	0.1	0.7	0.27	0.11	0.40
MAR N-MORB	0.4	104	24.0	57	1.1	0.005	4.6	1.8	6.0	1.1	6.3	2.37	0.94	3.28
MAR E-MORB	13	221	27.4	121	20	0.128	146	13.5	29.2	3.8	16.8	4.22	1.44	4.77

	Tb	Dy	Ho	Er	Tm	Yb	Lu	Hf	Ta	Pb	Th	U	TiO_2	Sc
DMM	0.08	0.53	0.122	0.37	0.060	0.4	0.063	0.20	0.014	0.02	0.01	0.005	4.49	16.3
MAR N-MORB	0.58	4.07	0.892	2.62	0.377	2.7	0.377	1.62	0.055	0.27	0.05	0.022	32.1	38.7
MAR E-MORB	0.73	4.94	1.06	3.08	0.432	3.0	0.428	2.25	0.347	1.1	0.38	0.127	41.5	40.3

Table 1. DMM composition calculated by Salters and Stracke (2004). Average MAR N-MORB and E-MORB data compiled from PetDB (Lehnert et al., 2000). TiO2 is reported in weight percent. All other concentrations are reported in ppm. N-MORB is defined as basalts (glass samples) having a La/Sm ratio of less than 0.8. E-MORB is defined as basalts (glass samples) having a La/Sm ratio of greater than 1.8.

It should be noted, however, that all E-MORBs are not compositionally identical, but instead, different suites of E-MORBs have been recognized (Fig. 2). For example,

Macquarie Island basalts (Fig. 2; Fig. 3; Kamenetsky et al., 2000) and Southwest Indian Ridge (SWIR) oblique segment basalts (Fig. 2; Fig. 3; Standish et al., 2008) can be considered to be E-MORB compositions, but their trace element patterns are also distinct from each other and from the average Mid-Atlantic Ridge (MAR) E-MORB. The distinctions between different enriched MORBs may indicate that all E-MORBs do not share the same reason for being enriched.

1.3) Trace element ratios - ternary plots

Ternary plots are triangular-shaped graphs on which data from three different variables can be plotted. Such plots are especially useful for comparing trace element concentration ratios, because they simultaneously illustrate relative proportions of three different trace elements.

Trace element ratios are useful in the study of MORB compositions because certain element ratios can remain relatively constant throughout the process of mantle melt extraction, even after the magmatic melts have experienced differentiation processes (Salters & Stracke, 2004). This resistance to change, which is especially apparent at low degrees of differentiation, means that the ratios in basalts closely reflect the original ratios in the mantle. For instance, La/Sm is one example of a ratio that is relatively insensitive to fractional crystallization (Holness & Richter, 1982).

Three sets of three trace elements each were chosen for the ternary plots throughout this thesis: Na_2O & K_2O & La (NKL), TiO_2 & K_2O & La (TKL), and Yb & Sm & La (YSL). The relative incompatibilities of these elements are: K>La>Sm>Ti>Yb (Sun & McDonough, 1989). Na_2O appears to be more compatible than K_2O and La and

similar in incompatibility to Sm (e.g., Fig. 3a). These elements were chosen for their variety in different relative levels of incompatibility and for some of their unique characteristics.

A unique characteristic of the rare earth elements (e.g., La, Sm, and Yb) is that they share similar chemical and physical properties, with the primary difference being that their ionic radii decrease with increasing atomic number, so the size of these atoms are the main factor determining differences in their differentiation behavior. The YSL ternary plot features only rare earth elements, ranging from one of the largest rare earth elements, La, to the intermediate-sized Sm, to one of the smallest rare earth elements, Yb. La is especially useful for comparisons between elements, because it is the most incompatible of the rare earth elements, which is why La is included in all three sets of elements.

K_2O is featured on both the TKL and NKL ternary plots primarily so that basalts from Gakkel Ridge can be compared to other basalts of the Arctic Basin, because many of the basalts of the Arctic Basin, notably those of central Lena Trough, feature unusually enriched K_2O compositions (Nauret, 2011).

One of the useful applications of the ternary plots is that they allow distinction of samples derived from more enriched sources from samples derived from more depleted sources. On each ternary plot, the trend between the depleted and enriched sources is easily identifiable, because it tends to trend between the average N-MORB and E-MORB points. The depleted to enriched trend also tends to correlate with the DMM to PM trend, although PM is not as enriched as the average E-MORB. Overall, this means that the samples from more depleted sources plot closer to the average N-MORB and depleted

MORB mantle (DMM) points, whereas the samples from more enriched sources plot closer to the average E-MORB points.

To illustrate the global variation in levels of enrichment in MORBs, Figure 3 presents the NKL, TKL, and YSL trace element ternary plots depicting relative trace element compositions in global MORB and enriched basalt datasets, along with points representing average N-MORB, T-MORB, and E-MORB from different ocean ridges.

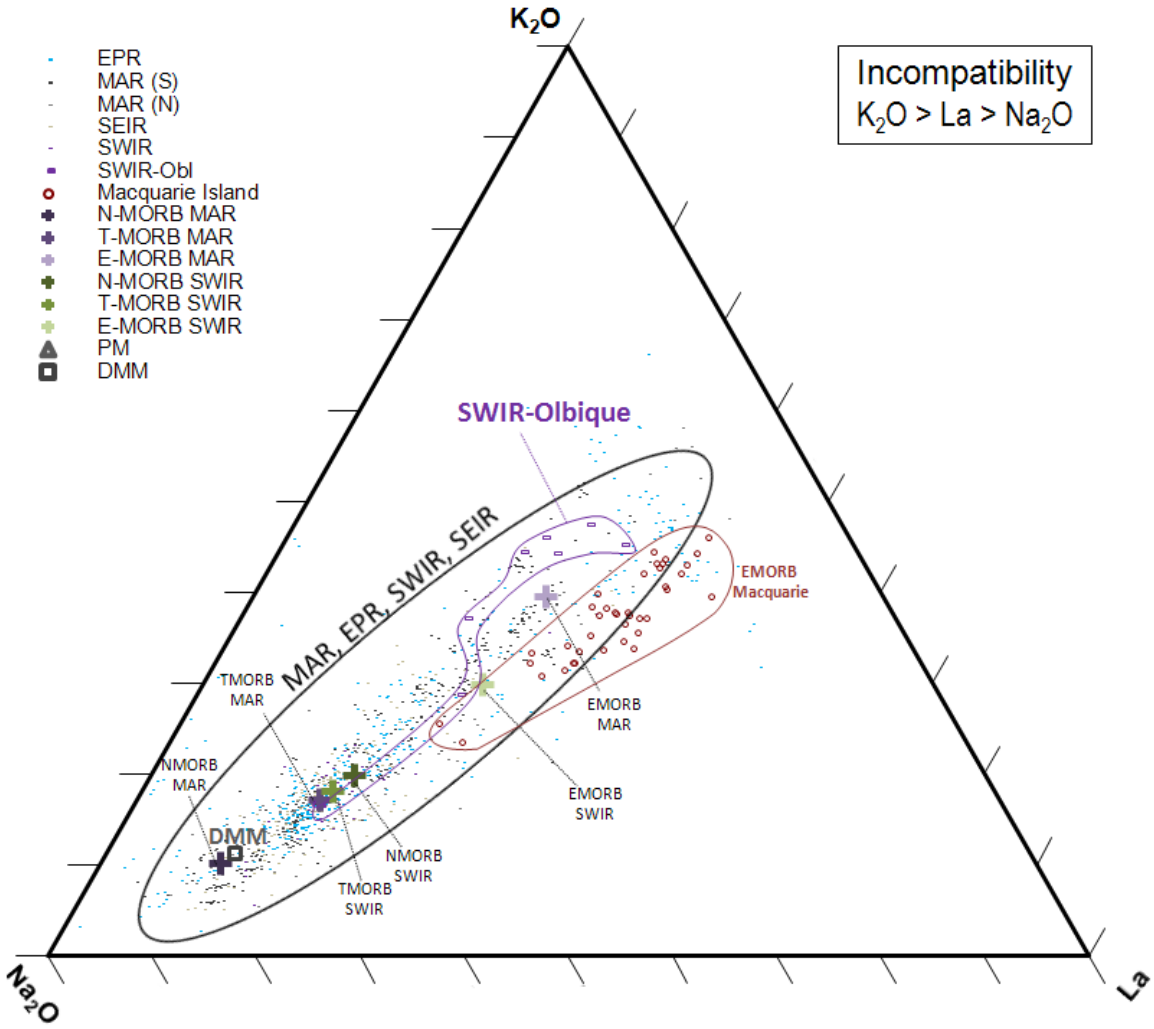

Figure 3a. NKL Ternary plot showing relative concentrations of Na_2O (wt.% x 5), K_2O (wt% x 30), & La (ppm) in basalt glass samples from the Mid-Atlantic Ridge (MAR), East Pacific Rise (EPR), Southwest Indian Ridge (SWIR), Southeast Indian Ridge (SEIR) (PetDB; Lehnert et al., 2000), and Southwest Indian Ridge – Oblique segment (Standish et al., 2008), and Macquarie Island (Kamenetsky et al., 2000). Average N-MORB, T-MORB, and E-MORB points for the MAR and SWIR are calculated based on the La/Sm ratio, with N-MORB La/Sm <0.8; T-MORB La/Sm 0.8-1.8; E-MORB La/Sm >1.8. Also plotted as reference points on these ternary plots are the depleted MORB mantle (DMM) (Salters & Stracke, 2004) and primitive mantle (PM) (Sun & McDonough, 1989), although a Na_2O concentration for PM was not found, so PM does not appear in this figure, but does appear in the TKL (Fig. 3b) and YSL (Fig. 3c) ternary plots.

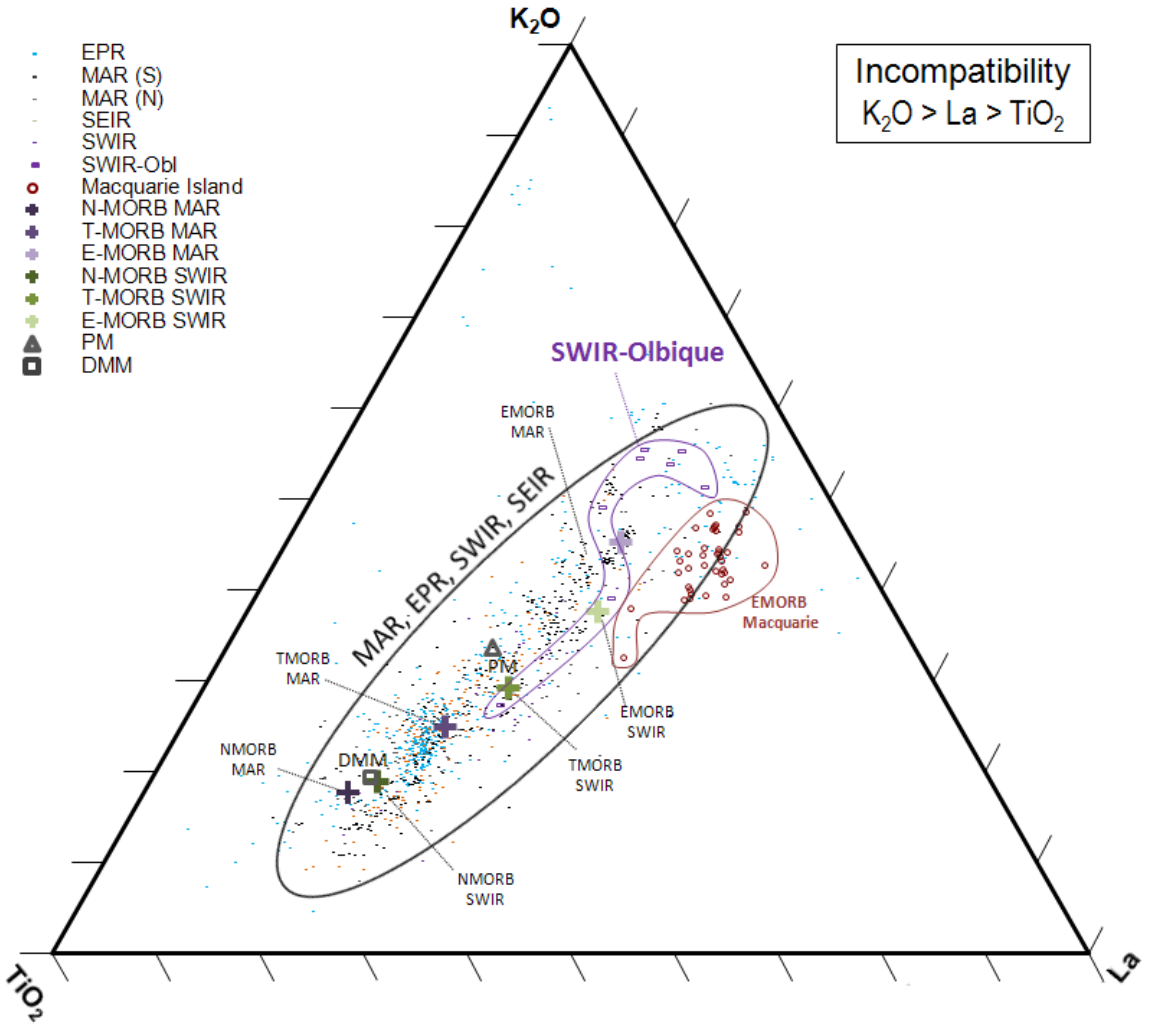

Figure 3b. TLK Ternary plot showing relative concentrations of TiO_2 (wt.% x 5), K_2O (wt.% x 30), & La (ppm) in MORB glass samples. Data are from the same references as those in Fig. 3a.

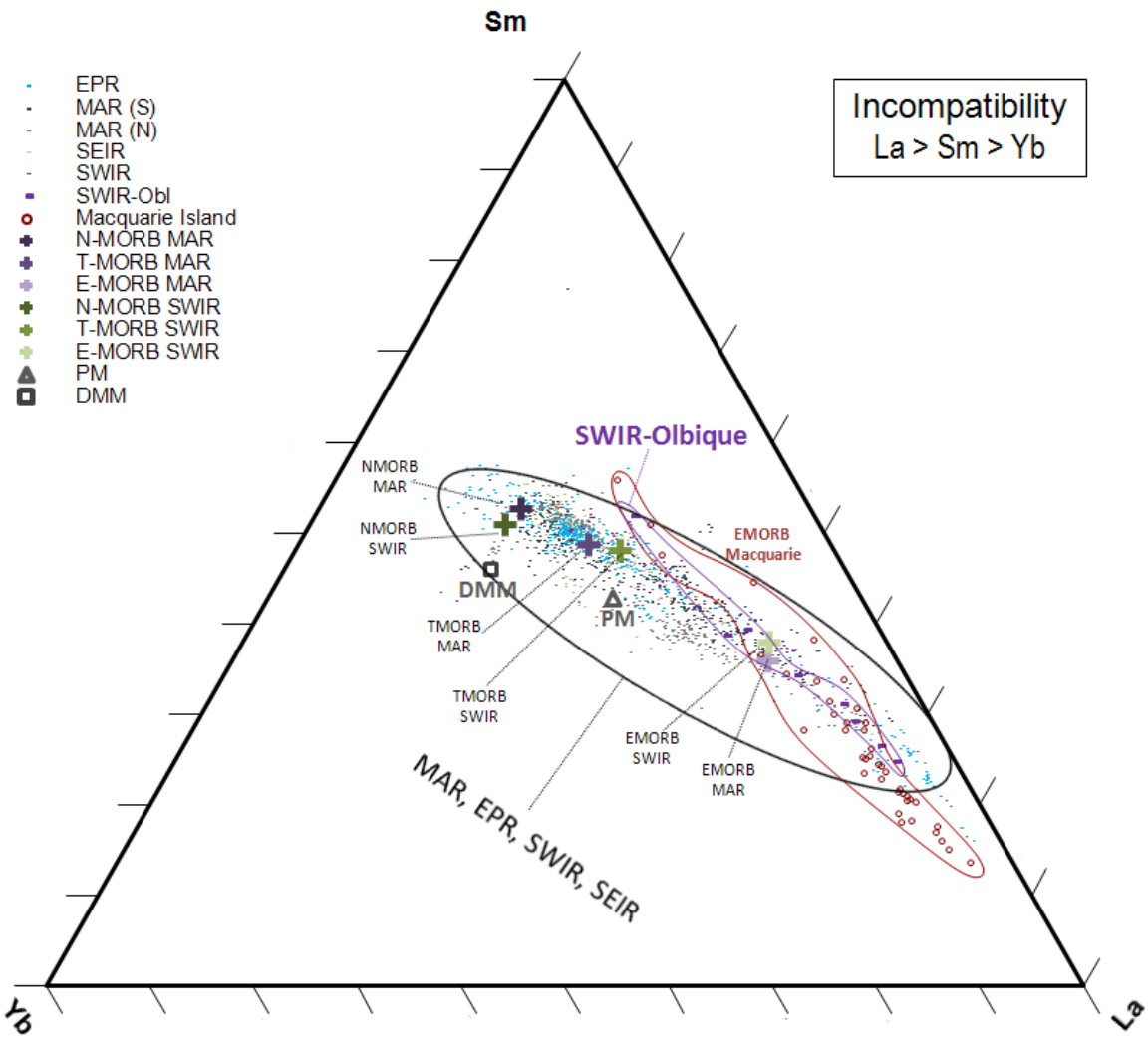

Figure 3c. YSL Ternary plot showing relative concentrations of Yb (ppm), Sm (ppm x 2), & La (ppm) in MORB glass samples. Data are from the same references as those in Figure 3a. Strangely, the DMM composition (Salters & Stracke, 2004) plots far off of the MORB array on the YSL triangle, even though it should plot close to average N-MORB as it does on the NKL (Fig. 3a) and TKL (Fig. 3b) triangles.

The NKL, TKL, and YSL ternary plots of Figure 3 all show oceanic basalts forming a single array between enriched and depleted endmembers in composition space.

On the YSL ternary plots (i.e., Fig. 3c), the estimated DMM composition (Salters & Stracke, 2004) plots significantly far off of the main MORB array on the YSL triangle

(e.g., Fig. 3c). This position is unexpected, because by definition, N-MORB is the melting product of DMM, so DMM should always plot close to average N-MORB, which is indeed how it appears on the NKL and TKL triangles. Also, these DMM compositions are not only inconsistent with the data from this study, but also with the global MORB composition data obtained from PetDB (Lehnert et al., 2000). An alternate estimated DMM composition estimated by Workman & Hart (2005), different from the composition from the estimate by Salters & Stracke (2004), was also plotted on the ternary plots as a test to see whether the same problem persists. However, much like the DMM from Salters & Stracke (2004), the alternate DMM also plotted off of the MORB array, significantly far away from average the average N-MORB point. The reason that the DMM composition estimated by Salters & Stracke (2004) and by Workman & Hart (2005) both appear to be wrong for the YSL triangle is unknown.

One possible explanation is that unlike the NKL triangle (e.g., Fig. 3a) and TKL triangle (e.g., Fig. 4b), which include oxides (i.e., Na_2O, TiO_2, K_2O), the YSL triangle features only rare earth elements (i.e., Yb, La, Sm), so it may be possible that something is wrong with the rare earth element estimates in the DMM composition by Salters & Stracke (2004). To investigate this possibility, Salters & Stracke's DMM composition concentrations of the rare earth elements Eu, Gd, Tb, Dy, Ho, Er, Tm, and Yb (calculated as a percentage relative to La and Sm, i.e., the percentage of the aforementioned element added to the percentages of La and Sm sum to 100%) were compared to the concentrations of those elements in the average MAR N-MORB composition. Those particular rare earth elements were chosen because Salters & Stracke (2004) used the same constraining ratio denominator in their calculations for all of those elements, but not

for the rest of the rare earth elements. The amount of deviation was calculated by comparing the compositions of those elements in DMM and MAR N-MORB as percentages relative to La and Sm (i.e., when the percentage of that element is added to the percentages of La and Sm, it sums to 100%) and then comparing the percent difference between the DMM concentration and the MAR N-MORB concentration of that element. The results of these calculations show that Eu, Gd, Tb, Dy, Ho, Er, Tm, and Yb in Salters and Stracke's DMM composition differs when compared to those compositions in the average MAR N-MORB by 4.8%, 0.7%, 1.1%, 4.5%, 8.0%, 10.6%, 20.7%, and 14.5%, respectively. There appears to be a trend of increasing deviation from the lighter rare earth elements (i.e., Eu, Gd, Tb, Dy) to the heavier rare earth elements (i.e., Ho, Er, Tm, Yb). The exact cause of the heavier rare earth elements being less correlated with MAR N-MORB (and thus, with the MORB array) is unknown, but the amount of discrepancy in Salters & Stracke's (2004) DMM compositions appears to increase in correlation with the gradual lanthanide contraction from light rare earth elements to heavy rare earth elements.

1.4) Magma differentiation

One idea that is often discussed by studies of MORB geochemistry is that the diversity observed in global MORB compositions reflects an influence from two main factors: 1) magmatic differentiation processes and/or 2) mantle heterogeneity (Klein, 2003b). The extent to which each factor influences the MORB composition is still a matter of debate, but one widely held belief is that among the many processes causing chemical differentiation in magmas, the most dominant processes that can affect the composition of MORBs are fractional crystallization and partial melting (e.g., Grove et al., 1992; Klein, 2003b). Between crystallization and melting, crystallization is often considered to have a greater impact on MORB compositions (e.g., Klein, 2003b), so this study devotes more attention to fractional crystallization.

1.4.1) Fractional crystallization

Fractional crystallization is the process of formation and removal of mineral precipitates from the magmatic melt, during cooling of the magmatic melt, which occurs at shallow levels in the uppermost mantle and crust (e.g., Grove et al., 1992; Klein, 2003b). By incorporating elements from the magmatic melt into the crystallizing solid mineral precipitates, the fractional crystallization process changes the chemical composition of the uncrystallized liquid magma (e.g., Grove et al., 1992; Klein, 2003b).

Basalts erupted from the same sub-axial magma reservoir may be derived from varying stages of crystallization, resulting in MORBs with different chemical compositions (Klein, 2003b). However, because the effects of fractional crystallization are well understood – to a better degree than any of the other magma differentiation

processes – the chemical signature of fractional crystallization can be distinguished from chemical signatures of other magma differentiation processes and variations in source composition (Fig. 4, Klein, 2003b). In general, fractional crystallization is only capable of causing relatively minor enrichments in incompatible elements in basalts (Hofmann, 1988).

The extent of the effect that the fractional crystallization process has on the concentrations of trace elements in magmatic melts can be calculated using the fractional crystallization equation:

$$C^l/C^o=(1-X)^{D-1}$$

with C^o denoting the concentration in the original liquid, C^l denoting the concentration in the remaining liquid, X denoting the fraction of the material crystallized, and D denoting the partition coefficient. The fractional crystallization equation was obtained from White (2013).

Figures 4a-4e show the results of fractional crystallization of olivine in a DMM (Salters & Stracke, 2004) magma composition. Fractional crystallization calculations were conducted for the mineral phases olivine (Fig. 4a-4b), clinopyroxene (Fig. 4c-4d), and plagioclase (Fig. 4e). The resulting compositions from these calculations are plotted on the YSL ternary plots (Fig. 4b; Fig. 4d) and TKL ternary plots (Fig. 4a; Fig. 4c; Fig. 4e). The crystallization value of 10% for the mineral phase olivine is more representative of the low degrees of fractional crystallization at ultraslow spreading ridge segments (Fig.

1b), while the higher fractional crystallization percentages and the other mineral phases are more representative of faster spreading ridge segments (Fig. 1a) (Walker et al., 1979).

The olivine and plagioclase crystallization diagrams (Fig. 4a; Fig 4b; Fig. 4e) show the original DMM composition remaining nearly unchanged in its relative trace element concentrations even after 10%, 30%, and 50% fractional crystallization. The different points representing different percentages of crystallization almost all nearly overlap each other. In contrast, a more significant change is seen on the clinopyroxene crystallization diagrams (Fig. 4c-4d), which shows that the points representing fractional crystallization of a DMM composition to 10%, 30%, and 50% plot noticeably farther away from the original DMM composition.

Importantly however, it should be noted that all of these mineral phases do not simultaneously start crystallizing at the same time. Olivine is the first mineral to crystallize from nearly all MORB magmas (Sobolev et al., 2007), so although the crystallization of clinopyroxene (Fig. 4c-4d) and plagioclase (Fig. 4e) are also shown, only the olivine crystallization diagrams (Fig. 4a-4b) are representative of the initial degrees of fractional crystallization. The other mineral phases would not crystallize until higher extents of crystal fractionation have occurred. At low degrees of fractional crystallization, the number of mineral phase that crystallize may be minimized more than at higher degrees of fractional crystallization.

Among the phases modeled in Figure 4, the next phases to crystallize after olivine are plagioclase, followed by clinopyroxene. The crystallization of clinopyroxene happens very late on the MORB liquidus (Walker et al., 1979) even at high pressures (Stolper, 1980). This means that clinopyroxene crystallization may affect the magma composition

(as seen on Figure 4) if the MORB magma is allowed to crystallize deeply at higher pressure, where higher extents of fractional crystallization occurs (Elthon et al., 1992), but the crystallization of clinopyroxene is unlikely to be a significant factor in affecting MORB magma compositions in the low pressure, low degree fractionation that occurs at ultraslow spreading ridges, such as Gakkel Ridge.

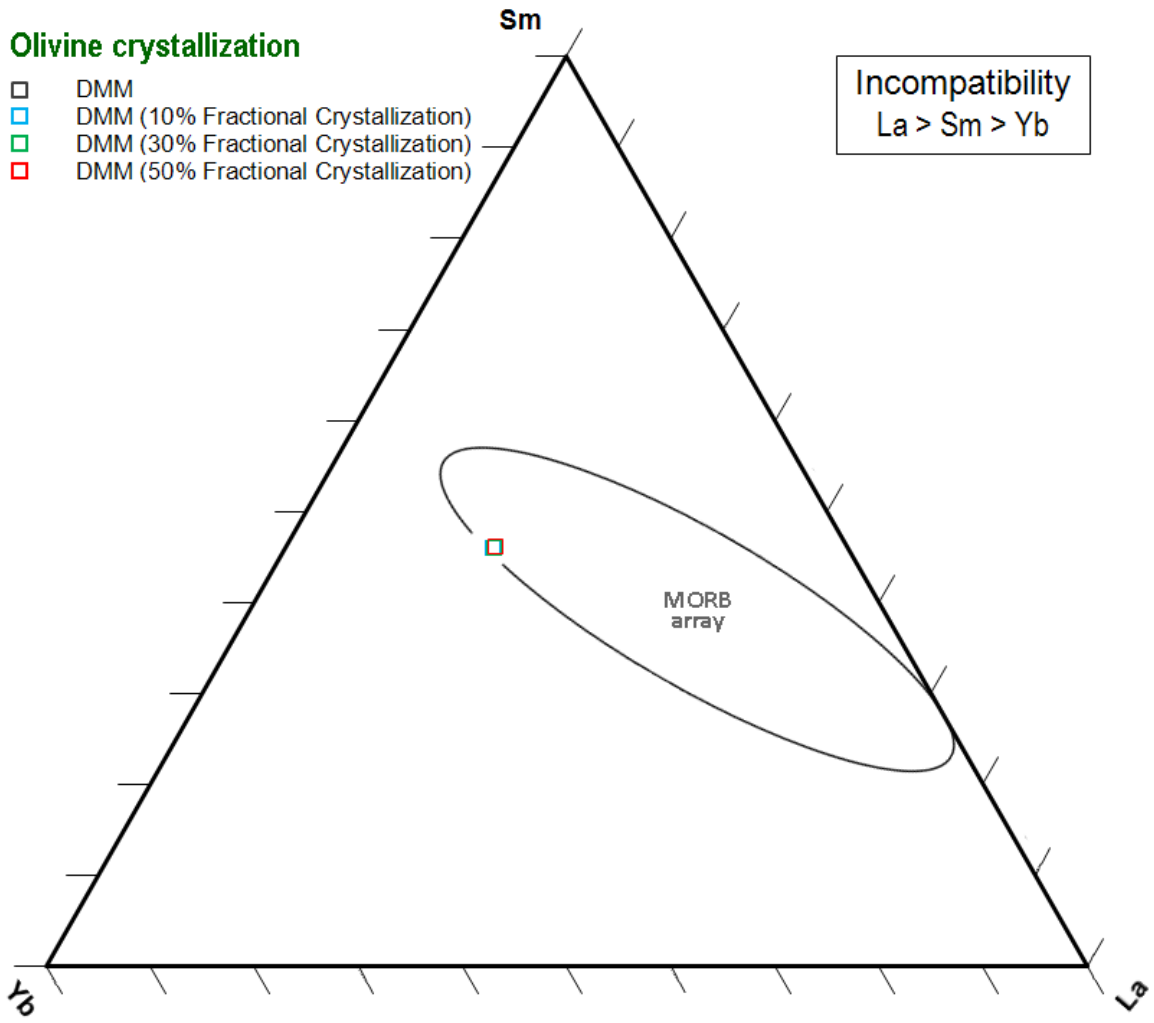

Figure 4a. Olivine crystallization diagram: YSL Ternary plot showing relative concentrations of the trace elements Yb (ppm), Sm (ppm x 2) and La (ppm) of a depleted MORB mantle composition (DMM) (Salters & Stracke, 2004), at 0%, 10%, 30%, and 50% fractional crystallization of the mineral phase olivine, respectively represented by a black square, blue square, green square, and red square. The four squares almost overlap each other. The partition coefficients of Yb, Sm, and La for olivine used in this calculation were obtained from Salters & Stracke (2004) and are for 2 GPa pressure. The global MORB array, comprising data from the MAR, EPR, SWIR, & SEIR, (PetDB; Lehnert et al., 2000) is encircled in black.

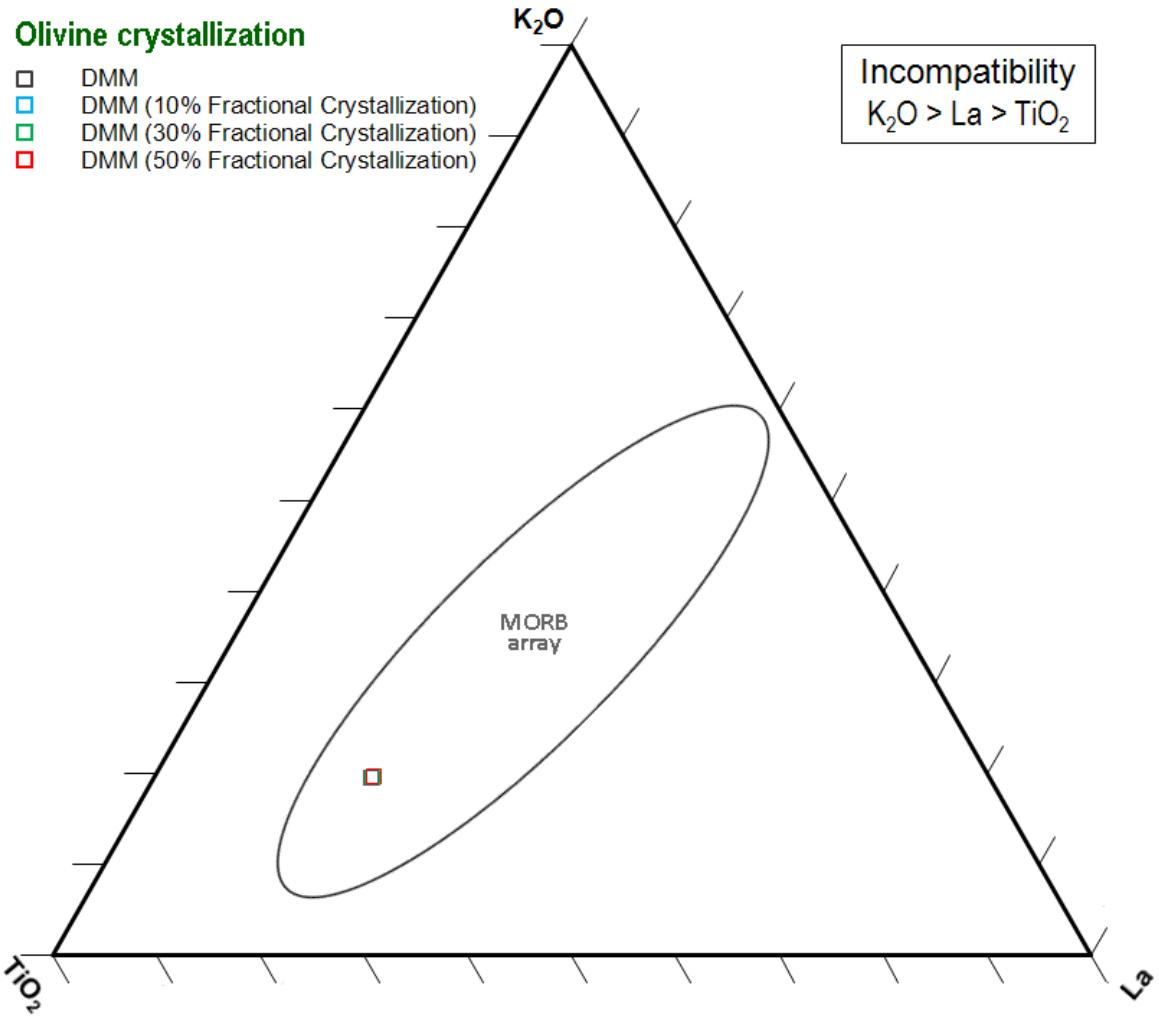

Figure 4b. Olivine crystallization diagram: TKL Ternary plot showing relative concentrations of the trace elements TiO_2 (wt.% x 5), K_2O (wt.% x 30) and La (ppm) of a depleted MORB mantle composition (DMM) (Salters & Stracke, 2004) at 0%, 10%, 30%, and 50% fractional crystallization of the mineral phase olivine, respectively represented by a black square, blue square, green square, and red square. The four squares almost overlap each other. The partition coefficients of Ti, K, and La for olivine used in this calculation were obtained from Salters & Stracke (2004) and are for 2 GPa pressure. The global MORB array, comprising data from the MAR, EPR, SWIR, & SEIR, (PetDB; Lehnert et al., 2000) is encircled in black.

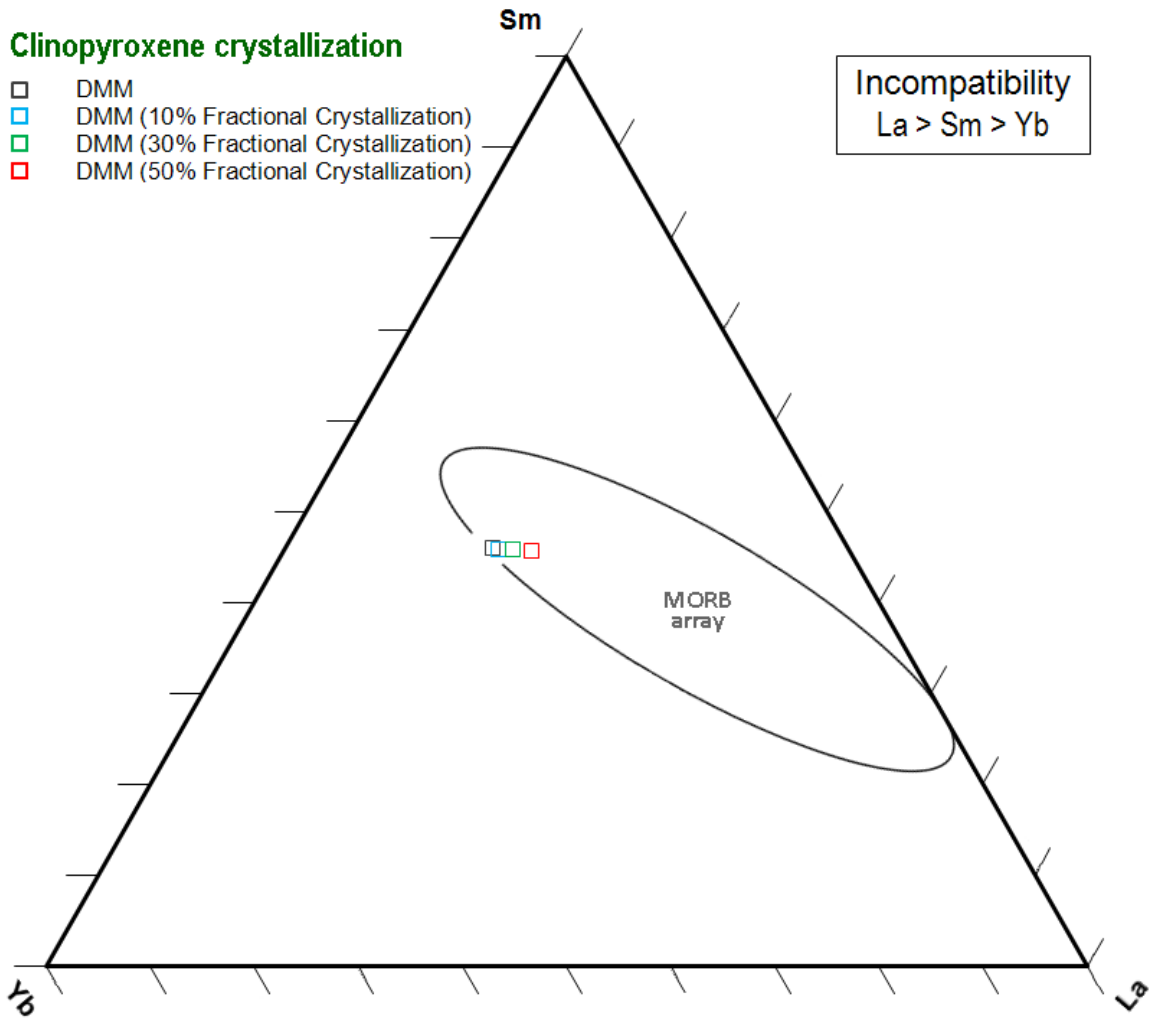

Figure 4c. Clinopyroxene crystallization diagram: YSL Ternary plot showing relative concentrations of the trace elements Yb (ppm), Sm (ppm x 2) and La (ppm) of a depleted MORB mantle composition (DMM) (Salters & Stracke, 2004) at 0%, 10%, 30%, and 50% fractional crystallization of the mineral phase clinopyroxene, respectively represented by a black square, blue square, green square, and red square. The partition coefficients of Yb, Sm, and La for olivine used in this calculation were obtained from Salters & Stracke (2004) and are for 2 GPa pressure. The global MORB array, comprising data from the MAR, EPR, SWIR, & SEIR, (PetDB; Lehnert et al., 2000) is encircled in black.

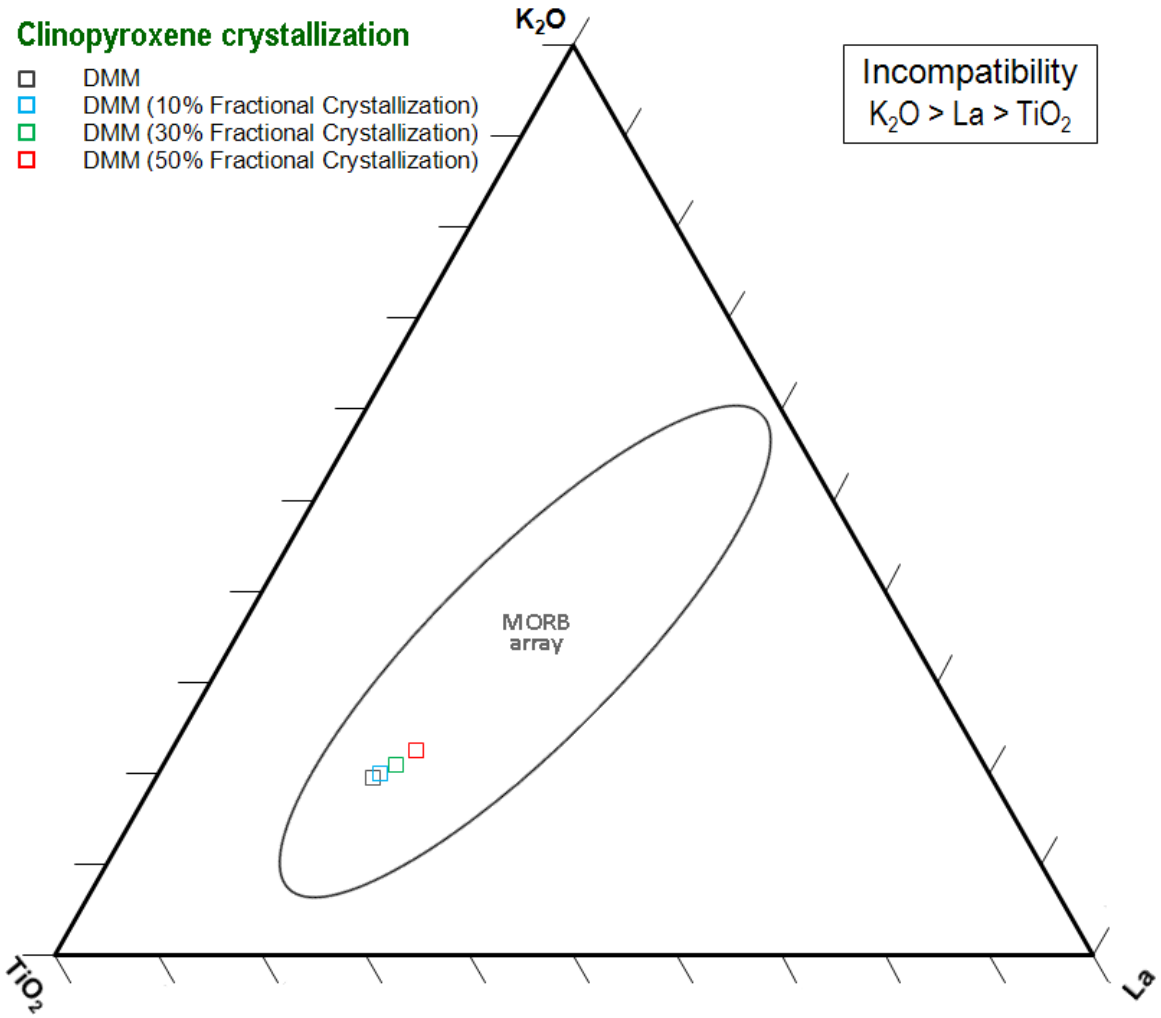

Figure 4d. Clinopyroxene crystallization diagram: TKL Ternary plot showing relative concentrations of the trace elements TiO_2 (Wt.% x 5), K_2O (Wt.% x 30) and La (ppm) of a depleted MORB mantle composition (DMM) (Salters & Stracke, 2004) at 0%, 10%, 30%, and 50% fractional crystallization of the mineral phase clinopyroxene, respectively represented by a black square, blue square, green square, and red square. The partition coefficients of Ti, K, and La for olivine used in this calculation were obtained from Salters & Stracke (2004) and are for 2 GPa pressure. The global MORB array, comprising data from the MAR, EPR, SWIR, & SEIR, (PetDB; Lehnert et al., 2000) is encircled in black.

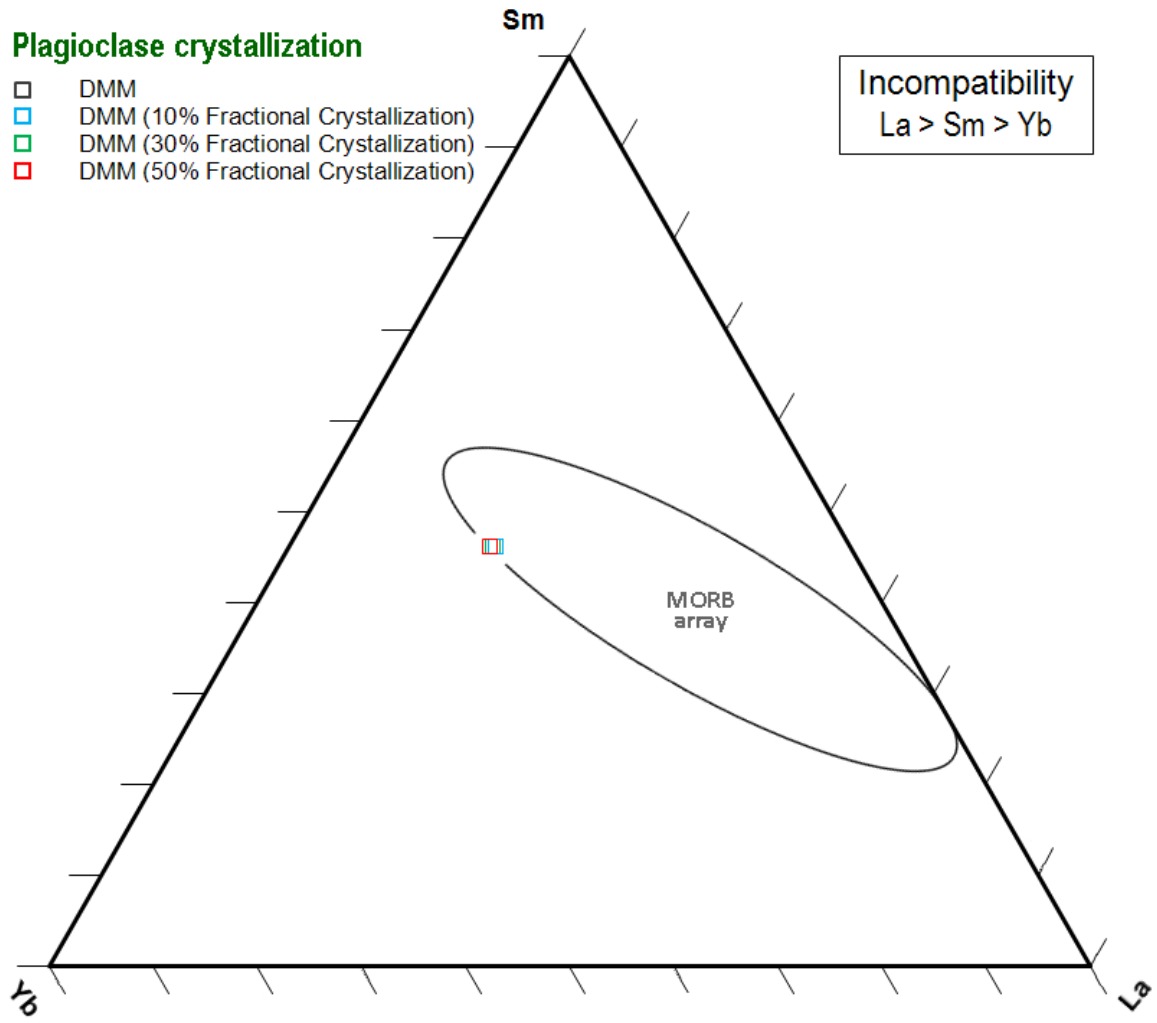

Figure 4e. Plagioclase crystallization diagram: YSL Ternary plot showing relative concentrations of the trace elements Yb (ppm), Sm (ppm x 2) and La (ppm) of a depleted MORB mantle composition (DMM) (Salters & Stracke, 2004) at 0%, 10%, 30%, and 50% fractional crystallization of the mineral phase plagioclase, respectively represented by a black square, blue square, green square, and red square. The partition coefficients of Yb, Sm, and La for olivine used in this calculation were obtained from White (2013). The global MORB array, comprising data from the MAR, EPR, SWIR, & SEIR, (PetDB; Lehnert et al., 2000) is encircled in black.

1.4.2) Partial melting

Upward convection of the mantle, which happens beneath the ridge axes at mid-ocean ridges as a response to the spreading of the lithospheric plates, leads to the

decompression of the mantle, resulting in partial melting, forming MORB magmas (Fig. 1; Langmuir et al., 1992; Klein, 2003b). The partial melting process, which forms MORB magmas, occurs within a melting region that extends from the base of the crust at ridge axes down to as deep as 30 km to 100 km depth within the mantle (Hofmann, 1997). Mid-ocean ridge partial melting does not melt mantle peridotite rocks entirely, but instead only partially, with the proportion of mantle melting in the melting region ranging as low as less than 1% (Zindler & Hart, 1986) to ranging between 10% and 20% (Snow et al., 2001) or from 5% to 20% (Helffrich & Wood, 2001) or up to as high as 30% (Zindler & Hart, 1986; Klein, 2003b). Since the proportion of melting is never as high as 100%, this means that partial melting always leaves an unmelted solid refractory peridotite residue remaining in the mantle after melt extraction (Hofmann, 1997; Klein, 2003b).

Partial melting is understood to have a less significant influence on the magmatic composition than fractional crystallization (e.g., Klein 2003b), so in circumstances in which fractional crystallization has a minimal effect (i.e., Fig 4a, Fig. 4b, Fig. 4d), partial melting would also be expected to have a minimal effect. For instance, mid-ocean ridges with an ultraslow spreading rate are settings where it has been suggested that the effects of fractional crystallization and partial melting on magmatic compositions are both minimized (Michael et al., 2003; Standish et al., 2008; Nauret et al., 2011).

1.4.3) Spreading rate effects

One parameter that has been suggested to control the degree to which partial melting, fractional crystallization, and magmatic mixing occurs is the mid-ocean ridge spreading rate, which is believed to be proportional to the extent of the melting column

(Michael et al., 2003; Standish et al., 2008; Nauret et al., 2011). Spreading at slower spreading ridges has been suggested to involve more conductive cooling from the surface, which produces thinner crust, thickens the lithosphere, and depresses the top of the melting column (Fig. 1b; Michael et al., 2003; Standish et al., 2008; Nauret et al., 2011). Consequently, the degrees to which magmatic differentiation processes occur along ultraslow spreading ridges are lower compared to faster spreading ridges (Michael et al., 2003; Standish et al., 2008; Nauret et al., 2011). For example, the degree of partial melting drops sharply at spreading rates slower than 1.6 cm/year (Snow et al., 2001). Also minimized are some processes that occur during melt migration, such as magma mixing. Consequently, the geochemical signatures of mantle components in basalts from ultraslow spreading ridges are less obscured by magmatic differentiation processes (Michael et al., 2003).

Gakkel Ridge, located in the Arctic Basin, is an example of an ultraslow spreading center, where the extents to which the processes of partial melting and fractional crystallization operate are believed to be minimized (Michael et al., 2003). Figure 4 has demonstrated that the low degrees of fractional crystallization – as expected at ultraslow spreading ridges, such as Gakkel Ridge - has a minimal effect on the magmatic composition, so it can thus be inferred that partial melting has an even more negligible influence on MORB composition (Klein, 2003b). Thus, the effects of partial melting do not need to be calculated for Gakkel Ridge, since it has already been demonstrated that the more dominant process of fractional crystallization has little effect on the varying degrees of enrichment in Gakkel Ridge MORBs.

1.5) Mantle heterogeneity

Although magmatic differentiation processes can produce a range of differences in basalt chemical compositions, differentiation of a single source component composition alone cannot account for the full diversity of differences in chemical composition observed in basalts, such as different amounts of enrichment in different incompatible trace elements, because varying degrees of differentiation affecting a single homogenous mantle source composition can only produce too a limited range of possible basalt compositions – more limited than the wide degree of variation observable in global basalt element compositions, as demonstrated by Figure 4.

A widely discussed view (e.g., Holness & Richter, 1989; Hofmann, 1997) is that in order to explain the full variety of chemical compositions observed in basalts, it is necessary to consider the presence of compositional heterogeneity in the mantle in the form of multiple magmatic source components, each with distinct mineralogical and/or chemical compositions, some of which are more enriched in certain elements than others.

These chemical heterogeneities may range in scale from as small as centimeters (mineralogical scale) (Zindler & Hart, 1986; Sun & McDonough, 1989) or less than one kilometer (Holness & Richter, 1989) or kilometers (Liu et al., 2008) up to as large as thousands of kilometers (Zindler & Hart, 1986; Holness & Richter, 1989; Sun & McDonough, 1989) or the size of ocean basins (Liu et al., 2008).

1.5.1) Recycling

One idea for the origin of the mantle's heterogeneity involves the recycling of crustal material, such as continental crust, oceanic crust, or sediments, into the mantle.

Recycling is the process by which crustal rocks and associated sediments are subducted or delaminated and become incorporated into the mantle (Hofmann & White, 1982; Holness & Richter, 1989; Helffrich & Wood, 2001). At the increased temperatures and pressures at increased depths in the mantle, the subducted oceanic crust would transform into eclogite, a denser material than the surrounding mantle, causing the subducted crust to detach from the lithosphere and sink deep into the mantle (Hofmann & White, 1982). Recycled components may become unstable and melt as a consequence of the increased temperatures at increased depths in the mantle (Hofmann & White, 1982). The recycled components may then be combined with the surrounding mantle by convective mixing (Holness & Richter, 1989; Klein, 2003b). Recycled material adds chemical heterogeneity to the mantle by introducing incompatible trace elements back into the mantle (Hofmann & White, 1982). Incompatible elements are generally more concentrated in crustal material, instead of in mantle rocks, because they were extracted from the mantle and concentrated into the crust during ancient partial melting (Hofmann, 1988; Helffrich & Wood, 2001; Hofmann, 1988; Hofmann, 2007).

Recycled material may be subducted to depths as deep as the core mantle boundary and then brought back up by mantle convection (Hofmann & White, 1982; Van Keken et al., 2002) or it may be material that has remained relatively shallow in the mantle, such as subcontinental lithospheric mantle (SCLM) (Nauret et al., 2010). The recycled material in the mantle is suggested to be dominantly composed of subducted oceanic crustal and lithospheric material; whereas, the amount of recycled continental material in the mantle is believed to be relatively smaller in comparison (Hoffman, 1997; Hofmann, 2007).

1.5.2) Veins

One form in which enriched heterogeneous recycled components have been suggested to exist in the mantle is in the form of "veins" of enriched material, composed of more melt fertile and more trace element enriched rock-types, embedded within the more abundant surrounding peridotite mantle (Wood, 1979; Dick et al., 2003; Nauret et al., 2011).

Mantle veins may be composed of pyroxenite or eclogite, both of which are rock-types that can form from subducted crustal material (Sobolev et al., 2005). Eclogite, which is composed of clinopyroxene and garnet, is the rock type that subducted oceanic basalts and gabbros transform into after being subducted (Hofmann & White, 1982; Sobolev, 2005 et al.; Sobolev et al., 2007). Pyroxenite is a rock type that may be produced when melted eclogite reacts with the peridotite (Sobolev et al., 2005; Sobolev et al., 2007). Pyroxenite and eclogite both have a lower solidus than peridotite, so these rock types start melting at higher pressure and greater depths than peridotite (Sobolev et al., 2005; Sobolev et al., 2007). In fact, a pyroxenite composition can melt at 35 to 50 km deeper than peridotite and can be 60% molten at the peridotite solidus (Dick et al., 2003). This means that veins of eclogite and pyroxenite in the mantle would melt completely during the MORB partial melting process, unlike the partial melting of peridotite, which leaves behind a refractory unmelted residue in the mantle (Sobolev et al., 2005). The 100% melting experienced by eclogite and pyroxenite components may explain the absence of veins composed of these rock types in abyssal peridotites recovered from the seafloor.

The existence of mantle veins remains a topic of debate, but their presence in the mantle would explain how sources of incompatible trace element enriched chemical signatures can be contained in the mantle, even while the upper mantle is dominantly composed of the more typical depleted MORB mantle source (Wood, 1979; Dick et al., 2003; Nauret et al., 2011). The lower degrees of partial melting expected to be associated with slower, means that an ultraslow spreading ridge with may sample melts from fertile enriched veins preferentially over the depleted mantle, resulting in enriched basalts (Snow et al., 2001; Liu et al., 2008).

1.5.3) Magmatic mixing

Mixing between magmatic melts derived from different mantle components can affect MORB compositions (Le Roex et al., 1992; Nauret et al., 2011). Mixing between magmatic melts is a process that operates as the melts derived from mantle partial melting rise upwards from the mantle prior to erupting at the surface. Following extraction from the mantle, these magmas mix together during their ascent, before ultimately cooling to form basalts. If the different mantle source components have distinct chemical compositions, the magmatic melts that they produce would also feature differences in chemical composition. When these different melts mix together, the chemical compositions of the basalts that ultimately form from them would end up reflecting an intermediate composition between the different compositions of the mantle source components from which they were derived. (Le Roex et al., 1992; Nauret et al., 2011).

Mixing lines are clearly observable in basalt data plotted on the ternary plots, such as Figure 3, which shows arrays of basalt composition data that plot between two endmember points. Such data arrays can be interpreted to represent mixing lines, showing the basalts resulting from the magmatic mixing that occurs between two endmember compositions. By examining the endpoints of these ternary plot mixing lines, the compositions of the endmember components in the mantle from which the magmatic melts were derived can be interpreted.

1.5.4) OIB mantle components

Although the various heterogeneous components of the mantle are not well defined and may have not all been identified, attempts have been made to identify certain components, based on their isotopic signatures. A large amount of these studies have focused on enriched ocean island basalts (OIB), because their enriched signatures are more distinct than those of different enriched MORBs. Most of this previous work on identifying mantle components has primarily focused on isotopes, not trace elements.

Three isotopically enriched mantle source components have been classified based on the chemical compositions of enriched OIBs (Zindler & Hart, 1986). The three defined OIB components along with DMM can together be considered to constitute four major endmember components in the mantle, each of which produce basalts featuring distinct isotopic signatures.

The three isotopically enriched OIB components are: enriched mantle 1 (EM1), enriched mantle (EM2), and high μ (HIMU) (Zindler & Hart, 1986; Sun & McDonough, 1989). Although the EM1, EM2, and HIMU components were defined based on OIB

element concentration data instead of MORB, they are of interest to MORB studies, because MORB trace element patterns may reveal information about their origins (Fig. 5; Weaver, 1991a; Weaver, 1991b; Hofmann, 1997); thus, comparing MORB trace element patterns to trace element patters of OIB components may yield information about the origins of MORB source components.

The chemical signatures of EM1, EM2, and HIMU all feature relatively enriched trace element concentrations compared to other oceanic basalts (Fig. 5; Hofmann, 1997). Their chemical signatures also feature differences from each other, reflecting their different origins (Weaver, 1991a; Weaver 1991b). Basalts derived from the EM1 and HIMU components feature trace element patterns that are similar to each other and resemble the trace element pattern of DMM-derived ocean crust MORB. Both of these components predominantly reflect a recycled oceanic crust signature, with the EM1 component also showing contamination from pelagic sediment (Weaver, 1991a; Weaver 1991b).

In contrast, the EM2 component produces basalts with a distinctive trace element pattern resembling not only ocean crust, but also continental crust (Hofmann, 1997). The EM2 component is also dominated by a recycled oceanic crust signature, just as HIMU and EM1 are, but the EM2 signature features the distinction of containing additional contamination by continental terrigenous sediment (Weaver, 1991a; Weaver 1991b).

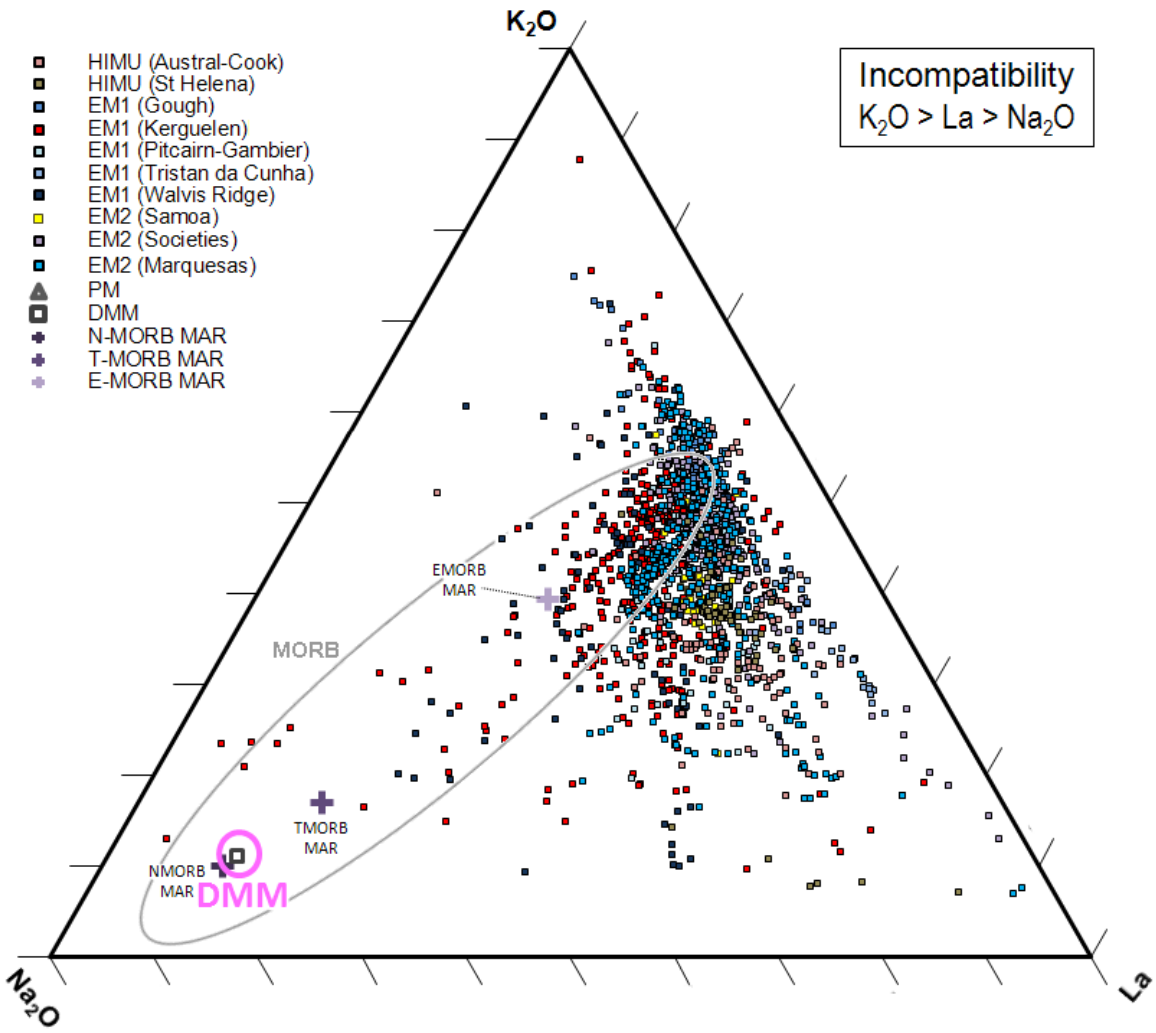

Figure 5a. NKL Ternary plot showing relative concentrations of Na_2O (wt.% x 5), K_2O (wt.% x 30), & La (ppm) in EM1, EM2, and HIMU basalt glass and whole rock samples. OIB composition data are from GEOROC (Lehnert et al., 2000). EM1, EM2, and HIMU datasets have been filtered to include only ICP-MS (inductively coupled plasma mass spectrometer) trace element data. Also plotted are DMM (Salters & Stracke, 2004) and PM (Sun & McDonough, 1989). Average N-MORB, T-MORB, and E-MORB are calculated from basalt glass data from PetDB (Lehnert et al., 2000). The global MORB array, comprising data from the MAR, EPR, SWIR, & SEIR, (PetDB; Lehnert et al., 2000) is encircled in gray.

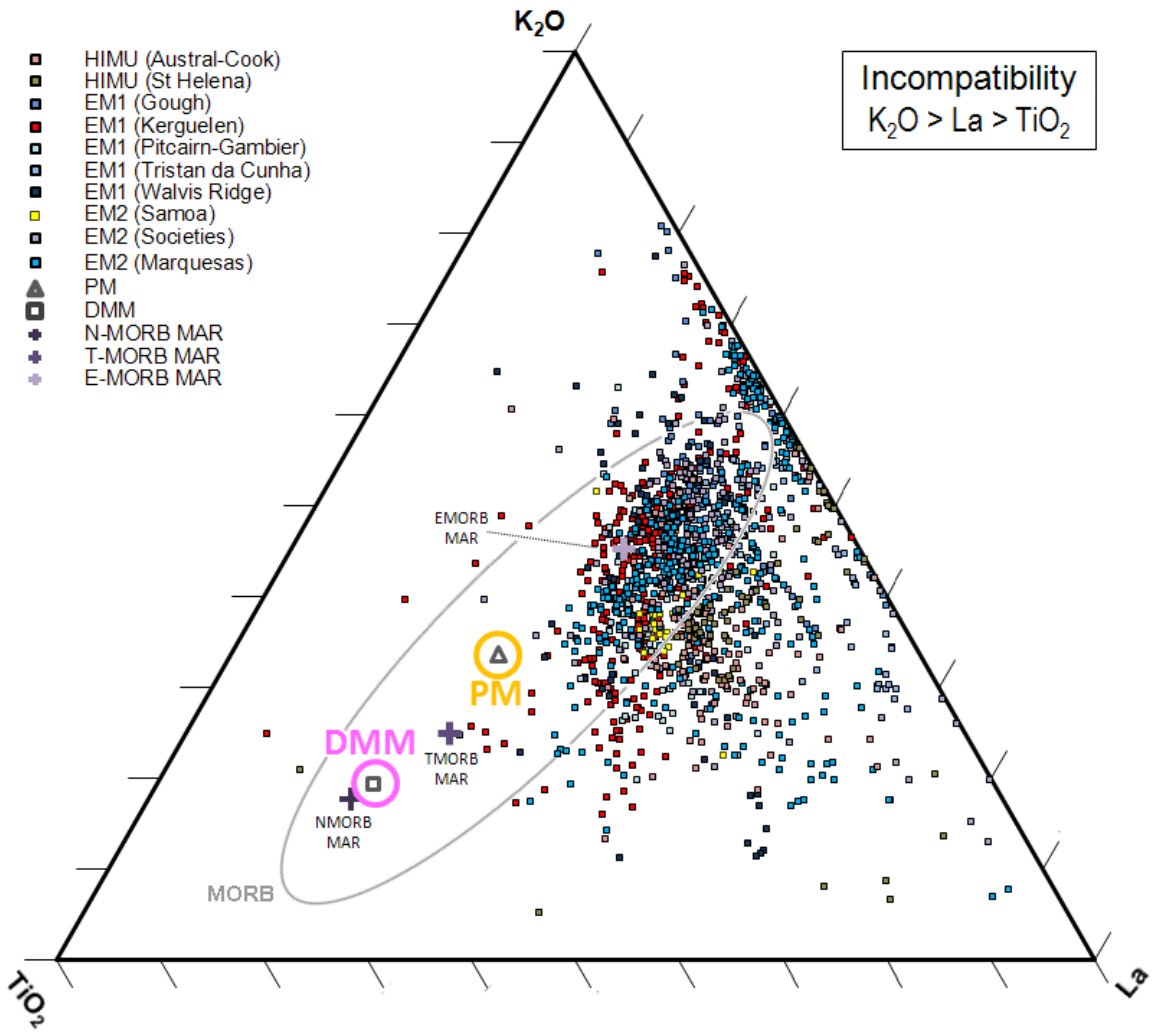

Figure 5b. TKL Ternary plot showing relative concentrations of TiO_2 (wt.% x 5), K_2O (wt.% x 30), & La (ppm) in EM1, EM2, and HIMU basalt glass and whole rock samples. EM1, EM2, and HIMU datasets have been filtered to include only ICP-MS trace element data. The global MORB array is encircled in gray. Data are from the same references as those in Figure 5a.

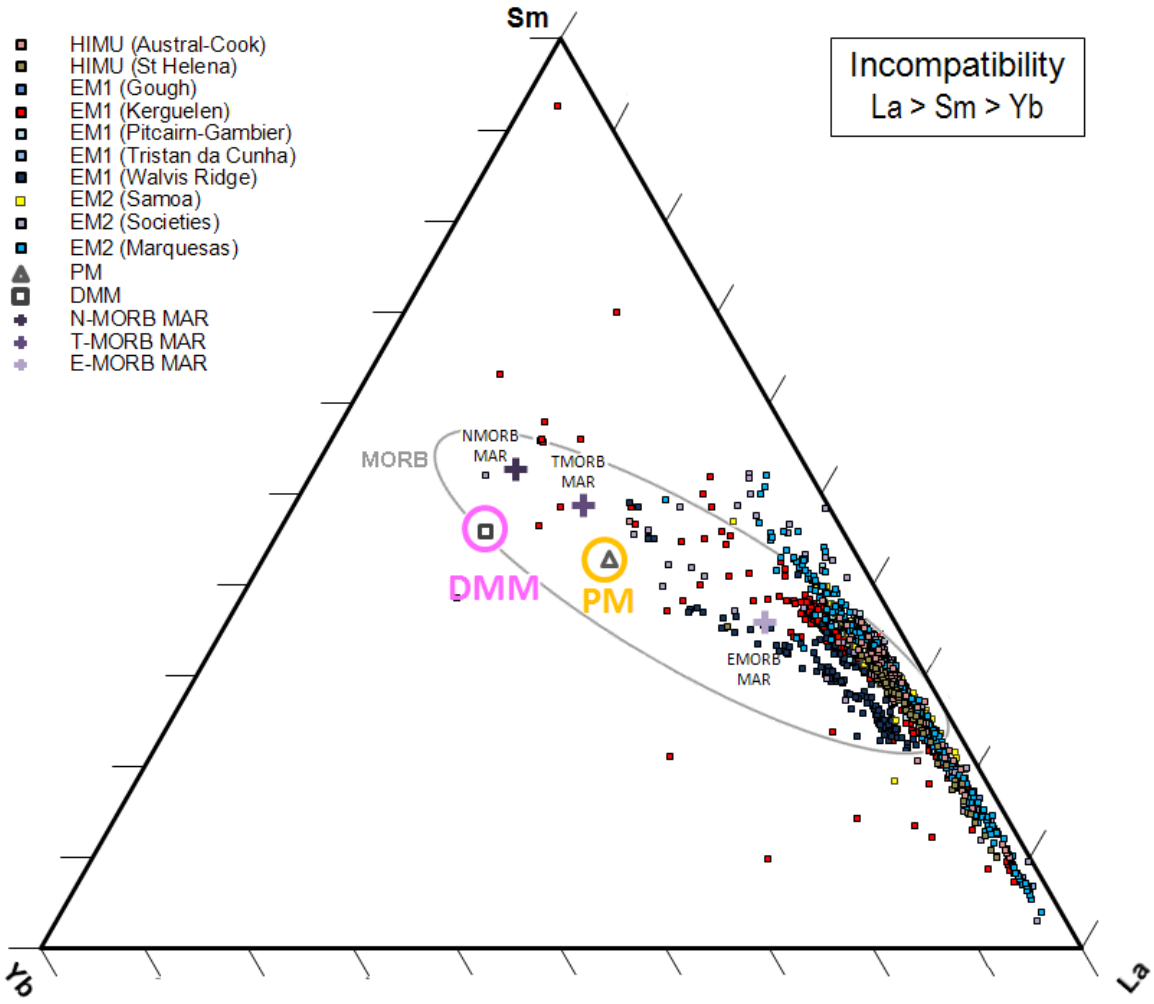

Figure 5c. YSL Ternary plot showing relative concentrations of Yb (ppm), Sm (ppm x 2), & La (ppm) in EM1, EM2, and HIMU in basalt glass and whole rock samples. EM1, EM2, and HIMU datasets have been filtered to include only ICP-MS trace element data. The global MORB array is encircled in gray. Data are from the same references as those in Figure 5a.

2) SETTING

Gakkel Ridge is 1800 km long. (Fig. 6; Fig. 7). It is located in the Arctic Basin (Fig. 6). It is the northernmost segment of the global mid-ocean ridge system (Klein,

2003a). Gakkel Ridge is the active plate boundary across which the North American and Eurasian Plates separate in the Arctic Basin (Fig. 6; Goldstein et al., 2008).

The western end of Gakkel Ridge is located at 82°N 2°W (Mühe et al., 1991; Mühe et al., 1997) near Greenland, where Gakkel Ridge connects with the Lena Trough (Fig. 6). The eastern end of Gakkel Ridge is located at 80°N 125°E (Mühe et al., 1991; Mühe et al., 1997), or about 60 kim from the Laptev seashelf edge (Engen et al., 2003), where the ridge terminates at the continental Siberian margin in the Laptev Sea (Fig. 6).

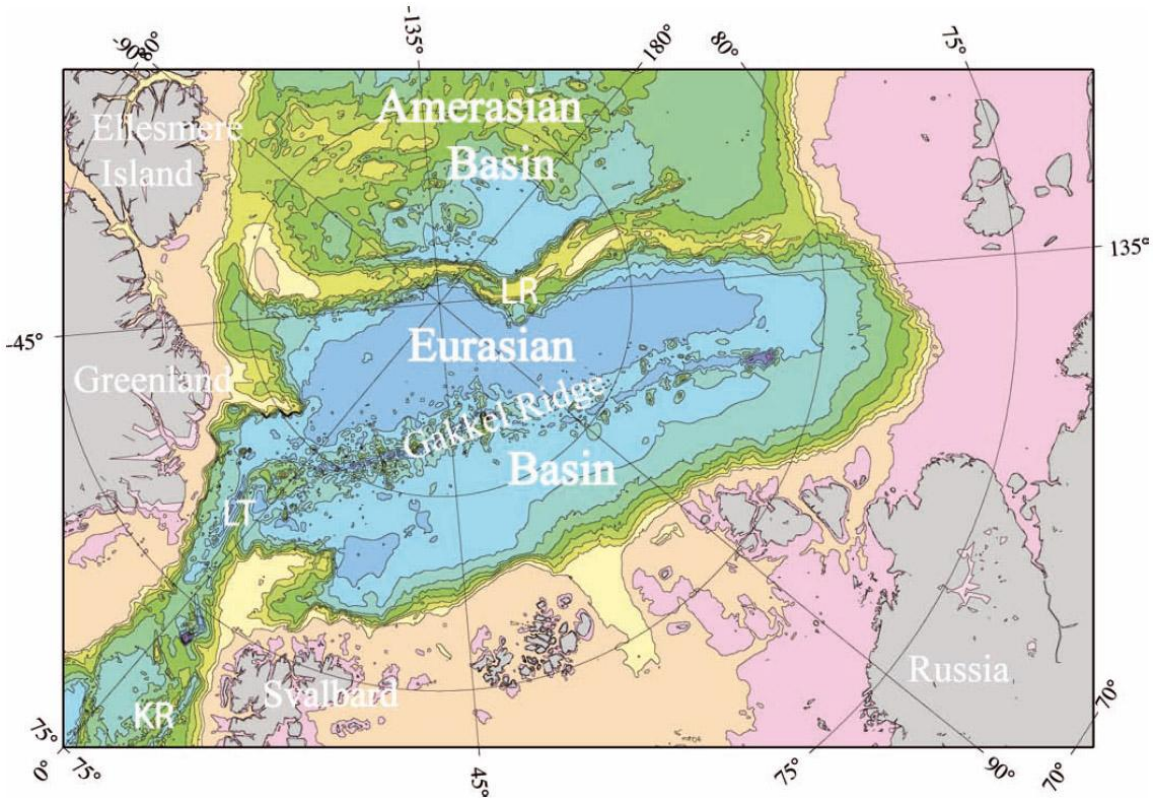

Figure 6. Bathymetric map showing the location of Gakkel Ridge and surrounding features in the Arctic Basin, including Lena Trough (LT), Knipovich Ridge (KR), and Lomonosov Ridge (LR) (Cochran, 2008). Spitsbergen island of the Svalbard archipelago is located south of western Gakkel Ridge.

Gakkel Ridge is the world's slowest spreading segment of the global mid-ocean ridge system (Mühe et al., 1991; Klein, 2003a; Michael et al., 2003; Goldstein et al., 2008; Liu et al., 2008; Shaw et al., 2010). The spreading rate is not consistent along its length, but instead decreases from west to east along its axis. The full spreading rate along Gakkel Ridge is the fastest at the western end of the ridge, where the full spreading rate is 1.5 cm/year (Mühe et al., 1997) or 1.46 cm/year (Michael et al., 2003; Liu et al., 2008) or ~1.4 cm/year (Shaw et al., 2010) or 1.3 cm/year (Jokat et al., 2003) or 1.28 cm/year (Cochran, 2008) or 1.27 cm/year (Dick, 2003). Spreading is slowest at the eastern Siberian end of Gakkel Ridge, where the full spreading rate is as low as 0.8 cm/year (Mühe et al., 1997) or 0.65 cm/year (Cochran, 2008) or 0.63 cm/ year (Michael et al., 2003; Liu et al., 2008) or 0.6 cm/year (Dick et al., 2003; Jokat et al., 2003) or ~0.6 cm/year (Shaw et al., 2010) or 0.3 cm/year (Klein, 2003a).

Gakkel Ridge is classified as an ultraslow spreading ridge (Fig. 1b). Ultraslow spreading ridges are defined as having full spreading rates of less than 2 cm/year (Dick et al., 2003; Jokat et al., 2003; Snow & Edmonds, 2007).

2.1) Magmato-tectonic zones

Michael et al., 2003 divided Gakkel Ridge into three "magmato-tectonic" segments, the Western Volcanic Zone (WVZ), the Sparsely Magmatic Zone (SMZ), and the Eastern Volcanic Zone (EVZ), each with different magmatic behavior and differing relative abundances of basalt and peridotite. Basalts recovered from each zone have distinctly different chemical characteristics (Fig. 11; Fig. 12; Table 3; Table 4).

There is a segmentation of relative abundances of rock-types along Gakkel Ridge, even though the it features no significant transform offsets (Goldstein et al., 2008) or major fracture zones (Michael et al., 2003) to form mantle flow and compositional boundaries along its length. This rules out physical boundaries as a possibility to explain the chemical segmentation in the mantle along the ridge.

The variations in mantle source components in basaltic rocks recovered along Gakkel Ridge do not vary in a consistent manner in correlation with the consistently changing spreading rate along the ridge length (Klein, 2003a; Michael et al., 2003; Goldstein et al., 2008). This rules out spreading rate variation as the primary factor controlling magma compositions, and thus basalt compositions, along the ridge.

Because the segmentation of the ridge cannot be directly attributed to transform, fractures, or spreading rate variation along the ridge, the segmentation instead must be controlled by variations within the mantle (Michael et al., 2003; Goldstein et al., 2008) Mantle characteristics that might be varying along the ridge may include different mantle temperatures or different mantle compositions, such as compositions with different melting fertility (Michael et al., 2003).

Each magmato-tectonic zone along Gakkel Ridge features multiple volcanic centers (Fig. 7), but the abundances of volcanic centers and the distance of the spacing between volcanic centers varies from zone to zone. Volcanic centers range in size from 15km to 50 km in diameter, typically 30 km along strike (Michael et al., 2003). The spacing between volcanic centers ranges from 50km to 160 km apart (Michael et al., 2003).

No basalt samples have been recovered east of the Eastern Volcanic Zone (EVZ) (Michael et al., 2003). One reason for this is that the eastern end of Gakkel Ridge is buried by sediment (Mühe et al., 1991; Engen et al., 2003). Specifically, the region between the 69°E and 85°E volcanic centers and the region eastward beyond the 85°E volcanic center is mostly covered in sediments (Cochran, 2008).

2.1.1) Western Volcanic Zone (WVZ) (7°W - 3°E)

The westernmost segment of the Gakkel Ridge is the Western Volcanic Zone (WVZ). It is 220 km long (Cochran, 2008), extending from its western end at 83°N, 7°W, where it connects with the northern Lena Trough, to 84°30'N, 3°E, where it transitions into the sparsely magmatic zone (SMZ) (Fig. 7, Michael et al., 2003; Cochran, 2008).

The WVZ features numerous closely spaced volcanic centers and abundant basalt on the seafloor (Michael et al., 2003; Cochran, 2008; Goldstein et al., 2008).

It should be noted that although the morphological distinction between Northern Lena Trough (NLT) and westernmost Gakkel Ridge is clearly defined (Snow et al., 2011), there is no clear geochemical boundary between the two; thus, the samples in this thesis labeled as belonging to NLT may also be considered to belong to the western end of the WVZ and vice versa.

2.1.2) Sparsely Magmatic Zone (SMZ) (3°E - 29°E)

The Sparsely Magmatic Zone (SMZ) is 275 km long (Michael et al., 2003; Cochran, 2008), extending from its western end near 84°38'N, 3°E, where it connects

with the WVZ, to its eastern end at 86°N, 29°E, where it connects with the Eastern Volcanic Zone (EVZ) (Fig. 7, Michael et al., 2003; Cochran, 2008).

Along most of its length, the SMZ is an amagmatic segment, with rock types on the seafloor along its length consisting of mostly abyssal peridotite and few basalts (Michael et al., 2003), which tend to be concentrated in along-ridge bathymetric highs. Between 8°E and 12°E a few rare basalt samples were recovered, but these were diabases or old fragments without glass, so their chemistry was not analyzed (Michael et al., 2003). The only volcanic areas within the SMZ where basalt samples were recovered are two separate volcanic centers located at 13°E and at 19°E. (Fig. 7; Michael et al., 2003; Goldstein et al., 2008; Cochran, 2008). These volcanic centers are labeled in this thesis as SMZ13 (13°E) and SMZ19 (19°E)

2.1.3) Eastern Volcanic Zone (EVZ) (29°E - 85°E)

The Eastern Volcanic Zone is at least 580 km long (Michael et al., 2003; Cochran, 2008). It extends from 29°E eastward (Fig. 7). Its eastern end is not well defined, either ending at 85°E (Michael et al., 2003), or extending as far eastward as 96°E (Cochran et al., 2008). Among the well identified volcanic centers of Gakkel Ridge, the most eastern volcanic center is at 85°E (Fig. 7a; Fig. 8), so in Fig. 7a, the eastern end of the EVZ is defined at 85°E, instead of 96°E.

The EVZ consists of widely spaced large volcanic centers connected by amagmatic segments (Fig. 7; Michael et al., 2003). Michael et al. (2003) defined six areas of concentrated volcanism within the EVZ centered at 31°E, 37°E, 43°E, 55°E, 69°E, and 85°E (Fig. 7a-7c). Additional volcanic centers within the EVZ have been suggested to

exist, including one at 92°-93°E (Dick et al., 2003; Cochran, 2008) and one in the sediment covered region between the 69°E and 85°E volcanic centers (Cochran, 2008). However these possible additional volcanic centers are not well defined, because no dredging has been conducted between the 69°E and 85°E volcanic centers, and because no basalts were recovered eastward beyond the 85° E volcanic center; thus, only the six volcanic centers defined by Michael et al. (2003) will be considered in this study. These six volcanic centers are labeled in this thesis from west to east as EVZ31 (31°E), EVZ37 (37°E), EVZ43 (43°E), EVZ55 (55°E), EVZ69 (69°E), and EVZ85 (85°E).

2.2) Adjacent Arctic Basin features

At its western end, the Gakkel Ridge is connected to the northern end of Lena Trough (Fig. 6; Snow et al., 2011). Lena Trough is divided into two sections with chemically distinct basalts, Northern Lena Trough (NLT) and Central Lena Trough (CLT) (Nauret et al., 2011). Like Gakkel Ridge, Lena Trough is an ultraslow spreading ocean ridge. The southern end of Lena Trough connects with Knipovich Ridge and from there, the ridge system extends beyond the Arctic Basin and connects with the rest of the Mid-Atlantic Ridge system (Fig. 6) (Engen et al., 2003). Spitsbergen is an island located to the south of the WVZ (Fig. 6) and is part of the Svalbard archipelago.

3) BACKGROUND

The earliest analyses of Gakkel Ridge MORB samples were conducted on a small number of whole rock samples (Mühe et al., 1991; Mühe et al., 1993; Mühe et al., 1997) recovered from early Arctic expeditions. However, the data in these studies included only

basalt glass samples; thus, data obtained from analyses of whole rock samples, such as those of the earliest Gakkel Ridge MORB analyses, are not examined in this study.

The Gakkel Ridge data examined in this study are from rock samples recovered, mostly by dredging, from later expeditions, one of which was the Arctic Mid Ocean Ridge Expedition (AMORE) 2001 cruises by the research icebreakers, US Coast Guard Cutter Healy and PFS Polarstern of the Alfred Wegener Institute for Polar and Marine Research of Bremerhaven, Germany (Michael et al., 2003; Snow & Edmonds, 2007) Later, additional samples were collected during the Arctic Gakkel Vents Expedition (AGAVE) 2007 cruise, conducted by the Woods Hole Oceanographic Institution, on the Swedish icebreaker Oden (Shaw et al., 2010).

The dredging stations where samples were collected during the AMORE 2001 cruises are shown on Figure 7. The dredging locations of samples collected during the AGAVE 2007 cruise are shown on Figure 8. No samples were collected farther east than the EVZ85 volcanic center (Fig. 7; Fig. 8).

3.1) AMORE 2001

Basalt samples collected by AMORE 2001 span across a range in longitude from 8° W to 86° E across a distance of 850 km along the ridge at over 200 dredging stations (Fig. 7; Michael et al., 2003; Snow et al., 2002). Goldstein et al. (2008) analyzed the chemistry of these samples and reported major element, trace element and isotope composition data of glasses of 38 samples: 16 WVZ samples, 3 SMZ13 samples, 6 SMZ19 samples, 2 EVZ31 samples, 2 EVZ37 samples, 2 EVZ43 samples, 3 EVZ69 samples, and 2 EVZ85 samples.

Michael et al. (2003) reported data for an additional 1 WVZ sample, 1 SMZ13 sample, and 1 EVZ85 sample not included in the data set of Goldstein et al. (2008).

The published data reported by Michael et al. (2003) and Goldstein et al. (2008) include only about one third of the total number of samples collected by AMORE 2001. This study examines 68 additional AMORE 2001 samples, ranging from SMZ13 to EVZ55, that were collected, but had not yet been analyzed until now (Table 3, Table 4).

Figure 7 is a bathymetric map showing the Gakkel Ridge as studied by the AMORE 2001 expedition. Dredging stations where rock samples were collected are represented as colored dots. The areas covered by each volcanic center along the ridge are designated by boxes. Displayed above each of those boxes are the sample numbers of basalt samples collected from each volcanic center.

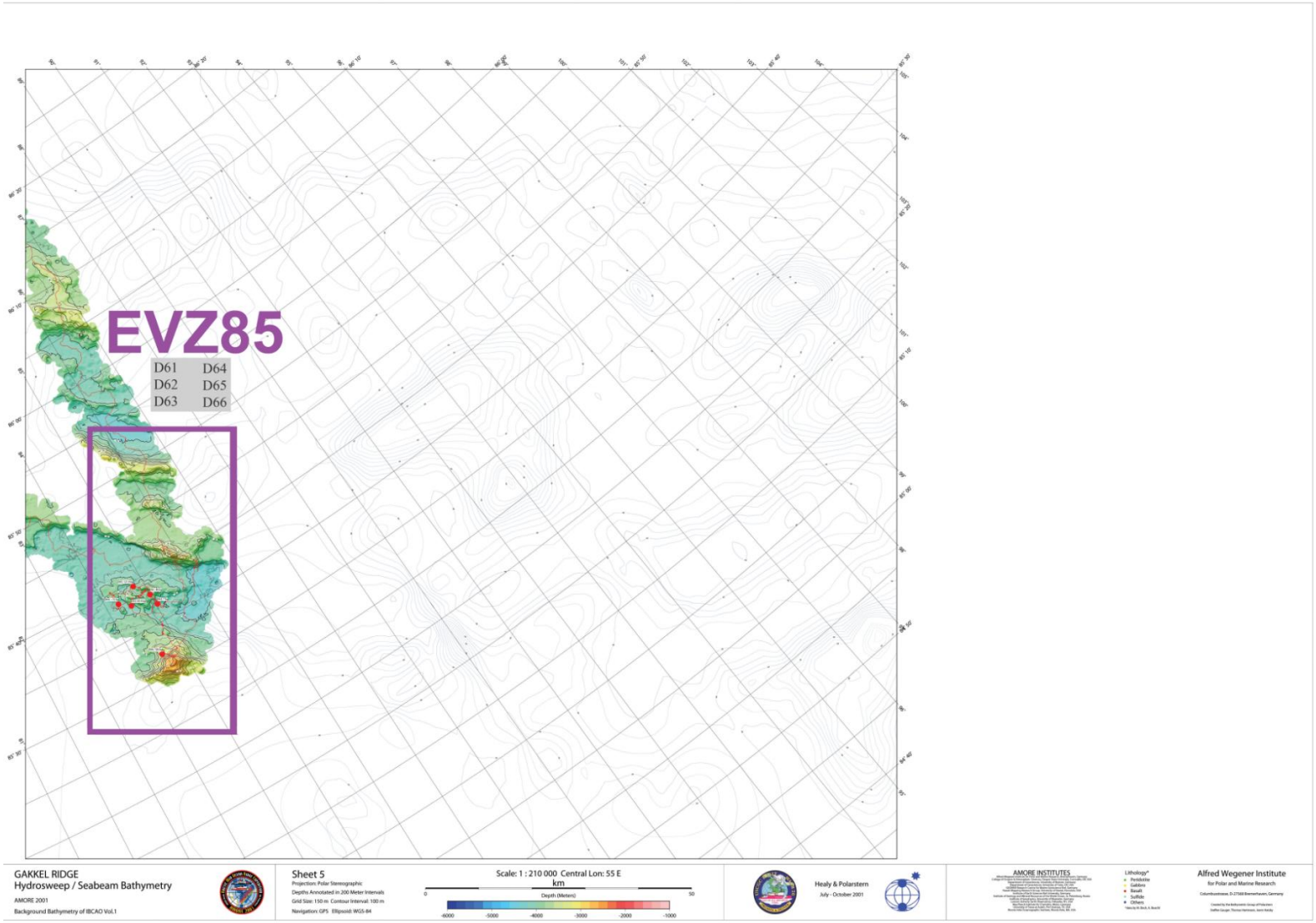

Figure 7a. Gakkel Ridge AMORE 2001 sample location map (Snow et al., 2002).

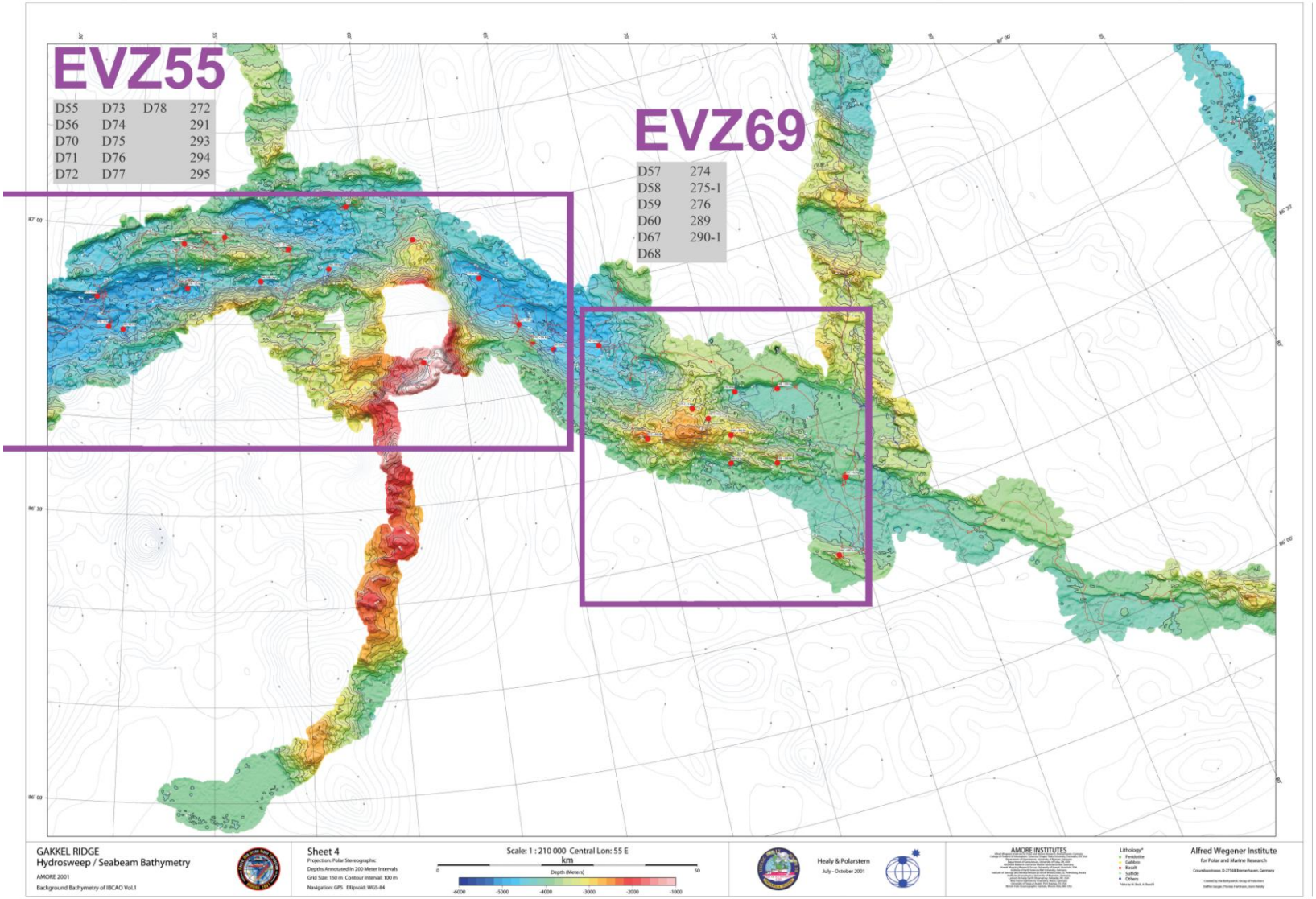

Figure 7b. Gakkel Ridge AMORE 2001 sample location map (Snow et al., 2002).

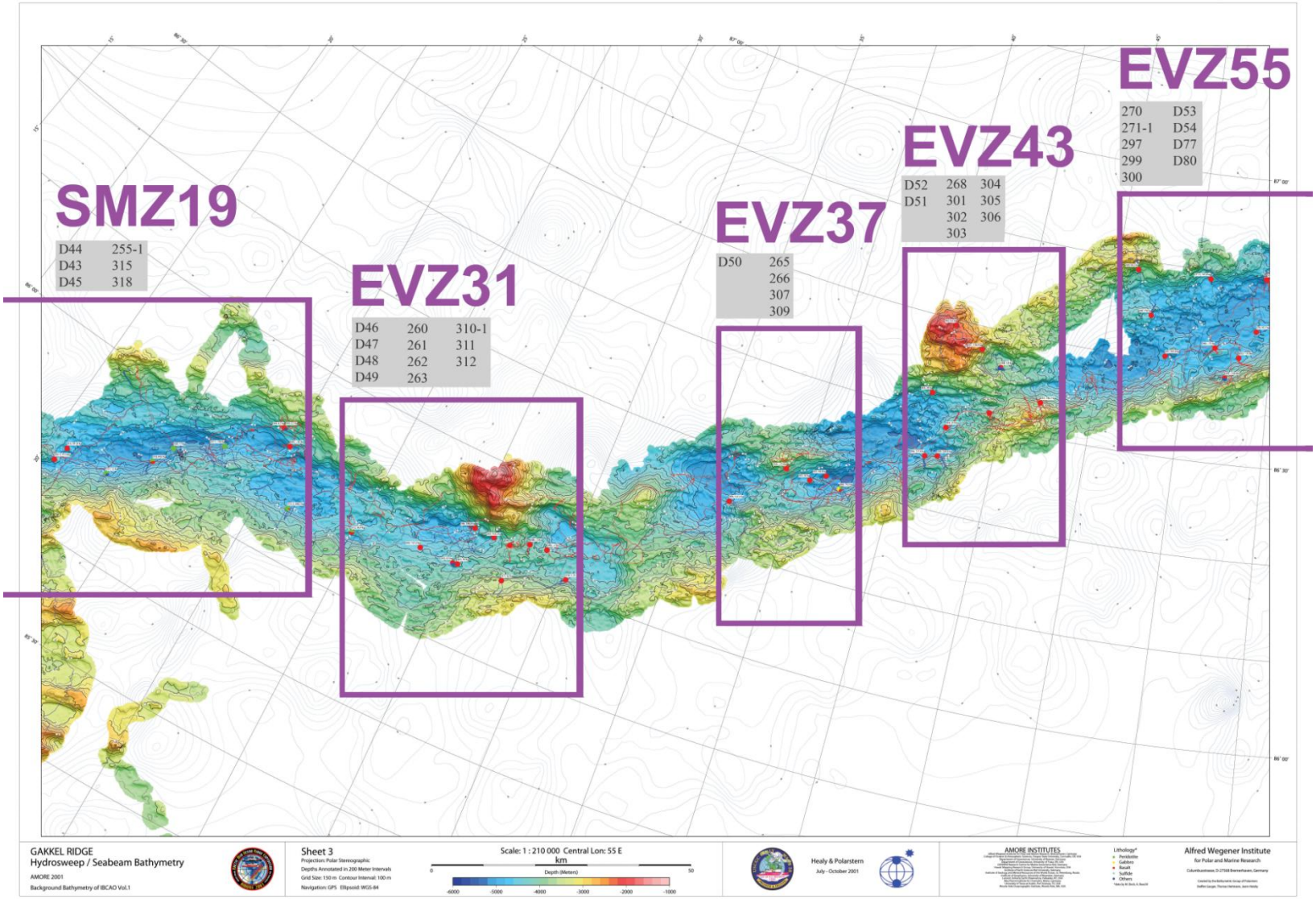

Figure 7c. Gakkel Ridge AMORE 2001 sample location map (Snow et al., 2002).

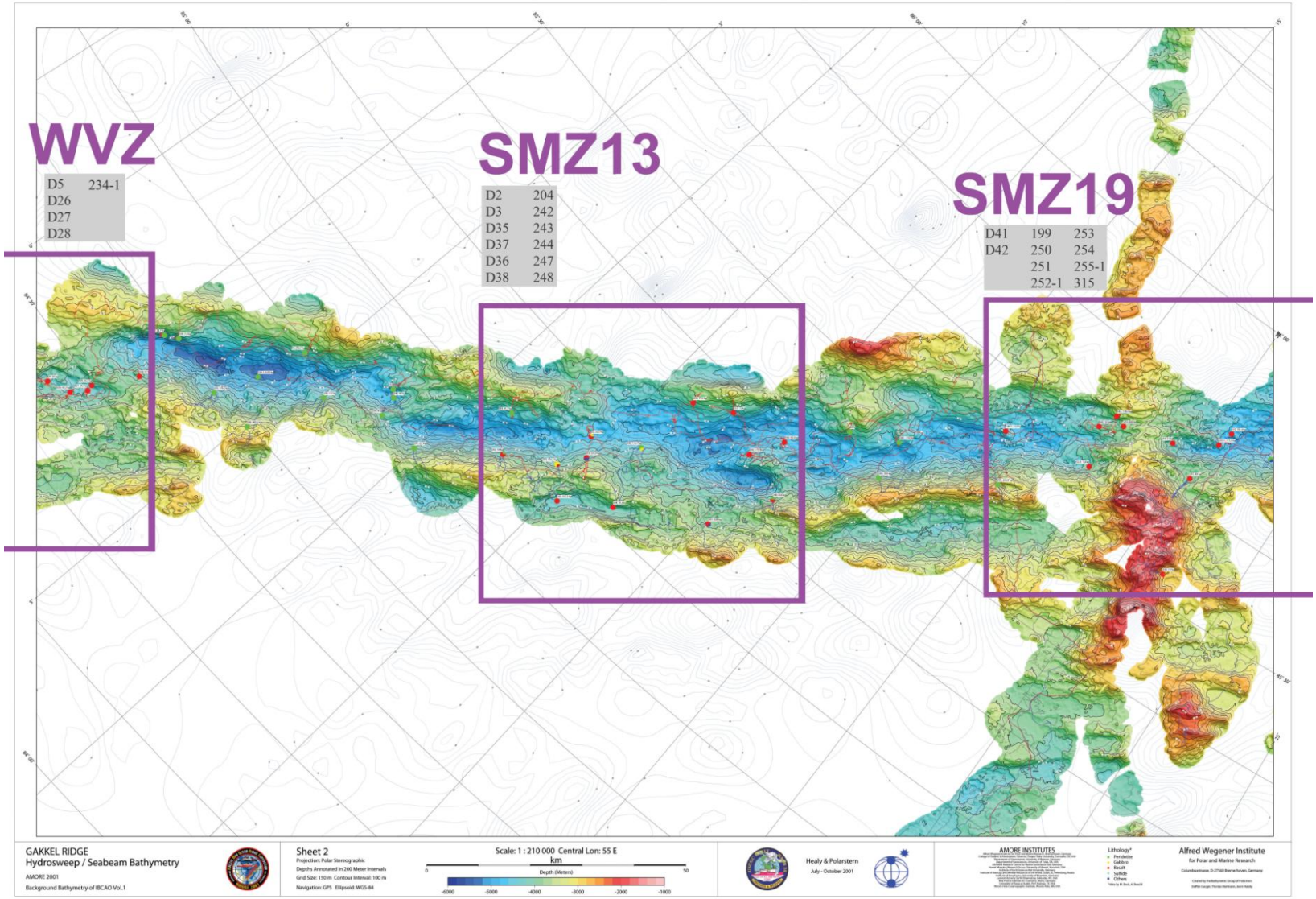

Figure 7d. Gakkel Ridge AMORE 2001 sample location map (Snow et al., 2002).

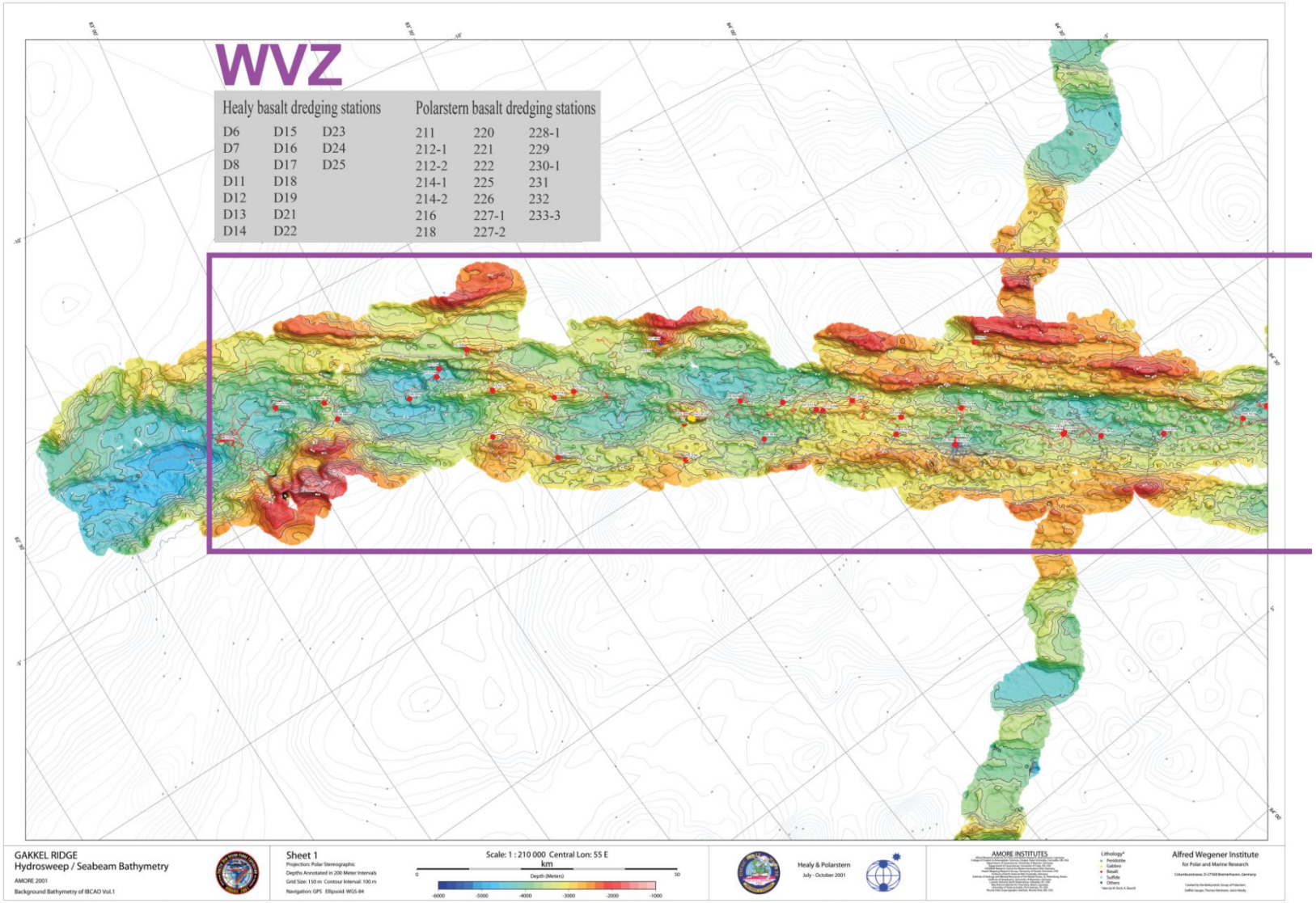

Figure 7e. Gakkel Ridge AMORE 2001 sample location map (Snow et al., 2002).

3.2) AGAVE 2007

All of the basalt samples collected and analyzed by AGAVE 2007 are from the EVZ85 volcanic center. Shaw et al. (2010) analyzed and reported trace element concentration data of 9 EVZ85 basalt glass samples.

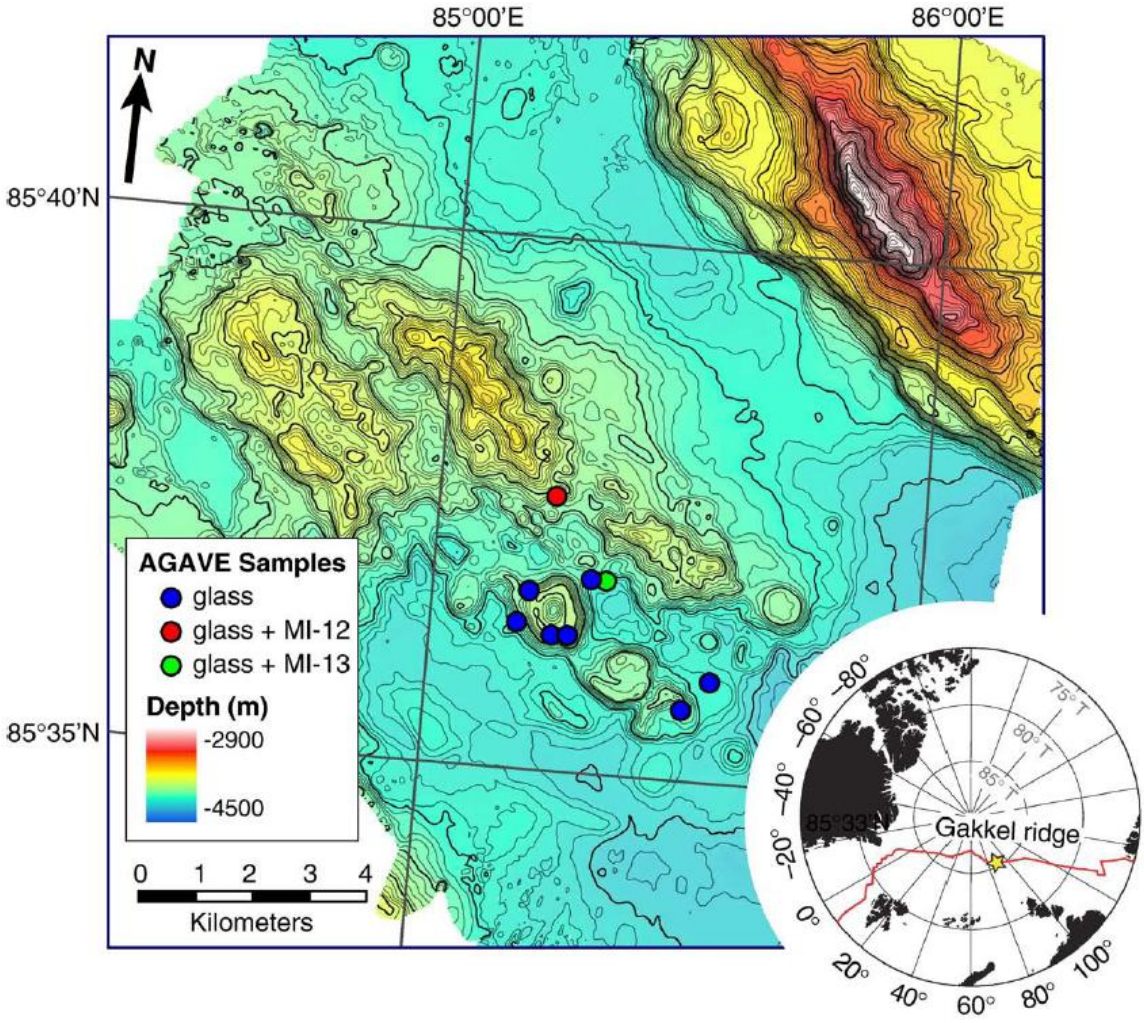

Figure 8. Locations of samples collected during the AGAVE 2007 cruise at the EVZ85 volcanic center (Shaw et al., 2010).

3.3) Earlier studies

3.3.1) Geochemistry of Gakkel Ridge MORBs

The Gakkel Ridge MORB geochemical data included on the plots in this study include data from earlier studies by Michael et al. (2003), Goldstein et al., (2008), Shaw et al., (2010), and Snow (in prep). Michael et al. (2003) and Goldstein et al. (2008) found that even though it might be expected for enrichment levels to increase with decreasing spreading rate, the isotope and trace element enrichment levels of MORBs along Gakkel Ridge actually do not correlate with the spreading rate, which slows down from west to east along the ridge. Instead, the enrichment levels in the Gakkel Ridge MORBs vary inconsistently with the distance along the ridge axis.

Goldstein et al. (2008) identified an isotopic boundary in the middle of Gakkel Ridge, apparently located in the middle of the SMZ, between the SMZ13 and SMZ19 volcanic centers. The boundary divides Gakkel Ridge into two isotopic provinces. To illustrate this boundary, they showed that the isotopic signature of MORBs from west of the isotopic boundary (i.e., WVZ, SMZ13) plots along a separate trend on a $^{143}Nd/^{144}Nd$ vs. $^{87}Sr/^{86}Sr$ isotope ratio plot than MORBs from east of the isotopic boundary (i.e., SMZ19, EVZ).

One of the characteristics displayed by the geochemistry of MORBs of the western province (i.e., WVZ, SMZ13), identified by Goldstein et al. (2008), is that they feature a "Dupal anomaly" signature, which is typically characteristic of southern hemisphere MORBs, not northern hemisphere MORBs. This makes MORBs from the western part of Gakkel Ridge the only example of MORBs with a significant Dupal anomaly signature in the northern hemisphere (Goldstein et al., 2008).

A Dupal anomaly is characterized by elevated Δ8/4 ratios (Hart, 1984). Δ8/4 is a measure of the amount of deviation in the $^{208}Pb/^{204}Pb$ ratio from the Northern Hemisphere Reference Line (NHRL), which is defined as a $^{208}Pb/^{204}Pb$ ratio representative of MORBs of the northern hemisphere (Hart, 1984).

Goldstein et al. (2008) found that the MORBs of the western province (i.e., WVZ, SMZ13) all feature a Δ8/4 ratio above 30, in contrast to Δ8/4 ratios of samples from the eastern province, which are all below 30 (Fig. 10b). Goldstein et al. (2008) interpreted that SCLM from Spitsbergen is the source of the Dupal anomaly signature in western Gakkel Ridge. In contrast, the eastern isotopic province of Gakkel Ridge, with its lower Δ8/4 ratio, does not feature a Dupal anomaly signature and instead resembles north Atlantic MORB; thus, does not contain SCLM in its source (Goldstein et al., 2008; Liu et al., 2008).

Shaw et al., (2010) analyzed the trace elements compositions in basalt glass samples from the EVZ85, but they did not measure their major element compositions. Consequently, EVZ85 data are capable of being plotted on the YSL ternary plots (e.g., Fig. 12c) but not on the NKL and TKL ternary plots (e.g., Fig. 12a-12b), because no Na_2O, K_2O, and TiO_2 concentration data are currently available for these samples.

3.3.2) Geochemistry of other Arctic Basin basalts

Basalts of the Lena Trough, particularly the CLT, possess unique isotopic (Fig. 10) and trace element (Fig. 11) characteristics, primarily characterized by being more alkalic than any other basalts ever dredged from the ocean floor (Snow et al., 2001). This trace element signature indicates the presence of a unique K-enriched CLT mantle source

component, likely to be SCLM in origin (Nauret et al., 2011). This compositionally distinct CLT component appears to be spatially widespread in the Arctic Basin mantle, being present along Gakkel Ridge as well, not simply confined to the CLT area, because the NLT and WVZ basalts also appear to be influenced by the CLT component (Fig. 12; Snow J.E., in prep).

The Spitsbergen basalt composition appears to constitute an enriched endmember composition that forms a trend with the WVZ compositions on isotope plots (Fig. 10; Goldstein et al., 2008). The enrichment of the Spitsbergen composition possibly indicates the presence of a SCLM component in the Arctic mantle (Goldstein et al., 2008; Nauret et al., 2011).

Even though the Knipovich Ridge (i.e., the mid-ocean ridge that connects to the southern end of Lena Trough) is geographically relatively close to Lena Trough, isotope ratios of MORBs from Knipovich Ridge, which were compiled from PetDB (Lehnert et al., 2000), when plotted on the $^{143}Nd/^{144}Nd$ vs. $^{87}Sr/^{86}Sr$ plot (Fig. 10a), aligns with the SMZ19-EVZ array in eastern Gakkel Ridge, not the western WVZ-SMZ13 array. The $\Delta 8/4$ values of Knipovich MORBs are also within range of the eastern isotopic province, not the western province.

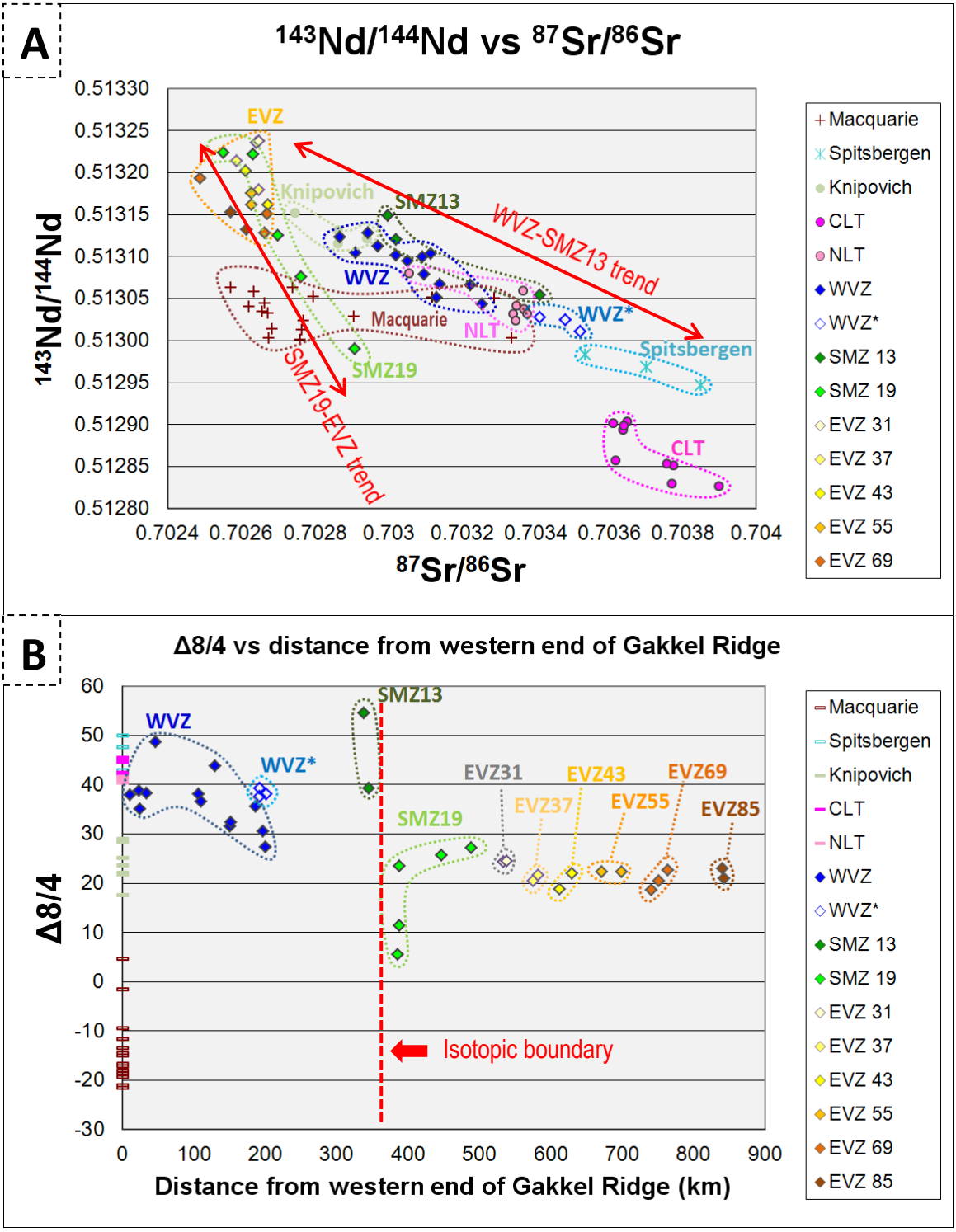

Figure 9. Radiogenic isotope ratios of Arctic Basin basalt glasses. A) $^{143}Nd/^{144}Nd$ vs. $^{87}Sr/^{86}Sr$ of Arctic basalt glasses. B) Δ8/4 of Gakkel Ridge samples, with basalts from other locations plotted at 0 km distance for comparison. Δ8/4 measures the amount of change in the $^{208}Pb/^{204}Pb$ ratio from a northern hemisphere reference line, which is an

average $^{208}Pb/^{204}Pb$ ratio in northern hemisphere basalts (Hart, 1984). Plotted samples are basalts from Gakkel Ridge (Michael et al., 2003; Goldstein et al., 2008). Samples plotted at "zero distance" are included for comparison – these samples are from Lena Trough (Nauret et al., 2011), Knipovich (PetDB; Lehnert et al., 2000), Spitsbergen (Ionov et al., 2002), and Macquarie Island (Kamenetsky et al., 2000), the last of which are included as a representative E-MORB composition. The isotopic boundary in the middle of the SMZ, described by Goldstein et al. (2008), is represented by a vertical red dashed line. (Modified from Goldstein et al., 2008).

4) METHODS

Major element composition analyses were performed by electron microprobe at the University of Houston and at the JEOL 7900 electron probe facility of the Max-Planck Institute for Chemistry in Mainz, Germany. Trace element composition analyses were performed by laser ablation inductively coupled plasma mass spectrometry (LA-ICP-MS) at the University of Houston.

Analyses were performed on mounted basalt glass chips. The major and trace element composition data reported in this study were averaged from three to four spots on two separate glass chips per sample to ensure reproducibility of the measured data. Major and trace elements were measured on the same glass chips.

All Gakkel Ridge data reported in this study were measured from basalt glass samples, not whole rock samples. The other data included on the diagrams of this study are mostly glass data, but some whole rock data were included from locations from which glass data were unavailable. The accompanying figure captions point out which data are whole rock data. Glass data are preferred over data measured from whole rock analyses to help minimize possible contamination of in whole rock compositions, such as by seawater. However, Brodholt and Batiza (1989) pointed out in their analysis of global

MORB data that plotting glass and whole rock analyses separately showed no difference between the two subsets. Thus, although glass data were plotted whenever possible as an extra precaution for this study, it may not have actually made a significant difference.

Major and trace elements from a total of 68 Gakkel Ridge samples were analyzed for this study: 27 SMZ13 samples, 17 SMZ19 samples, 5 EVZ31 samples, 7 EVZ37 samples, 2 EVZ43 samples, and 10 EVZ55 samples. The figures in this thesis combine data from these newly analyzed Gakkel Ridge basalt samples with all the previously analyzed Gakkel Ridge basalt glass samples (Michael et al., 2003; Goldstein et al., 2008; Shaw et al., 2010).

4.1) LA-ICP-MS

Laser ablation inductively coupled plasma mass spectrometry is an analytical procedure for determining the trace element concentrations of solid samples. The laser ablates particles from spots on the surface of the glass of the basalt samples. These ablated particles are then ionized by a plasma torch, producing charged ions that are then separated according to their mass by a quadrupole mass spectrometer, allowing for concentration data for each trace element to be recorded.

The LA-ICP-MS system used for alayzing trace elements, along with the major element Ti, comprised of a CETAC LSX-213 Laser Ablation System coupled with a Varian ICP-MS. Analyses were performed using a 50 μm beam diameter spot size. The quality of the data was checked and ensured by repeated measurements of the basalt glass standards KL2-G and BIR-1 (Appx. 6). Standard compositions were obtained from the

Geological and Environmental Reference Materials (GeoReM; Jochum et al., 2005). One measurement of a standard was made for every two sample measurements.

4.2) Electron microprobe

An electron microprobe works by bombarding the polished surfaces of the basalt glass samples coated with a thin layer of carbon with a beam of high-energy electrons. The electron beam ionizes atoms within several microns of the sample surface, removing electrons from inner orbitals of the atoms, producing electron orbital vacancies, causing electrons from higher energy orbitals to drop down into the lower energy vacancies; thus, emitting photons of characteristic energies and wavelengths for each element; thus, allowing element concentrations to be measured after counts are corrected for atomic number, absorption, and fluorescence effects.

The electron microprobe used for analyzing the major elements of the Gakkel Ridge basalt samples was a CAMECA SX50. Major element analyses were performed using a 15 kV accelerating voltage, ~2 micron spot size, and 20 nA beam intensity. The secondary standard used was VG-2 (Appx. 6; Jarosewich, 1980; Jarosewich, 2002).

4.3) Uncertainty

Precision is a measure of the reproducibility of a measurement. Repeated measurements that produce similar values are more precise; repeated measurements that deviate from each other to a greater extent are less precise. Analyses with the greatest possible level of precision would reproduce the exact same value every time the same measurement is repeated. The amount of deviation from one measurement to another is

defined as the amount of uncertainty or error. Analyses are considered to be of better quality when uncertainty is minimized.

Accuracy is defined as the closeness of a measured value to the true or accepted value. Accuracy was constrained by analyzing basalt standards as unknowns during the electron microprobe and LA-ICP-MS analyses. These check standard measurements were compared to the published accepted values of those standards. The measured elements were found to be within the analytical error of the true values (Appx. 6).

The uncertainty of the analyses is represented on the figures of this thesis as "uncertainty polygons" (i.e., uncertainty fields) surrounding each plotted data point. The extents covered by these polygons show the degree of precision for each data point measurement that is plotted on the ternary plots. Uncertainty polygons were calculated by first calculating the standard deviations of the analyses of the independent check standards for all three elements of each ternary plot. Those calculated standard deviations are then added and subtracted to and from the average concentrations of each element in each sample, in order to calculate the points of the uncertainty polygons surrounding each plotted sample.

A	SMZ19: 199-1-2 Uncertainty		
	K_2O	^{139}La	TiO_2
std	0.01	0.02	0.00
199-1-2	0.08	2.17	1.21
+++	0.09	2.20	1.21
++-	0.09	2.20	1.20
+-+	0.09	2.15	1.21
-++	0.07	2.20	1.21
--+	0.07	2.15	1.21
-+-	0.07	2.20	1.20
+--	0.09	2.15	1.20
---	0.07	2.15	1.20

B	SMZ19: 252-1 Uncertainty		
	K_2O	^{139}La	TiO_2
std	0.01	0.02	0.00
252-1	0.61	9.80	1.39
+++	0.62	9.82	1.39
++-	0.62	9.82	1.39
+-+	0.62	9.77	1.39
-++	0.60	9.82	1.39
--+	0.60	9.77	1.39
-+-	0.60	9.82	1.39
+--	0.62	9.77	1.39
---	0.60	9.77	1.39

Table 2. Average concentrations in ppm (yellow row) (averaged from four measurements) of K_2O, La, and TiO_2 for the samples 199-1-2 (Table 2a) and 252-1 (Table 2b) from SMZ19, along with the corresponding standard deviations (std) (green row), and the calculated results from adding and subtracting the standard deviations to the average concentrations for each of the three elements (orange rows).

Table 2 shows the results from adding and subtracting the standard deviations of the check standard analyses to and from the concentrations of the elements Sm, La, and Yb for the samples 199-1-2 and 252-1 from the volcanic center EVZ55 to produce the "uncertainty points" shown on Table 2 (orange rows). These points, when plotted on a ternary plot (Fig. 10; Fig. 12), form a polygon around each data point. The field that is covered by each polygon represents the field of uncertainty corresponding to each data point. Two of the points (the "+++" and "---" points) plot within the uncertainty polygon; thus, do not define the polygon, so they have been removed from the ternary plots showing the uncertainty polygons (Fig. 10; Fig. 12), leaving the polygon with six points, forming six sides.

Figure 10 plots only two samples and for an unobstructed look at their accompanying uncertainty polygons. The uncertainty polygons are defined by the black dots surrounding the samples 199-1-2 and 252-1 from the volcanic center SMZ19,

produced from the uncertainty points calculated on Table 2. The uncertainty points of sample 199-1-2 are more spread out and its resulting uncertainty polygon is larger than the uncertainty points and uncertainty polygon of sample 252-1. This is a consequence of sample 199-1-2 having smaller elemental abundances that sample 252-1. Smaller elemental abundances yield lower accuracy than higher elemental abundance. As a general trend, the samples plotting towards the depleted end of the global MORB array (e.g., 199-1-2) have larger uncertainty polygons than samples plotting towards the enriched end (e.g., 252-1).

Uncertainty polygons were calculated for all of the samples that were analyzed in this study (Fig. 12; Fig. 13).

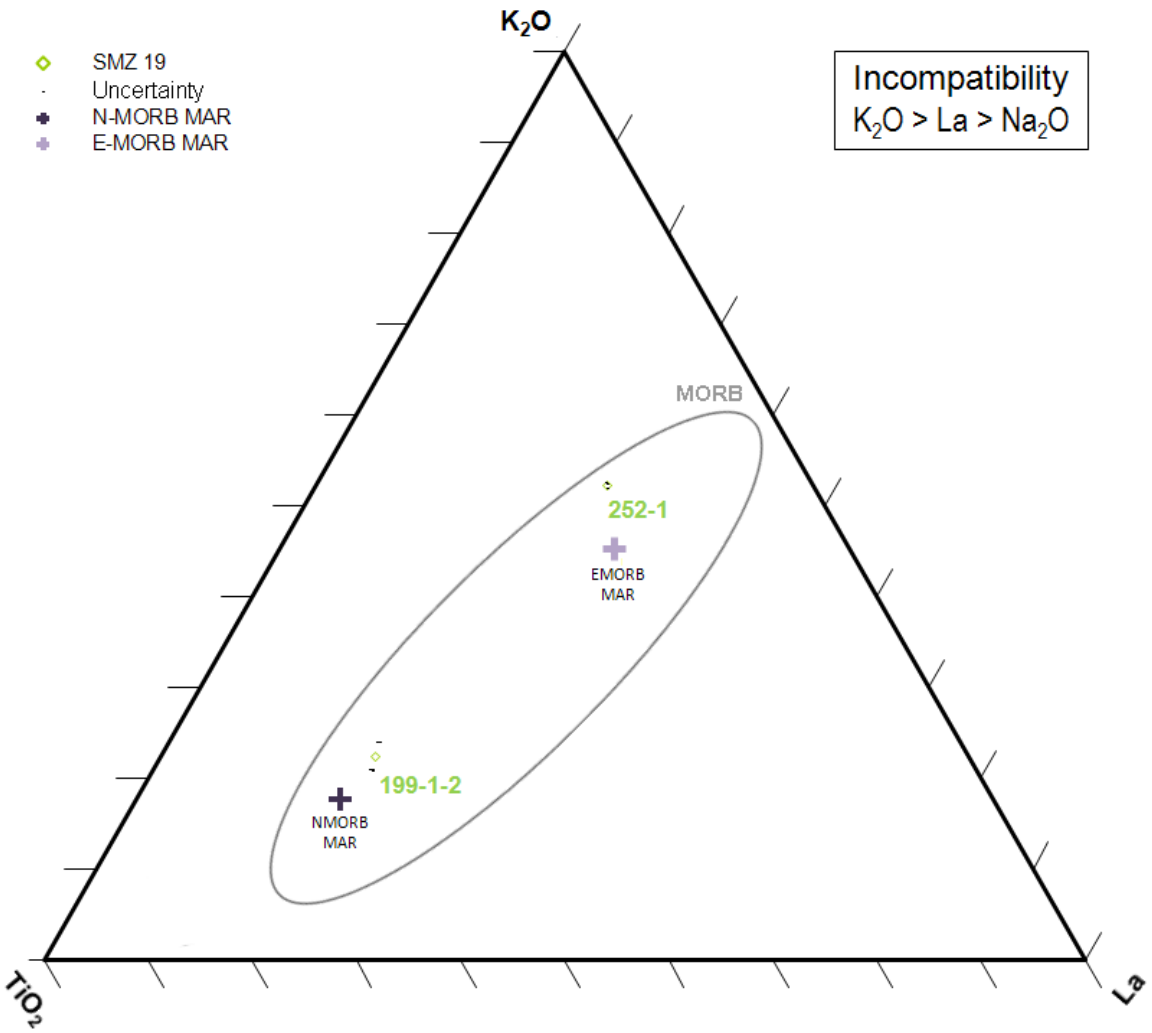

Figure 10. TKL ternary plot, featuring the elements La (ppm), Sm (ppm x 2), and Yb (ppm), showing six uncertainty points, forming a six-sided polygon, surrounding each of the plotted samples, 199-1-2 and 252-1 from SMZ19. Average MAR N-MORB and E-MORB and global MORB array (circled in gray) data compiled from PetDB (Lehnert et al., 2000).

4.4) Two-component mixing lines

Two-component mixing lines were calculated using the equation:

$$X_M = X_A f_A + X_B(1-f_A)$$

where X_M denotes the concentration of element X in a two-component mixture, X_A denotes the concentration of X in component A, X_B denotes the concentration of X in component B, and f_A denotes the abundance of component A in the given mixture. The two-component mixing equation was obtained from White (2013). Mixing lines were plotted on trace element ternary plots (Fig. Z).

5) RESULTS

Results from this study are presented as element concentration tables (Table 3, Table 4), a trace element spidergram (Fig. 11), and trace element concentration ternary plots (Fig. 12).

Figure 11 shows averaged Gakkel Ridge basalt trace elements on a spidergram, along with other averaged MORBs for comparison, including Lena Trough MORBs and other enriched MORBs.

Gakkel Ridge basalts are all more enriched than the average MAR N-MORB. This relative enrichment is visible on the trace element spidergram (Fig. 11), which shows the averaged compositions from each volcanic center of Gakkel Ridge all plotting higher than MAR N-MORB in nearly all the different trace elements. The average enrichment in MORB is not consistent across Gakkel Ridge, but instead, varies from

volcanic center to volcanic center (Fig. 11). The volcanic centers SMZ13 and SMZ19 are noticeably more enriched than the others along Gakkel Ridge (Fig. 11). Overall, however, the level of enrichment in Gakkel Ridge MORBs does not appear to reach that of the E-MORBs, such as average MAR E-MORB, Macquarie Island basalts, and SWIR-oblique segment MORBs.

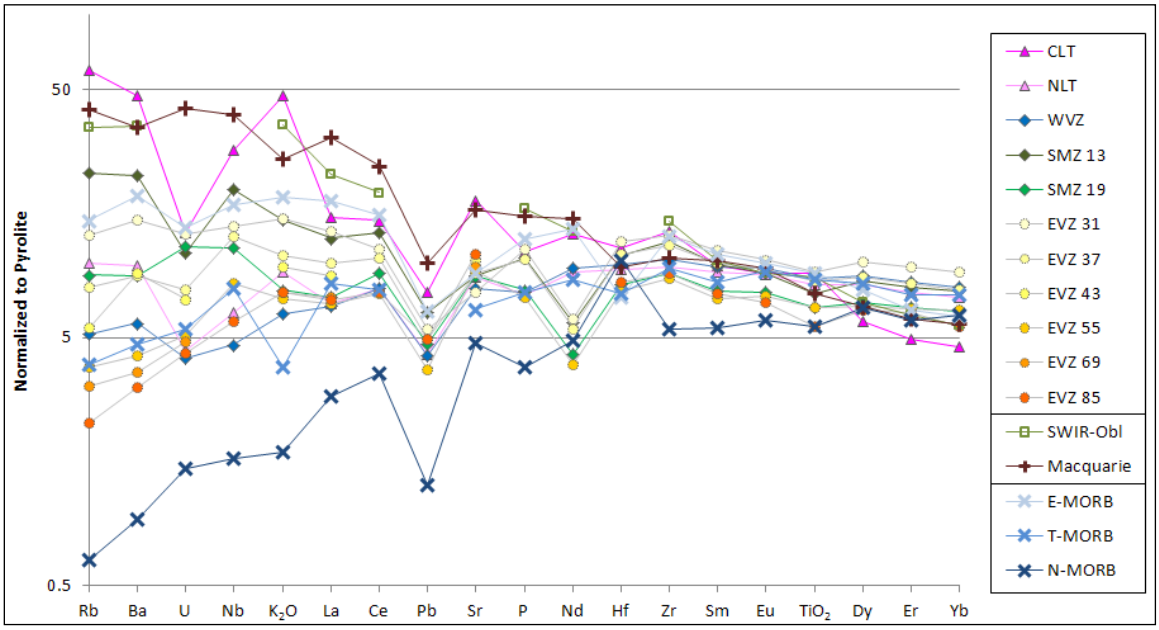

Figure 11. Spidergram showing relative trace element concentrations of Arctic basalt glasses from the Central and Northern Lena Trough (CLT, NLT) (Nauret et al., 2011), Gakkel Ridge (WVZ) (Snow J.E., in prep), SMZ, EVZ (Michael et al., 2003; Goldstein et al., 2008), Southwest Indian Ridge oblique segment (SWIR-Obl) (Standish et al., 2008), Macquarie Island (Kamenetsky et al., 2000), and average Mid-Atlantic Ridge E-MORB, T-MORB, and N-MORB (Klein, 2003b). Elements are normalized to pyrolite (McDonough & Sun, 1995). Elements are arranged in order of decreasing incompatibility from left to right. (Modified from Shaw et al., 2010).

5.1) Data

Major element concentrations of Gakkel Ridge basalt glass samples from the volcanic centers SMZ 13, SMZ 19, EVZ 31, EVZ 37, EVZ 43, and EVZ 55 are shown in Table 3. Trace element concentration data for those volcanic centers are shown in Table 4. The EVZ69 and EVZ85 volcanic centers were not a focus of this study, because samples recovered from the region of Gakkel Ridge located east of the EVZ55 were not analyzed for this study. All EVZ69 and EVZ85 basalt composition data included in the figures in this study are from earlier studies (Michael et al., 2003; Goldstein et al., 2008; Shaw et al., 2010). The chemistry of the WVZ and NLT is analyzed and discussed in detail in another study (Snow J. E., in prep), so the WVZ and NLT are not a focus of this study. WVZ and NLT basalt compositions that are included in the figures of this study are from Snow J.E. (in prep).

5.1.1) Gakkel Ridge major element compositions

Sample	Zone	Lon	Lat	Distance	Mg#	MgO	SiO_2	Al_2O_3	Na_2O	K_2O	TiO_2	CaO	FeO	MnO	Cl	S	P_2O_5	Total
D35-69	SMZ 13	10.71	85.27	308	0.62	6.66	52.0	16.3	3.77	0.659	1.53	9.81	8.24	0.15	0.042	0.091	0.240	99.508
D35-38	SMZ 13	10.71	85.27	308	0.62	7.36	51.0	15.6	3.63	0.469	1.64	9.74	9.08	0.16	0.037	0.097	0.241	99.003
D35-4	SMZ 13	10.71	85.27	308	0.62	7.36	50.9	15.6	3.70	0.478	1.64	9.77	9.06	0.17	0.037	0.095	0.237	99.083
D35-2	SMZ 13	10.71	85.27	308	0.61	7.36	51.0	15.6	3.74	0.483	1.64	9.77	9.14	0.16	0.035	0.089	0.235	99.192
D35-34	SMZ 13	10.71	85.27	308	0.62	7.38	50.9	15.6	3.58	0.479	1.65	9.82	9.11	0.17	0.036	0.101	0.243	99.051
244-10	SMZ 13	11.04	85.05	312	0.63	6.58	50.8	16.5	3.36	0.744	1.71	10.4	7.81	0.15	0.078	0.083	0.295	98.448
244-2	SMZ 13	11.04	85.05	312	0.58	6.65	50.8	15.8	3.56	0.292	1.63	9.84	9.53	0.18	0.018	0.106	0.207	98.613
244-SG	SMZ 13	11.04	85.05	312	0.58	6.76	51.6	16.0	3.49	0.342	1.63	9.73	9.59	0.18	0.018	0.100	0.204	99.590
D37-8	SMZ 13	11.39	85.30	316	0.56	6.27	51.3	15.7	3.91	0.463	1.78	9.55	9.78	0.18	0.029	0.113	0.255	99.358
D36-53	SMZ 13	12.48	85.27	329	0.61	6.45	50.9	16.6	3.83	0.655	1.53	9.83	8.22	0.16	0.044	0.080	0.241	98.537
D36-63	SMZ 13	12.48	85.27	329	0.61	6.46	51.0	16.6	3.73	0.653	1.51	9.89	8.23	0.15	0.046	0.083	0.243	98.627
D36-66	SMZ 13	12.48	85.27	329	0.61	6.48	51.6	16.5	3.95	0.652	1.51	9.93	8.18	0.16	0.042	0.091	0.231	99.406
D36-64	SMZ 13	12.48	85.27	329	0.61	6.48	51.2	16.6	3.84	0.657	1.52	9.87	8.27	0.14	0.043	0.082	0.244	98.896
D36-70	SMZ 13	12.48	85.27	329	0.61	6.49	50.7	16.5	3.92	0.646	1.54	9.93	8.19	0.14	0.044	0.084	0.241	98.390
D36-68	SMZ 13	12.48	85.27	329	0.61	6.53	51.6	16.5	3.83	0.648	1.52	9.90	8.18	0.15	0.044	0.087	0.237	99.254
D36-59	SMZ 13	12.48	85.27	329	0.61	6.53	51.4	16.5	3.74	0.643	1.54	9.87	8.20	0.15	0.042	0.086	0.243	98.962
D36-62	SMZ 13	12.48	85.27	329	0.61	6.55	51.0	16.5	3.84	0.645	1.52	9.85	8.19	0.15	0.045	0.085	0.237	98.596
D36-2	SMZ 13	12.48	85.27	329	0.61	6.59	52.0	16.2	3.83	0.651	1.52	9.86	8.19	0.16	0.045	0.072	0.220	99.288
D36-45	SMZ 13	12.48	85.27	329	0.61	6.62	52.0	16.2	3.65	0.647	1.51	9.84	8.22	0.15	0.046	0.084	0.228	99.181
D38-26	SMZ 13	12.68	85.31	332	0.62	7.00	51.1	16.5	3.64	0.326	1.50	10.6	8.56	0.17	0.017	0.104	0.190	99.65
D38-25	SMZ 13	12.68	85.31	332	0.62	7.00	51.2	16.5	3.63	0.328	1.50	10.6	8.54	0.18	0.018	0.096	0.177	99.85
D38-27	SMZ 13	12.68	85.31	332	0.64	7.39	50.9	16.5	3.52	0.280	1.43	10.6	8.40	0.17	0.015	0.097	0.171	99.45
D38-29R	SMZ 13	12.68	85.31	332	0.64	7.39	51.1	16.6	3.57	0.284	1.40	10.7	8.35	0.17	0.015	0.096	0.164	99.81
D38-12	SMZ 13	12.68	85.31	332	0.63	7.43	51.0	16.5	3.54	0.283	1.41	10.7	8.49	0.14	0.018	0.100	0.175	99.80
D38-4	SMZ 13	12.68	85.31	332	0.64	7.46	50.9	16.6	3.46	0.280	1.40	10.7	8.44	0.16	0.019	0.099	0.167	99.70
D38-29	SMZ 13	12.68	85.31	332	0.64	7.49	50.8	16.5	3.49	0.290	1.39	10.7	8.41	0.17	0.016	0.096	0.169	99.56
248-59	SMZ 13	13.45	85.21	341	0.66	7.60	51.0	16.6	3.41	0.337	1.27	10.4	7.84	0.15	0.022	0.070	0.174	98.806
199-1-1	SMZ 19	16.21	85.56	371	0.60	8.17	48.0	17.4	2.82	0.055	1.16	11.0	10.7	0.17	0.009	0.096	0.075	99.603
199-1-2	SMZ 19	16.21	85.56	371	0.61	8.19	47.9	17.6	3.01	0.080	1.21	10.9	10.5	0.19	0.008	0.099	0.073	99.68
199-8	SMZ 19	16.21	85.56	371	0.65	9.29	48.5	16.6	3.09	0.277	1.19	10.1	9.87	0.15	0.013	0.100	0.113	99.28
D41-18	SMZ 19	17.95	85.69	390	0.67	7.64	50.9	16.4	3.34	0.240	1.17	11.3	7.48	0.14	0.010	0.090	0.139	98.80
D41-17	SMZ 19	17.95	85.69	390	0.68	7.86	51.0	16.7	3.27	0.246	1.14	11.5	7.43	0.15	0.010	0.078	0.135	99.52
D42-16	SMZ 19	18.09	85.73	391	0.64	7.49	50.8	16.6	3.42	0.363	1.34	10.6	8.43	0.15	0.022	0.084	0.176	99.47
D42-18	SMZ 19	18.09	85.73	391	0.64	7.50	50.9	16.6	3.48	0.370	1.34	10.7	8.53	0.16	0.021	0.096	0.173	99.85
D42-12	SMZ 19	18.09	85.73	391	0.63	7.52	50.8	16.6	3.51	0.372	1.34	10.5	8.57	0.16	0.022	0.083	0.176	99.64
252-1	SMZ 19	18.22	85.62	392	0.66	7.25	51.3	16.9	3.68	0.611	1.40	10.1	7.47	0.15	0.038	0.082	0.218	99.07
253-1	SMZ 19	18.30	85.71	393	0.63	6.89	51.5	16.0	3.57	0.370	1.44	11.0	8.11	0.17	0.018	0.094	0.187	99.36
254-1	SMZ 19	19.50	85.74	405	0.64	6.98	51.2	16.1	3.37	0.401	1.41	11.3	7.77	0.14	0.022	0.089	0.206	98.96
255-1	SMZ 19	20.28	85.79	413	0.66	7.38	51.4	16.5	3.37	0.340	1.22	11.3	7.41	0.14	0.020	0.085	0.170	99.33
255-3	SMZ 19	20.28	85.79	413	0.67	7.40	51.4	16.5	3.37	0.346	1.22	11.3	7.38	0.13	0.018	0.084	0.163	99.30
255-5	SMZ 19	20.28	85.79	413	0.67	7.41	51.4	16.6	3.43	0.336	1.23	11.4	7.32	0.13	0.015	0.080	0.168	99.52
315-1	SMZ 19	20.45	85.81	415	0.62	6.96	51.5	16.1	3.51	0.324	1.50	10.8	8.43	0.17	0.016	0.101	0.188	99.59
D45-10	SMZ 19	25.14	86.03	459	0.63	8.63	49.2	16.2	3.29	0.167	1.44	10.4	10.1	0.18	0.010	0.116	0.153	99.86
260-1	EVZ 31	29.14	85.97	494	0.48	5.55	50.8	14.3	3.79	0.424	2.33	9.71	11.8	0.22	0.014	0.145	0.299	99.39
263-12	EVZ 31	30.66	86.06	507	0.59	7.06	50.6	15.8	3.38	0.232	1.77	10.3	9.86	0.18	0.010	0.105	0.222	99.42
263-19	EVZ 31	30.66	86.06	507	0.58	7.29	50.5	15.4	3.56	0.327	2.04	10.2	10.5	0.19	0.012	0.111	0.259	100.28
263-16	EVZ 31	30.66	86.06	507	0.64	8.16	50.4	16.6	3.02	0.283	1.35	11.1	8.91	0.16	0.013	0.095	0.159	100.14
D47-7	EVZ 31	31.27	86.05	512	0.59	6.76	50.9	15.8	3.62	0.357	1.76	10.9	9.22	0.18	0.013	0.099	0.249	99.87
309-5	EVZ 37	36.01	86.23	551	0.60	7.31	50.7	15.8	3.45	0.353	1.79	10.3	9.62	0.18	0.015	0.107	0.239	99.79
265-2A	EVZ 37	37.75	86.33	565	0.56	6.65	51.0	15.4	3.63	0.242	1.78	10.6	10.3	0.19	0.011	0.131	0.196	100.12
265-2	EVZ 37	37.75	86.33	565	0.57	6.78	51.6	15.5	3.27	0.254	1.80	10.8	10.3	0.17	0.014	0.119	0.205	100.84
265-5	EVZ 37	37.75	86.33	565	0.66	8.20	51.0	16.5	3.23	0.241	1.46	10.9	8.28	0.15	0.009	0.087	0.179	100.17
307-8	EVZ 37	38.16	86.36	568	0.64	7.48	50.7	16.5	3.25	0.337	1.60	10.8	8.39	0.15	0.014	0.097	0.206	99.54
266-15	EVZ 37	38.76	86.31	573	0.58	6.84	50.7	15.6	3.57	0.395	2.06	10.1	9.82	0.19	0.021	0.117	0.290	99.76
266-13	EVZ 37	38.76	86.31	573	0.64	7.92	50.5	16.0	3.42	0.383	1.72	10.2	8.92	0.17	0.017	0.095	0.250	99.62
304-3	EVZ 43	40.99	86.48	591	0.64	7.81	50.8	16.2	3.33	0.247	1.56	10.7	8.71	0.17	0.008	0.088	0.187	99.73
304-2	EVZ 43	40.99	86.48	591	0.64	7.82	50.7	16.2	3.34	0.241	1.55	10.8	8.71	0.16	0.011	0.104	0.203	99.86
297-2	EVZ 55	47.11	86.68	639	0.64	8.74	48.3	17.9	2.84	0.134	1.06	11.0	9.65	0.18	0.004	0.093	0.094	100.09
297-36	EVZ 55	47.11	86.68	639	0.65	8.81	48.5	17.7	2.88	0.174	1.14	10.9	9.36	0.16	0.006	0.089	0.117	99.89
297-1	EVZ 55	47.11	86.68	639	0.65	8.98	48.7	17.7	2.74	0.150	1.05	11.0	9.58	0.17	0.005	0.090	0.102	100.33
297-SG	EVZ 55	47.11	86.68	639	0.65	9.08	48.7	17.6	2.88	0.144	1.06	10.9	9.57	0.17	0.007	0.099	0.096	100.33
271-1-11	EVZ 55	47.72	86.84	644	0.66	7.90	49.9	16.9	3.39	0.342	1.49	10.8	8.09	0.15	0.012	0.090	0.203	99.19
271-1-9	EVZ 55	47.72	86.84	644	0.66	8.26	49.8	16.4	3.52	0.252	1.47	10.9	8.52	0.17	0.010	0.093	0.167	99.63
270-2	EVZ 55	50.12	86.75	663	0.67	8.41	49.7	16.8	3.31	0.390	1.55	10.8	8.16	0.15	0.013	0.097	0.205	99.50
270-19	EVZ 55	50.12	86.75	663	0.68	8.60	49.7	16.7	3.42	0.389	1.55	10.7	8.16	0.15	0.012	0.088	0.214	99.64
295-2	EVZ 55	52.30	86.80	681	0.66	7.80	49.9	16.9	3.34	0.333	1.45	11.0	8.08	0.15	0.011	0.102	0.203	99.34
294-2	EVZ 55	56.06	86.89	713	0.65	8.19	49.0	17.2	3.41	0.113	1.38	11.0	8.73	0.17	0.006	0.096	0.128	99.37

Table 3. Gakkel Ridge SMZ and EVZ basalt sample major element concentration data (wt.%), measured by electron microprobe. The distance column shows the distance along the ridge from west to east, with the western end of the WVZ set as a distance of 0 km. Magnesium number (Mg#) is defined as Mg#=MgO/40.3/(MgO+0.9*FeO/71.85), with MgO and FeO denoting element concentrations. The total column displays the sum of all of the major element concentrations. Although TiO_2 alues were measured by electron microprobe and reported in this table, the TiO_2 values that were actually plotted in the figures are the more precise values in Table 4, which were measured by LA-ICP-MS.

5.1.2) Gakkel Ridge trace element compositions

Sample	Zone	Lon	Lat	Distance	Rb	Sr	Y	Zr	Nb	Cs	Ba	La	Ce	Pr	Nd	Sm	Eu	Gd
D35-69	SMZ 13	10.71	85.27	308	24	212	33.2	138	16	0.383	264	11.9	25.9	3.4	15.8	4.24	1.45	5.26
D35-38	SMZ 13	10.71	85.27	308	15	178	34.3	129	14	0.212	163	9.8	22.5	3.1	14.7	4.08	1.44	5.21
D35-4	SMZ 13	10.71	85.27	308	16	188	36.7	137	15	0.223	179	10.8	24.6	3.4	16.0	4.52	1.58	5.78
D35-2	SMZ 13	10.71	85.27	308	15	186	35.9	136	14	0.225	177	10.6	24.3	3.3	16.0	4.54	1.54	5.66
D35-34	SMZ 13	10.71	85.27	308	16	188	36.3	136	15	0.220	183	10.9	25.2	3.4	16.1	4.57	1.58	5.79
244-10	SMZ 13	11.04	85.05	312	32	304	27.1	120	26	0.369	371	16.8	33.5	3.9	16.8	3.72	1.34	4.33
244-2	SMZ 13	11.04	85.05	312	10	155	35.2	131	6	0.118	81.5	6.4	18.3	2.8	14.2	4.31	1.50	5.38
244-SG	SMZ 13	11.04	85.05	312	10	155	36.0	132	6	0.143	81.9	6.6	18.3	2.8	14.1	4.02	1.49	5.42
D37-8	SMZ 13	11.39	85.30	316	14	172	39.5	150	14	0.183	144	10.2	24.3	3.4	16.7	4.67	1.68	6.08
D36-53	SMZ 13	12.48	85.27	329	24	215	32.6	136	17	0.384	268	11.9	26.3	3.4	15.7	4.19	1.43	5.09
D36-63	SMZ 13	12.48	85.27	329	24	212	32.3	134	17	0.373	262	11.7	25.6	3.3	15.3	4.11	1.40	5.03
D36-66	SMZ 13	12.48	85.27	329	24	215	33.7	139	16	0.371	265	12.0	25.6	3.4	15.5	4.14	1.41	5.11
D36-64	SMZ 13	12.48	85.27	329	25	217	33.9	141	17	0.387	269	12.2	26.3	3.4	15.9	4.30	1.48	5.34
D36-70	SMZ 13	12.48	85.27	329	24	213	32.5	136	16	0.365	265	12.0	26.0	3.4	15.6	4.18	1.40	4.98
D36-68	SMZ 13	12.48	85.27	329	25	213	32.5	136	17	0.373	264	11.9	25.9	3.4	15.7	4.14	1.43	5.13
D36-59	SMZ 13	12.48	85.27	329	24	211	32.5	135	16	0.370	255	11.4	25.0	3.3	15.0	4.03	1.37	4.90
D36-62	SMZ 13	12.48	85.27	329	25	214	32.5	136	17	0.377	262	11.7	25.7	3.3	15.3	4.14	1.39	4.89
D36-2	SMZ 13	12.48	85.27	329	23	209	32.1	135	16	0.373	257	11.4	25.1	3.3	15.4	4.01	1.39	4.95
D36-45	SMZ 13	12.48	85.27	329	24	215	32.5	136	17	0.395	258	11.5	25.2	3.3	15.4	4.12	1.39	5.12
D38-26	SMZ 13	12.68	85.31	332	8.8	160	31.5	113	8	0.111	92	6.5	16.2	2.4	11.9	3.67	1.28	4.70
D38-25	SMZ 13	12.68	85.31	332	9.1	158	32.3	116	8	0.111	94	6.7	16.8	2.5	12.4	3.72	1.31	4.89
D38-27	SMZ 13	12.68	85.31	332	8.0	152	29.6	105	7	0.102	84	6.1	15.1	2.2	11.3	3.43	1.25	4.51
D38-29R	SMZ 13	12.68	85.31	332	8.3	154	28.3	100	7	0.147	80	5.8	14.6	2.1	10.9	3.31	1.20	4.22
D38-12	SMZ 13	12.68	85.31	332	7.9	152	29.8	104	7	0.098	83	6.0	15.0	2.2	11.2	3.42	1.19	4.47
D38-4	SMZ 13	12.68	85.31	332	7.7	154	29.9	105	7	0.098	84	6.0	15.1	2.2	11.2	3.42	1.18	4.41
D38-29	SMZ 13	12.68	85.31	332	8.0	154	29.6	104	7	0.101	85	6.0	15.2	2.2	11.3	3.43	1.23	4.54
248-59	SMZ 13	13.45	85.21	341	13	171	29.5	114	7	0.162	112	6.7	17.3	2.7	12.9	3.67	1.31	4.69
199-1-1	SMZ 19	16.21	85.56	371	0.7	139	25.2	63	1	0.044	9	2.1	6.8	1.2	6.9	2.40	1.03	3.63
199-1-2	SMZ 19	16.21	85.56	371	1.0	141	25.9	67	2	0.016	12	2.2	7.1	1.2	6.7	2.35	0.99	3.35
199-8	SMZ 19	16.21	85.56	371	9.0	172	22.9	79	5	0.143	84	4.6	11.7	1.7	8.3	2.51	0.98	3.32
D41-18	SMZ 19	17.95	85.69	390	5.5	171	22.7	81	6	0.085	60	4.7	12.4	1.8	8.8	2.79	0.99	3.29
D41-17	SMZ 19	17.95	85.69	390	5.7	182	23.5	88	6	0.070	64	4.9	12.7	1.9	9.4	2.86	1.05	3.77
D42-16	SMZ 19	18.09	85.73	391	12	179	26.2	99	10	0.166	121	7.4	17.9	2.4	11.7	3.19	1.22	4.18
D42-18	SMZ 19	18.09	85.73	391	12	180	25.9	97	10	0.168	119	7.2	17.8	2.4	11.5	3.22	1.16	4.00
D42-12	SMZ 19	18.09	85.73	391	12	176	25.3	95	10	0.170	121	7.2	18.0	2.4	11.4	3.18	1.11	3.84
252-1	SMZ 19	18.22	85.62	392	19	217	25.8	114	14	0.280	198	9.8	22.2	2.9	13.2	3.43	1.20	4.10
253-1	SMZ 19	18.30	85.71	393	9.1	189	28.3	110	10	0.110	99	7.5	18.2	2.6	12.3	3.38	1.20	4.22
254-1	SMZ 19	19.50	85.74	405	8.7	201	25.5	101	10	0.108	102	7.3	17.6	2.4	11.6	3.20	1.16	4.07
255-1	SMZ 19	20.28	85.79	413	9.3	194	24.6	97	8	0.129	103	6.6	16.2	2.3	11.1	3.11	1.13	3.89
255-3	SMZ 19	20.28	85.79	413	9.3	195	24.5	97	8	0.131	103	6.5	15.8	2.2	10.7	3.03	1.10	3.70
255-5	SMZ 19	20.28	85.79	413	10	200	25.0	99	8	0.129	105	6.7	16.2	2.3	11.1	3.16	1.15	3.88
315-1	SMZ 19	20.45	85.81	415	8.7	171	31.0	109	8	0.154	81	6.6	16.9	2.4	12.8	3.71	1.34	4.60
D45-10	SMZ 19	25.14	86.03	459	2.6	149	27.1	85	4	0.031	33	4.0	12.0	1.9	10.2	3.33	1.33	4.41
260-1	EVZ 31	29.14	85.97	494	7.9	137	51.9	178	11	0.083	98	9.3	23.9	3.7	19.1	5.96	1.97	7.99
263-12	EVZ 31	30.66	86.06	507	4.5	136	37.3	129	7	0.052	50	6.0	16.3	2.5	13.6	4.32	1.49	5.83
263-19	EVZ 31	30.66	86.06	507	6.5	157	40.2	145	10	0.069	78	7.8	19.7	3.0	15.6	4.85	1.66	6.49
263-16	EVZ 31	30.66	86.06	507	5.4	165	25.3	87	7	0.057	69	5.6	13.5	1.9	9.7	2.91	1.09	3.90
D47-7	EVZ 31	31.27	86.05	512	6.9	158	36.1	136	10	0.082	79	8.1	21.7	3.1	15.9	4.73	1.66	5.93
309-5	EVZ 37	36.01	86.23	551	7.0	172	35.1	132	11	0.080	80	7.7	19.2	2.9	14.4	4.28	1.52	5.60
265-2A	EVZ 37	37.75	86.33	565	4.3	144	38.2	122	7	0.048	54	5.9	15.7	2.5	13.4	4.30	1.54	5.84
265-2	EVZ 37	37.75	86.33	565	4.4	147	38.7	123	7	0.049	55	6.0	16.2	2.6	13.7	4.39	1.58	6.00
265-5	EVZ 37	37.75	86.33	565	3.8	176	26.8	103	6	0.059	44	5.3	14.1	2.2	11.2	3.23	1.21	4.24
307-8	EVZ 37	38.16	86.36	568	5.5	189	28.0	110	9	0.081	62	6.4	17.1	2.5	12.4	3.74	1.26	4.36
266-15	EVZ 37	38.76	86.31	573	8.9	164	40.1	154	13	0.114	97	9.1	23.5	3.5	17.2	5.15	1.66	6.31
266-13	EVZ 37	38.76	86.31	573	7.1	191	31.0	126	11	0.083	81	7.9	20.0	2.9	14.4	3.97	1.43	5.06
304-3	EVZ 43	40.99	86.48	591	4.0	169	31.0	118	6	0.053	45	5.7	15.8	2.4	12.2	3.49	1.33	4.77
304-2	EVZ 43	40.99	86.48	591	4.1	175	31.7	120	7	0.062	47	6.1	16.0	2.6	13.4	3.80	1.41	5.16
297-2	EVZ 55	47.11	86.68	639	1.3	157	24.9	64	3	0.041	15	2.6	7.24	1.1	6.2	2.09	0.87	3.15
297-36	EVZ 55	47.11	86.68	639	1.8	164	24.7	71	3	0.042	21	3.2	9.0	1.4	7.2	2.36	0.89	3.37
297-1	EVZ 55	47.11	86.68	639	1.4	162	24.6	64	3	0.031	16	2.7	7.8	1.3	6.7	2.23	0.94	3.22
297-SG	EVZ 55	47.11	86.68	639	1.4	161	25.3	65	3	0.047	16	2.8	7.8	1.3	7.0	2.15	1.02	3.50
271-1-11	EVZ 55	47.72	86.84	644	5.1	202	24.5	102	8	0.069	56	6.0	15.7	2.3	11.3	3.08	1.20	3.96
271-1-9	EVZ 55	47.72	86.84	644	4.4	178	26.6	100	6	0.057	50	5.3	14.1	2.1	10.8	3.32	1.23	4.26
270-2	EVZ 55	50.12	86.75	663	5.1	240	26.6	117	9	0.065	61	7.5	18.3	2.7	13.3	3.55	1.31	4.49
270-19	EVZ 55	50.12	86.75	663	4.8	235	26.7	117	9	0.070	60	7.2	18.4	2.7	12.5	3.59	1.30	4.37
295-2	EVZ 55	52.30	86.80	681	4.7	193	27.5	111	8	0.066	56	6.6	16.6	2.4	12.2	3.40	1.24	4.38
294-2	EVZ 55	56.06	86.89	713	1.2	164	29.1	97	2	0.035	11	3.3	10.8	1.8	9.9	3.24	1.19	4.27

Table 4a. Gakkel Ridge SMZ and EVZ basalt sample trace element concentration data (ppm), measured by LA-ICP-MS. The distance column shows the distance along the ridge from west to east, with the western end of the WVZ set as a distance of 0 km.

Sample	Zone	Lon	Lat	Distance	Tb	Dy	Ho	Er	Tm	Yb	Lu	Hf	Ta	Pb	Th	U	TiO_2	Sc
D35-69	SMZ 13	10.71	85.27	308	0.89	5.89	1.23	3.57	0.509	3.5	0.520	3.28	0.943	1.06	1.58	0.373	1.52	33.8
D35-38	SMZ 13	10.71	85.27	308	0.88	5.74	1.21	3.52	0.501	3.4	0.482	3.01	0.742	0.90	1.09	0.266	1.65	34.4
D35-4	SMZ 13	10.71	85.27	308	0.98	6.50	1.37	4.01	0.571	3.9	0.571	3.50	0.859	1.03	1.28	0.309	1.67	35.2
D35-2	SMZ 13	10.71	85.27	308	0.98	6.51	1.34	3.88	0.564	3.8	0.563	3.38	0.828	0.99	1.26	0.310	1.67	34.7
D35-34	SMZ 13	10.71	85.27	308	0.98	6.43	1.36	3.96	0.579	3.9	0.573	3.44	0.855	1.05	1.26	0.316	1.69	35.4
244-10	SMZ 13	11.04	85.05	312	0.73	4.65	0.971	2.69	0.408	2.7	0.385	2.76	1.290	1.40	2.14	0.466	1.63	31.4
244-2	SMZ 13	11.04	85.05	312	0.91	6.10	1.26	3.58	0.540	3.6	0.510	3.08	0.359	0.82	0.52	0.124	1.62	36.7
244-SG	SMZ 13	11.04	85.05	312	0.97	6.48	1.31	3.70	0.535	3.8	0.540	3.11	0.376	0.87	0.56	0.170	1.67	36.3
D37-8	SMZ 13	11.39	85.30	316	1.0	6.81	1.45	4.24	0.591	4.0	0.596	3.59	0.791	1.04	1.09	0.275	1.80	34.5
D36-53	SMZ 13	12.48	85.27	329	0.87	5.83	1.20	3.57	0.508	3.5	0.509	3.26	0.948	1.08	1.57	0.353	1.58	33.5
D36-63	SMZ 13	12.48	85.27	329	0.86	5.70	1.17	3.52	0.497	3.4	0.501	3.17	0.904	1.04	1.52	0.330	1.58	33.8
D36-66	SMZ 13	12.48	85.27	329	0.89	5.87	1.21	3.56	0.522	3.4	0.526	3.22	0.923	1.10	1.58	0.338	1.56	34.6
D36-64	SMZ 13	12.48	85.27	329	0.90	6.00	1.23	3.67	0.528	3.6	0.530	3.34	0.977	1.12	1.59	0.342	1.57	34.0
D36-70	SMZ 13	12.48	85.27	329	0.86	5.66	1.18	3.55	0.491	3.4	0.503	3.10	0.914	1.02	1.54	0.340	1.58	34.1
D36-68	SMZ 13	12.48	85.27	329	0.88	5.91	1.19	3.57	0.506	3.5	0.509	3.24	0.936	1.08	1.55	0.347	1.59	33.9
D36-59	SMZ 13	12.48	85.27	329	0.84	5.64	1.15	3.44	0.482	3.3	0.483	3.05	0.898	1.02	1.48	0.328	1.58	33.8
D36-62	SMZ 13	12.48	85.27	329	0.85	5.66	1.15	3.49	0.490	3.4	0.487	3.12	0.917	1.08	1.53	0.331	1.57	33.4
D36-2	SMZ 13	12.48	85.27	329	0.85	5.49	1.16	3.43	0.489	3.3	0.487	3.09	0.911	1.02	1.50	0.346	1.53	33.6
D36-45	SMZ 13	12.48	85.27	329	0.85	5.56	1.17	3.44	0.485	3.3	0.479	3.05	0.900	0.99	1.48	0.347	1.55	33.6
D38-26	SMZ 13	12.68	85.31	332	0.82	5.46	1.14	3.47	0.479	3.3	0.490	2.78	0.489	0.76	0.65	0.152	1.43	34.7
D38-25	SMZ 13	12.68	85.31	332	0.84	5.61	1.18	3.50	0.496	3.4	0.502	2.84	0.509	0.77	0.67	0.155	1.49	35.9
D38-27	SMZ 13	12.68	85.31	332	0.78	5.11	1.06	3.16	0.447	3.1	0.452	2.54	0.455	0.71	0.58	0.131	1.40	34.9
D38-29R	SMZ 13	12.68	85.31	332	0.76	5.03	1.01	2.96	0.429	3.0	0.435	2.45	0.441	0.66	0.60	0.157	1.38	34.1
D38-12	SMZ 13	12.68	85.31	332	0.77	5.18	1.07	3.22	0.452	3.1	0.460	2.58	0.444	0.69	0.58	0.133	1.40	35.0
D38-4	SMZ 13	12.68	85.31	332	0.76	5.02	1.08	3.13	0.449	3.1	0.444	2.53	0.448	0.68	0.58	0.136	1.40	35.1
D38-29	SMZ 13	12.68	85.31	332	0.76	5.17	1.09	3.17	0.455	3.1	0.471	2.65	0.463	0.76	0.59	0.136	1.39	34.7
248-59	SMZ 13	13.45	85.21	341	0.81	5.32	1.12	3.14	0.477	3.2	0.471	2.86	0.444	0.85	0.60	0.148	1.30	34.1
199-1-1	SMZ 19	16.21	85.56	371	0.64	4.64	0.976	2.91	0.436	2.9	0.433	1.68	0.083	0.35	0.10	0.038	1.18	40.5
199-1-2	SMZ 19	16.21	85.56	371	0.63	4.33	0.941	2.83	0.409	2.8	0.419	1.70	0.098	0.34	0.11	0.033	1.21	39.5
199-8	SMZ 19	16.21	85.56	371	0.59	4.03	0.824	2.51	0.344	2.4	0.360	1.86	0.326	0.58	0.43	0.113	1.18	33.7
D41-18	SMZ 19	17.95	85.69	390	0.59	3.91	0.786	2.45	0.337	2.4	0.347	2.03	0.327	0.58	0.40	0.129	1.12	36.5
D41-17	SMZ 19	17.95	85.69	390	0.63	4.25	0.886	2.56	0.359	2.5	0.371	2.18	0.345	0.62	0.43	0.103	1.14	37.0
D42-16	SMZ 19	18.09	85.73	391	0.70	4.74	0.959	2.93	0.419	2.8	0.431	2.37	0.580	0.79	0.78	0.219	1.34	35.6
D42-18	SMZ 19	18.09	85.73	391	0.70	4.65	0.941	2.82	0.415	2.9	0.415	2.37	0.562	0.78	0.79	0.216	1.35	35.9
D42-12	SMZ 19	18.09	85.73	391	0.66	4.45	0.943	2.92	0.410	2.9	0.404	2.07	0.589	0.80	0.77	0.219	1.33	34.9
252-1	SMZ 19	18.22	85.62	392	0.68	4.42	0.922	2.76	0.391	2.7	0.390	2.59	0.824	1.02	1.20	0.289	1.39	31.1
253-1	SMZ 19	18.30	85.71	393	0.70	4.68	0.978	2.96	0.418	2.8	0.413	2.48	0.567	0.76	0.72	0.226	1.43	38.3
254-1	SMZ 19	19.50	85.74	405	0.69	4.52	0.934	2.79	0.393	2.7	0.386	2.34	0.573	0.71	0.74	0.194	1.24	34.3
255-1	SMZ 19	20.28	85.79	413	0.68	4.45	0.906	2.73	0.379	2.6	0.378	2.28	0.495	0.74	0.66	0.165	1.21	37.4
255-3	SMZ 19	20.28	85.79	413	0.64	4.41	0.886	2.65	0.380	2.6	0.371	2.30	0.494	0.71	0.67	0.162	1.20	37.0
255-5	SMZ 19	20.28	85.79	413	0.66	4.49	0.911	2.71	0.378	2.6	0.373	2.27	0.491	0.73	0.67	0.169	1.22	37.6
315-1	SMZ 19	20.45	85.81	415	0.84	5.56	1.12	3.42	0.492	3.1	0.481	2.83	0.497	0.90	0.63	0.356	1.50	36.9
D45-10	SMZ 19	25.14	86.03	459	0.76	5.06	1.02	3.12	0.440	3.0	0.420	2.37	0.275	0.58	0.33	0.105	1.44	32.1
260-1	EVZ 31	29.14	85.97	494	1.4	9.08	1.91	5.66	0.811	5.5	0.814	4.48	0.699	1.02	0.83	0.278	2.30	41.0
263-12	EVZ 31	30.66	86.06	507	1.0	6.62	1.38	4.09	0.576	3.9	0.581	3.24	0.425	0.68	0.52	0.157	1.75	36.3
263-19	EVZ 31	30.66	86.06	507	1.1	7.17	1.50	4.43	0.623	4.2	0.635	3.76	0.631	0.81	0.72	0.199	2.04	38.6
263-16	EVZ 31	30.66	86.06	507	0.67	4.39	0.913	2.70	0.377	2.6	0.381	2.10	0.409	0.60	0.49	0.141	1.35	35.2
D47-7	EVZ 31	31.27	86.05	512	1.0	6.74	1.38	4.11	0.589	4.1	0.589	3.68	0.620	0.95	0.77	0.234	1.76	37.6
309-5	EVZ 37	36.01	86.23	551	0.96	6.29	1.31	3.81	0.530	3.7	0.535	3.33	0.646	0.80	0.75	0.219	1.76	36.0
265-2A	EVZ 37	37.75	86.33	565	1.0	6.78	1.41	4.17	0.585	4.0	0.590	3.21	0.429	0.68	0.50	0.139	1.74	39.8
265-2	EVZ 37	37.75	86.33	565	1.0	6.83	1.43	4.25	0.606	4.1	0.604	3.24	0.440	0.71	0.50	0.147	1.79	40.0
265-5	EVZ 37	37.75	86.33	565	0.72	4.63	1.01	2.94	0.381	2.8	0.408	2.42	0.350	0.63	0.41	0.119	1.43	34.7
307-8	EVZ 37	38.16	86.36	568	0.76	4.94	1.01	3.01	0.413	2.7	0.417	2.58	0.491	0.70	0.52	0.146	1.54	33.1
266-15	EVZ 37	38.76	86.31	573	1.1	6.82	1.46	4.25	0.575	4.0	0.587	3.77	0.719	0.91	0.85	0.234	1.98	34.2
266-13	EVZ 37	38.76	86.31	573	0.85	5.45	1.19	3.35	0.461	3.2	0.473	3.04	0.616	0.85	0.72	0.211	1.68	34.2
304-3	EVZ 43	40.99	86.48	591	0.81	5.40	1.15	3.26	0.448	3.1	0.455	2.80	0.387	0.67	0.44	0.126	1.52	34.8
304-2	EVZ 43	40.99	86.48	591	0.87	5.74	1.25	3.51	0.489	3.3	0.490	3.08	0.400	0.69	0.44	0.137	1.56	36.3
297-2	EVZ 55	47.11	86.68	639	0.56	4.05	0.873	2.70	0.378	2.7	0.428	1.51	0.172	0.34	0.17	0.057	1.05	40.7
297-36	EVZ 55	47.11	86.68	639	0.60	3.94	0.902	2.75	0.388	2.7	0.424	1.66	0.215	0.36	0.22	0.088	1.10	38.5
297-1	EVZ 55	47.11	86.68	639	0.63	4.15	0.918	2.76	0.416	2.8	0.435	1.61	0.174	0.36	0.18	0.057	1.03	40.2
297-SG	EVZ 55	47.11	86.68	639	0.63	4.38	0.980	2.90	0.419	3.1	0.454	1.71	0.180	0.35	0.18	0.064	1.03	40.2
271-1-11	EVZ 55	47.72	86.84	644	0.66	4.23	0.905	2.63	0.350	2.5	0.370	2.39	0.495	0.68	0.51	0.180	1.46	32.6
271-1-9	EVZ 55	47.72	86.84	644	0.71	4.79	1.00	2.83	0.404	2.9	0.408	2.44	0.389	0.62	0.42	0.147	1.42	34.8
270-2	EVZ 55	50.12	86.75	663	0.71	4.78	1.00	2.98	0.390	2.9	0.410	2.70	0.588	0.79	0.59	0.202	1.59	35.3
270-19	EVZ 55	50.12	86.75	663	0.71	4.66	0.981	2.89	0.400	2.6	0.396	2.65	0.550	0.76	0.57	0.189	1.52	34.0
295-2	EVZ 55	52.30	86.80	681	0.74	4.78	1.03	2.98	0.408	3.0	0.420	2.63	0.501	0.71	0.54	0.167	1.44	34.9
294-2	EVZ 55	56.06	86.89	713	0.73	4.88	1.03	3.11	0.447	3.1	0.448	2.37	0.167	0.55	0.16	0.057	1.37	35.6

Table 4b. Gakkel Ridge SMZ and EVZ basalt sample trace element concentration data (ppm), measured by LA-ICP-MS (continued from Table 4a). The major element TiO_2 was also measured by LA-ICP-MS and its values are reported in this table.

5.2) Ternary plots – Arctic MORBs

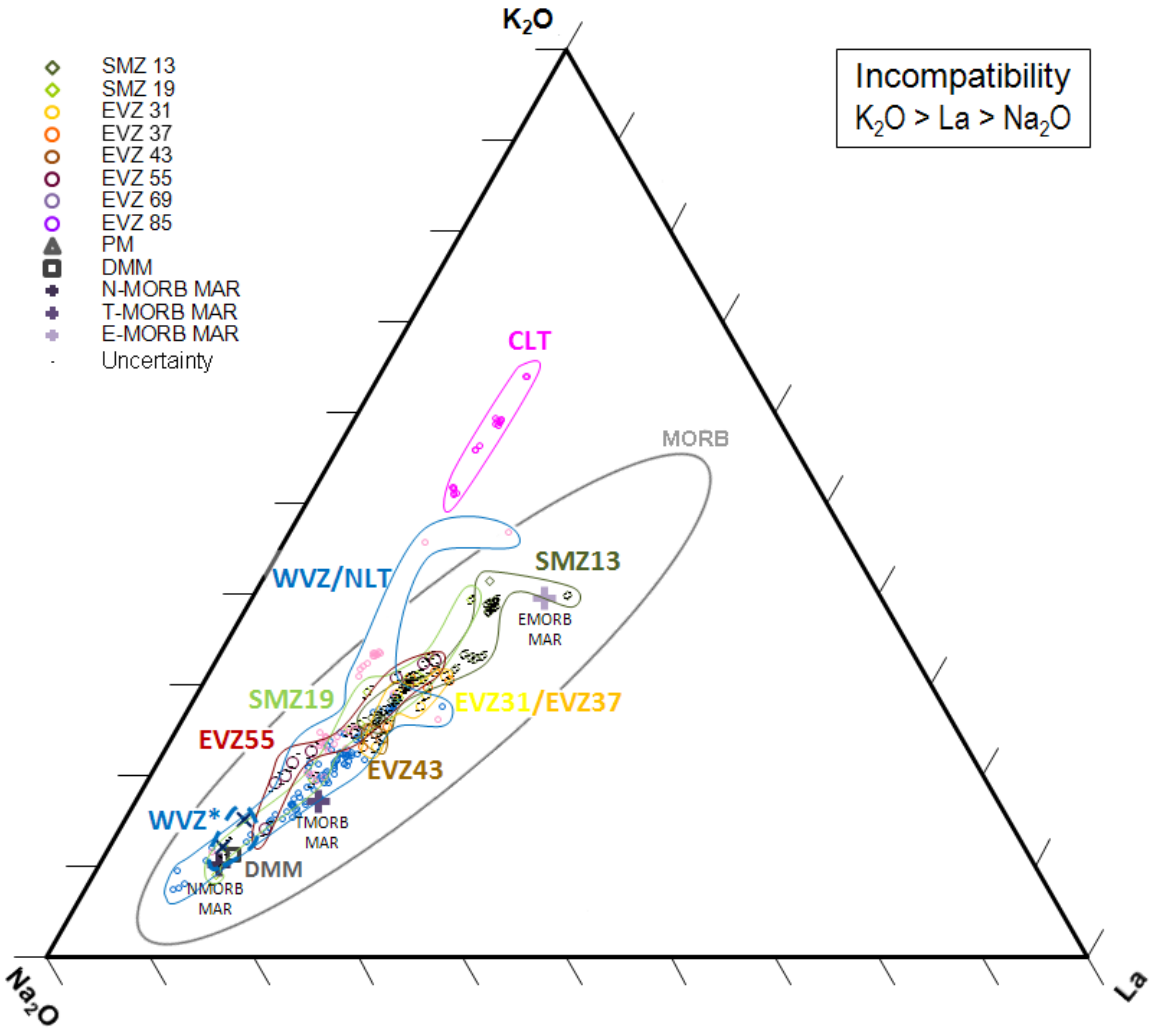

Figure 12a. NKL ternary plot showing relative concentrations of Na_2O (wt.% x 5), K_2O (wt.% x 30), & La (ppm) concentrations in Arctic Basin Gakkel Ridge and Lena Trough MORB glass samples. Uncertainty polygons are shown as black dots surrounding the sample points analyzed in this study. Samples that were not analyzed in this study do not have uncertainty polygons. Gakkel Ridge data are a combination of data from this study and from previously published data (Michael et al., 2003; Goldstein et al., 2008; Shaw et al., 2010). Also plotted are CLT basalt data (Nauret et al., 2011), WVZ & NLT (Snow J.E., in prep), PM (Sun & McDonough, 1989), and DMM (Salters & Stracke, 2004). Average N-MORB and E-MORB are calculated from basalt glass data from PetDB (Lehnert et al., 2000). The global MORB array, comprising data from the MAR, EPR, SWIR, & SEIR, (PetDB; Lehnert et al., 2000) is encircled in gray. Sample 297-2 from EVZ55 and its uncertainty points (from the YSL ternary plot) are shown in the legend to represent a typical analytical uncertainty for Gakkel samples.

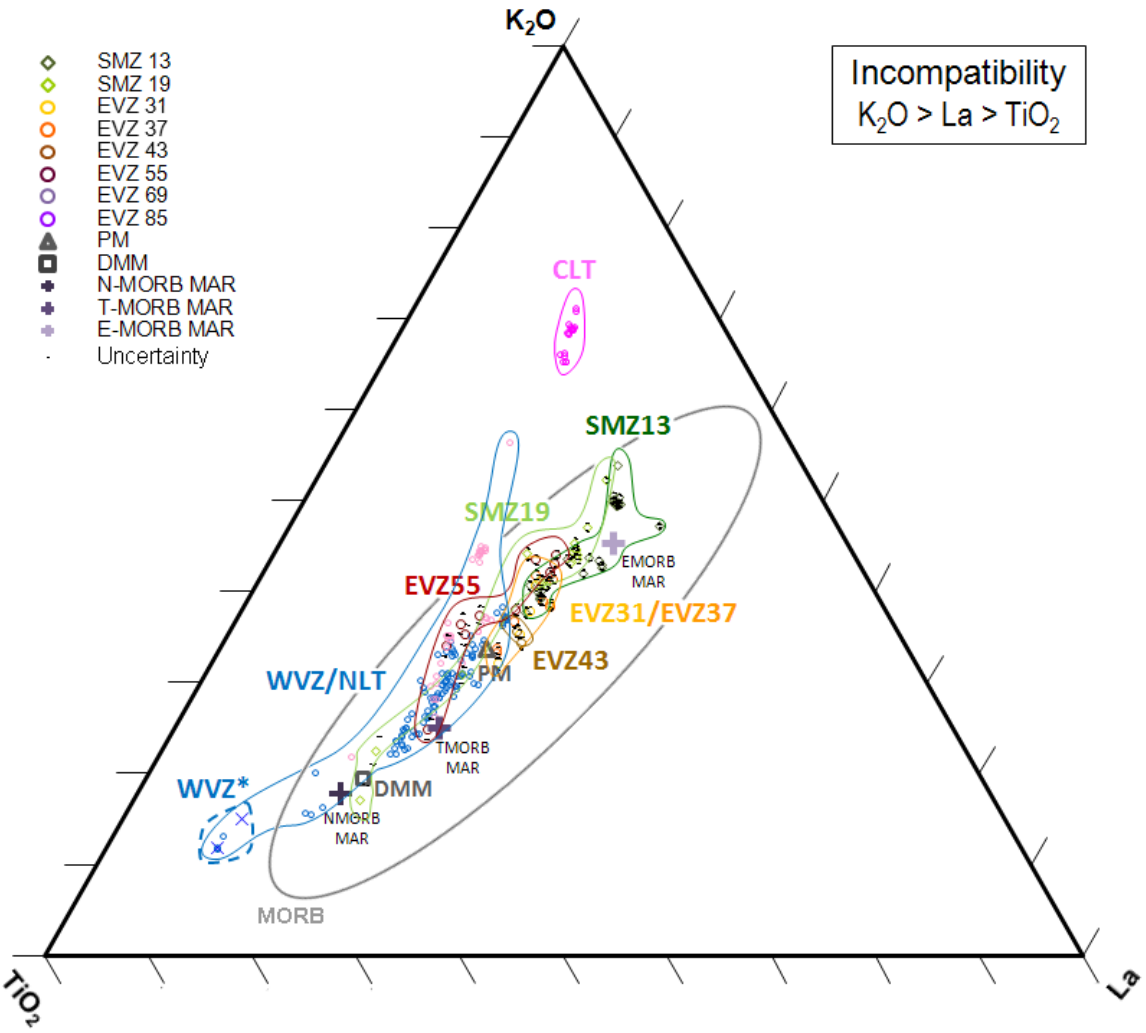

Figure 12b. TKL ternary plot showing relative concentrations of TiO_2 (wt.% x 5), K_2O (wt.% x 30), & La (ppm) in Gakkel Ridge and Lena Trough basalt glasses. Uncertainty polygons are shown as black dots surrounding the sample points analyzed in this study. The global MORB array is encircled in gray. Sample 297-2 from EVZ55 and its uncertainty points (from the YSL ternary plot) are shown in the legend to represent a typical analytical uncertainty for Gakkel samples. Data are from the same references as those in Figure 12a.

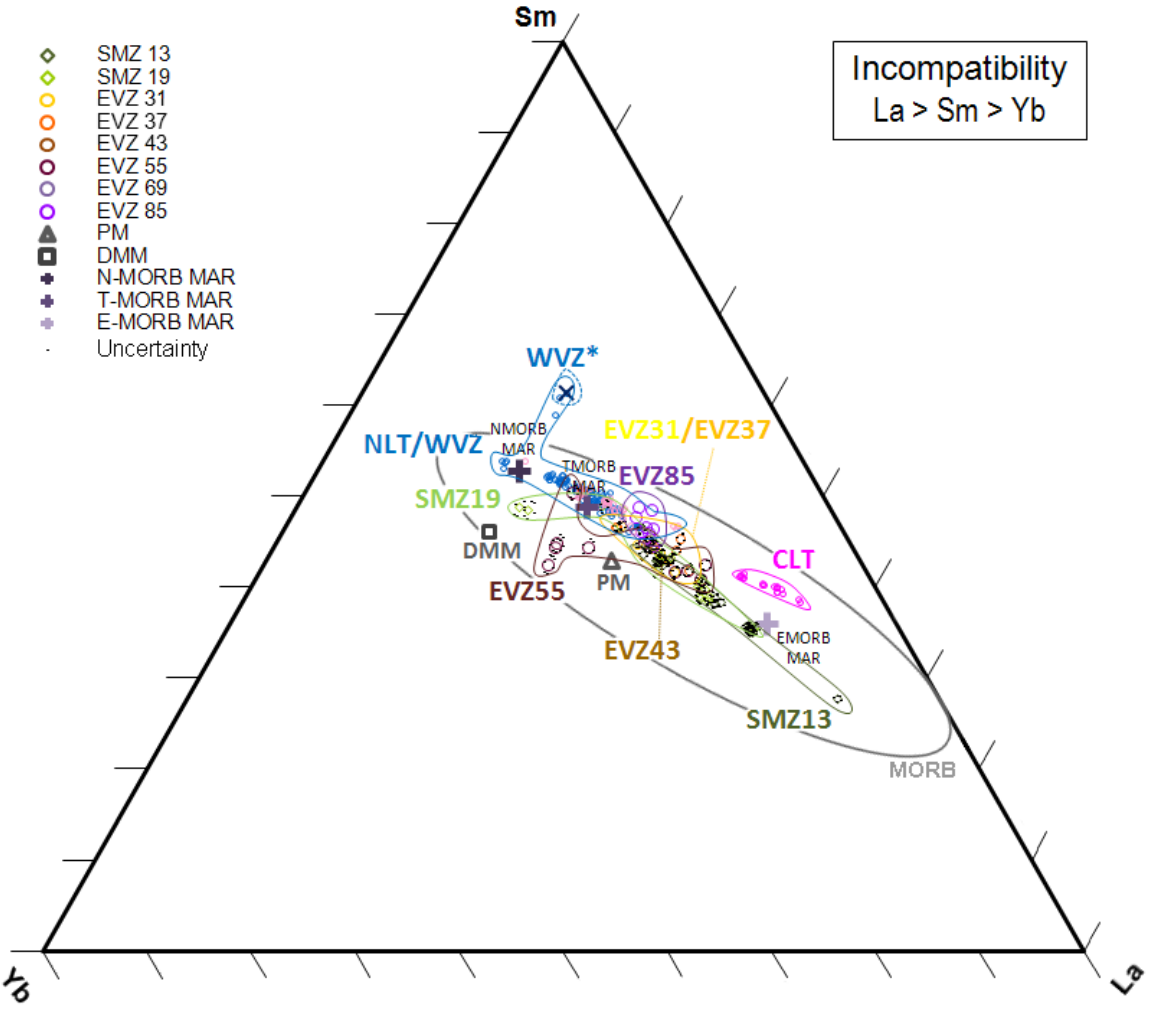

Figure 12c. YSL ternary plot showing relative Yb (ppm), Sm (ppm x 2), & La (ppm) concentrations in Gakkel Ridge and Lena Trough basalt glasses. Uncertainty polygons are shown as black dots surrounding the sample points analyzed in this study. The global MORB array is encircled in gray. Sample 297-2 from EVZ55 and its uncertainty points (from the YSL ternary plot) are shown in the legend to represent a typical analytical uncertainty for Gakkel samples. Data are from the same references as those in Figure 12a.

Figure 12 shows trends in the Arctic Basin basalt composition data when plotted onto ternary diagrams. The data appear split into two separately trending data arrays. One array contains WVZ, NLT, and CLT data, while the other array contains SMZ, EVZ, and most of the global MORB data. WVZ*'s plotting position makes it seem like it may be

the depleted endmember of the data array trending between WVZ-CLT, while CLT appears to be its enriched endmember. WVZ* is distinguished from WVZ samples by their characteristic depletion in certain trace elements (Goldstein et al., 2008). SMZ and EVZ data, instead of trending towards the unusual CLT composition, appear to plot more in line with the general depleted-to-enriched trend of most global MORBs.

6) DISCUSSION

In this study, trace element concentrations were measured in Gakkel Ridge basalt glass samples to determine the number of source components in the mantle along Gakkel Ridge and the nature of those components. To accomplish this, major element and trace element concentrations were measured in basalt glass samples recovered from the SMZ13, SMZ19, EVZ31, EVZ37, EVZ43, and EVZ55 volcanic centers. The newly acquired major and trace element concentration data were combined with previously published Gakkel Ridge major and trace element concentration data (Michael et al., 2003; Goldstein et al., 2008; Shaw et al., 2010) and plotted on ternary plots (Fig. 12) to compare relative differences between sets of trace elements. Interpretations regarding the nature of the mantle source components along Gakkel Ridge were made based on these diagrams.

6.1) Enriched component reservoirs

On the ternary plots produced for this study, basalt sample trace element composition data points that plot within each other's fields of uncertainty are likely to have formed from the identical magma compositions. However, samples that do not plot

within uncertainty of each other must have cooled from magmas with different compositions. If these basalts plot as an array between two endpoints, then it's likely an indication that those basalts are the products of mixing between two endmember source component compositions. The chemical compositions of those endmember components can be interpreted to resemble the compositions represented at the endpoints of the two-component mixing lines. Such interpretations can be made for basalt samples from ultraslow spreading ridges such as Gakkel Ridge or Lena Trough, because ultraslow spreading rates can minimize the extent of the fractional crystallization process.

The most significant mineral phase to crystallize at such low degrees of crystallization is olivine, which is a mineral into which many trace elements are extremely incompatible, so the trace element composition of the magma changes very little as it crystallizes (Fig. 4a-4b). Crystallization of additional phases, such as clinopyroxene (Fig. 4c-4d), generate more significant changes in magma trace element compositions than during olivine crystallization (Fig. 4). But at ultraslow spreading ridges, the extent to which these other phases can crystallize would be insignificant (Walker, 1979; Stolper, 1980), so their effects on magma compositions are negligible. The minimal crustal thickness associated with ultraslow spreading, such as at Gakkel Ridge, where the crust is especially thin (Jokat et al., 2003), further implies that clinopyroxene crystallization would be irrelevant at Gakkel Ridge. Also, it's notable that even at the calculated 50% crystallization of clinopyroxene (Fig. 4c-4d), the effect on the diagram is still close to analytical uncertainty. As a consequence of all these factors, MORB samples from ultraslow spreading ridges, including Gakkel Ridge and Lena

Trough, and the magma compositions corresponding to those basalt compositions end up plotting nearly identically on trace element ternary plots, as demonstrated by Figure 4.

6.1.1) Enriched reservoirs: size & distribution

The uncertainty of the data points plotted on the trace element concentration ternary plots were calculated by adding and subtracting the calculated standard deviations for each trace element concentration measurement plotted on each ternary plot, forming six-sided uncertainty polygons surrounding each plotted data point (Fig. 13). The uncertainties of the elements of the YSL ternary plot were all calculated from the standard deviations of the analyses of those elements from the analyses of the basalt standard BIR-1.

Uncertainty polygons are shown for samples of the SMZ13 (Fig. 13a), SMZ19 (Fig. 13b), EVZ31, EVZ37, EVZ43 (Fig. 13c), and EVZ55 (Fig. 13d) volcanic centers on YSL ternary plots. The size of the uncertainty polygons correlate with the level of precision associated with the trace element concentration measurements for each basalt sample data point. Smaller uncertainty polygons (e.g., sample 199-1-2, Fig. 10) represent less uncertainty and greater precision, while larger uncertainty polygons (e.g., sample 252-1, Fig. 10) represent more uncertainty and less precision.

Basalt samples, recovered from a distance spanning 97 kilometers along Gakkel Ridge across three volcanic centers EVZ31, EVZ37, and EVZ43, all plot relatively close to each other, with many points plotting within each other's uncertainty polygons on the YSL ternary plot (Fig. 13c). In contrast, basalt samples, recovered from the SMZ13 (Fig. 13a), SMZ19 (Fig. 13b), and EVZ55 (Fig. 13d) volcanic centers, plot relatively far apart

from each other on the YSL ternary plot, with many samples plotting outside of each other's uncertainty polygons. The large amount of trace element variations within the SMZ13, SMZ19, and EVZ55 volcanic centers, with many samples plotting outside of each other's uncertainty fields (Fig. 13a; Fig. 13b; Fig. 13d), indicate a relatively large degree of variation in the size and distribution of the enriched reservoirs in the mantle beneath each of these volcanic centers. These enriched heterogeneities must be at least small enough and distributed widely enough to produce significant trace element variations between individual sample dredging stations.

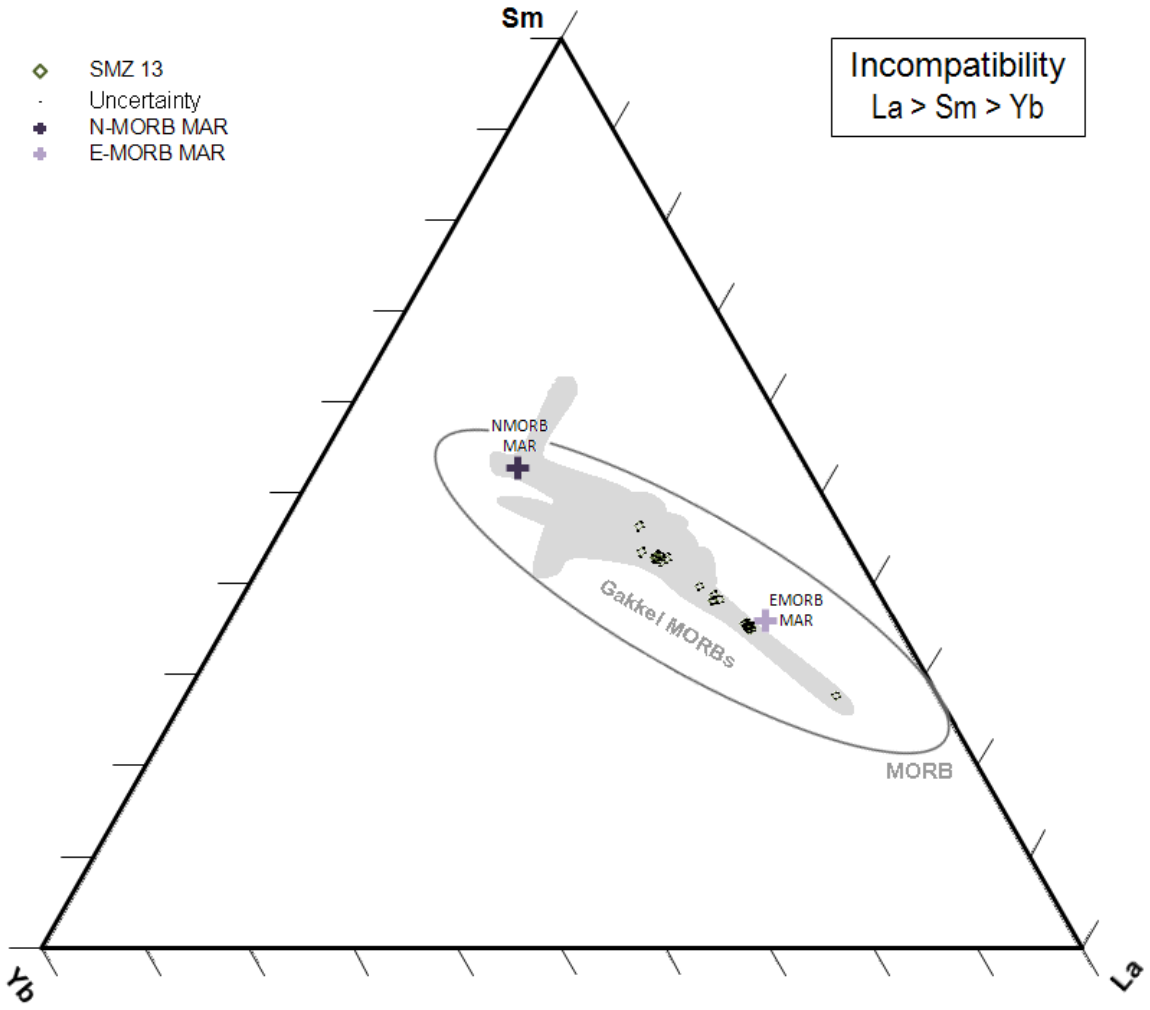

Figure 13a. Uncertainty polygons surrounding the data points of SMZ13 basalt samples plotted on an NKL ternary plot comparing Na_2O (wt.% x 5), K_2O (wt.% x 30), & La (ppm). The filled gray area encompasses the Gakkel Ridge data set from this study. The global MORB array, comprising data from the MAR, EPR, SWIR, & SEIR, (PetDB; Lehnert et al., 2000) is encircled in gray. Average N-MORB and E-MORB are calculated from basalt glass data from PetDB (Lehnert et al., 2000). Data are from this study and earlier studies (Michael et al., 2003; Goldstein et al., 2008). SMZ13 samples are recovered from a span of 33 kilometers along the ridge (Fig. 7).

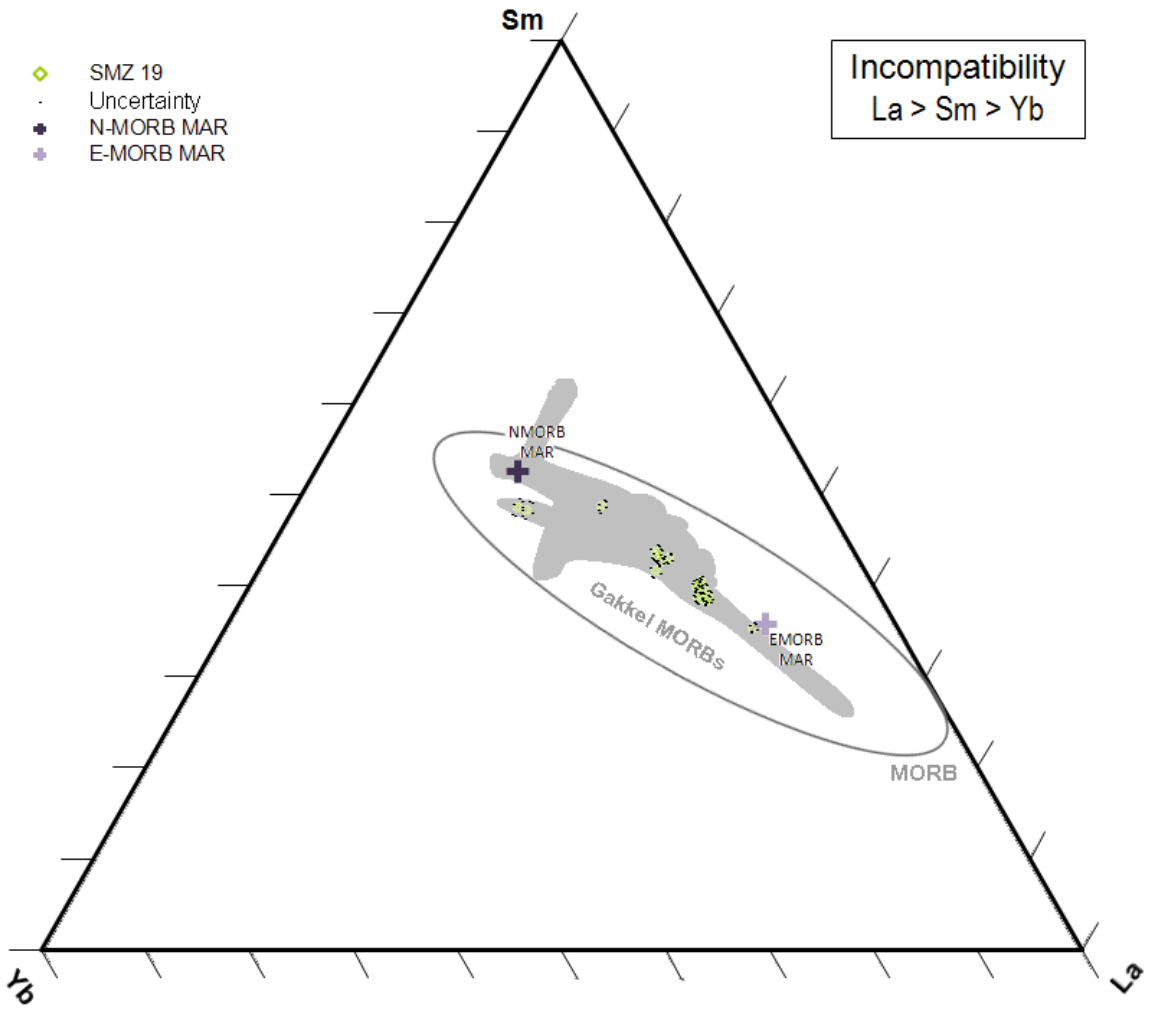

Figure 13b. Uncertainty polygons surrounding the data points of NKL ternary plot comparing Na_2O (wt.% x 5), K_2O (wt.% x 30), & La (ppm). The filled gray area encompasses the Gakkel Ridge data set from this study. The global MORB array is encircled in gray. Data are from the same references as those in Figure 13a. SMZ19 samples are recovered from a span of 87 kilometers along the ridge (Fig. 7).

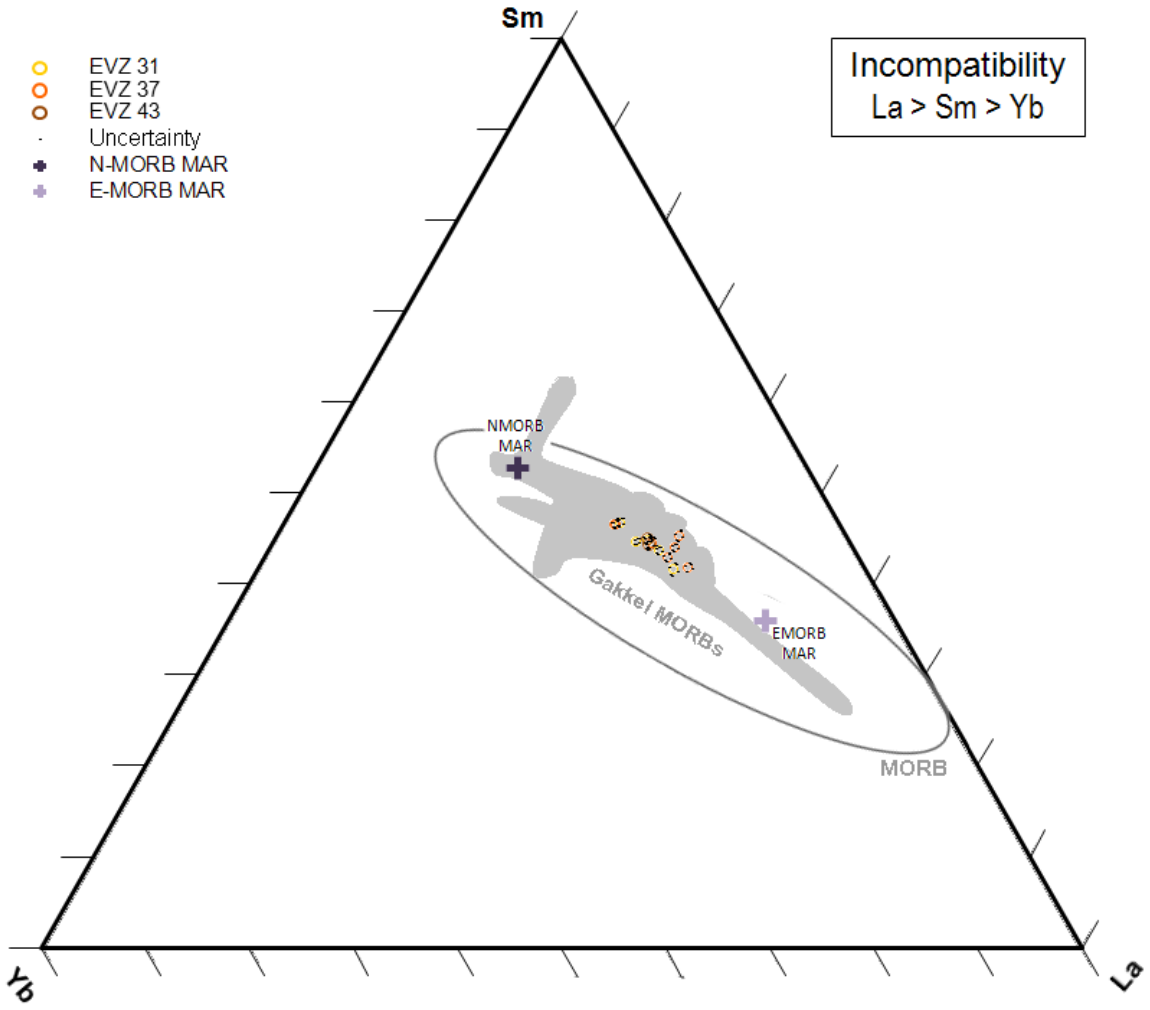

Figure 13c. Uncertainty polygons surrounding the data points of EVZ31, EVZ37, and EVZ43 basalt samples plotted a NKL ternary plot comparing Na_2O (wt.% x 5), K_2O (wt.% x 30), & La (ppm). The filled gray area encompasses the Gakkel Ridge data set from this study. The global MORB array is encircled in gray. Data are from the same references as those in Figure 13a. EVZ31, EV37, and EVZ43 basalts were all recovered from a distance spanning 97 kilometers.

The EVZ31, EVZ37, and EVZ43 basalt samples, despite spanning a relatively long distance of 97 kilometers along Gakkel Ridge, all plot relatively closer together, with several samples plotting within range of each other's uncertainties (Fig. 13c). Such a signature shows that the magmatic mixing behavior along the entire length across the

EVZ31, EVZ37, and EVZ43 volcanic centers is relatively consistent. This may be interpreted to indicate that there is relatively limited variation in the size and distribution of the enriched reservoirs along this length of Gakkel Ridge.

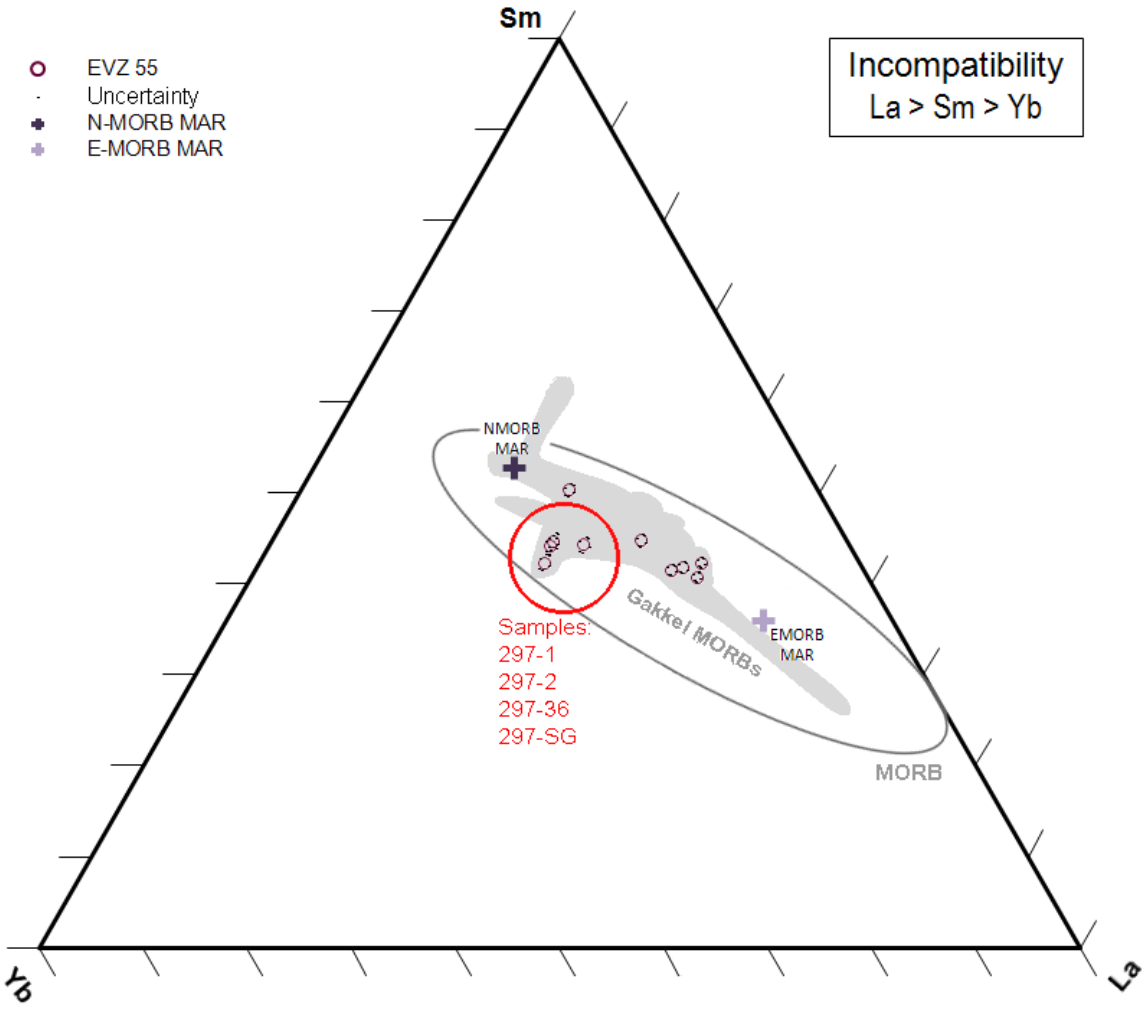

Figure 13d. Uncertainty polygons surrounding the data points of EVZ55 basalt samples plotted on a YSL ternary plot comparing La (ppm), Sm (ppm x 2), and Yb (ppm). Samples from dredging station 297 (AMORE 2001) are circled in red The filled gray area encompasses the Gakkel Ridge data set from this study. The global MORB array is encircled in gray. Data are from the same references as those in Figure 13a. EVZ55 samples are recovered from a span of 74 kilometers along the ridge (Fig. 7).

The plotted trace element signature in basalts from EVZ55 does not simply follow one mixing line from one depleted point to one enriched point, but instead, features samples plotting along at least two different trajectories (Fig. 13d). Such a pattern can only be produced by mixing between at least three distinct source component compositions. This means that in addition to the enriched component resembling MAR E-MORB, at least one other enriched component must exist along Gakkel Ridge.

Two of the components present along the SMZ and EVZ magmatic zones of Gakkel Ridge are the DMM component and an enriched component resembling MAR E-MORB. The third component is distinct in its trace element chemistry from both the DMM and MAR E-MORB-like components and cannot be produced by magmatic mixing between melts derived from those two components, because its composition does not plot anywhere in between those two components. This is indicated most clearly by the chemical signature of the basalts of the EVZ55 volcanic center, which display on the ternary plots a trace element pattern that can only be produced by at least three different source component compositions, because the plotted samples do not follow a single trajectory between two endpoints, but instead appear to plot along at least two different trajectories (Fig. 13d). The influence of the third component is exemplified by samples 297-1, 297-2, 297-36, and 297-SG (circled in red in Fig. 13d), all of which were dredged from station 297, which is located at the western end of the volcanic center EVZ55 (Fig. 8).

6.1.2) Enriched component: origin

As a result of the limited effect of melt differentiation processes on melt compositions (Fig. 4), basalt compositions and their respective mantle melting source component reservoir compositions should plot so that they overlap each other and should be nearly indistinguishable from each other on trace element composition ternary plots (Fig. 3; Fig. 5; Fig. 12). This means that basalt compositions plotted on trace element concentration ternary plots are representative of both the basalt composition and the magma from which that basalt was derived. Knowing this, two-component mixing lines can be drawn on the ternary plots and mantle endmember source component compositions can be determined. The origins of those enriched components can then be interpreted.

Two-component mixing lines were calculated and plotted on the TKL ternary plot (Fig. 14). CLT, NLT, and WVZ data plot along a mixing line between DMM and CLT. The SMZ and EVZ data array plots along a mixing line between DMM and average MAR E-MORB (Fig. 14c). The SMZ and EVZ trace element concentration data array plots closer to the mixing line between DMM and EM1 (Fig. 14b) than the mixing line between DMM and EM2 (Fig. 14a).

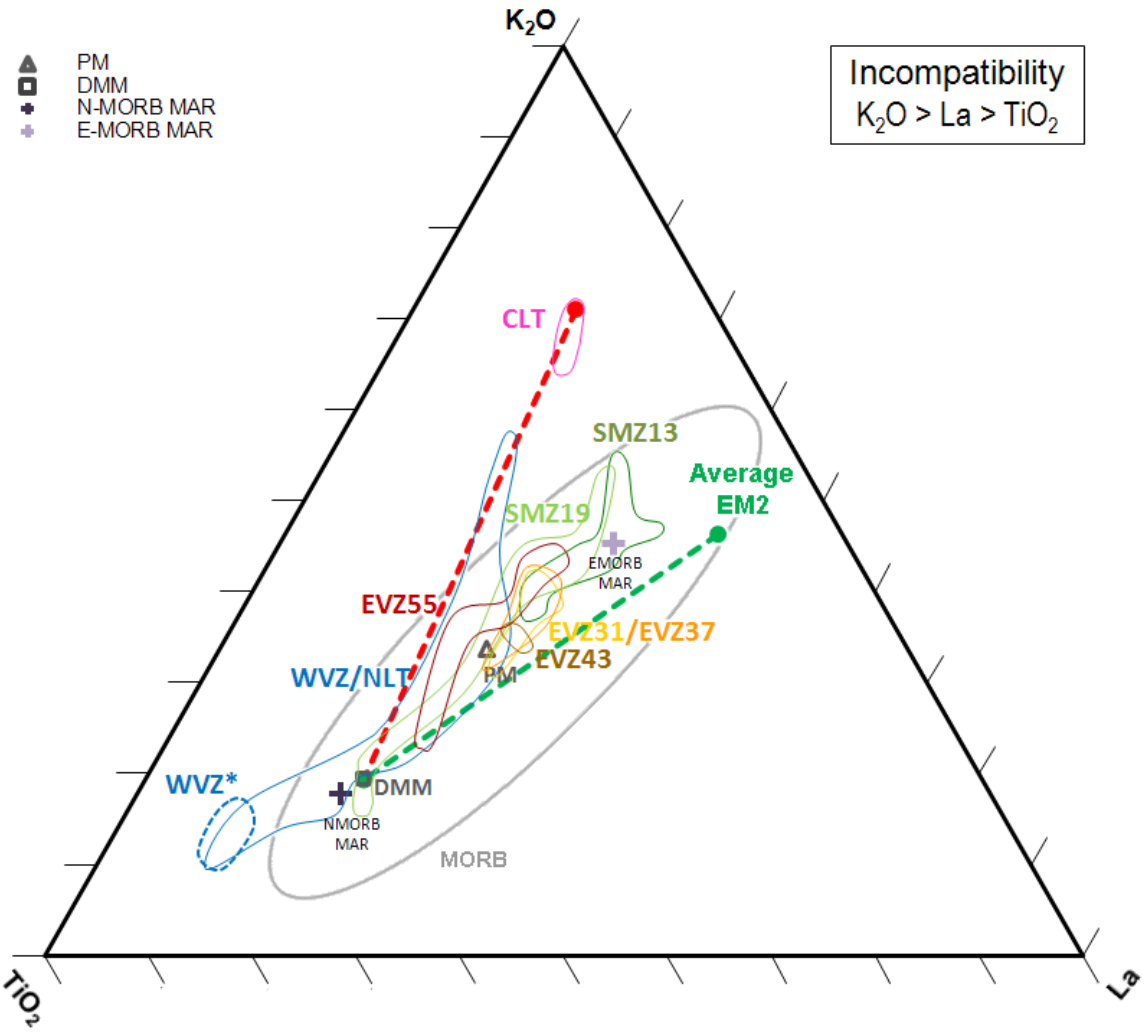

Figure 14a. TKL ternary plot, showing La (ppm), K_2O (wt.% x 30), & TiO_2 (wt.% x 5), displaying a mixing line, colored red, between DMM (Salters & Stracke, 2004) and the extreme-K_2O CLT sample (Nauret et al., 2011) and a separate mixing line, colored green, between the DMM and the averaged EM2 composition, calculated by combining EM2 OIB whole rock and glass concentration data from the Samoa and Societies islands (EM2 data are compiled from GEOROC (Lehnert et al., 2000)). Average N-MORB and E-MORB are calculated from basalt glass data from PetDB (Lehnert et al., 2000). The global MORB array, comprising data from the MAR, EPR, SWIR, & SEIR, (PetDB; Lehnert et al., 2000) is encircled in gray.

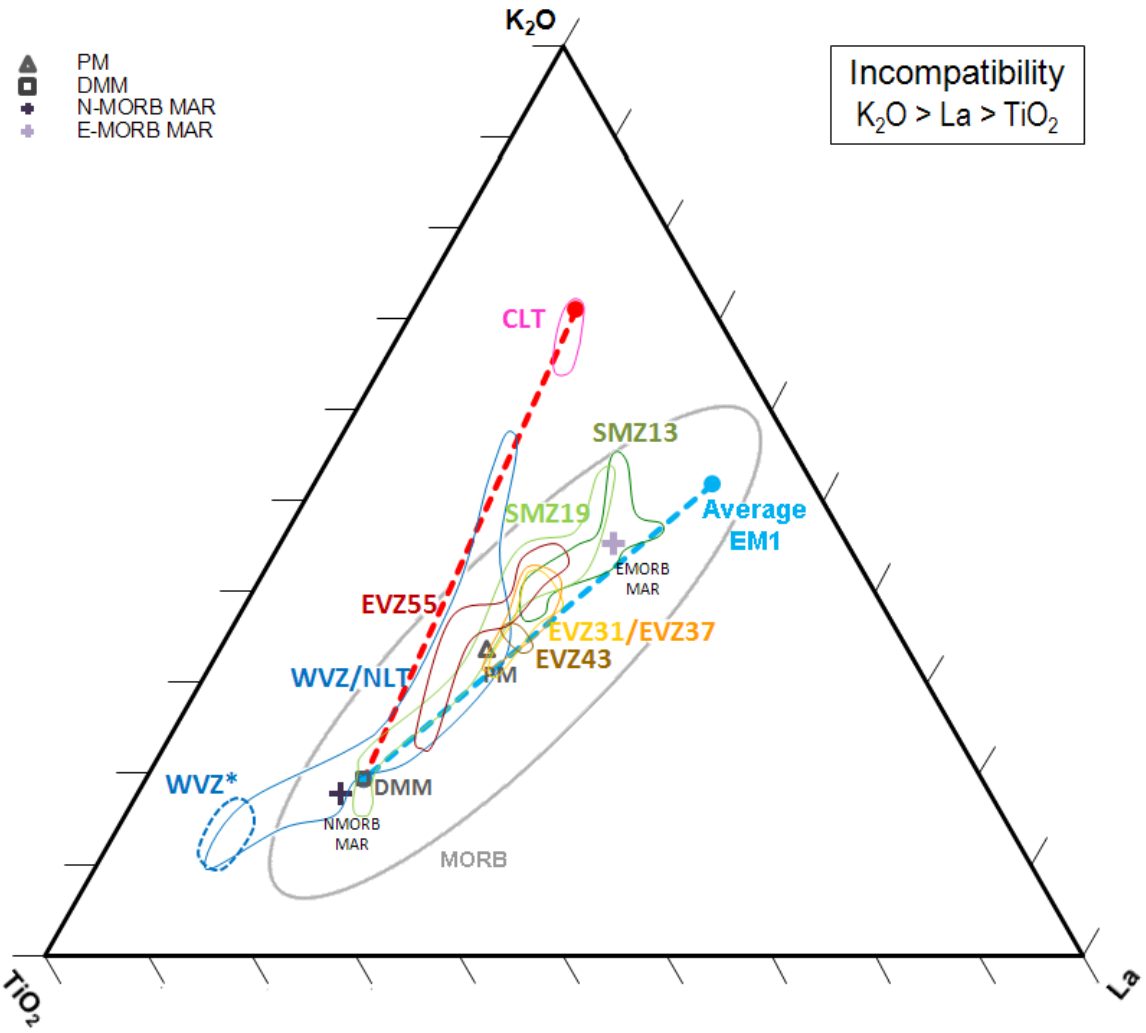

Figure 14b. TKL ternary plot showing La (ppm), K_2O (wt.% x 30), & TiO_2 (wt.% x 5), displaying a mixing line, colored red, between DMM (Salters & Stracke, 2004) and the extreme-K_2O CLT sample (Nauret et al., 2011) and a separate mixing line, colored blue, between the DMM and the averaged EM1 composition, calculated by combining EM1 OIB whole rock and glass concentration data from the Austral-Cook, St. Helena, Gough, Kerguelen, Pitcairn-Gambier, Tristan da Cunha, and Walvis Ridge islands (EM1 data compiled from GEOROC (Lehnert et al., 2000)). Average N-MORB and E-MORB are calculated from basalt glass data from PetDB (Lehnert et al., 2000). The global MORB array, comprising data from the MAR, EPR, SWIR, & SEIR, (PetDB; Lehnert et al., 2000) is encircled in gray.

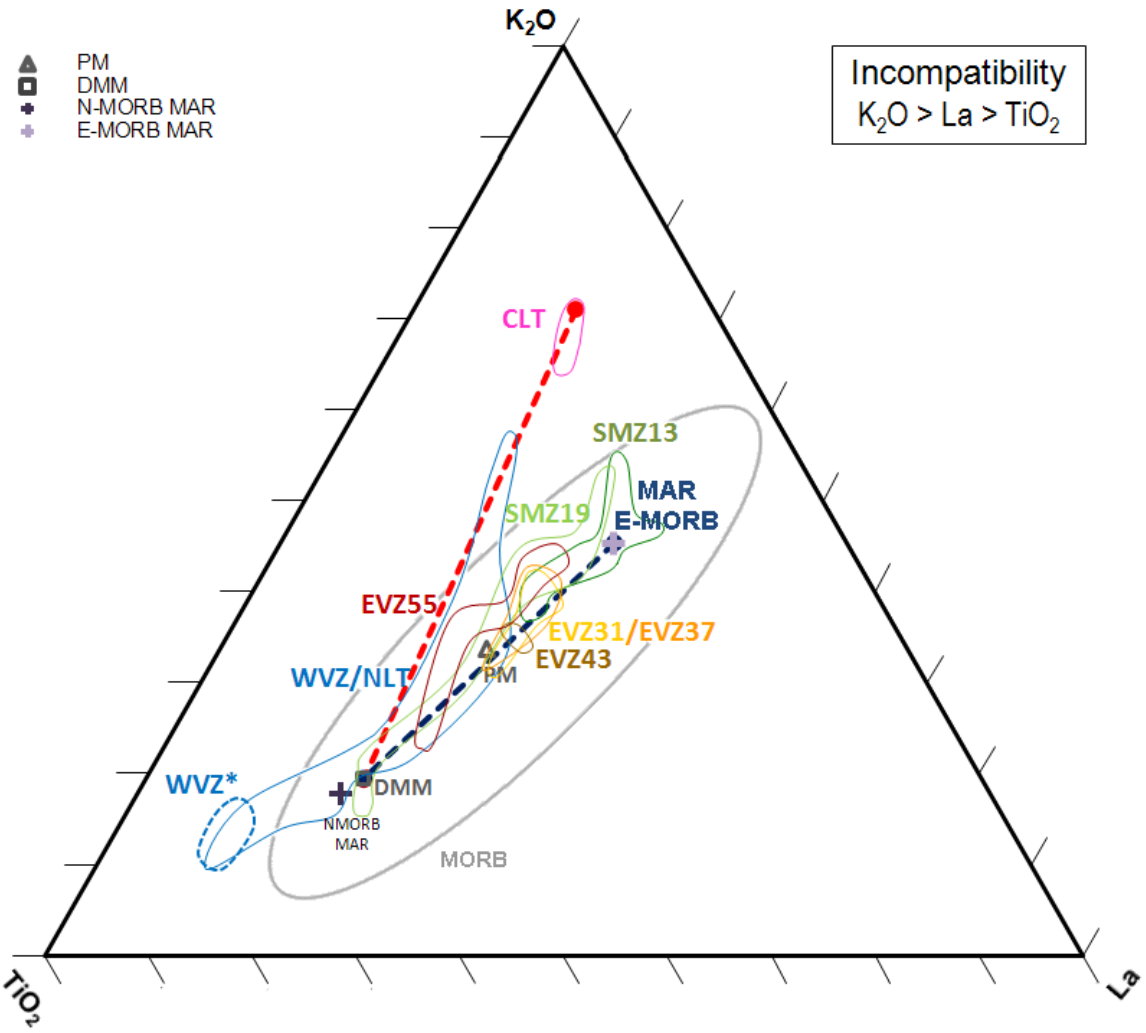

Figure 14c. TKL ternary plot showing La (ppm), K_2O (wt.% x 30), & TiO_2 (wt.% x 5), displaying a mixing line, colored red, between DMM (Salters & Stracke, 2004) and the extreme-K_2O CLT sample (Nauret et al., 2011) and a separate mixing line, colored blue, between the DMM and the averaged MAR E-MORB composition. MAR basalt glass data compiled from PetDB (Lehnert et al., 2000). MAR E-MORB is defined as all MAR MORB samples with a La/Sm ratio greater than 1.8. The global MORB array, comprising data from the MAR, EPR, SWIR, & SEIR, (PetDB; Lehnert et al., 2000) is encircled in gray.

The averaged compositions of basalts derived from the enriched OIB components, EM1, EM2, and HIMU, were compared to the enrichment in the SMZ and EVZ, because

the origins of the enriched OIB components have been thoroughly interpreted and described (Weaver 1991a; Weaver 1991b). If the enriched component in the SMZ and EVZ resemble any of the OIB enriched components, it may mean that they share the same origin. The EM2 chemical signature is said to be indicative of a continental crust component in the mantle (Weaver, 1991a; Weaver 1991b; Hofmann, 1997). The EM1 and HIMU chemical signatures are said to be indicative of recycled oceanic crust (Weaver, 1991a; Weaver 1991b). The data array on which SMZ and EVZ basalt trace element data plot, which trends between DMM and average MAR E-MORB on the trace element concentration ternary plots (Fig. 14), can be compared to the two-component mixing lines between DMM and average EM1 or between DMM and average EM2 to see whether EM1 or EM2 – thus, whether recycled oceanic crust or recycled continental crust, respectively – is the origin for the enriched component at the SMZ and EVZ. Most HIMU basalt trace element concentration data clearly plot off the trend between DMM and average MAR E-MORB (Fig. 5; Fig. 14), so a mixing line between DMM and average HIMU was not calculated and plotted. The mixing line between DMM and average MAR E-MORB (Fig. 14c) appears to be more similar in its trending direction to the mixing line between DMM and average EM1 (Fig. 14b) than the mixing line between DMM and average EM2 (Fig. 14a). This appears to suggest that recycled oceanic crust is a more likely origin for the SMZ and EVZ enriched component than recycled continental crust. This result is consistent with previous studies, which concluded that no signature of any continental mantle has been found in MORB samples of eastern Gakkel Ridge (Liu et al., 2008).

A Spitsbergen SCLM component has been suggested to be a source of enrichment influencing western Gakkel Ridge (Goldstein et al., 2008), so Spitsbergen basalts were considered to be worth examining as a possible source of enrichment in the SMZ and EVZ. The influence of the Spitsbergen SCLM component on Gakkel Ridge is visible on basalt isotope concentration plots (Fig. 10a), which show Spitsbergen basalts plotting along the same trend as Lena Trough and western Gakkel Ridge samples. However, although the Spitsbergen isotope data have been published (Ionov, 2002), the trace element data required to compare Spitsbergen samples with Gakkel Ridge samples are not available, so the Spitsbergen samples could not be included on the trace element figures in this study. The Spitsbergen SCLM being present in eastern Gakkel Ridge is unlikely, however, because according to Liu et al. (2008) no signature of any continental mantle in the mantle source of eastern Gakkel Ridge has been found.

Another enriched component considered as a possible source of enrichment for the SMZ and EVZ is the unique K-enriched CLT component, which has been described to possibly be SCLM in origin (Nauret et al., 2011). Based on the two-component mixing lines calculated for the trace element ternary plots however, the CLT component does not influence the trace element enrichment of the SMZ and EVZ, despite the CLT component being a clear influence on the trace element enrichment of the WVZ and NLT (Fig. 14). This distinction between the DMM-CLT mixing trend, on which the WVZ basalt trace element data plot, and the DMM-MAR E-MORB trend, on which the SMZ and EVZ basalt trace element data plot, is shown on Figure 14. This means that the k-enriched CLT component, which likely has a SCLM origin (Nauret et al., 2011), is not the same enriched component present in the SMZ and EVZ.

6.2) Isotopic boundary

If the isotopic boundary defined by Goldstein et al. (2008) is also reflected in trace elements, then SMZ13 samples might be expected to plot on the same mixing trend as WVZ, which trends towards CLT on trace element diagrams. However, the isotopic boundary apparently does not correlate with the observable trends seen on trace element ternary plots (Fig. 14), which show SMZ13 samples plotting along a more similar trend to SMZ19 and EVZ samples in the eastern part of Gakkel Ridge, instead of along with the WVZ and Lena Trough samples in the western part of Gakkel Ridge. There is an apparent inconsistency between the location of the isotopic boundary suggested by Goldstein et al. (2008), located in the middle of the SMZ, and the separation of the two mixing lines observable on the trace element ternary plots (Fig. 14), which occurs in between the WVZ and SMZ volcanic zones. The reason why the isotopic boundary identified by Goldstein et al. (2008) does not manifest itself in the trace element signature along Gakkel Ridge is not clear.

7) CONCLUSIONS

The following conclusions about the mantle melting source components along Gakkel Ridge were made based on analysis of the major and trace element and isotope data:

1) The enriched mantle source component in the SMZ and EVZ is similar in chemical composition to MAR E-MORB. This is suggested by the similarities in trends between the SMZ and EVZ data array on trace element composition ternary plots to the calculated two-component mixing line between DMM and average MAR E-MORB. The

enriched component in the SMZ and EVZ is chemically distinct from the CLT component, which is present as a mixing component in the NLT and WVZ, but not in the SMZ and EVZ.

2) The MAR E-MORB-like enriched mixing component in the SMZ and EVZ is not likely to be subducted continental crust in origin, because the SMZ-EVZ data array does not correlate with the two-component mixing line between the DMM and EM2 on the trace element ternary plots (Fig. 14a), which has been suggested to have a subducted continental crust origin.

3) The two-component mixing line between DMM and average EM1 is close in trend to the mixing line between DMM and average EM1. The source of enrichment for EM1 has been suggested to be recycled oceanic crust in origin, so the origin of the main enriched SMZ and EVZ component may also be recycled oceanic crust.

4) In addition to the enriched component resembling MAR E-MORB, at least one other enriched composition exists along Gakkel Ridge. This additional enriched component is most clearly identifiable from the EVZ55 trace element signature, which shows a pattern that can only be produced from melts derived at least three different endmember source compositions.

5) The level of variation in trace element enrichment between volcanic centers along Gakkel Ridge is minimal along a lengthy section of Gakkel Ridge. Samples collected from a 97 kilometer length spanning the EVZ31, EVZ37, and EVZ43 volcanic centers show relatively little trace element variation between samples, with all samples mostly plotting relatively close to each other, with many samples plotting within uncertainty of each other on the trace element concentration ternary plots. The limited

trace element variation across these volcanic centers suggests that the size and distribution of the enriched reservoirs beneath Gakkel Ridge across this entire length is relatively consistent. This results in consistent mixing behavior between enriched and depleted magmas, so that the basalts produced have relatively similar compositions along that entire length along Gakkel Ridge.

6) The trace element variation within the each of the three volcanic centers SMZ13, SMZ19, and EVZ55 is significantly greater than the minimal variation observable across the three volcanic centers EVZ31, EVZ37, and EVZ43. This is despite each of the volcanic centers SMZ13, SMZ19, and EVZ55 spanning a distance that is less than the combined distance spanned by all three of the EVZ31, EVZ37, and EVZ43 volcanic centers. The large amount of trace element variation that exists between samples from within the SMZ13, SMZ19, and EVZ55 volcanic centers suggests that the enriched reservoirs in the mantle beneath these volcanic centers are small enough and distributed with enough spacing in between them to produce significant trace element variation in mixed magmas between distances as short as the distances in between dredging stations.

8) APPENDIX

8.1) Appendix 1: XY plots

X-Y plots showing Gakkel Ridge trace element ratios plotted against magnesium oxide (MgO), magnesium number (Mg#), and longitude. Gakkel Ridge data include new data from this study, and previously published data (Michael et al., 2003; Goldstein et al., 2008). Knipovich data compiled from PetDB (Lehnert et al., 2000). Macquarie Island data (Kamenetsky et al., 2000) is included as a representative E-MORB composition. MgO, K_2O, and TiO_2 concentrations are in wt.%; Ba, Dy, Yb, La, Sm, and Nb concentrations are in ppm.

The X-Y plots are:

Fig. A1a: Ba/TiO_2 vs. MgO
Fig. A1b: Dy/Yb vs. MgO
Fig. A1c: K_2O/La vs. MgO
Fig. A1d: K_2O/TiO_2 vs. MgO
Fig. A1e: La/Sm vs. MgO
Fig. A1f: Nb/La vs. MgO

Fig. A1g: Ba/TiO_2 vs. Mg#
Fig. A1h: Dy/Yb vs. Mg#
Fig. A1i: K_2O/La vs. Mg#
Fig. A1j: K_2O/TiO_2 vs. Mg#
Fig. A1k: La/Sm vs. Mg#
Fig. A1l: Nb/La vs. Mg#

Fig. A1m: Ba/TiO_2 vs. Longitude
Fig. A1n: Dy/Yb vs. Longitude
Fig. A1o: K_2O/La vs. Longitude
Fig. A1p: K_2O/TiO_2 vs. Longitude
Fig. A1q: La/Sm vs. Longitude
Fig. A1r: Nb/La vs. Longitude

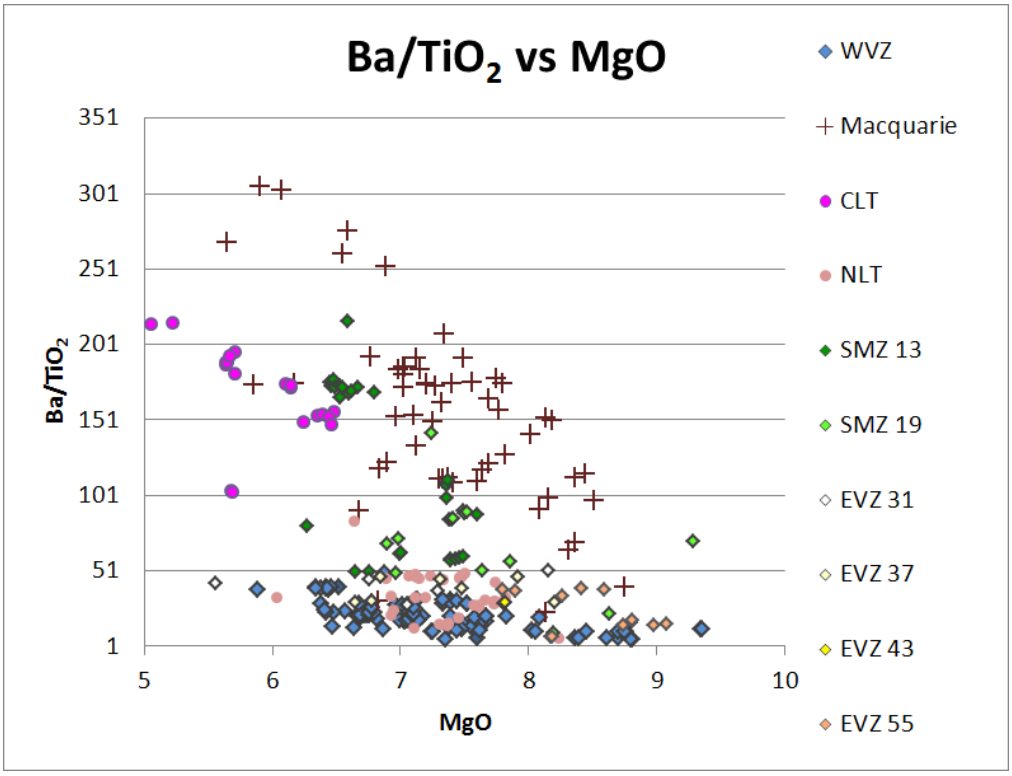

Figure A1a. Comparison of Ba/TiO_2 (ppm) to MgO (wt.%).

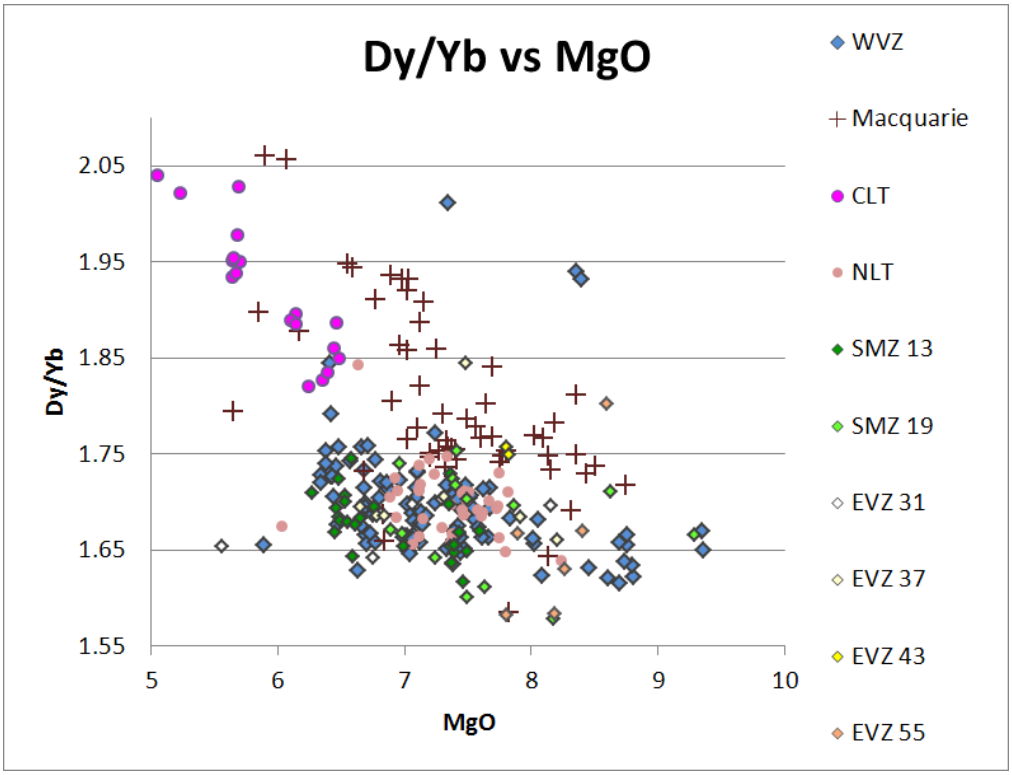

Figure A1b. Comparison of Dy/Yb (ppm) to MgO (wt.%).

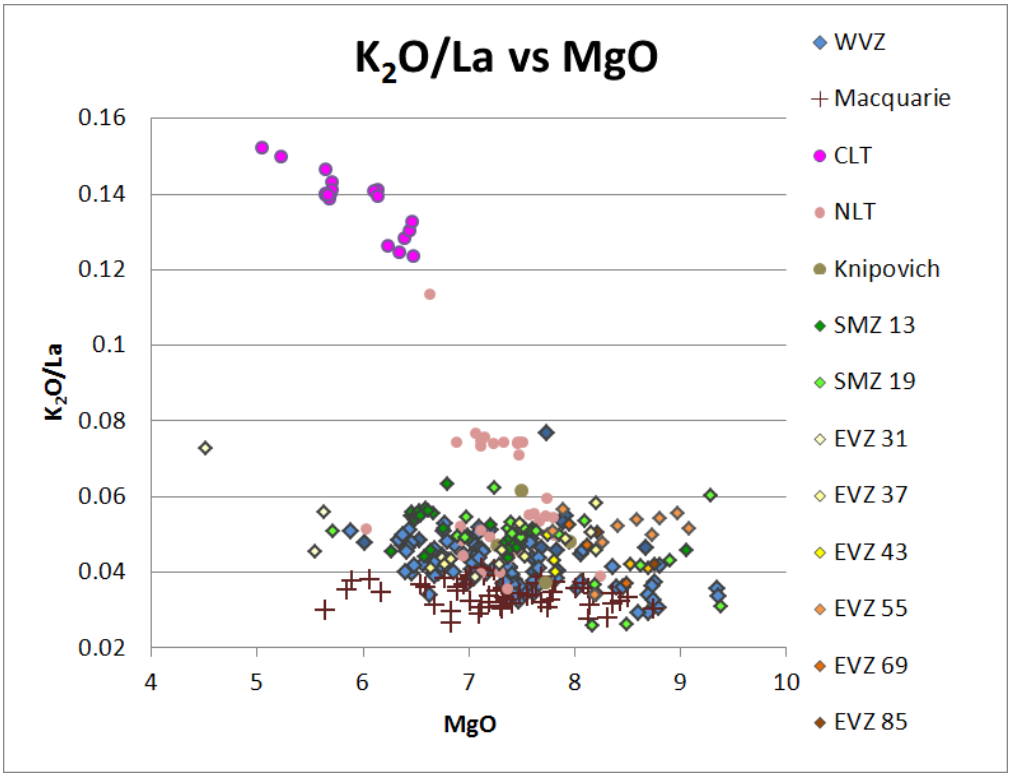

Figure A1c. Comparison of K_2O/La to MgO (wt.%). K_2O is in wt.%. La is in ppm.

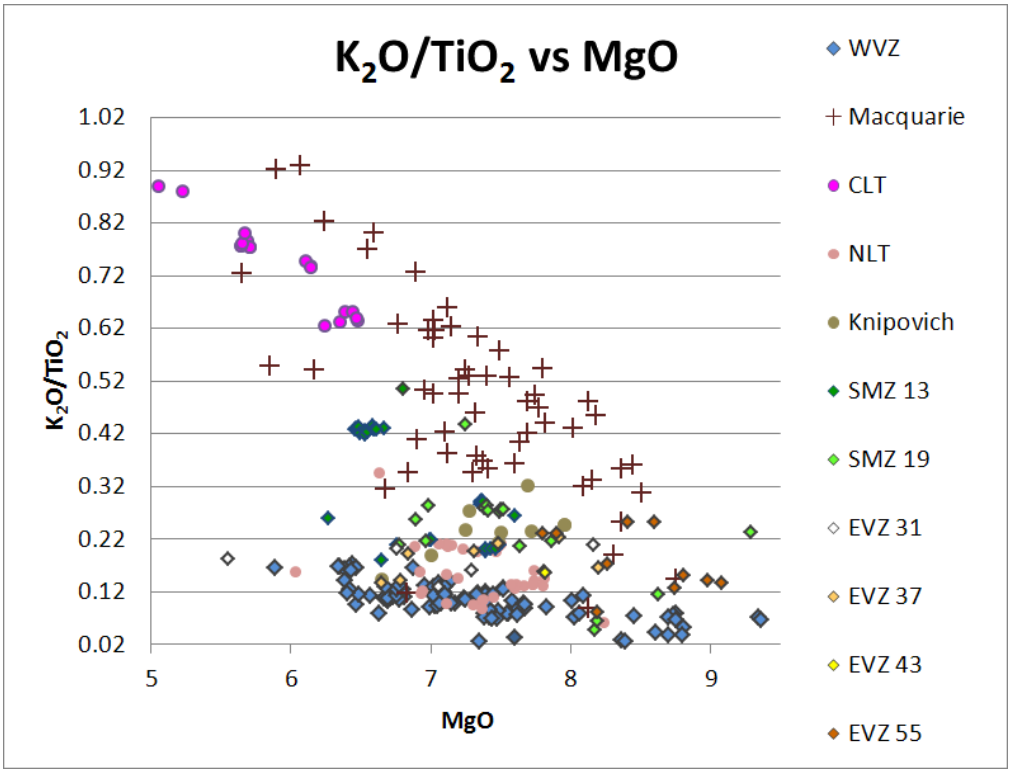

Figure A1d. Comparison of K_2O/TiO_2 (wt.%) to MgO (wt.%).

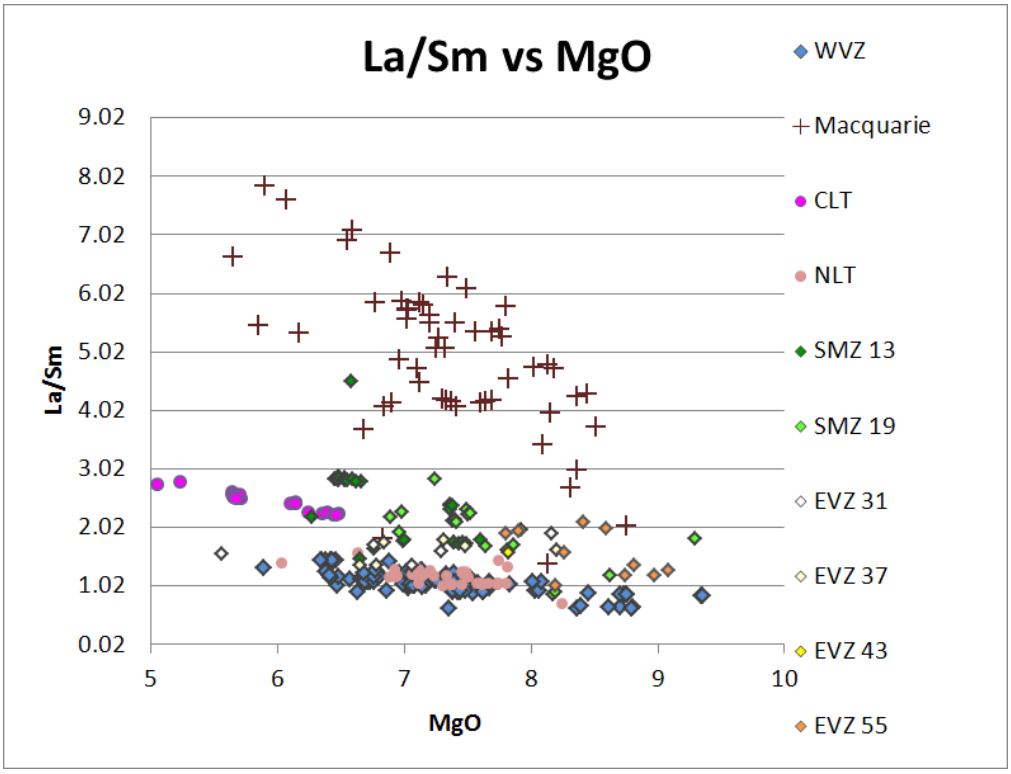

Figure A1e. Comparison of La/Sm (ppm) to MgO (wt.%).

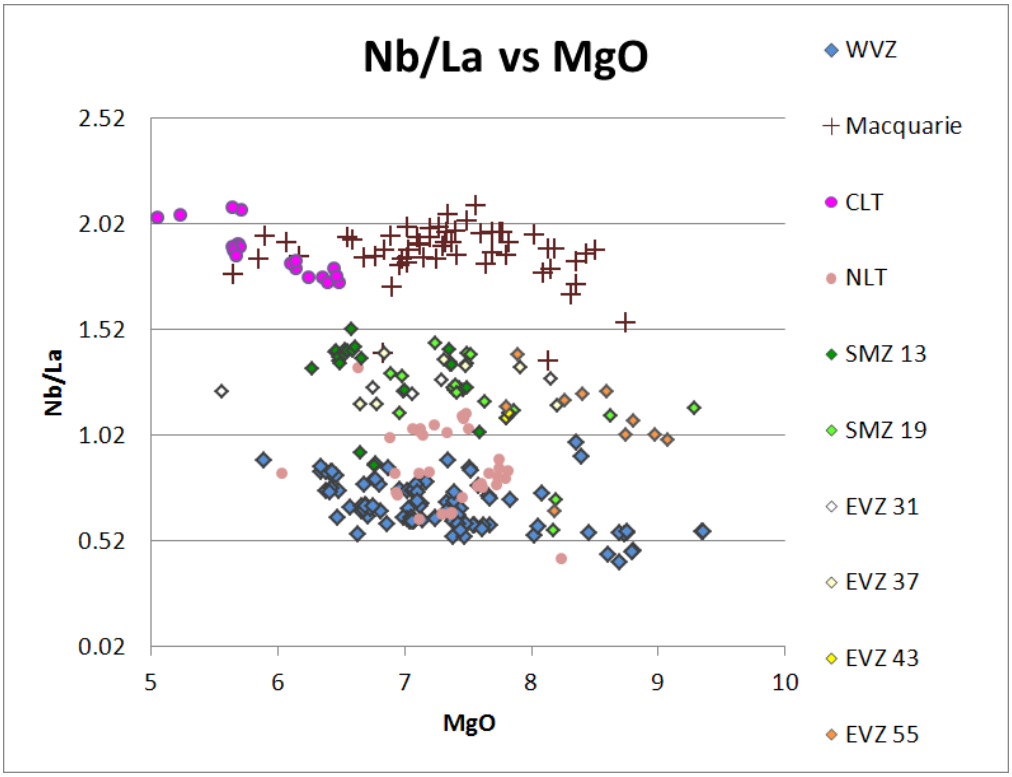

Figure A1f. Comparison of Nb/La (ppm) to MgO (wt.%).

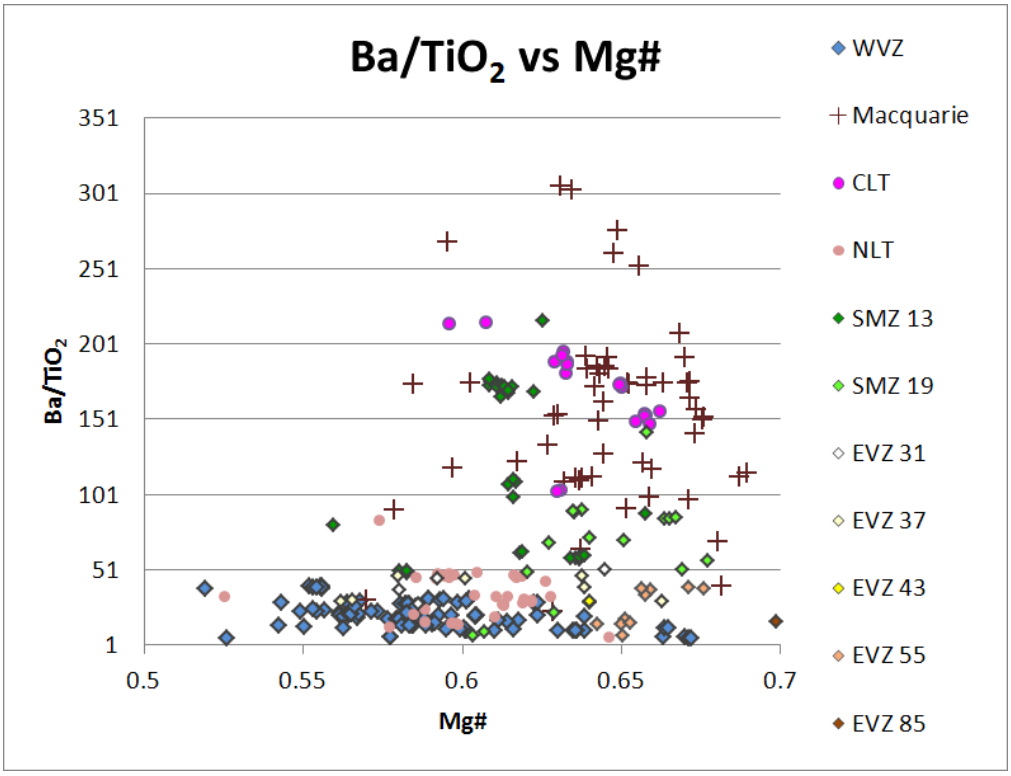

Figure A1g. Comparison of Ba/TiO_2 to MgO (wt.%). Ba is in ppm. TiO_2 is in wt.%.

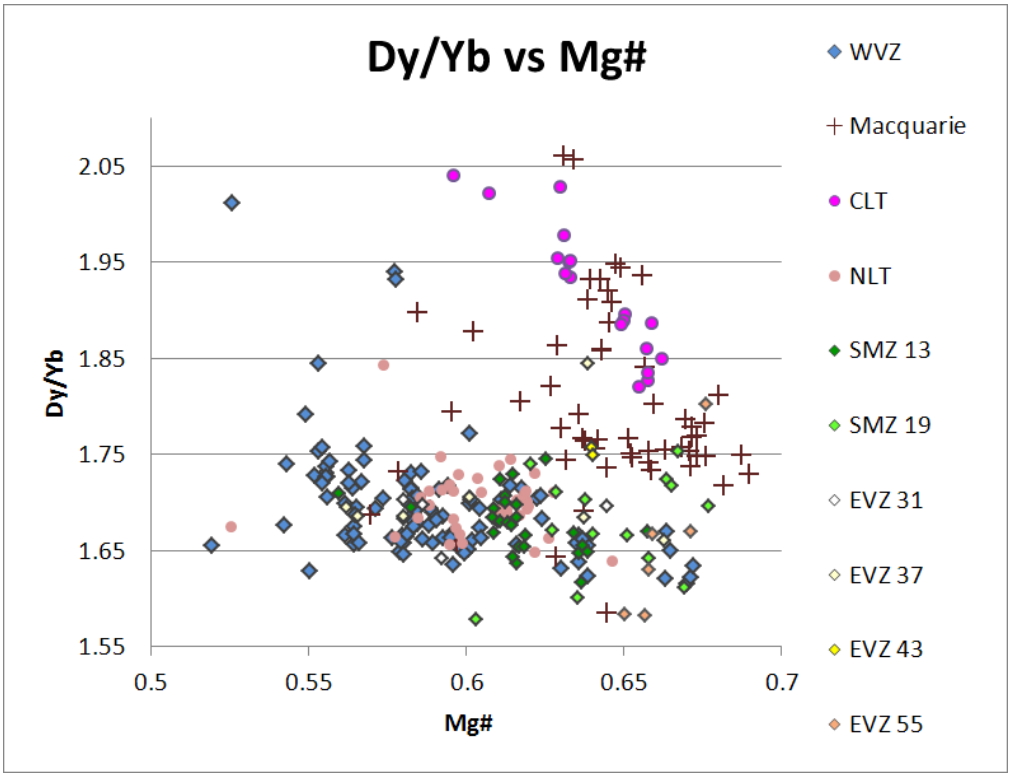

Figure A1h. Comparison of Dy/Yb (ppm) to Mg#.

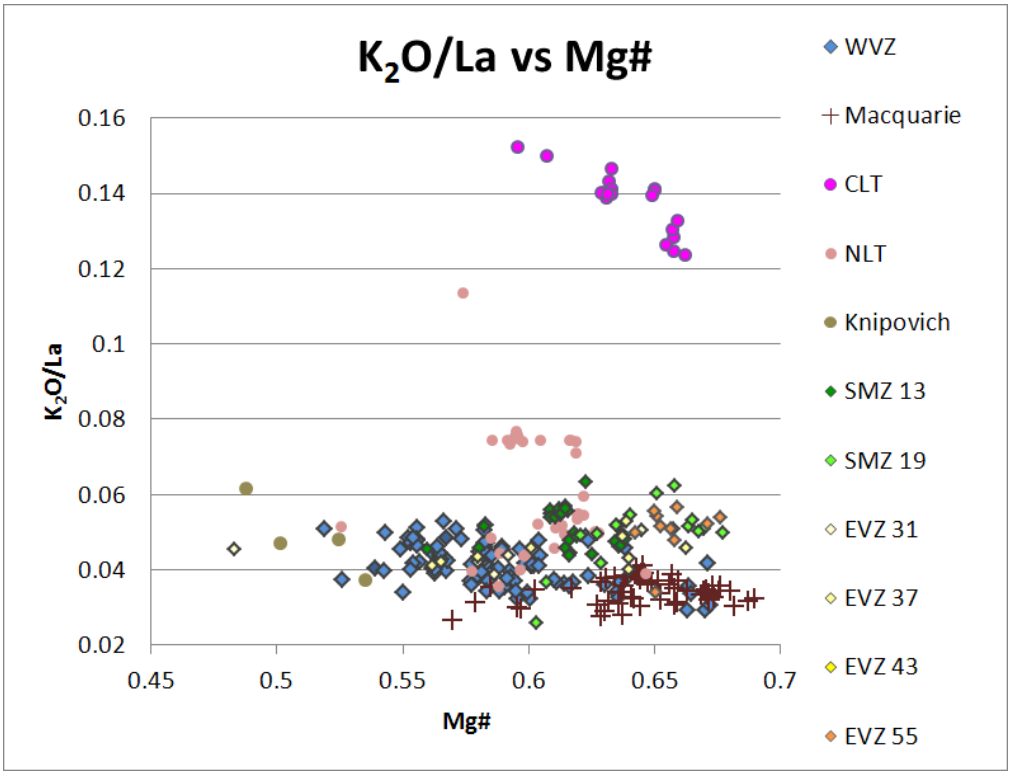

Figure A1i. Comparison of K_2O/La to Mg#. K_2O is in wt.%. La is in ppm.

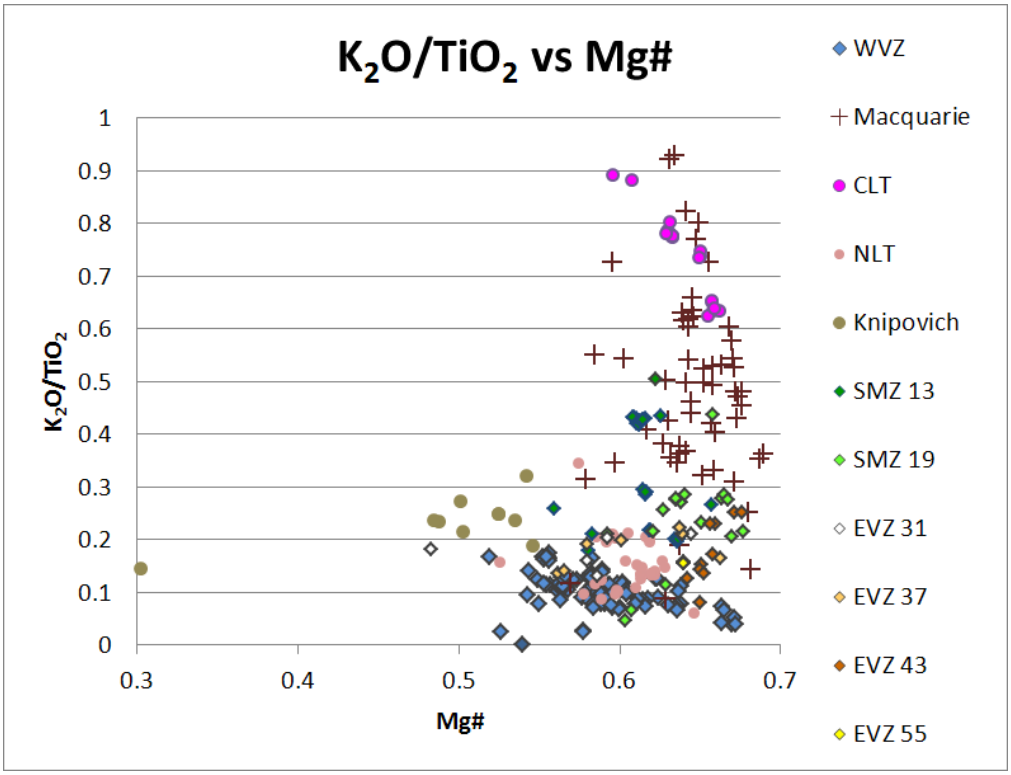

Figure A1j. Comparison of K_2O/TiO_2 (wt.%) to Mg#.

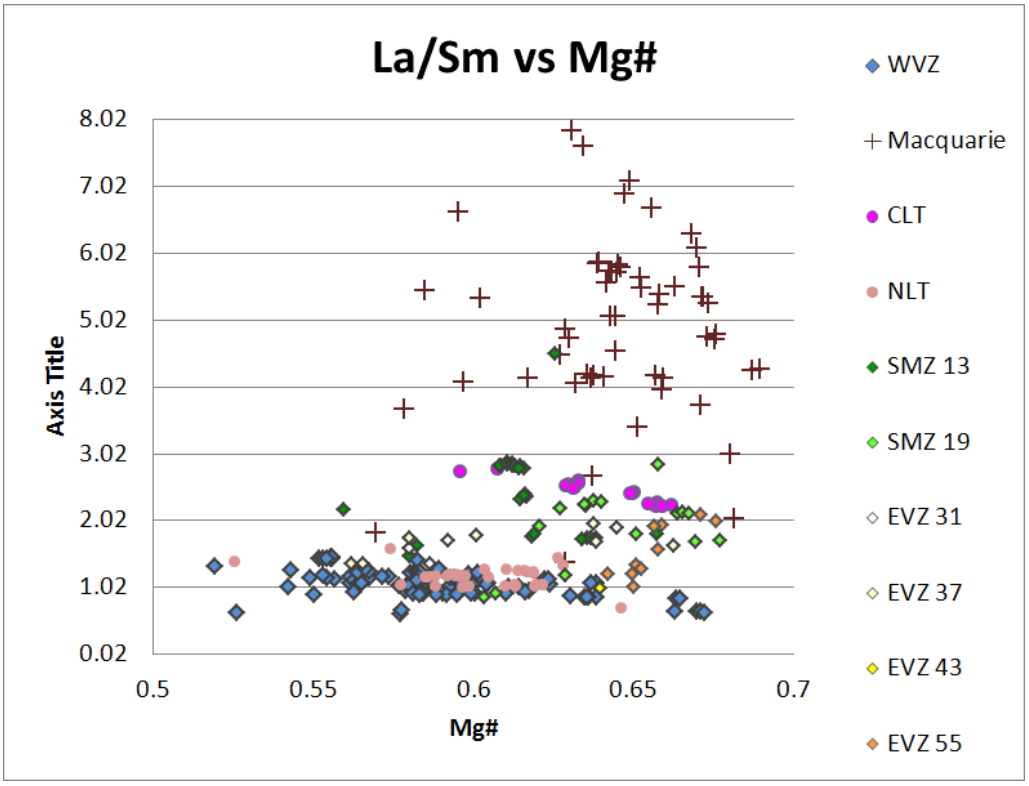

Figure A1k. Comparison of La/Sm (ppm) to Mg#.

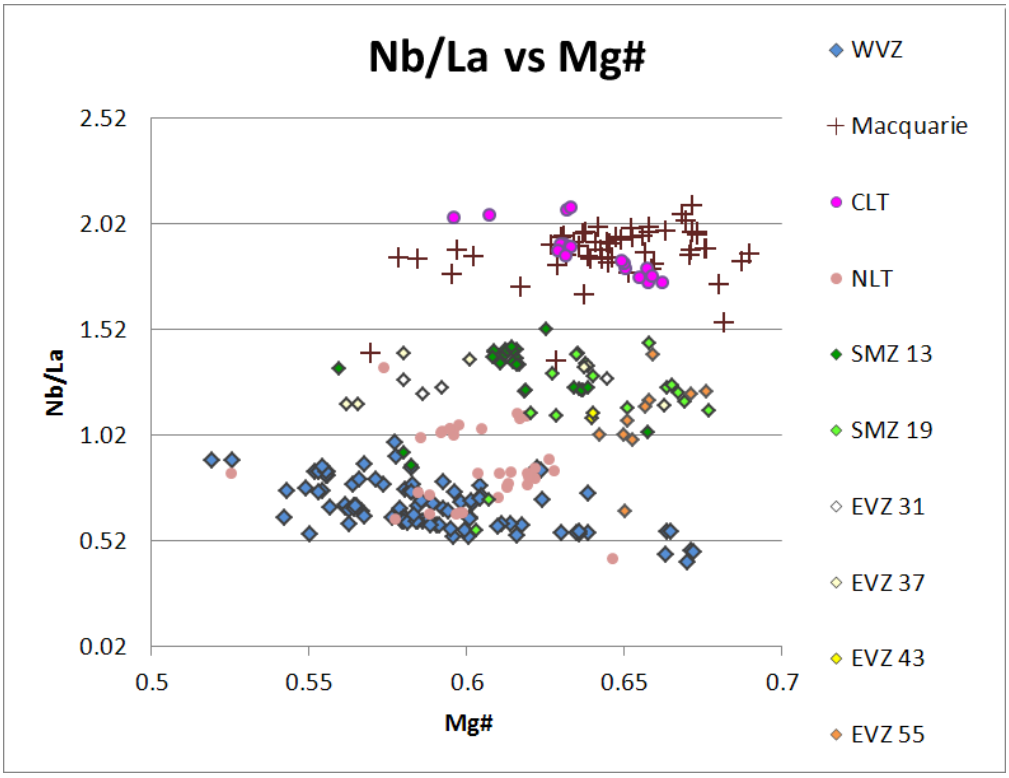

Figure A1l. Comparison of Nb/La (ppm) to Mg#.

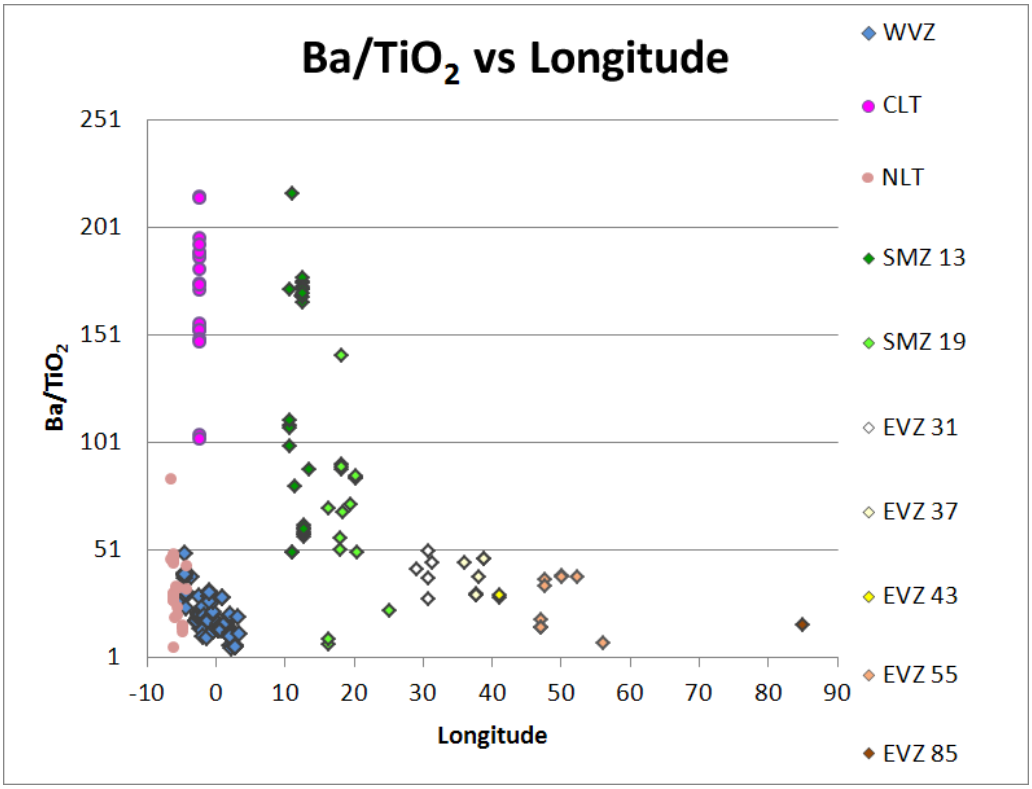

Figure A1m. Comparison of Ba/TiO_2 to longitude (°). Ba is in ppm. TiO_2 is in wt.%.

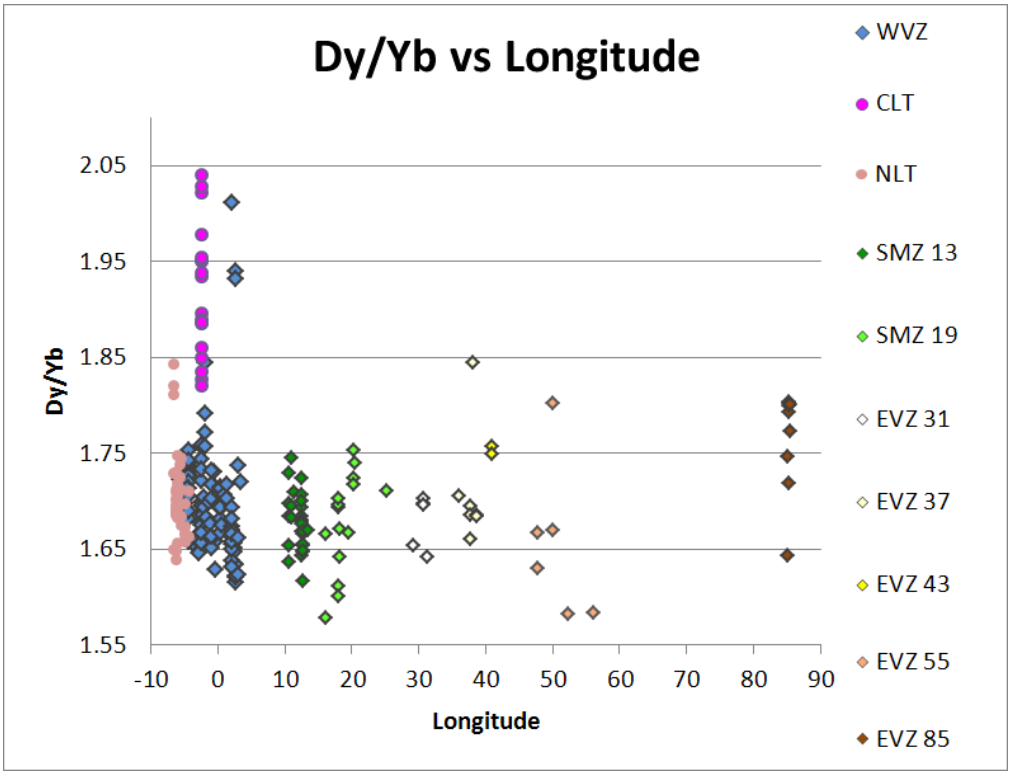

Figure A1n. Comparison of Dy/Yb (ppm) to longitude (°).

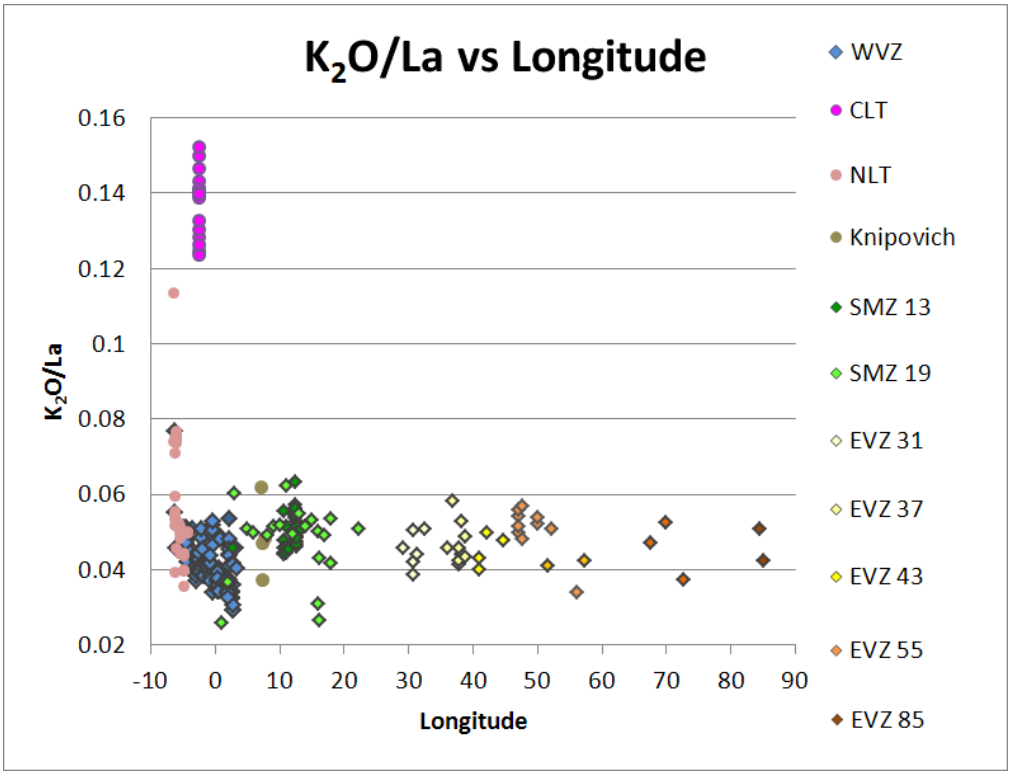

Figure A1o. Comparison of K_2O/La to longitude (°). K_2O is in wt.%. La is in ppm.

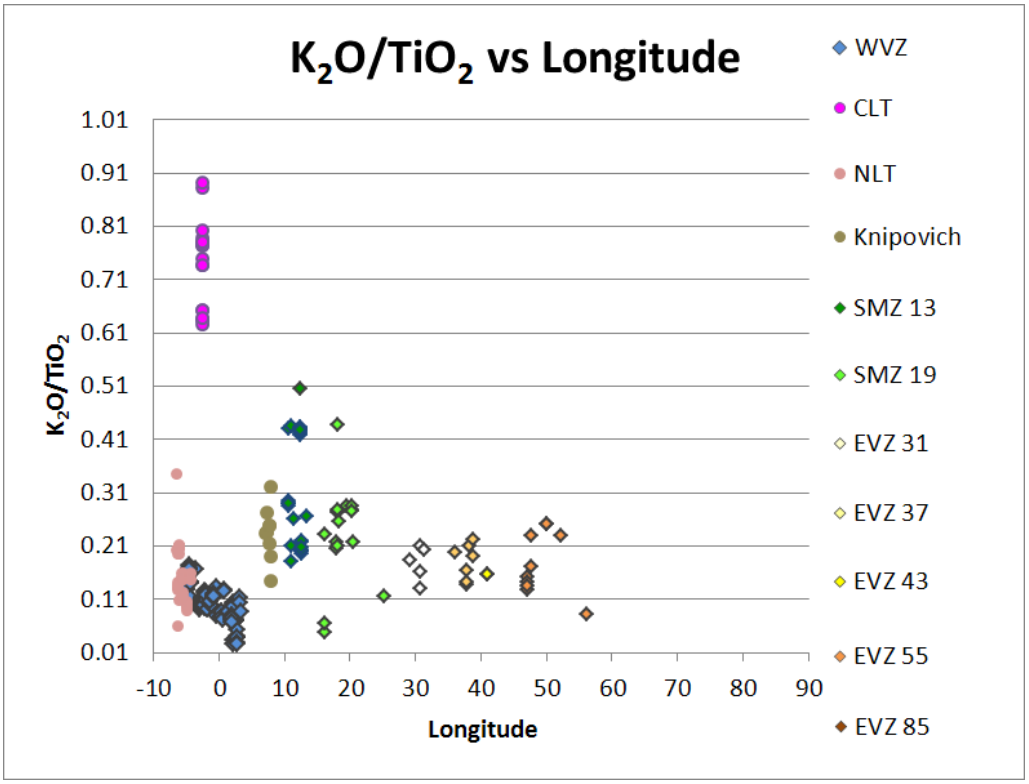

Figure A1p. Comparison of K_2O/TiO_2 (wt.%) to longitude (°).

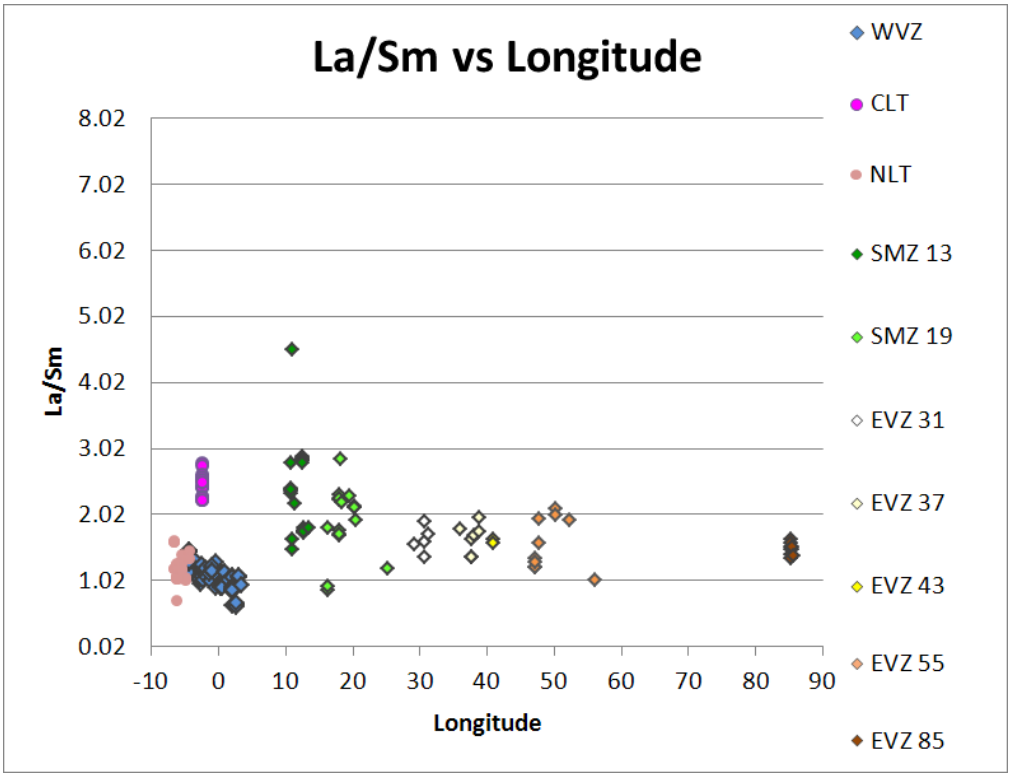

Figure A1q. Comparison of La/Sm (ppm) to longitude (°).

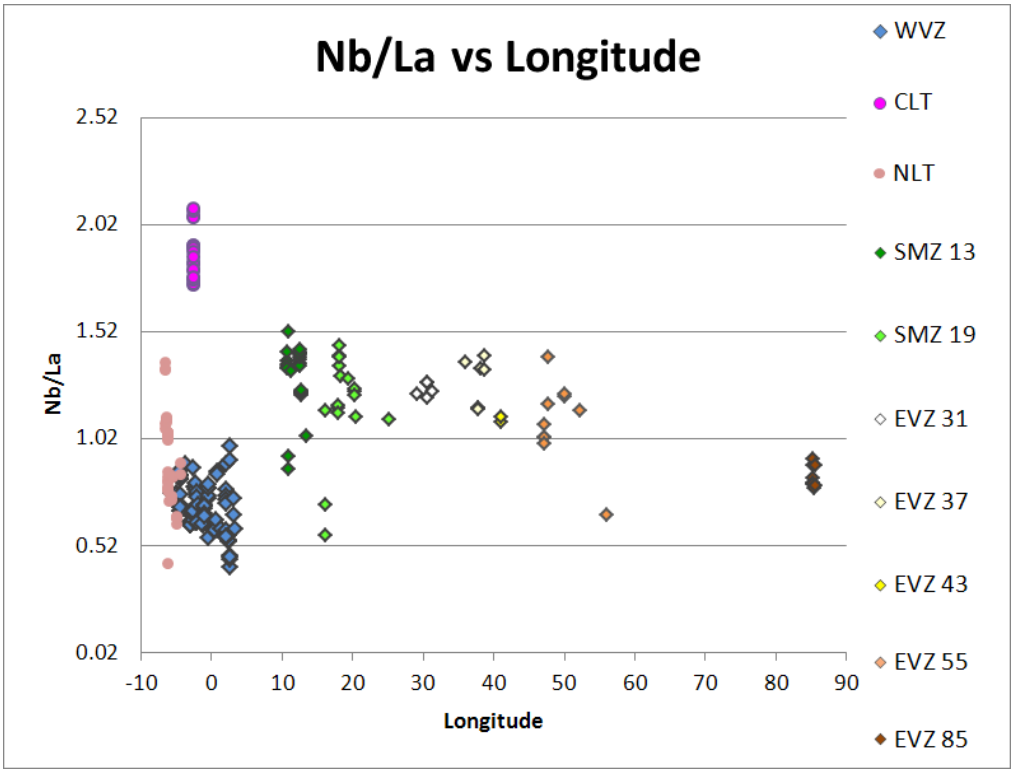

Figure A1r. Comparison of Nb/La (ppm) to longitude (°).

8.2) Appendix 2: Global MORB ternary plots

Global MORBs plotted on NKL, TKL, & YSL ternary plots.

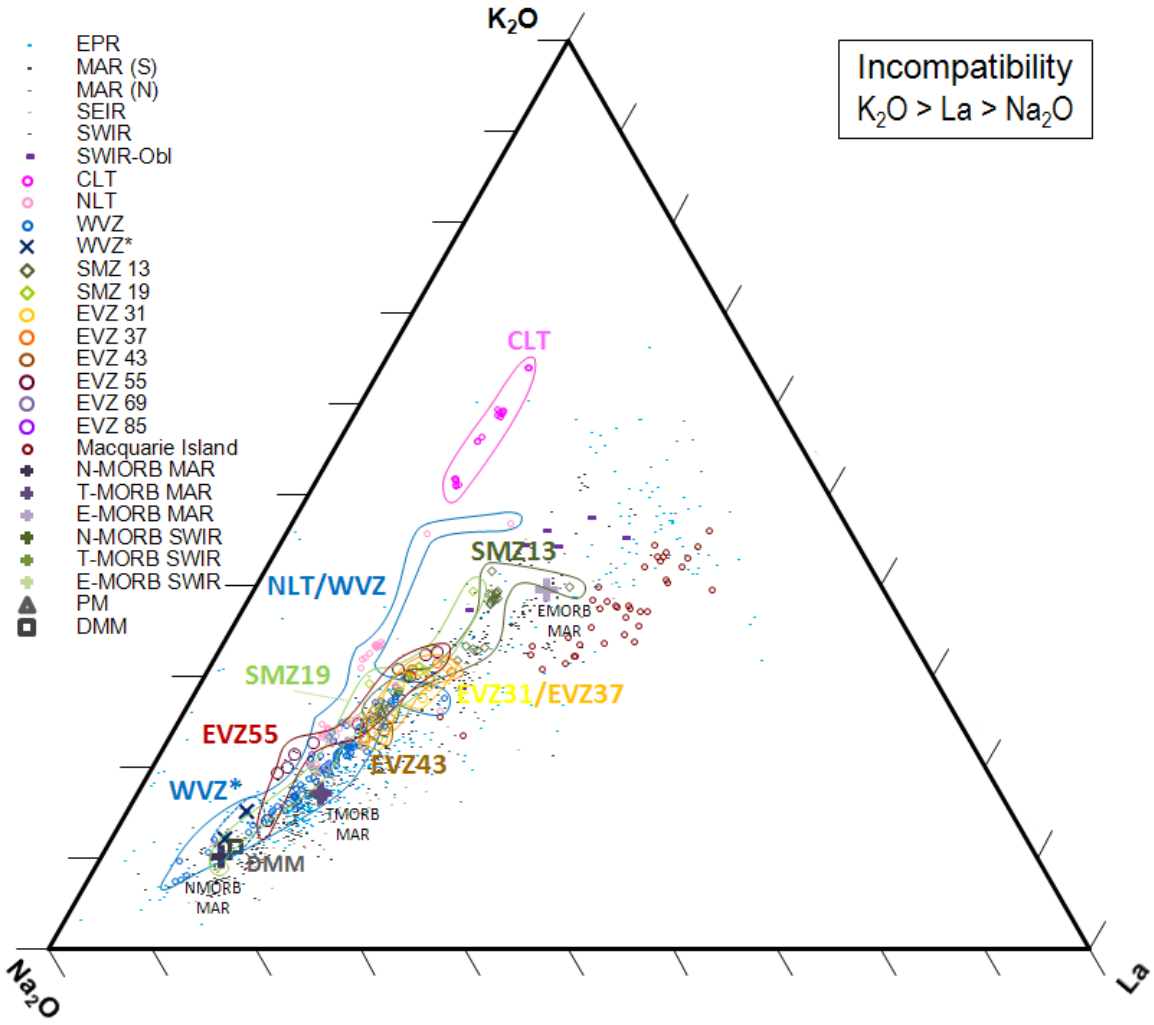

Figure A2a. NKL ternary plot showing relative concentrations of Na_2O (wt.% x 5), K_2O (wt.% x 30), & La (ppm) in a variety of basalt glass and whole rock samples. These include enriched continental magmatic rocks (GEOROC; Lehnert et al., 2000), global MORBs (PetDB; Lehnert et al., 2000), enriched basalts (Kamenetsky et al., 2000), and Arctic ridge samples from Lena Trough (Nauret et al., 2011) and Gakkel Ridge (Michael et al., 2003; Goldstein et al., 2008; Shaw et al., 2010; Snow J.E., in prep; and data from this study). Also plotted are DMM (Salters & Stracke, 2004) and PM (Sun & McDonough, 1989).

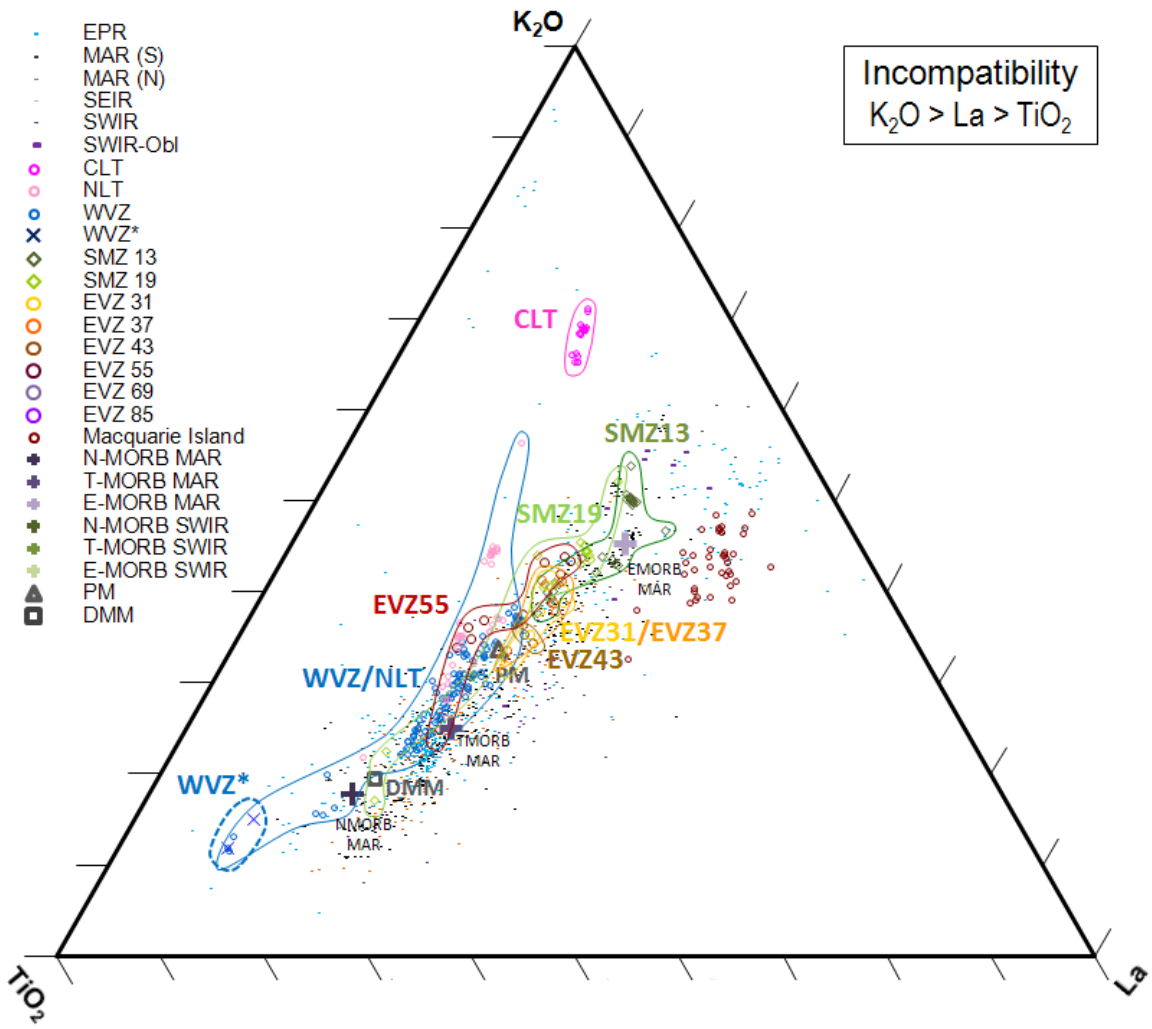

Figure A2b. TKL ternary plot showing relative concentrations of TiO_2 (wt.% x 5), K_2O (wt.% x 30), & La (ppm) in basalt glasses and whole rock samples. Data are from the same references as those in Figure 12a.

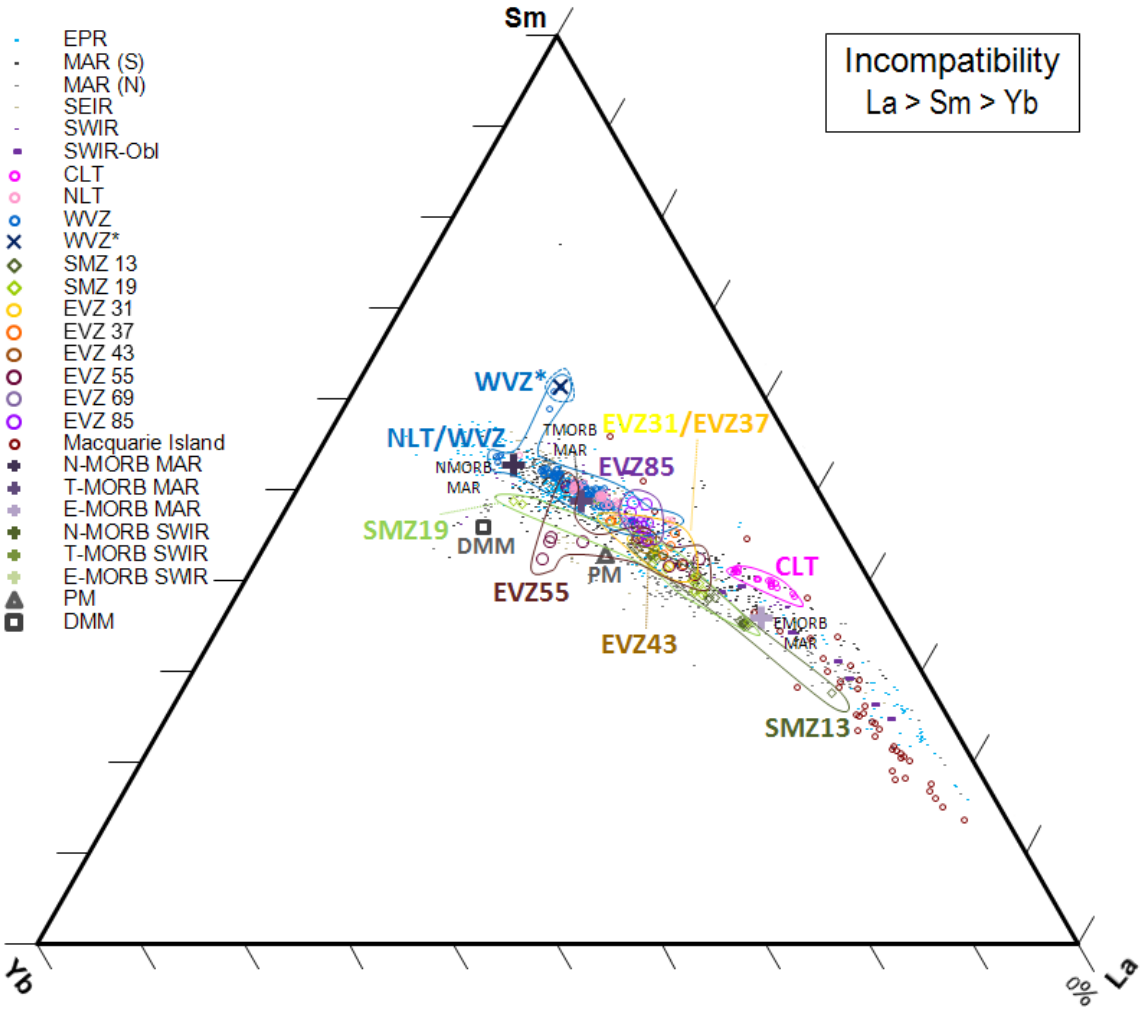

Figure A2c. YSL ternary plot showing relative concentrations of Yb (ppm), Sm (ppm x 2), & La (ppm) in basalt glasses and whole rock samples. Data are from the same references as those in Figure 12a.

8.3) Appendix 3: NbKL & DSL ternary plots

Ternary plots showing relative concentrations of Nb (ppm), K_2O (wt. % x 30), & La (ppm) (NbKL), followed by ternary plots showing relative concentrations of Dy (ppm), Sm (ppm x 2), & La (ppm) (DSL). Nb is more incompatible than La and K_2O. K_2O and La have close incompatibilities, with K_2O being slightly more incompatible than La. Sm is less incompatible than K_2O and La.

Data plotted are from this study and from other studies (Sun & McDonough, 1989; Kamenetsky et al., 2000; Goldstein et al., 2003; Michael et al., 2003; Salters & Stracke, 2004; Standish et al., 2008; Nauret et al., 2011; Shaw et al., 2010; PetDB (Lehnert et al., 2000); GEOROC (Lehnert et al., 2000)).

Data plotted include: MORB glass samples, continental enriched magma volcanic whole rock samples, EM1, EM2, and HIMU basalt glass and whole rock samples, global basalts and enriched continental magmas, and Gakkel Ridge and Lena Trough basalt glasses.

Ternary plots are:

Fig. A3a: NbKL - global & enriched MORBs
Fig. A3b: NbKL - OIB mantle components
Fig. A3c: NbKL - global & Arctic MORBs
Fig. A3d: DSL - global & enriched MORBs
Fig. A3e: DSL - OIB mantle components
Fig. A3f: DSL - global and Arctic MORBs

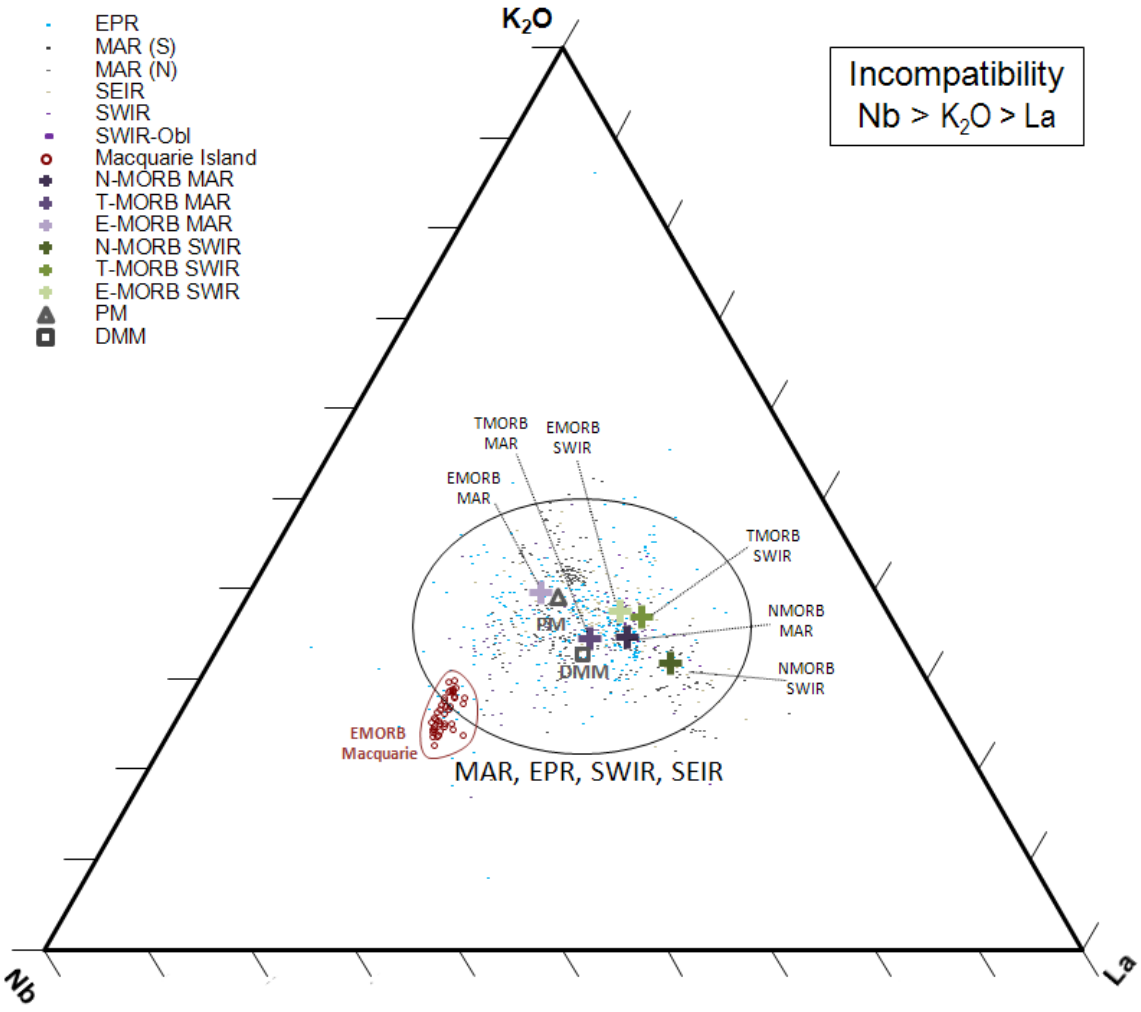

Figure A3a. NbKL trace element ternary plot: Nb (ppm) & K_2O (wt.% x 30) & La (ppm). Global MORB and enriched basalt glass samples

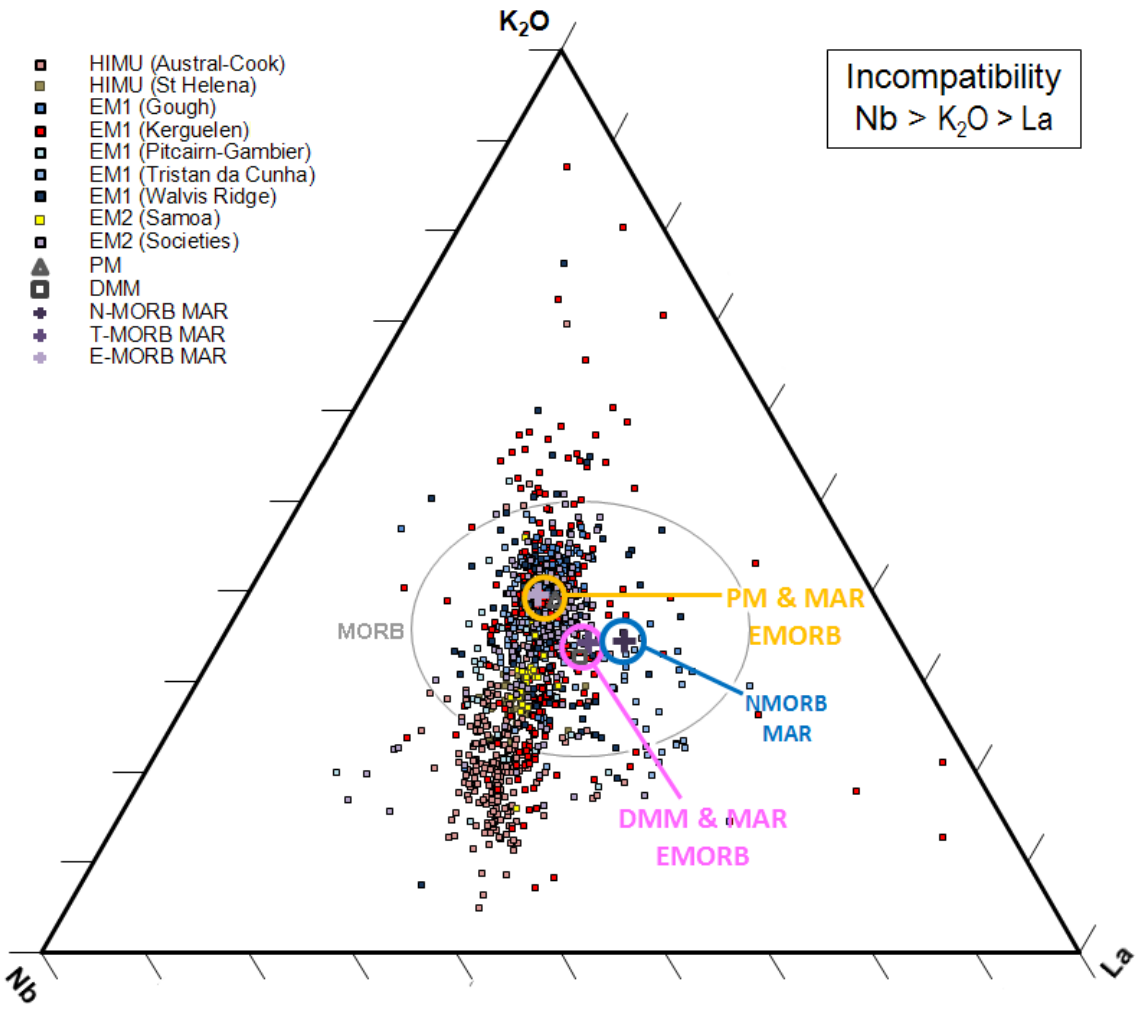

Figure A3b. NbKL trace element ternary plot: Nb (ppm) & K_2O (wt.% x 30) & La (ppm). EM1, EM2, and HIMU basalt glass and whole rock samples

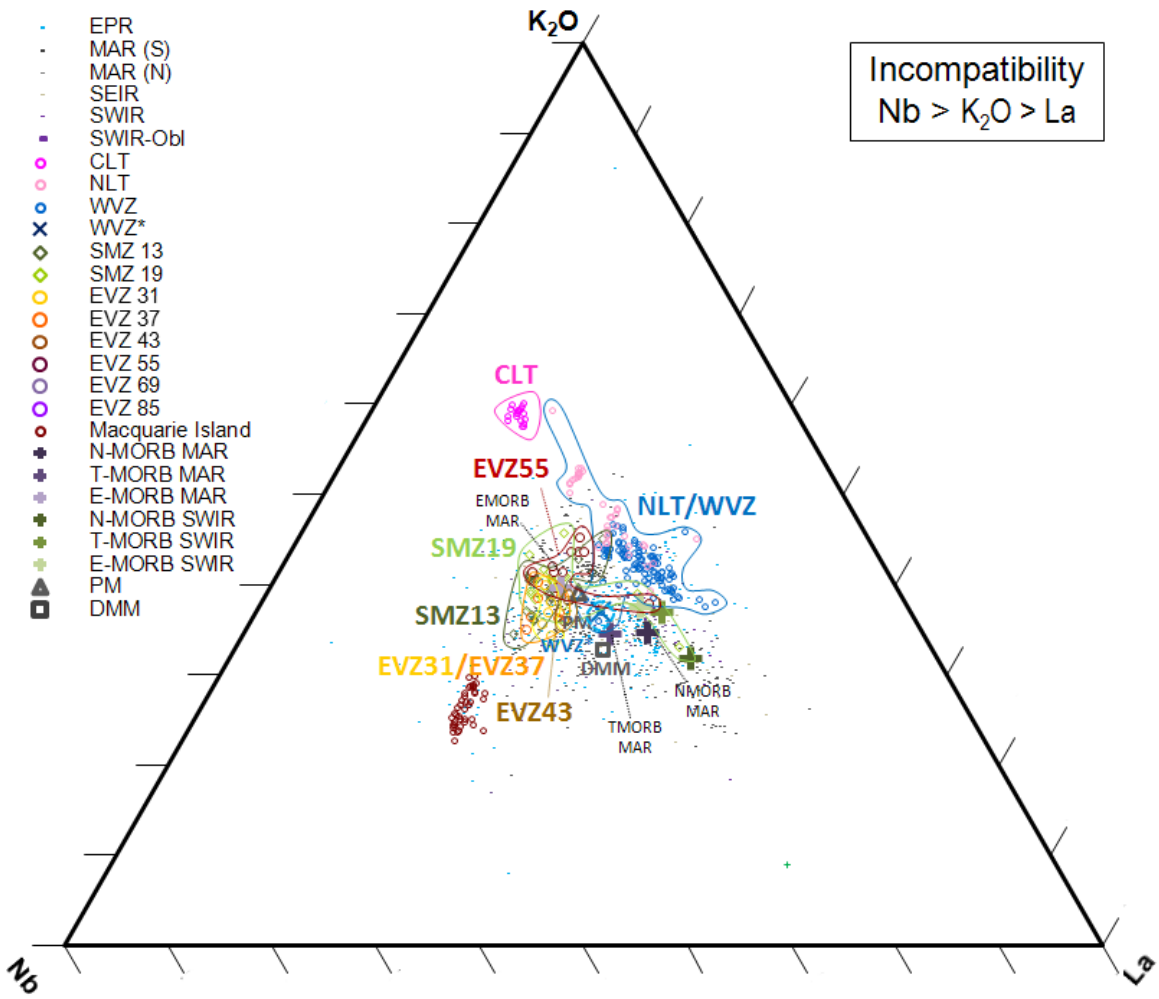

Figure A3c. NbKL trace element ternary plot: Nb (ppm) & K_2O (wt.% x 30) & La (ppm). Global basalts and whole rock samples.

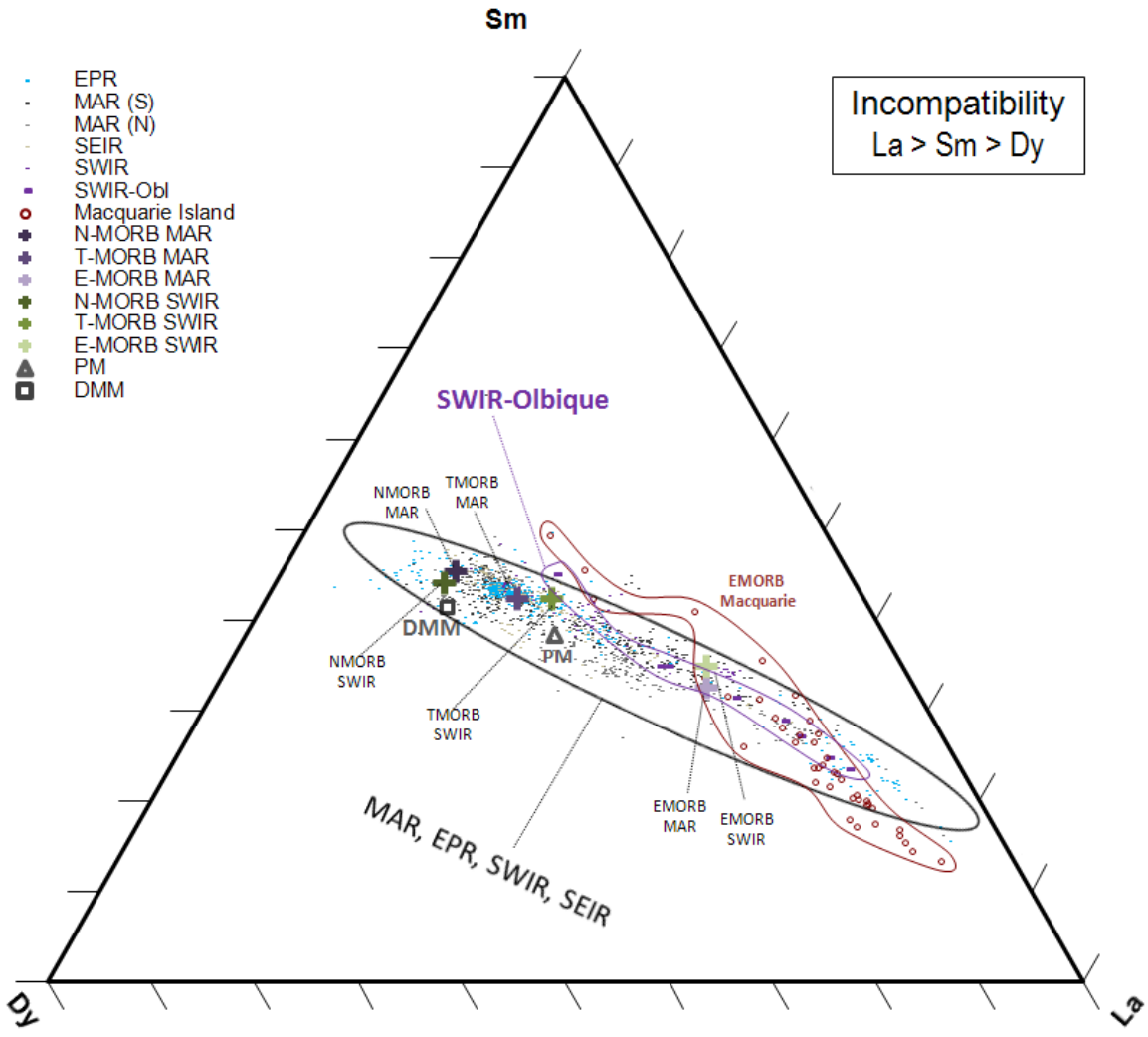

Figure A3d. DSL trace element ternary plot: Dy (ppm) & Sm (ppm x 2) & La (ppm). Global MORB glass samples.

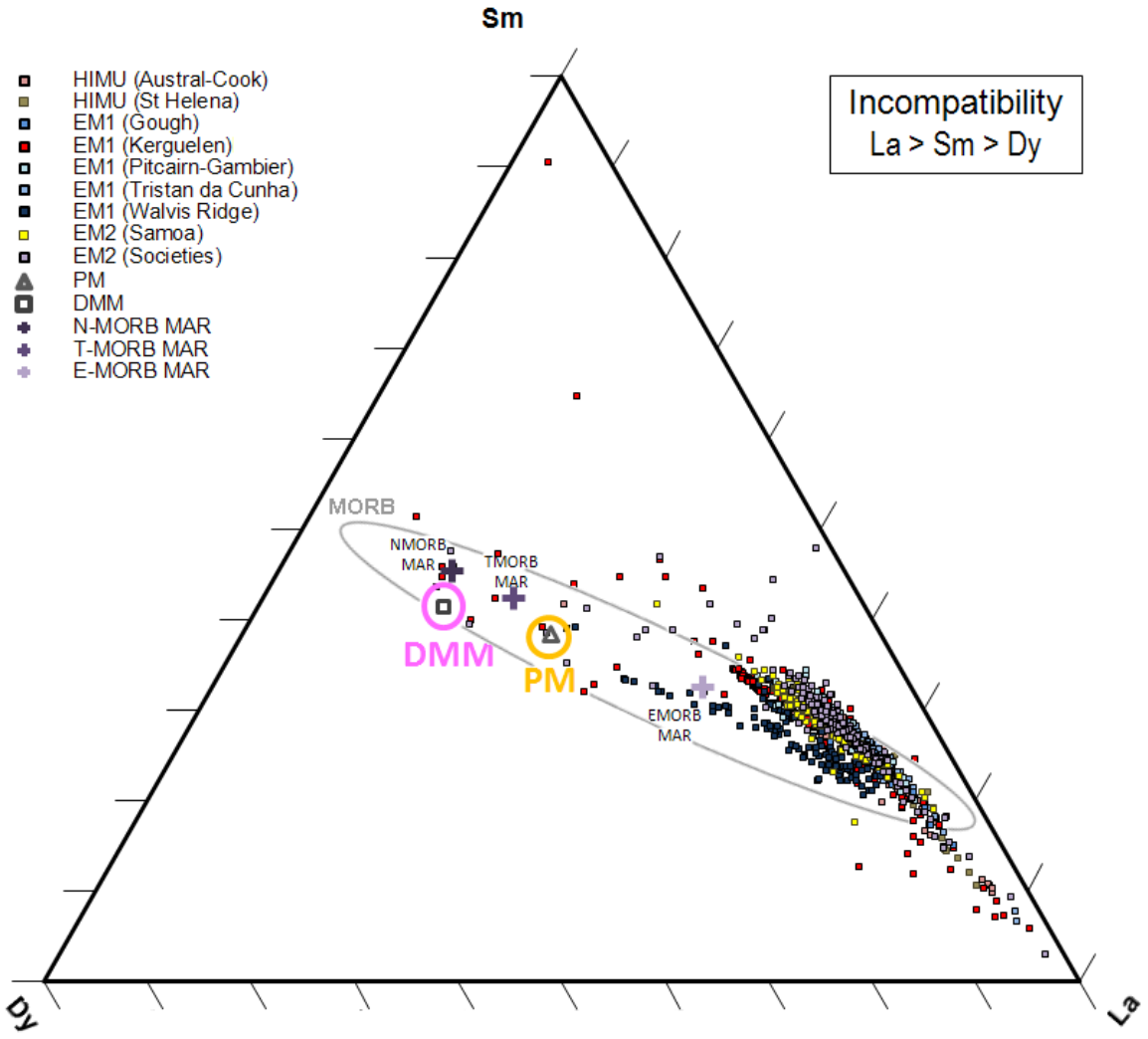

Figure A3e. DSL trace element ternary plot: Dy (ppm) & Sm (ppm x 2) & La (ppm). EM1, EM2, and HIMU basalt glass and whole rock samples.

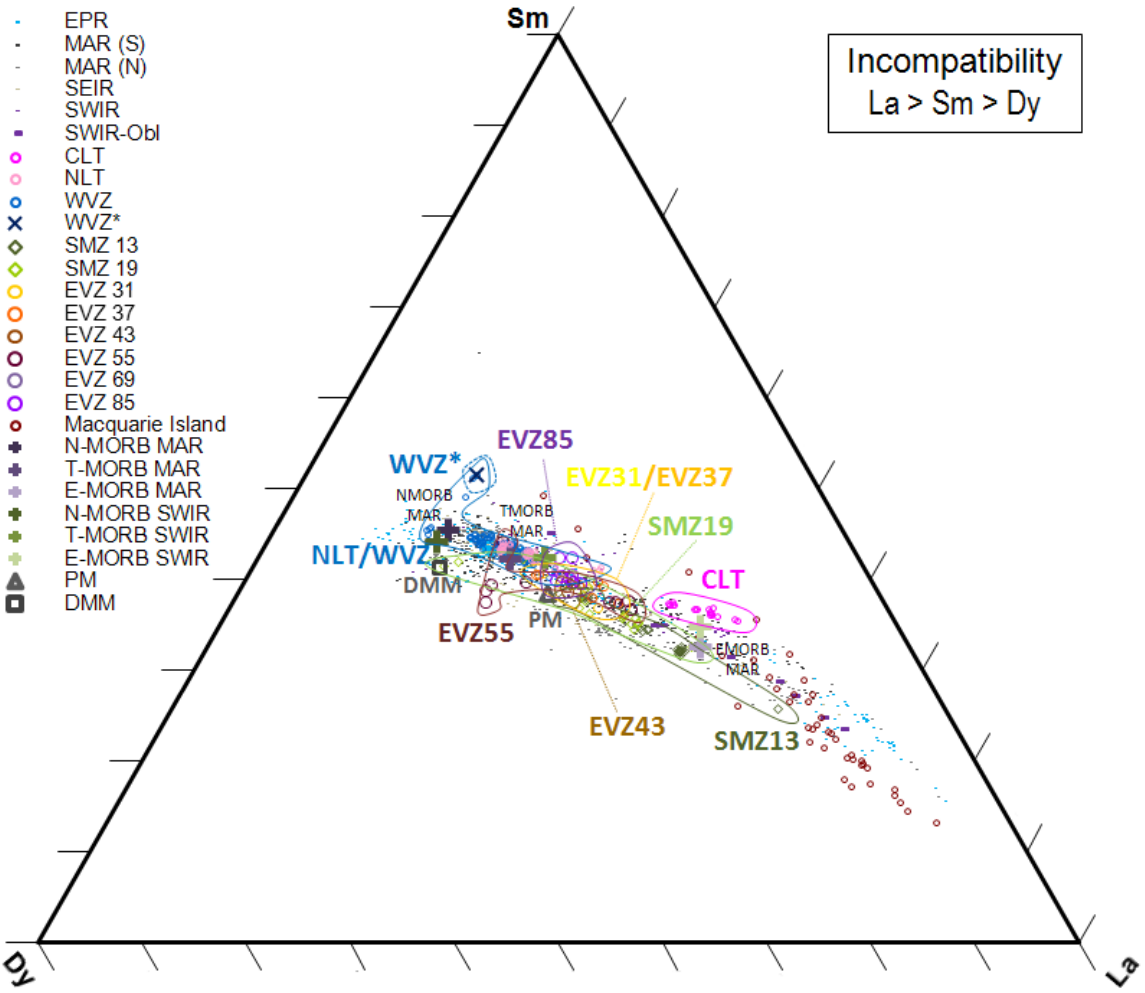

Figure A3f. DSL trace element ternary plot: Dy (ppm) & Sm (ppm x 2) & La (ppm). Global basalt glasses and whole rock samples.

8.4) Appendix 4: NKL ternary plots - mixing lines

NKL ternary plots displaying relative concentrations of Na_2O (wt.% x 5), K_2O (wt.% x 30), & La (ppm) showing two-component mixing lines. K_2O and La have close incompatibilities, with K_2O being slightly more incompatible than La. Na_2O is less incompatible than K_2O and La. All diagrams depict the DMM – extreme-K_2O CLT mixing line.

The other mixing lines shown are:

Fig. A4a: NKL - DMM to EM2
Fig. A4b: NKL - DMM to EM1
Fig. A4c: NKL - DMM to average MAR E-MORB

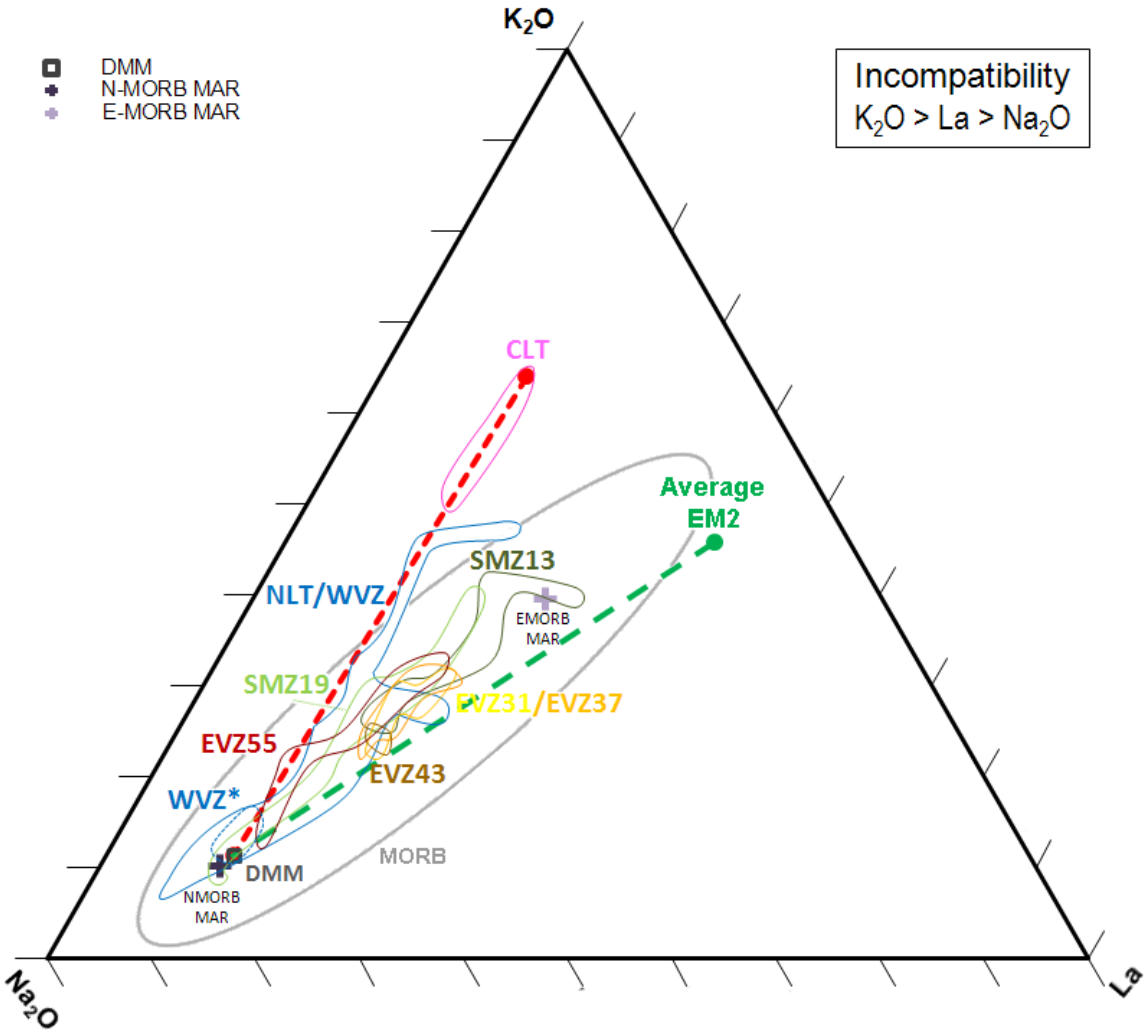

Figure A4a. NKL trace element ternary plot showing relative concentrations of Na_2O (wt.% x 5) & K_2O (wt.% x 30) & La (ppm). The red two-component mixing line connects DMM and CLT. The green two-component mixing line connects DMM and EM2.

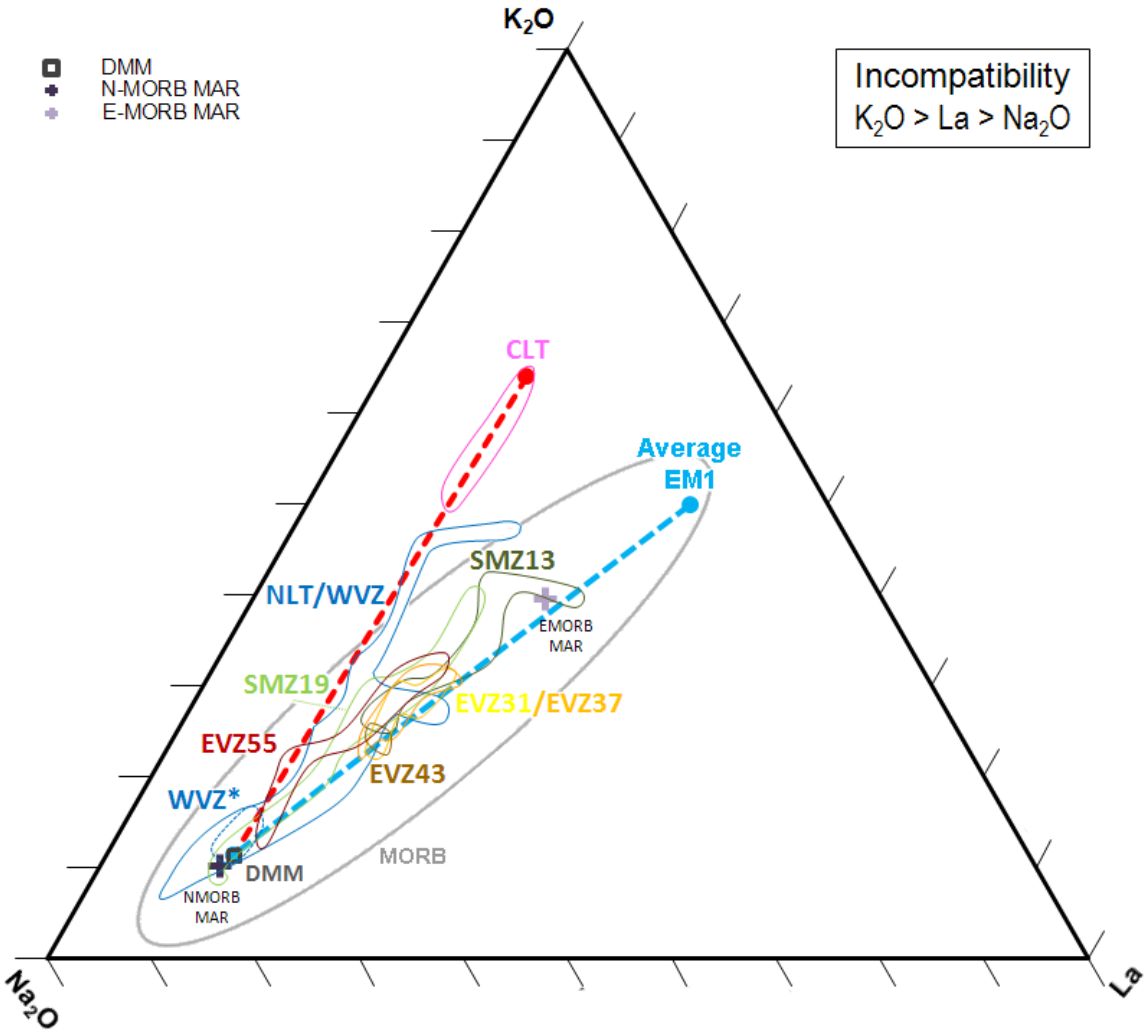

Figure A4b. NKL trace element ternary plot showing relative concentrations of Na_2O (wt.% x 5) & K_2O (wt.% x 30) & La (ppm). The red two-component mixing line connects DMM and CLT. The blue two-component mixing line connects DMM and EM1.

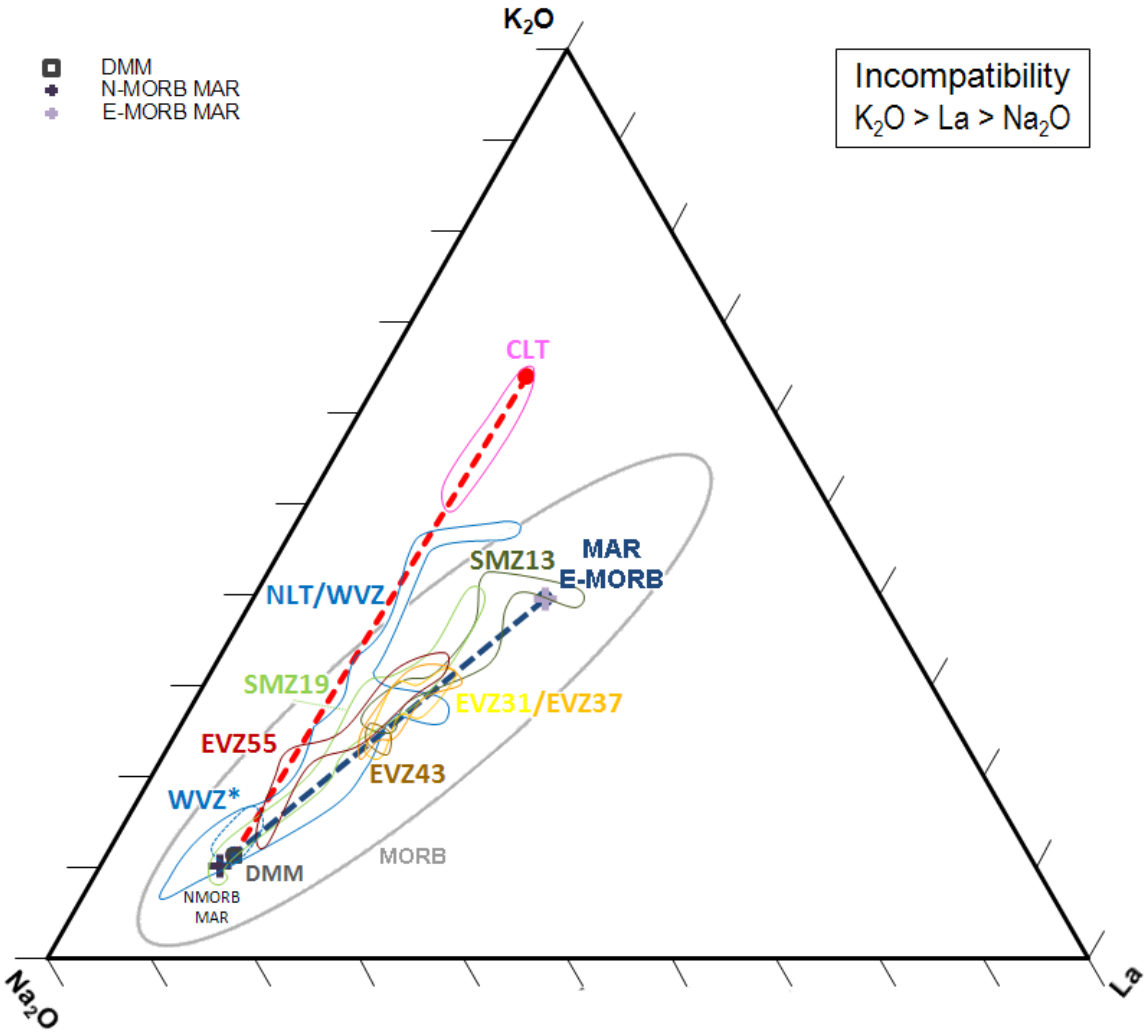

Figure A4c. NKL trace element ternary plot showing relative concentrations of Na_2O (wt.% x 5) & K_2O (wt.% x 30) & La (ppm). The red two-component mixing line connects DMM and CLT. The dark blue two-component mixing line connects DMM and MAR E-MORB.

8.5) Appendix 5: Ternary plots - enriched continental magmas

NKL, TKL, YSL, NbKL, and DSL ternary plots showing the enriched continental magmas: shoshonite, carbonatite, phonolite, and adakite from the GEOROC database (Lehnert et al., 2000). Rock types plotted are adakite, carbonatite, phonolite, and shoshonite. Also plotted are depleted MORB mantle (Salters & Stracke, 2004) and primitive mantle (Sun & McDonough, 1989). The global MORB array, comprising data from the MAR, EPR, SWIR, & SEIR, (PetDB; Lehnert et al., 2000) is encircled in gray. Ternary plots are:

Fig. A5a: NKL - Na_2O (wt.% x 5), K_2O (wt.% x 30), & La (ppm)
Fig. A5b: TKL - TiO_2 (wt.% x 5), K_2O (wt.% x 30), & La (ppm)
Fig. A5c: YSL - Yb (ppm), Sm (ppm x 2), & La (ppm)
Fig. A5d: NbKL - Nb (ppm), K_2O (wt. % x 30), & La (ppm)
Fig. A5e: DSL - Dy (ppm), Sm (ppm x 2), & La (ppm)

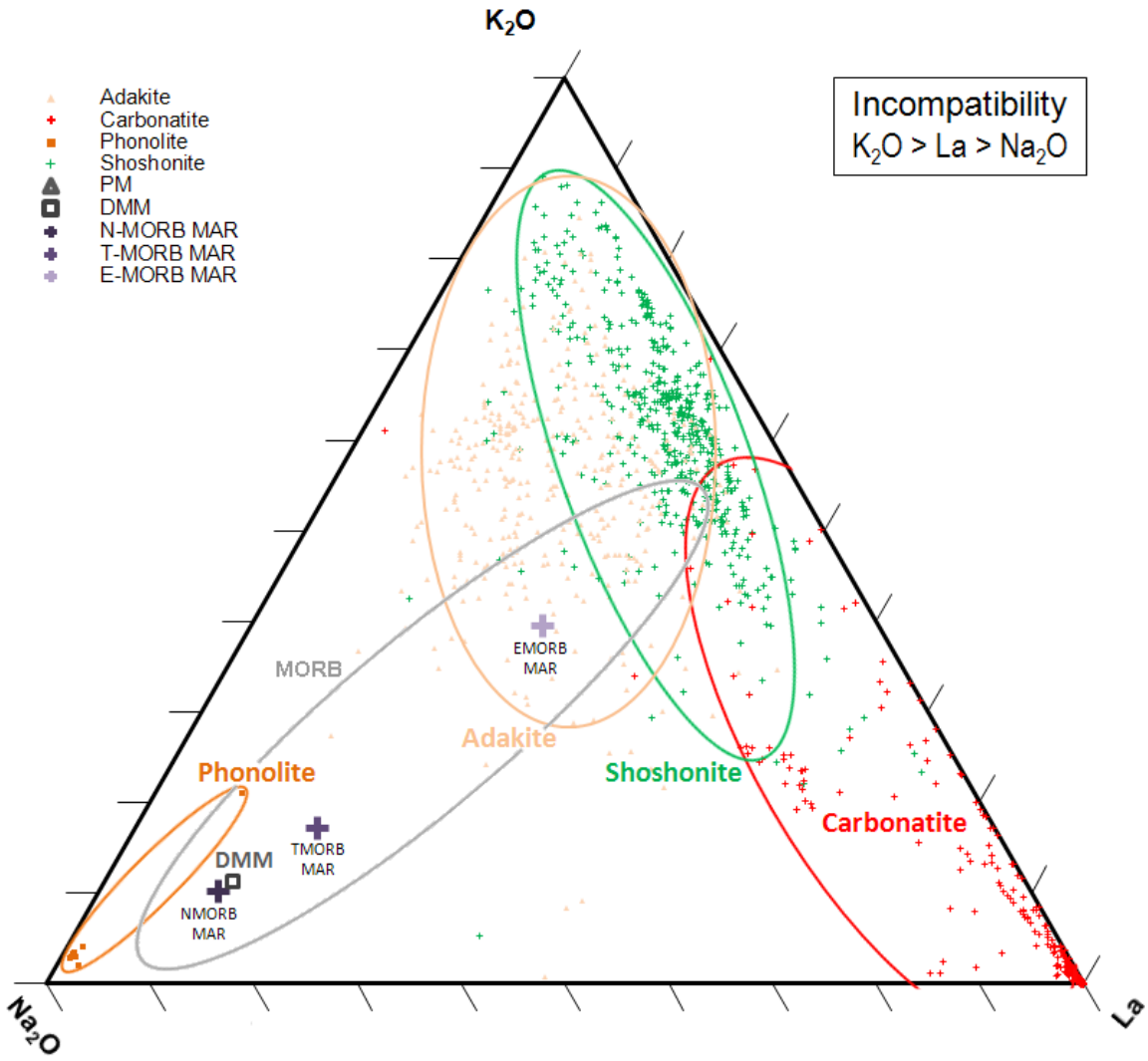

Figure A5a. NKL ternary plot showing relative concentrations of Na_2O (wt.% x 5), K_2O (wt.% x 30), & La (ppm) in continental volcanic whole rock samples.

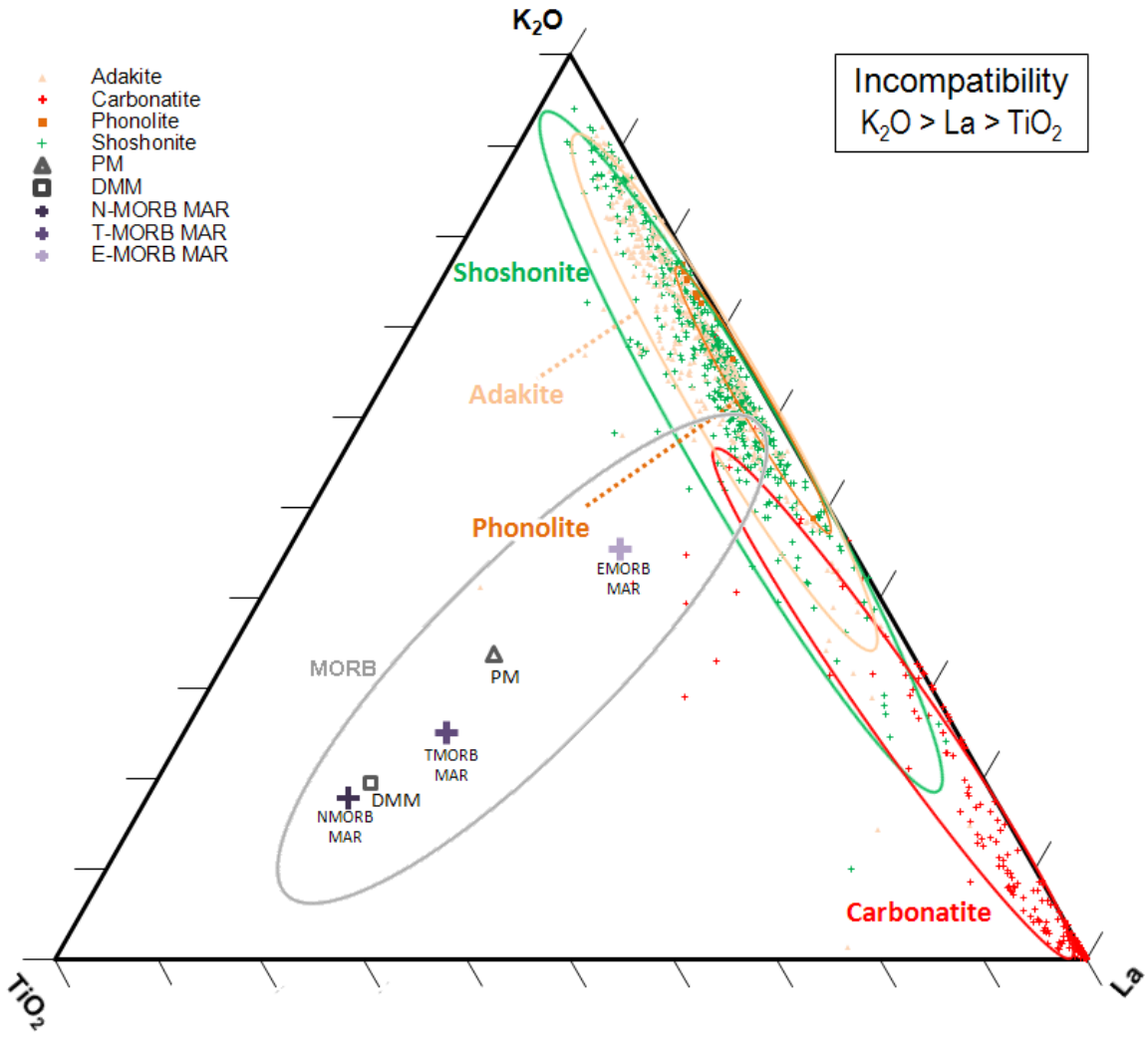

Figure A5b. TKL ternary plot showing TiO_2 (wt.% x 5), K_2O (wt.% x 30), & La (ppm) in continental volcanic whole rock samples.

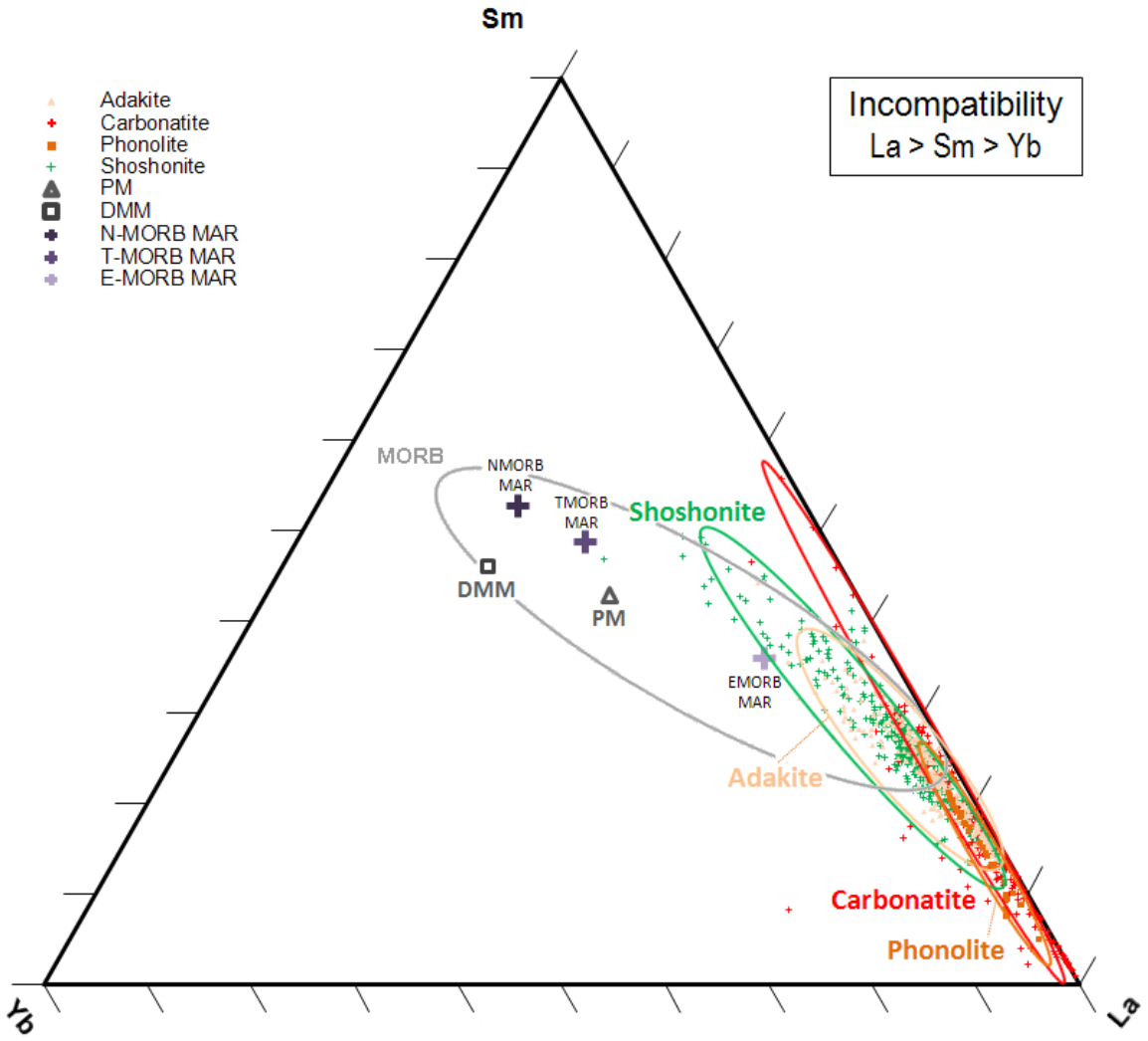

Figure A5c. YSL ternary plot showing relative concentrations of Yb (ppm), Sm (ppm x 2), & La (ppm) in continental volcanic whole rock samples.

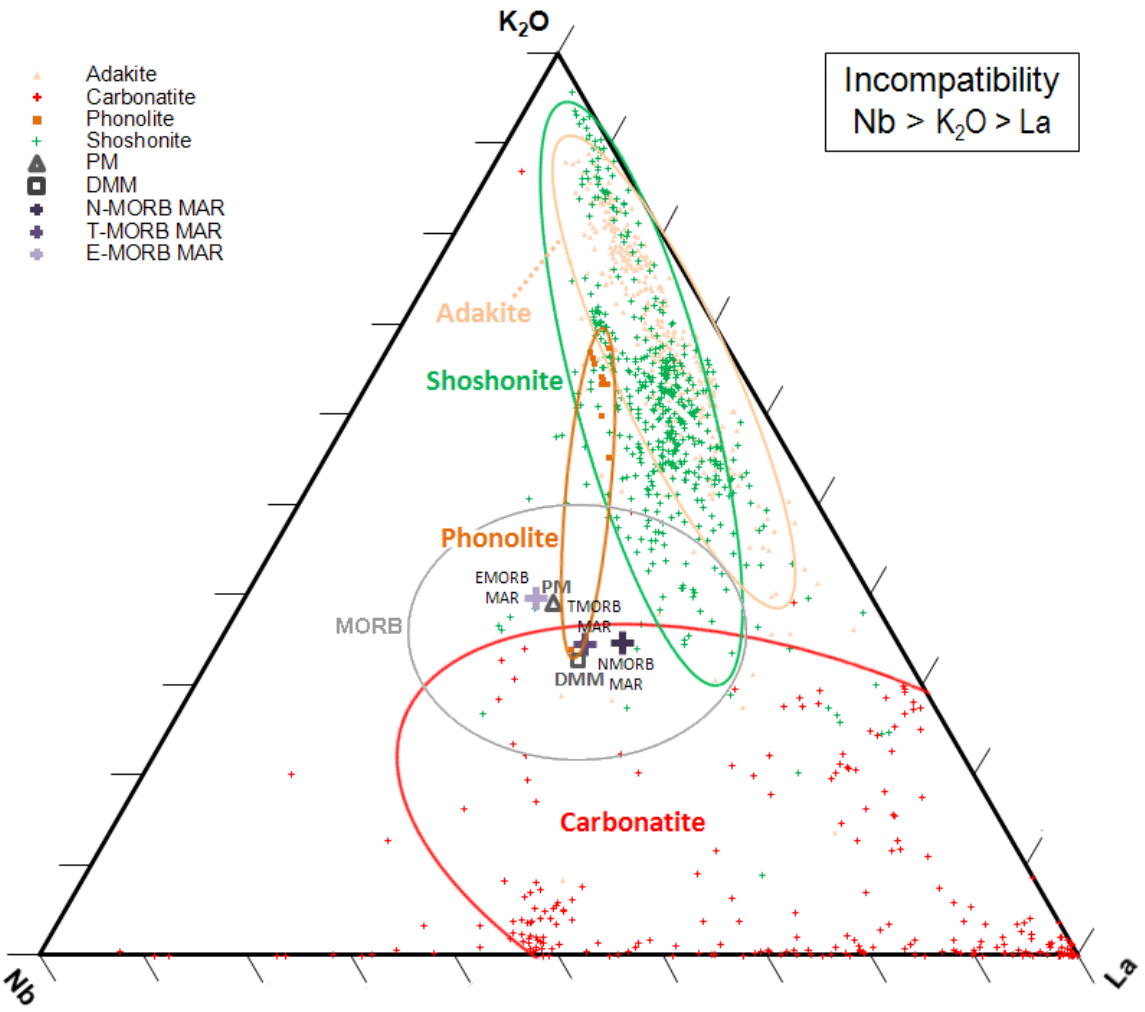

Figure A5d. NbKl trace element ternary plot: Nb (ppm) & K_2O (wt.% x 30) & La (ppm). Continental enriched magma volcanic whole rock samples

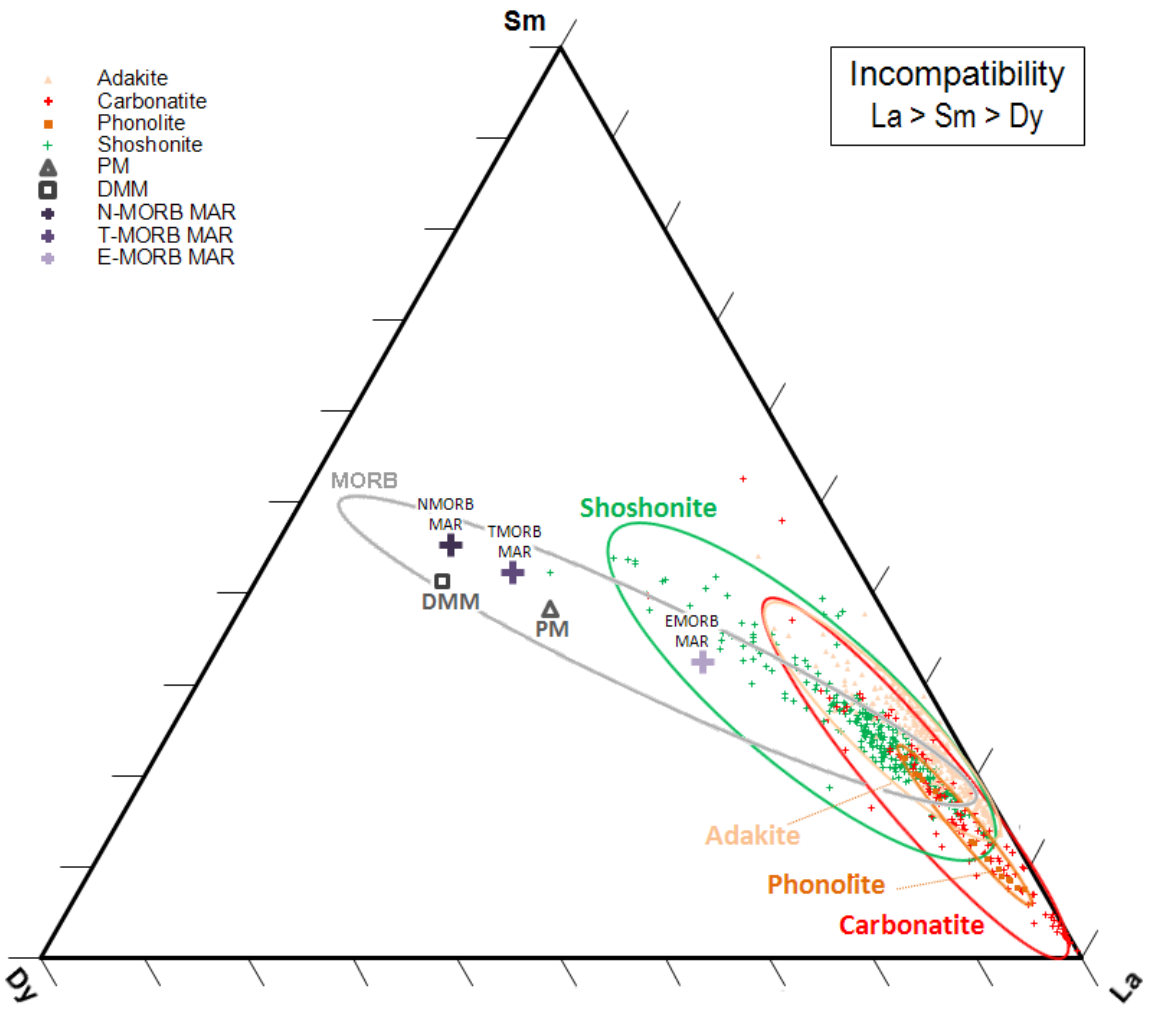

Figure A5e. DSL trace element ternary plot: Dy (ppm) & Sm (ppm x 2) & La (ppm). Continental volcanic whole rock samples

8.6) Appendix 6: NKL & TKL ternary plots - Gakkel Ridge volcanic centers

NKL (Na_2O (wt.% x 5), K_2O (wt.% x 30), La (ppm)) & TKL (TiO_2 (wt.% x 5), K_2O (wt.% x 30), La (ppm)) ternary plots showing the uncertainty polygons surrounding each plotted sample. Uncertainties were calculated from the standard deviations of the analyses of the basalt standard VG-2 for the elements Na_2O and K_2O from electron microprobe analyses and the basalt standard BIR-1 for the elements La and TiO_2 from LA-ICP-MS analyses. Each plot shows a different section of Gakkel Ridge, separated by volcanic centers. The global MORB array, comprising data from the MAR, EPR, SWIR, & SEIR, (PetDB; Lehnert et al., 2000) is encircled in gray. The gray blob represents all Gakkel Ridge samples from this study and earlier studies (Michael et al., 2003; Goldstein et al., 2008; Shaw et al., 2010; Snow J.E., in prep).

Ternary plots are:

Fig. A6a: NKL - SMZ13
Fig. A6b: NKL - SMZ19
Fig. A6c: NKL - EVZ31-EVZ37-EVZ-43
Fig. A6d: NKL - EVZ55
Fig. A6e: TKL - SMZ13
Fig. A6f: TKL - SMZ19
Fig. A6g: TKL - EVZ31-EVZ37-EVZ43
Fig. A6h: TKL - EVZ55

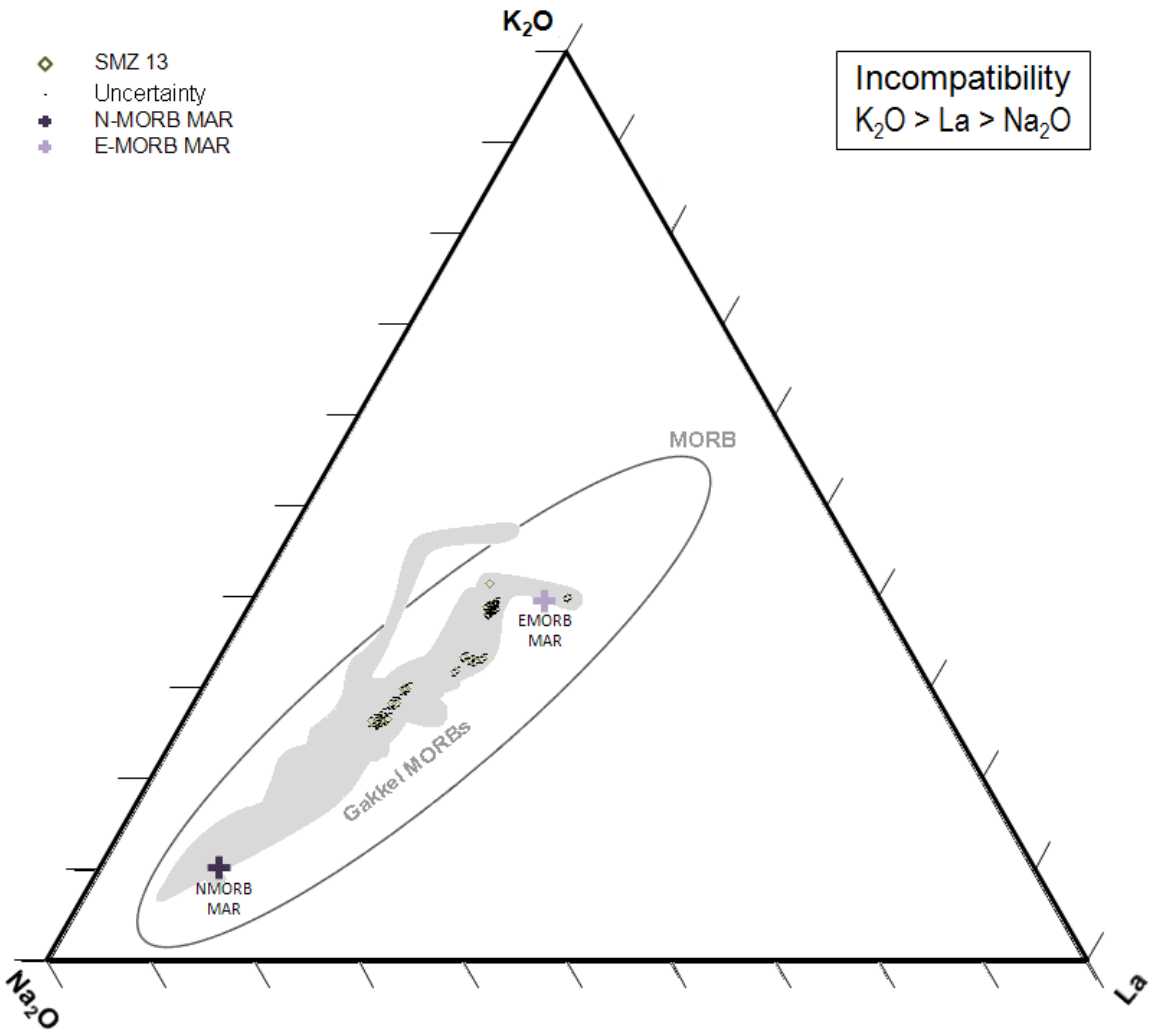

Figure A6a. NKL ternary plot showing SMZ13 samples and their uncertainty polygons.

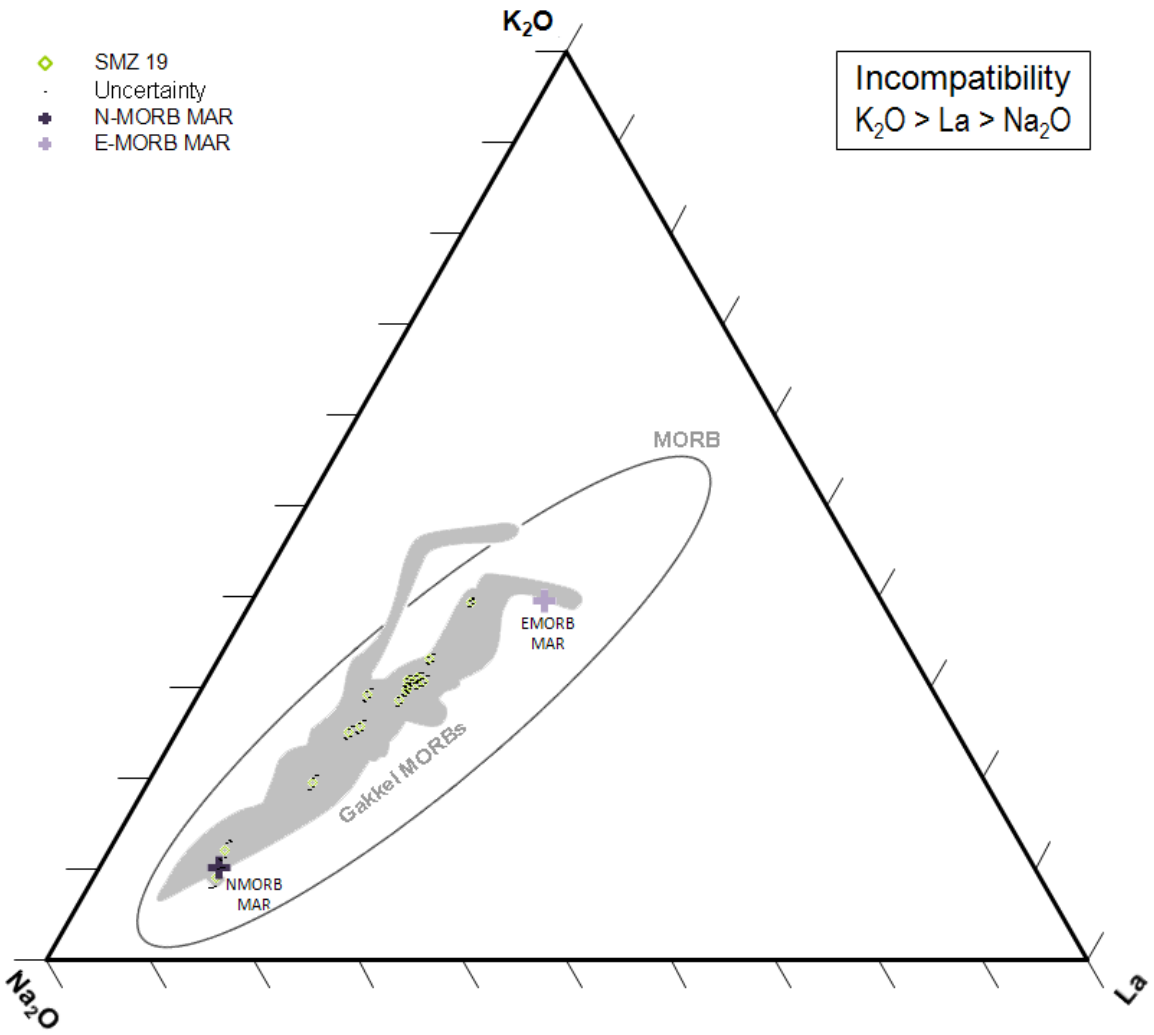

Figure A6b. NKL ternary plot showing SMZ19 samples and their uncertainty polygons.

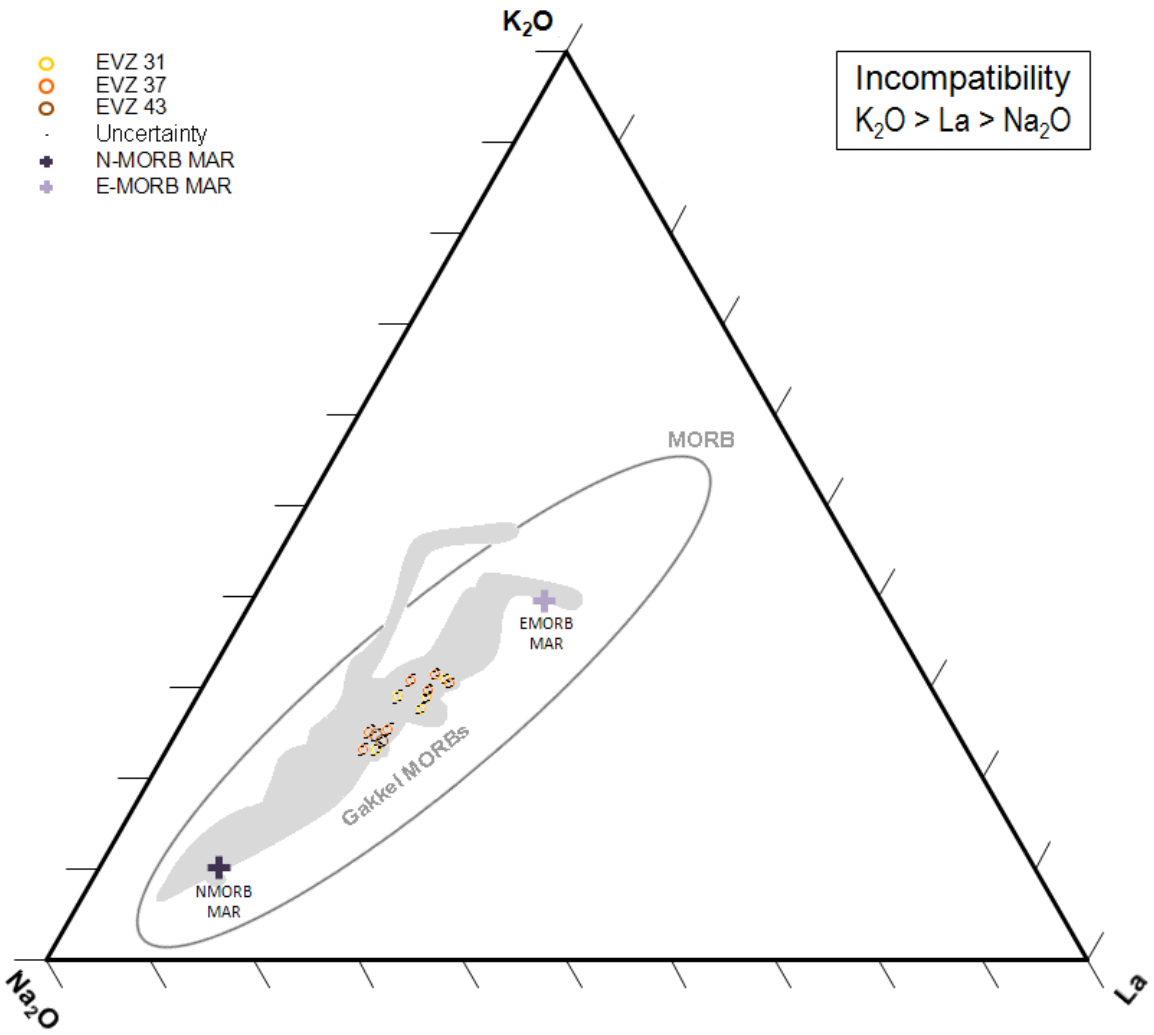

Figure A6c. NKL ternary plot showing EVZ31, EVZ37, & EVZ43 samples and their uncertainty polygons.

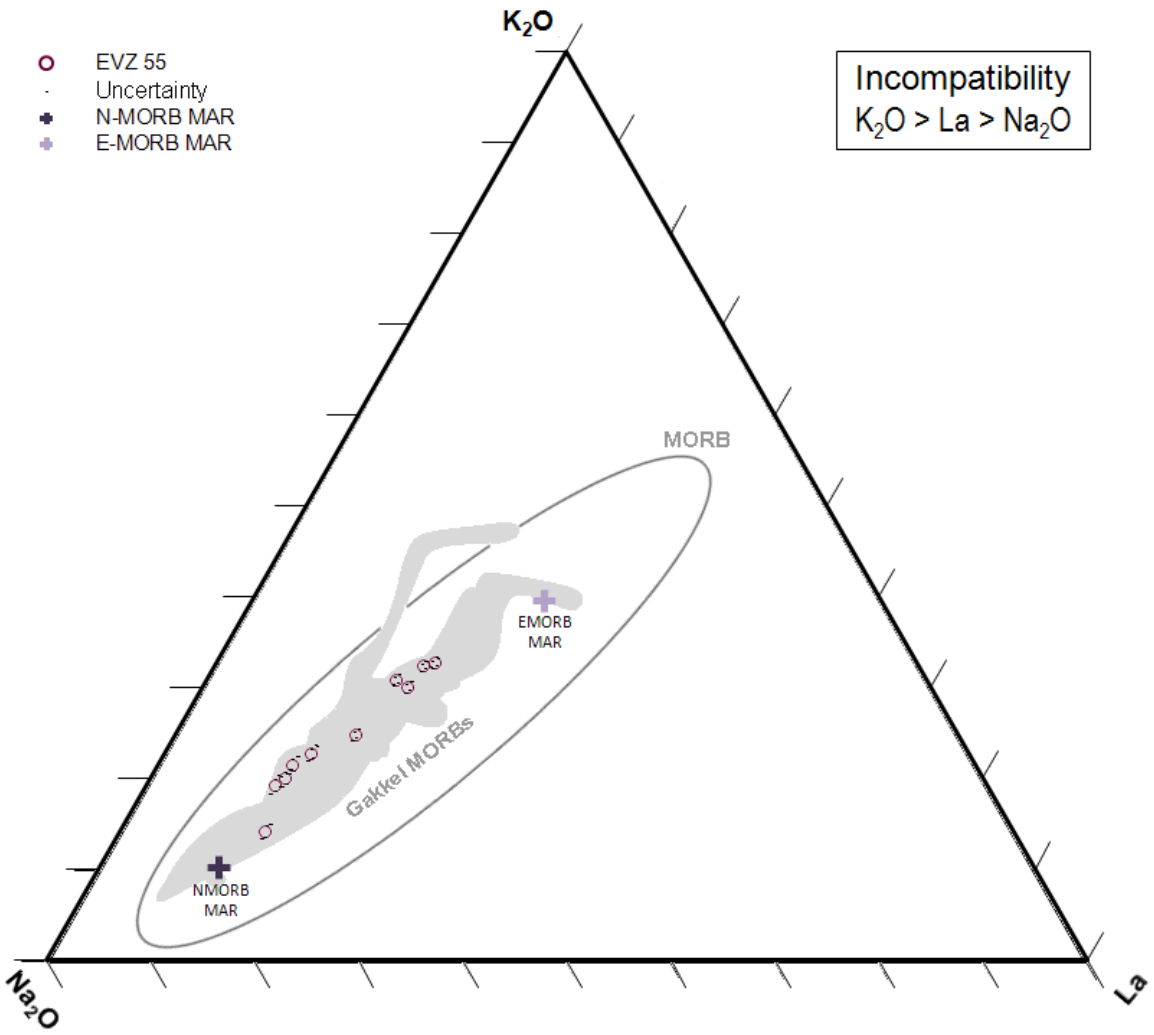

Figure A6d. NKL ternary plot showing EVZ55 samples and their uncertainty polygons.

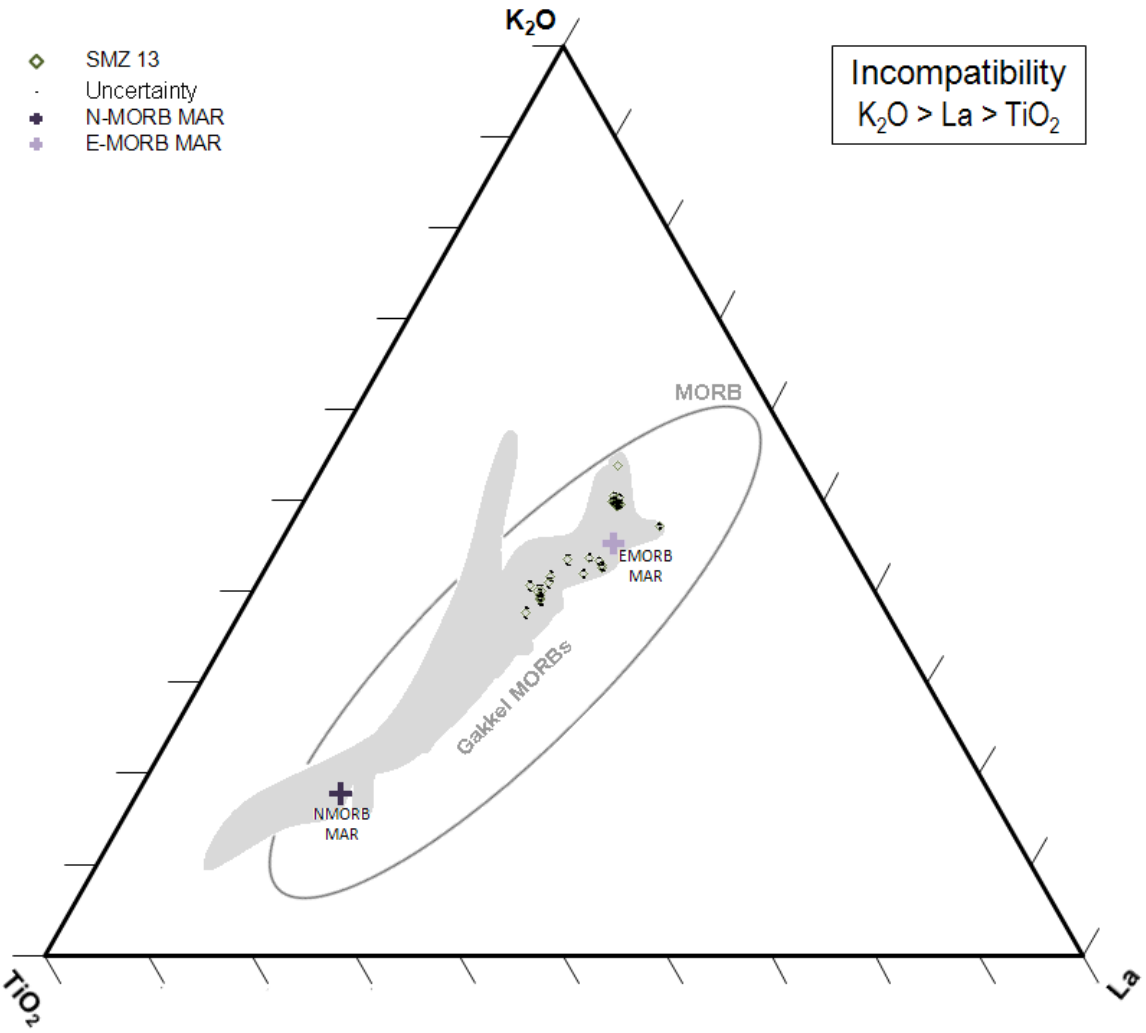

Figure A6e. TKL ternary plot showing SMZ13 samples and their uncertainty polygons.

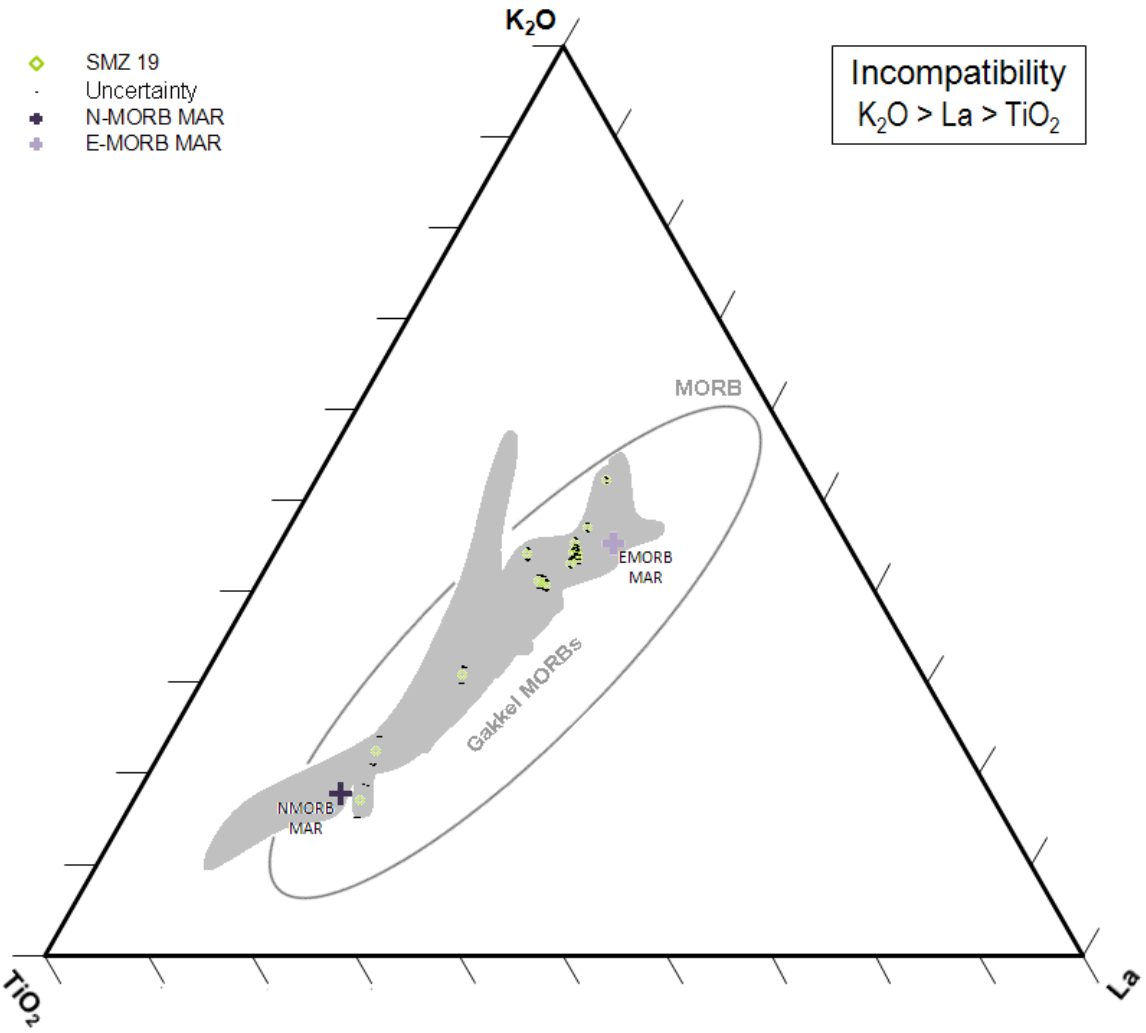

Figure A6f. TKL ternary plot showing SMZ19 samples and their uncertainty polygons.

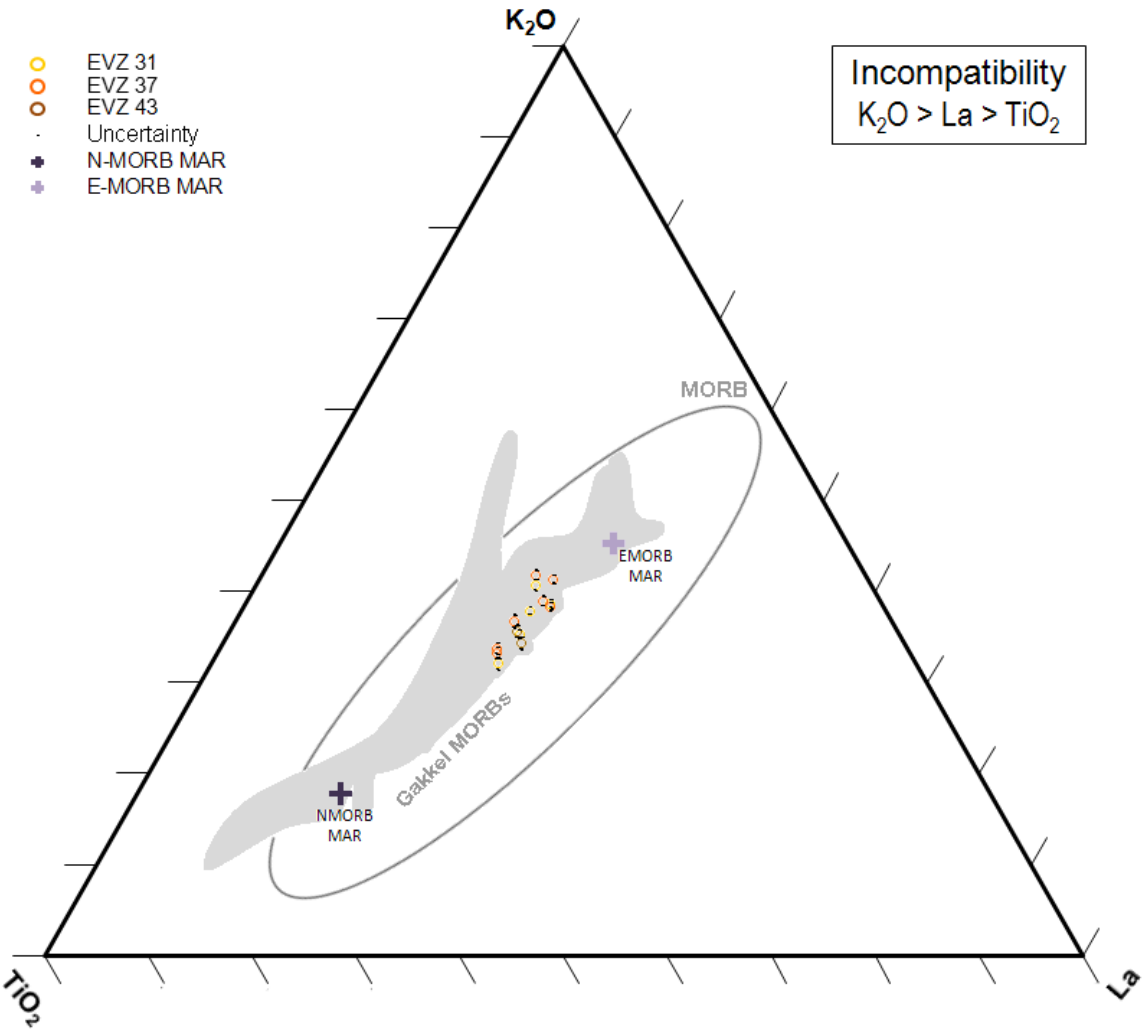

Figure A6g. TKL ternary plot showing EVZ31, EVZ37, & EVZ43 samples and their uncertainty polygons.

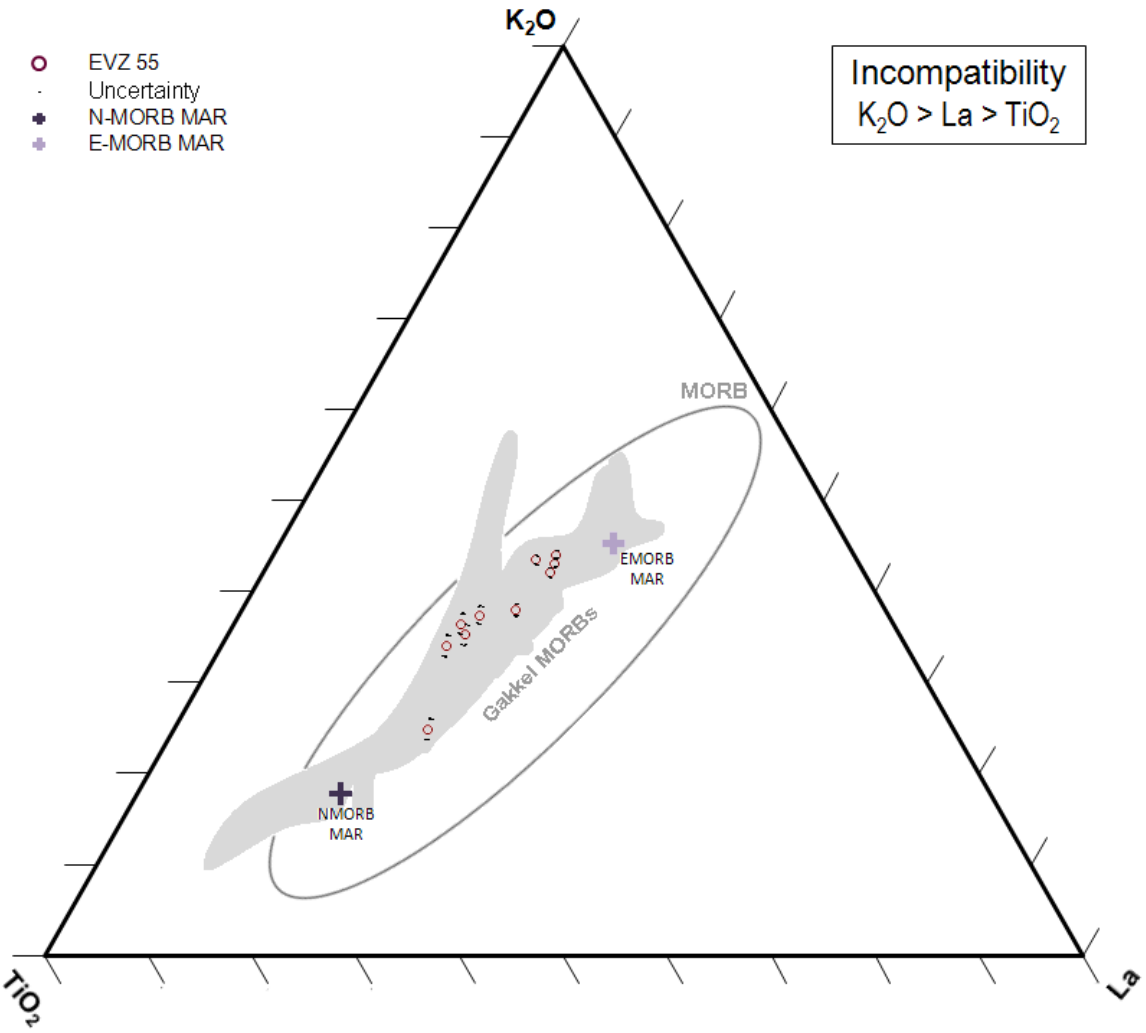

Figure A6h. TKL ternary plot showing EVZ55 samples and their uncertainty polygons.

8.7) Appendix 7: Tables - basalt standards

The basalt standard VG-2 was used as the independent check standard during electron microprobe analyses of the major elements of the Gakkel Ridge samples of this study. The basalt standard BIR-1 was used as the independed check standard during LA-ICP-MS analyses of the trace elements and the major element TiO_2 of the Gakkel Ridge samples of this study. The basalt standard KL2-G was used as the primary standard during the LA-ICP-MS analyses of the trace elements and the major element TiO_2 of the Gakkel Ridge samples of this study.

Multiple measurements of each basalt standard were averaged together into unknowns. The column N is the number of measurements averaged into each unknown. The "Date" column shows the date on which the measurements were made for each unknown along with a number for each unknown when there are multiple unknowns for a single date.

Accepted values of VG-2 are from Jarosewich (1980). Accepted values of KL2-G and BIR-1 are from (GeoReM; Jochum et al., 2005).

Elemental abundances of zero were not included in the average and standard deviation calculations.

Tables shown are:

Table A7a: Major element analyses of VG-2
Table A7b: Trace element analyses of BIR-1 (part 1)
Table A7c: TiO_2 and trace element analyses of BIR-1 (part 2)
Table A7d: Trace element analyses of KL2-G (part 1)
Table A7e: TiO_2 and trace element analyses of KL2-G (part 2)

VG-2

Date	Na_2O	SiO_2	K_2O	FeO	TiO_2	Al_2O_3	MgO	CaO	MnO	Cl	S	P_2O_5	Total	N
20050718 #01	2.83	50.9	0.188	12.0	1.88	14.0	6.65	11.1	0.22	0.03	0.13	0.22	100.00	4
20050718 #02	2.82	50.9	0.201	12.0	1.87	14.1	6.68	11.1	0.20	0.03	0.14	0.22	100.25	5
20050720 #01	2.80	50.7	0.191	11.9	1.88	14.1	6.68	11.0	0.21	0.03	0.14	0.20	99.81	5
20050720 #02	2.77	50.8	0.192	11.9	1.88	14.0	6.68	11.1	0.18	0.03	0.13	0.22	99.89	4
20050720 #03	2.83	51.0	0.195	11.9	1.90	14.1	6.70	11.0	0.20	0.03	0.14	0.22	100.25	4
20050720 #04	2.85	51.1	0.193	11.9	1.88	14.0	6.66	11.2	0.22	0.03	0.14	0.23	100.39	2
20050720 #05	2.89	50.9	0.191	12.0	1.89	14.0	6.69	11.0	0.22	0.03	0.13	0.23	100.27	4
20050720 #06	2.86	50.9	0.190	11.9	1.87	14.0	6.68	11.0	0.19	0.03	0.13	0.23	99.94	5
20050720 #07	2.83	51.1	0.197	12.0	1.88	14.2	6.70	11.1	0.23	0.03	0.14	0.23	100.55	3
20050720 #08	2.77	50.9	0.192	12.0	1.88	14.1	6.67	11.1	0.20	0.03	0.15	0.24	100.15	3
20050720 #09	2.78	50.8	0.213	11.8	1.86	14.0	6.59	11.1	0.22	0.03	0.14	0.23	99.74	3
20050721 #01	2.81	50.9	0.193	11.9	1.87	14.0	6.66	11.1	0.20	0.03	0.14	0.21	100.00	3
20050721 #02	2.84	50.8	0.187	12.0	1.86	14.0	6.70	11.1	0.20	0.03	0.13	0.21	100.02	6
Average	2.82	50.9	0.194	11.9	1.88	14.0	6.67	11.1	0.21	0.03	0.14	0.22	100.10	
Standard Deviation	0.04	0.1	0.01	0.06	0.01	0.06	0.03	0.05	0.01	0.00	0.01	0.01	0.24	
Relative Standard Deviation	1%	0.0	4%	1%	1%	0%	0%	0%	7%	6%	4%	5%	0%	
Accepted Values	2.62	50.81	0.19	12.1	1.85	14.06	6.71	11.12	0.22			0.2	99.86	

Table A7a. Major element analyses of the basalt standard VG-2.

BIR-1 (part 1)

Date	Rb	Sr	Y	Zr	Nb	Cs	Ba	La	Ce	Pr	Nd	Sm	Eu	Gd	N
20130309 #01	0.2	115	15.9	15	0.54	0.039	6.99	0.644	2.07	0.38	2.55	1.11	0.57	1.96	6
20130309 #02	0.2	110	15.6	14	0.55	0.049	6.37	0.599	1.97	0.37	2.36	1.14	0.54	1.77	4
20130309 #03	0.2	116	16.1	15	0.56	0.050	6.85	0.619	1.96	0.38	2.45	1.20	0.56	1.92	4
20130309 #04	0.2	113	15.3	14	0.55	0.025	6.65	0.601	1.92	0.38	2.49	1.08	0.53	1.90	5
20130309 #05	0.2	114	15.5	15	0.56	0.024	6.91	0.626	2.06	0.40	2.52	1.13	0.54	1.97	5
20130309 #06	0.3	109	15.0	14	0.52	0.022	6.35	0.567	1.87	0.36	2.28	1.05	0.51	1.75	5
20130309 #07	0.2	114	15.4	15	0.57	0.026	6.91	0.625	2.00	0.38	2.48	1.14	0.54	1.97	5
Average	0.2	113	15.5	15	0.55	0.033	6.72	0.612	1.98	0.38	2.45	1.12	0.54	1.89	
Standard Deviation	0.04	3	0.4	0.4	0.02	0.012	0.27	0.025	0.07	0.01	0.09	0.05	0.02	0.09	
Relative Standard Deviation	17%	2%	2%	3%	3%	36%	4%	4%	4%	3%	4%	4%	4%	5%	
Accepted Values	0.2	109	15.6	14	0.55	0.007	7.14	0.615	1.92	0.37	2.38	1.12	0.53	1.87	

Table A7b. Trace element analyses of the basalt standard BIR-1.

BIR-1 (part 2)

Date	Tb	Dy	Ho	Er	Tm	Yb	Lu	Hf	Ta	Pb	Th	U	TiO_2	Ni(60)	N
20130309 #01	1.97	2.73	0.60	1.76	0.26	1.88	0.26	0.594	0.0427	4.05238	0.038	0.02	1.01	197	6
20130309 #02	1.80	2.60	0.55	1.71	0.26	1.78	0.24	0.577	0.0371	3.85858	0.034	0.03	1.01	191	4
20130309 #03	1.80	2.69	0.60	1.79	0.25	1.77	0.24	0.585	0.0522	3.95675	0.055	0.03	1.01	194	4
20130309 #04	1.86	2.58	0.58	1.73	0.24	1.70	0.25	0.552	0.0386	3.96506	0.029	0.01	1.01	192	5
20130309 #05	1.92	2.65	0.62	1.81	0.26	1.79	0.27	0.597	0.0418	4.33158	0.041	0.03	1.00	194	5
20130309 #06	1.75	2.42	0.53	1.62	0.23	1.66	0.24	0.527	0.0316	3.67548	0.031	0.02	1.01	188	5
20130309 #07	1.86	2.64	0.57	1.74	0.26	1.76	0.26	0.559	0.0363	3.92934	0.034	0.01	1.01	193	5
Average	1.85	2.62	0.58	1.74	0.25	1.76	0.25	0.570	0.0400	3.96702	0.037	0.02	1.01	193	
Standard Deviation	0.08	0.10	0.03	0.06	0.01	0.07	0.01	0.025	0.0065	0.19936	0.009	0.01	0.004	3	
Relative Standard Deviation	4%	4%	5%	4%	5%	4%	5%	4%	16%	5%	23%	30%	0.4%	2%	
Accepted Values*	0.36	2.51	0.56	1.66	0.25	1.65	0.25	0.582	0.0357	2.87047	0.032	0.01	0.93	166	

Table A7c. TiO_2 and trace element analyses of the basalt standard BIR-1.

KL2-G (part 1)

Date	Rb	Sr	Y	Zr	Nb	Cs	Ba	La	Ce	Pr	Nd	Sm	Eu	Gd	N
20100707 #01	8.7	356	25.4	152	15	0.115	123	13.1	32.9	4.6	21.7	5.55	1.92	5.92	3
20110209 #01	8.6	348	24.6	148	15	0.112	119	12.6	31.9	4.4	21.0	5.34	1.86	5.66	5
20110209 #02	8.8	364	26.2	156	15	0.118	127	13.6	33.9	4.8	22.4	5.76	1.98	6.18	5
20110209 #03	8.7	353	25.2	151	15	0.113	120	12.8	32.1	4.5	21.1	5.34	1.86	5.82	5
20110209 #04	8.7	358	25.6	153	15	0.117	125	13.4	33.6	4.7	22.2	5.72	1.97	6.00	6
20110209 #05	8.6	353	25.0	150	15	0.116	121	12.8	32.6	4.5	21.3	5.45	1.88	5.79	5
20110209 #06	8.8	360	25.9	154	15	0.114	125	13.4	33.3	4.7	22.2	5.68	1.97	6.08	4
20110209 #07	0	0	25.4	153	15	0.115	122	12.9	32.5	4.5	0	5.48	1.89	5.81	5
20110209 #08	0	0	25.4	151	15	0.115	125	13.3	33.4	4.7	0	5.64	1.96	6.05	4
20110209 #09	8.6	352	24.8	148	15	0.113	122	12.8	32.7	4.5	21.2	5.37	1.89	5.73	5
20110209 #10	8.8	361	26.1	157	15	0.118	124	13.5	33.2	4.7	22.3	5.78	1.96	6.15	4
20110304 #01	8.5	348	24.6	148	15	0.111	119	12.6	31.9	4.4	21.0	5.34	1.86	5.66	5
20110304 #02	8.8	364	26.2	156	15	0.119	127	13.6	33.9	4.8	22.4	5.76	1.98	6.18	5
20110304 #03	8.7	353	25.0	149	15	0.113	120	12.7	32.1	4.5	21.1	5.34	1.86	5.74	5
20110304 #04	8.7	359	25.4	152	15	0.116	125	13.4	33.6	4.7	22.2	5.72	1.97	5.93	6
20110304 #05	8.6	351	25.0	150	15	0.115	121	12.8	32.6	4.5	21.3	5.45	1.88	5.79	5
20110304 #06	8.8	358	25.9	154	15	0.115	125	13.4	33.3	4.7	22.2	5.68	1.97	6.08	4
20110304 #07	8.7	354	25.0	151	15	0.114	119	12.5	32.1	4.4	21.1	5.39	1.86	5.63	5
20110304 #08	8.7	359	25.5	154	15	0.121	127	13.4	34.0	4.7	22.4	5.75	1.99	6.04	4
20110304 #09	8.6	352	24.5	148	15	0.112	122	12.8	32.7	4.5	21.2	5.37	1.89	5.73	5
20110304 #10	8.8	361	25.8	157	15	0.119	124	13.5	33.2	4.7	22.3	5.78	1.95	6.15	4
20120309 #01	8.1	341	24.0	140	14	0.090	109	11.8	29.5	4.1	19.5	4.86	1.70	5.19	6
20120309 #02	9.0	356	25.4	151	15	0.124	124	13.5	33.7	4.7	22.4	5.73	2.00	6.17	6
20120309 #03	9.1	363	26.1	153	15	0.128	131	14.3	36.0	5.0	23.5	6.13	2.08	6.47	5
20120309 #04	7.9	327	23.3	135	14	0.106	103	11.1	28.0	3.9	18.3	4.71	1.66	4.89	4
20120309 #05	8.9	351	25.9	152	15	0.124	122	13.0	32.9	4.6	21.6	5.52	1.98	5.93	4
20120309 #06	8.4	336	24.0	143	14	0.103	107	11.5	28.7	4.0	18.8	4.81	1.67	5.08	4
20120309 #07	9.1	356	25.4	153	15	0.131	123	13.0	33.0	4.6	22.1	5.53	2.01	6.00	3
20120309 #08	8.3	338	24.0	145	14	0.103	114	12.1	30.6	4.3	20.1	5.19	1.77	5.44	6
20120309 #09	8.6	356	25.5	152	15	0.110	122	13.1	32.8	4.7	22.0	5.46	1.93	6.10	6
20120309 #10	9.1	365	26.1	155	16	0.132	128	13.6	34.1	4.9	23.1	5.81	2.06	6.22	6
20120309 #11	8.0	316	22.3	134	13	0.092	100	10.6	26.5	3.7	17.3	4.46	1.56	4.73	5
20120309 #12	8.6	354	25.5	153	15	0.122	123	13.0	32.6	4.6	21.3	5.35	1.89	5.92	5
20120309 #13	8.7	356	25.5	151	15	0.109	122	13.0	33.0	4.6	22.0	5.64	1.92	5.87	5
20120309 #14	9.0	366	25.6	154	15	0.142	127	13.7	34.1	4.7	22.6	5.83	1.99	6.14	4
Average	8.7	353	25.2	150	15	0.115	121	12.9	32.5	4.5	21.4	5.48	1.90	5.84	
Standard Deviation	0.28	10.88	0.85	5.53	0.47	0.01	6.91	0.75	1.84	0.26	1.34	0.35	0.11	0.38	
Relative Standard Deviation	3%	3%	3%	4%	3%	9%	6%	6%	6%	6%	6%	6%	6%	7%	
Accepted Values	8.7	356	25.4	152	15	0.115	123	13.1	32.4	4.6	21.6	5.54	1.92	5.92	

Table A7d. Trace element analyses of the basalt standard KL2-G.

KL2-G (part 2)

Date	Tb	Dy	Ho	Er	Tm	Yb	Lu	Hf	Ta	Pb	Th	U	TiO_2	Ni(60)	N
20100707 #01	0.89	5.22	0.961	2.54	0.331	2.1	0.285	3.93	0.961	2.07	1.03	0.548	2.56	112	3
20110209 #01	0.85	4.94	0.913	2.40	0.314	2.0	0.269	3.70	0.918	2.00	0.97	0.534	2.52	112	5
20110209 #02	0.93	5.50	1.01	2.68	0.348	2.2	0.301	4.16	1.00	2.14	1.09	0.562	2.60	112	5
20110209 #03	0.87	5.08	0.932	2.48	0.323	2.0	0.281	3.83	0.942	2.04	1.00	0.519	2.55	114	5
20110209 #04	0.91	5.34	0.986	2.59	0.338	2.1	0.288	4.01	0.977	2.10	1.06	0.572	2.57	110	6
20110209 #05	0.87	5.08	0.934	2.49	0.319	2.0	0.276	3.77	0.923	2.01	1.00	0.549	2.54	113	5
20110209 #06	0.92	5.39	1.00	2.60	0.346	2.2	0.296	4.13	1.01	2.15	1.07	0.547	2.59	110	4
20110209 #07	0	5.12	0	2.47	0.325	2.0	0.279	0	0.946	0	0	0.523	0	115	5
20110209 #08	0	5.35	0	2.62	0.338	2.2	0.292	0	0.980	0	0	0.579	0	109	4
20110209 #09	0.87	5.01	0.924	2.46	0.317	2.0	0.276	3.78	0.925	2.02	1.00	0.528	2.54	111	5
20110209 #10	0.92	5.48	1.01	2.64	0.349	2.2	0.296	4.12	1.01	2.13	1.07	0.573	2.58	113	4
20110304 #01	0.85	4.94	0.913	2.40	0.314	2.0	0.269	3.70	0.918	2.00	0.97	0.533	2.48	112	5
20110304 #02	0.93	5.50	1.01	2.68	0.348	2.2	0.301	4.16	1.00	2.14	1.09	0.563	2.56	112	5
20110304 #03	0.86	5.07	0.913	2.48	0.320	2.0	0.280	3.82	0.941	2.04	1.00	0.519	2.54	116	5
20110304 #04	0.90	5.34	0.968	2.59	0.335	2.1	0.289	4.02	0.978	2.10	1.06	0.572	2.56	112	6
20110304 #05	0.87	5.08	0.934	2.49	0.319	2.0	0.276	3.77	0.923	2.01	1.00	0.549	2.54	113	5
20110304 #06	0.92	5.39	1.00	2.60	0.346	2.2	0.296	4.13	1.01	2.15	1.07	0.547	2.59	110	4
20110304 #07	0.84	4.95	0.910	2.39	0.315	2.0	0.270	3.71	0.933	2.06	0.99	0.516	2.57	116	5
20110304 #08	0.91	5.36	0.985	2.61	0.338	2.2	0.293	4.03	0.997	2.08	1.09	0.588	2.55	110	4
20110304 #09	0.86	5.00	0.924	2.46	0.317	2.0	0.276	3.77	0.922	2.03	1.00	0.548	2.54	111	5
20110304 #10	0.92	5.50	1.01	2.64	0.349	2.2	0.297	4.13	1.01	2.13	1.07	0.594	2.58	113	4
20120309 #01	0.78	4.60	0.843	2.19	0.293	1.8	0.252	3.39	0.846	1.77	0.90	0.463	2.56	106	6
20120309 #02	0.92	5.43	1.02	2.62	0.344	2.2	0.289	4.01	1.01	2.19	1.07	0.592	2.56	115	6
20120309 #03	0.98	5.72	1.03	2.71	0.353	2.4	0.317	4.18	1.05	2.29	1.13	0.581	2.57	115	5
20120309 #04	0.75	4.30	0.812	2.10	0.280	1.9	0.234	3.26	0.815	1.74	0.85	0.497	2.54	109	4
20120309 #05	0.89	5.26	0.943	2.55	0.328	2.3	0.285	3.91	1.00	2.09	1.02	0.599	2.58	112	4
20120309 #06	0.75	4.51	0.837	2.20	0.286	1.8	0.243	3.41	0.841	1.88	0.89	0.476	2.56	110	4
20120309 #07	0.92	5.54	1.01	2.54	0.349	2.1	0.300	3.91	0.947	2.09	1.07	0.644	2.56	114	3
20120309 #08	0.84	4.92	0.889	2.35	0.300	1.9	0.262	3.68	0.895	1.89	0.94	0.519	2.51	110	6
20120309 #09	0.90	5.16	0.963	2.62	0.338	2.1	0.292	3.97	0.962	2.11	1.02	0.581	2.56	111	6
20120309 #10	0.93	5.58	1.03	2.65	0.355	2.2	0.301	4.15	0.990	2.21	1.08	0.545	2.61	115	6
20120309 #11	0.70	4.26	0.769	2.03	0.260	1.6	0.233	3.07	0.780	1.64	0.83	0.422	2.51	109	5
20120309 #12	0.88	5.10	0.953	2.47	0.330	2.1	0.277	3.92	0.940	2.02	1.01	0.544	2.58	113	5
20120309 #13	0.90	5.29	0.958	2.56	0.327	2.0	0.283	3.93	0.957	2.04	1.03	0.539	2.55	112	5
20120309 #14	0.93	5.33	1.00	2.67	0.349	2.2	0.300	4.07	1.00	2.20	1.06	0.640	2.60	114	4
Average	0.88	5.16	0.948	2.50	0.327	2.1	0.282	3.86	0.950	2.05	1.02	0.549	2.56	112	
Standard Deviation	0.06	0.34	0.06	0.16	0.02	0.15	0.02	0.27	0.06	0.14	0.07	0.04	0.03	2.28	
Relative Standard Deviation	7%	7%	7%	7%	7%	7%	7%	7%	6%	7%	7%	8%	1%	2%	
Accepted Values	0.89	5.22	0.961	2.54	0.331	2.1	0.285	3.93	0.961	2.07	1.02	0.548	2.56	112	

Table A7e. TiO_2 and tracele element analyses of the basalt standard KL2-G.

8.8) Appendix 8: Tables - relative uncertainty ranges

Relative uncertainties for each element for each sample were calculated by dividing the uncertainty of each element (the standard deviation of all measurements of the standard VG-2 for major elements and BIR-1 for trace elements) by the measured concentration (ppm) of that element in each sample and multiplying by 100 to result in a percent value. Percentages were rounded to zero decimal places. Aggregated relative uncertainty ranges are presented for each Gakkel Ridge volcanic zone in the tables below. Volcanic centers EVZ31, EVZ37, and EVZ43 are all grouped together as EVZ31-37-43.

Major elements

Zone	Mg#	MgO	SiO_2	Al_2O_3	Na_2O	K_2O	TiO_2	CaO	FeO	MnO	Cl	S	P_2O_5
SMZ13	<1%	<1%	<1%	<1%	1%	1-2%	1%	<1%	1%	8-10%	4-11%	6-8%	3-6%
SMZ19	<1%	<1%	<1%	<1%	1%	1-12%	1%	<1%	1%	8-11%	4-20%	5-7%	5-14%
EVZ31-37-43	<1%	<1-1%	<1%	<1%	1%	2-3%	<1-1%	<1%	1%	7-10%	7-20%	4-6%	3-6%
EVZ55	<1%	<1%	<1%	<1%	1%	2-6%	1%	<1%	1%	8-10%	12-41%	5-6%	5-11%

Table A8a. Relative uncertainty ranges of the major elements.

Trace elements (part 1)

Zone	Rb	Sr	Y	Zr	Nb	Cs	Ba	La	Ce	Pr	Nd	Sm	Eu	Gd
SMZ13	<1-1%	1-2%	1%	<1%	<1%	3-12%	<1%	<1%	<1%	<1-1%	1%	1%	1-2%	2%
SMZ19	<1-6%	1-2%	1-2%	<1-1%	<1-1%	4-74%	<1-3%	<1-1%	<1-1%	<1-1%	1%	1-2%	1-2%	2-3%
EVZ31-37-43	<1-1%	1-2%	1%	<1%	<1%	11-25%	<1-1%	<1%	<1-1%	<1-1%	<1-1%	1-2%	1-2%	1-2%
EVZ55	1-3%	1-2%	1-2%	<1-1%	<1-1%	17-34%	<1-3%	<1-1%	<1-1%	<1-1%	1-2%	1-2%	2%	2-3%

Table A8b. Relative uncertainty ranges of the trace elements.

Trace elements (part 2)

Zone	Tb	Dy	Ho	Er	Tm	Yb	Lu	Hf	Ta	Pb	Th	U	TiO_2	Sc
SMZ13	8-11%	1-2%	2-3%	1-2%	2-3%	2-3%	2-3%	1%	1-2%	14-30%	<1-2%	1-5%	<1%	8-9%
SMZ19	9-13%	2-3%	3-4%	2%	2-4%	2-3%	3%	1-2%	1-8%	20-58%	1-8%	2-19%	<1%	7-10%
EVZ31-37-43	6-12%	1-2%	2-3%	1-2%	2-3%	1-3%	1-3%	1%	1-2%	20-33%	1-2%	2-5%	<1%	7-9%
EVZ55	11-14%	2%	3-4%	2%	3-4%	2-3%	3%	1-2%	1-4%	26-58%	1-5%	3-11%	<1%	7-9%

Table A8c. Relative uncertainty ranges of trace elements and TiO_2.

9) REFERENCES

Brodholt J.P., Batiza R. (1989) *Global systematics of unaveraged mid-ocean ridge basalt compositions: comment on "global correlations of ocean ridge basalt chemistry with axial depth and crustal thickness" by E.M. Klein and C.H. Langmuir*. Journal of Geophysical Reasearch, vol 94, p 4231-4239.

Cochran J.R. (2008) *Seamount volcanism along the Gakkel Ridge, Arctic Ocean*. Geophysics Journal International, vol 174, p 1153-1173.

Collier M.L., Kelemen P.B. (2010) *The case for reactive crystallization at mid-ocean ridges*. Journal of Petrology, vol 51, p 1913-1940.

Dick H.J.B., Lin J., Schouten H. (2003) *An ultraslow-spreading class of ocean ridge*. Nature, vol 426, p 405-412.

Elthon D., Stewart M., Ross D.K. (1992) *Compositional trends of minerals in oceanic cumulates*. Journal of Geophysical Research, vol 97, p 189-199.

Engen O., Eldholm O., Bungum H. (2003) *The Arctic plate boundary*. Journal of Geophysical Research, vol 108(B2), 2075

Goldstein S.L., Soffer G., Langmuir C.H., Lehnert K.A., Graham D.W., and Michael P.J. (2008) *Origin of a 'southern hemisphere' geochemical signature in the arctic upper mantle*. Nature, vol 453, Issue 7191, p 89-93. DOI:10.1038/nature06919

Graham D.J., Midgley N.G. (2000) *Graphical representation of particle shape using triangular diagrams: an Excel spreadsheet method*. Earth Surface Processes and Landforms, vol 25, p 1473-1477.

Grove T.L., Kinzler R.J., Bryan W.B. (1992) *Fractionation of mid-ocean ridge basalt (MORB).* In: Morgan J.P., Blackman D.K., Sinton J.M. (Eds.), Mantle Flow and Melt Generation at Mid-Ocean Ridges, Geophysical Monograph Series, American Geophysical Union, Washington, vol 71, p 281-310.

Hart S.R. (1984) *A large-scale isotopic anomaly in the Southern Hemisphere mantle*. Nature, vol 309, p 753-757.

Hart S.R., Zindler A. (1986) *In search of a bulk-earth composition*. Chemical Geology, vol 57, p 247-267.

Helffrich G.R., Wood B.J. (2001) *The Earth's mantle*. Nature, vol 412, p 501-507.

Hofmann A.W. (1988) *Chemical differentiation of the Earth: the relationship between mantle, continental crust, and oceanic crust*. Earth and Planetary Science Letters, vol 90, p 297-314.

Hofmann A.W. (1997) *Mantle geochemistry: the message from oceanic volcanism*. Nature, vol 385, p 219-229.

Hofmann A.W. (2007) *The lost continents*. Nature, vol 448, p 655-656.

Hofmann A.W., White W.M. (1982) *Mantle plumes from ancient oceanic crust. Earth and Planetary Science Letters*, vol 57, p 421-436.

Holness M.B., Richter F.M. (1989) *Possible effects of spreading rate on MORB isotopic and rare earth composition arising*. The Journal of Geology, vol 97, p 247-260.

Ionov D.A., Mukasa, S.B., Bodinier J.L. (2002) *Sr-Nd-Pb isotopic compositions of peridotite xenoliths from Spitsbergen: Numerical modeling indicates Sr-Nd decoupling in the mantle by melt percolation metasomatism*. Journal of Petrology, vol 43, p 2261-2278.

Jarosewich, E., Nelen J.A., Norberg J.A. (1980) Reference samples for electron microprobe analysis. Geostandards Newsletter, vol 4, p 43-47.

Jarosewich, E. (2002) *Smithsonian microbeam standards.* Journal of Research of the National Institute of Standards and Technology, vol 107, p 681-685.

Jochum K.P., Nohl U., Herwig K., Lammel E., Stoll B., Hofmann, A.W. (2005) *GeoReM: A new geochemical database for reference materials and isotopic standards*. Geostandards and Geoanalytical Research, vol 29, p 333-338.

Jokat W., Ritzmann O., Schmidt-Aursch M.C., Drachev S., Gauger S., Snow J. (2003) *Geophysical evidence for reduced melt production on the Arctic ultraslow Gakkel mid-ocean ridge*. Nature, vol 423, p 462-465.

Kamenetsky V.S., Everard J.L., Crawford A.J., Varne R., Eggins, S.M., Layton R. (2000) *Enriched end-member of primitive MORB melts: Petrology and geochemistry of glasses from Macquarie Island (SW Pacific*). Journal of Petrology, vol 41, p 411-430.

Kay R., Hubbard N.J., Gast P.W. (1970) *Chemical characteristics and origin of oceanic ridge volcanic rocks*. Journal of Geophysical Research, vol 75, p 1585-1613.

Kelemen P.B., Hirth G., Shimizu N., Spiegelman M., Dick H.J.B. (1997) *A review of melt migration processes in the adiabatically upwelling mantle beneath oceanic spreading ridges.* Philosophical Transactions of the Royal Society of London A, vol 355, p 283-318.

Klein E.M. (2003a) *Spread thin in the arctic*. Nature, vol 423, Issue 6943, p 932-933. DOI:10.1038/423932a

Klein E.M., (2003b) *Geochemistry of the igneous ocean crust*. In: Rudnick, R.L. (Ed.), The Crust: Treatise on Geochemistry, Elsevier-Pergamon, Oxford, vol 3, p 443-463.

Langmuir C.H., Klein E.M., Plank T. (1992) *Petrological systematics of mid-ocean ridge basalts: constraints on melt generation beneath ocean ridges*. In: Morgan J.P., Blackman D.K., Sinton J.M. (Eds.), Mantle Flow and Melt Generation at Mid-Ocean Ridges, Geophysical Monograph Series, American Geophysical Union, Washington D.C., vol 71, p 183-280.

Langmuir C.H., Forsyth D.W. (2007) *Mantle melting beneath mid-ocean ridges*. Oceanography, vol 20, p 78-89.

Lehnert K., Su Y., Langmuir C.H., Sarbas B., Nohl U. (2000) *A global geochemical database structure for rocks*. Geochemistry Geophysics Geosystems, vol 1, DOI:10.1029/1999GC000026.

Le Roex A.P., Dick H.J.B., Watkins R.T. (1992) *Petrogenesis of anomalous K-enriched MORB from the Southwest Indian Ridge: 11°53'E to 14°38'E*. Contributions to Mineralogy and Petrology, vol 110, p 253-268.

Liu C.Z., Snow J.E., Hellebrand E., Brugmann G., Handt A.V.D., Buchl A., Hofmann A.W. (2008) *Ancient, highly heterogeneous mantle beneath Gakkel ridge, Arctic Ocean*. Nature, vol 452, p 311-316.

McDonough W.F., Sun S.S. (1995) *The composition of the Earth*. Chemical Geology, vol 120, p 223-353.

Michael P.J., Langmuir C.H., Dick H.J.B., Snow J.E., Goldstein S.L., Graham D.W., Lehnert K., Kurras G., Jokat W., Mühe R., and Edmonds HN. (2003) *Magmatic and amagmatic seafloor generation at the ultraslow-spreading Gakkel ridge, Arctic Ocean*. Nature, vol 423, Issue 6943, p 956-U1. DOI:10.1038/nature01704

Mühe R.K., Bohrmann H., Hormann P.K., Thiede J., Stoffers P. (1991) *Spinifex basalts with komatiite-tholeitte trend from the Nansen-Gakkel Ridge (Arctic-Ocean)*. Tectonophysics, vol 190, p 95-108.

Mühe R., Devey C.W., Bohrmann H. (1993) *Isotope and trace element geochemistry of MORB from the Nansen-Gakkel ridge at 86° north*. Earth and Planetary Science Letters, vol 120, p 103-109.

Mühe R., Bohrmann H., Garbe-Schonberg D., Kassens H. (1997) *E-MORB glasses from the Gakkel Ridge (Arctic Ocean) at 87°N: evidence for the Earth's most northerly volcanic activity*. Earth and Planetary Science Letters, vol 152, p 1-9.

Nauret F., Moreira M., Snow J.E. (2010) *Rare gases in lavas from the ultraslow spreading Lena Trough, Arctic Ocean*. Geochemistry Geophysics Geosystems, vol 11, Q0AC04

Nauret E., Snow J.E., Hellebrand E., Weis D. (2011) *Geochemical Composition of K-rich Lavas from the Lena Trough (Arctic Ocean). Journal of Petrology*, vol 52, p 1185-1206.

Navon O., Stolper E. (1987) *Geochemical consequences of melt percolation: the upper mantle as a chromatographic column*. The Journal of Geology, vol 95, p 285-307.

Ohara M.J. (1965) *Are ocean floor basalts primary magma?* Nature, vol 220, p 683-686.

Salters V.J.M., Stracke A. (2004) *Composition of the depleted mantle*. Geochemistry Geophysics Geosystems, vol 5, Q05004.

Schilling J.G. (1971) *Sea-floor evolution: rare-earth evidence*. Philosophical Transactions of the Royal Society of London. Series A, Mathematical and Physical Sciences, vol 268, p 663-706.

Schilling J.G. (1973) *Iceland mantle plume: Geochemical study of Reykjanes Ridge*. Nature, vol 242, p 565-571.

Shaw A.M., Behn M.D., Humphris S.E., Sohn R.A., Gregg P.M. (2010) *Deep pooling of low degree melts and volatile fluxes at the 85E segment of Gakkel Ridge: Evidence from olivine-hosted melt inclusions and glasses*. Earth and Planetary Science Letters, vol 289, p 311-322.

Snow J.E., Jokat W., Hellebrand E., Mühe R. (2001) *Magmatic and hydrothermal activity in Lena Trough, Arctic Ocean*. EOS, Transactions American Geophysical Union, vol 82, p 193, 197-198.

Snow, J.E. and Petrology Group, ARK VXII-2 (2002) *Petrogenesis of crustal rocks*. In: Thiede, J. et al. (2002) *Cruise report, ARK XVII/2*. Reports on Polar and Marine Research, vol 421, p 118-164.

Snow J.E., Edmonds H.M. (2007) *Ultraslow-spreading ridges rapid paradigm changes.* Oceanography, vol 20, p 90-101.

Snow J.E., Hellebrand E., Handt A.V.D., Nauret F., Gao Y., Schenke H.W. (2011) *Oblique nonvolcanic seafloor spreading in Lena Trough Arctic Ocean*. Geochemistry Geophysics Geosystems, Vol 12, Q10009.

Sobolev A.V., Hofmann A.W., Sobolev S.V., Nikogosian I.K. (2005) *An olivine-free mantle source of Hawaiian shield basalts*. Nature, vol 434, p 590-597.

Sobolev A.V, Hofmann A.W., Kuzmin D.V., Yaxley G.M., Arndt N.T., Chung S.L., Danyushevsky L.V., Elliot T., Frey F.A., Garcia M.O., Gurenko A.A., Kamenetsky V.S., Kerr A.C., Krivolutskaya N.A., Matvienkov V.V., Nikogosian I.K., Rocholl A., Sigurdsson I.A., Sushchevskaya N.M., Teklay M. (2007) *The amount of recycled crust in sources of mantle-derived melts*. Science, vol 316, p 412-417.

Standish J.J., Dick H.J.B., Michael P.J., Melson W.G., O'Hearn T. (2008) *MORB generation beneath the ultraslow spreading Southwest Indian Ridge (9-25E): Major element chemistry and the importance of process versus source*. Geochemistry Geophysics Geosystems, vol 9, Q05004.

Stolper E. (1980) *A phase diagram for mid-ocean ridge basalts: preliminary results and implications for petrogenesis*. Contributions to Mineralogy and Petrology, vol 74, p 13-27.

Sun S.S., McDonough W.F. (1989) *Chemical and isotopic systematics of oceanic basalts: implications for mantle composition and processes*. Geological Society, London, Special Publications, vol 42, p 313-345.

Van Keken P.E., Hauri E.H., Ballentine C.J. (2002) *Mantle mixing: generation, preservation, and destruction of chemical heterogeneity*. Annual Review of Earth and Planetary Sciences, vol 30, p 493-525

Walker D., Shibata T., DeLong S.E. (1979) Abyssal *tholeiites from the Oceanographer Fracture Zone*. Contributions to Mineralogy and Petrology, vol 70, p 111-125.

Weaver B.L. (1991a) *The origin of ocean island basalt end-member compositions: Trace element and isotopic constraints*. Earth and Planetary Science Letters, vol 104, p 381-397.

Weaver B.L. (1991b) *Trace element evidence for the origin of ocean-island basalts*. Geology, vol 19, p 123-126.

White, W.M. (2013) *Geochemistry*, 1st edition. West Sussex: Wiley-Blackwell.

Winter, J.D. (2001) *An Introduction to Igneous and Metamorphic Petrology*. Prentice-Hall Inc.

Wood D.A. (1979) *A variably veined suboceanic upper mantle – Genetic significance for mid-ocean ridge basalts from geochemical evidence*. Geology, vol 7, p 499-503.

Workman R.K., Hart S.R. (2005) *Major and trace element composition of the depleted MORB mantle (DMM)*. Earth and Planetary Science Letters, vol 231, p 53-72.

Zindler A., Hart S.R. (1986) *Chemical geodynamics*. Annual Review of Earth and Planetary Sciences. vol, 14, p 493-571.